Global Hall Magnetohydrodynamics and Coupled Fluid-Kinetic Simulations of Mercury's Dayside Magnetopause Dynamics

by

Changkun Li

A dissertation submitted in partial fulfillment
of the requirements for the degree of
Doctor of Philosophy
(Climate and Space Sciences and Engineering and Scientific Computing)
in the University of Michigan
2023

Doctoral Committee:

Professor Xianzhe Jia, Chair
Professor Emeritus James A. Slavin
Professor Alexander G. R. Thomas
Research Professor Gábor Tóth

Changkun Li

changkul@umich.edu

ORCID iD: 0000-0002-9623-7883

Dedication

To my parents, whose unwavering support and encouragement have been the driving force behind my doctoral journey and my transition into a future career in software engineering.

Acknowledgements

With heartfelt appreciation, I extend my gratitude to the individuals who have played an integral role in bringing this dissertation to fruition. Foremost, I express my sincere thanks to my advisor, Prof. Xianzhe Jia, for his generous financial support and invaluable, patient guidance. Working under his mentorship at the University of Michigan has been an exceptional privilege, and the knowledge, numerical techniques, and diligent work ethic I learnt from him will undoubtedly shape my future career. I am also deeply thankful to Prof. James Slavin and Prof. Gábor Tóth for their valuable insights into my research, and I extend my appreciation to Prof. Alexander Thomas for serving on my committee. Gratitude is also due to my cherished colleagues and friends at the University of Michigan, whose companionship and support have enriched my academic journey. Finally, I would like to thank my parents for their unwavering love and encouragement throughout this endeavor. Their constant presence and support have been a source of inspiration and strength.

Table of Contents

List of Tables

List of Figures

Abstract

Mercury possesses a miniature yet dynamic magnetosphere driven primarily by the solar wind through magnetic reconnection. Because Mercury is 60% closer to the Sun than Earth, its magnetosphere routinely experiences stronger external drivings than typically seen at Earth, thereby providing a natural laboratory for comparative studies of magnetic reconnection and the resultant magnetospheric dynamics.

A prominent feature of Mercury's interaction with the solar wind at the dayside magnetopause is frequent occurrence of flux transfer events (FTEs), which are thought to play an important role in driving the global convection. To investigate the generation and characteristics of FTEs under different solar wind Alfvénic Mach numbers (M_A) and IMF orientations, we first conducted a series of global simulations using the BATSRUS Hall Magnetohydrodynamics (MHD) model, which facilitates the occurrence of fast reconnection in current sheets by allowing separate bulk motions of plasma ions and electrons. An automated algorithm was also developed to consistently identify FTEs and extract their key properties from the simulations. In all simulations driven by steady upstream conditions, FTEs are formed quasi-periodically with recurrence time ranging from 2 to 9 seconds, and their characteristics vary in time as they evolve and interact with the surrounding environment. Our statistical analysis of the simulated FTEs reveals that the key properties of FTEs, including spatial size, traveling speed and core field strength, all exhibit notable dependence on the solar wind M_A and IMF orientation, and the trends identified from the simulations are generally consistent with previous MESSENGER observations.

It is also found that FTEs formed in the simulations contribute about 3% - 13% of the total open flux created at the dayside magnetopause that participates in the global circulation.

Next, we performed a series of Magnetohydrodynamics with Adaptively Embedded Particle-in-Cell (MHD-AEPIC) simulations using the same input parameters as used in the Hall-MHD runs to study in detail the kinetic signatures, asymmetries, and FTEs associated with Mercury's dayside magnetopause reconnection. By treating both ions and electrons kinetically, the embedded PIC model reveals crescent-shaped phase-space distributions near reconnection sites, counter-streaming ion populations in the cusp region, and temperature anisotropies within FTEs. A novel metric and algorithm are developed to automatically identify reconnection X-lines in our 3D simulations. The spatial distribution of reconnection sites as modeled by the PIC code exhibits notable dawn-dusk asymmetries, likely due to kinetic effects such as X-line spreading and Hall effects. The properties of FTEs in the MHD-AEPIC simulations also show clear dependencies on the solar wind M_A and IMF orientation, consistent with MESSENGER observations and previous Hall-MHD simulations. FTEs formed in our MHD-AEPIC model tend to carry a large amount of open flux, contributing 3% - 36% of total open flux generated at the dayside, suggesting that FTEs indeed play an important role in driving the Dungey cycle at Mercury.

Finally, we further analyzed the MHD-AEPIC simulation results to investigate the properties of simulated cusp filaments and proton precipitation, both of which have important consequences on the space weathering at Mercury. Our analysis reveals that cusp filaments map directly to FTEs and the ions and electrons within cusp filaments are significantly energized by the magnetopause reconnection. Dawn-dusk asymmetries in proton precipitation are also observed in close correspondence to the asymmetries in magnetopause reconnection occurrence. The global

proton precipitation rate is found to increase with decreasing solar wind M_A and decreasing IMF clock angle.

Chapter 1 Introduction

This chapter starts by introducing the solar wind and its interaction with Mercury's magnetosphere. Subsequently, it offers an overview of prior research efforts devoted to simulating Mercury's magnetosphere through numerical models. Finally, this chapter provides an outline of the structure and organization of this dissertation.

1.1 Solar Wind and Mercury's Magnetosphere

1.1.1 Solar Wind

Being the sole star within our Solar System, the Sun serves as a continuous source of energy for a variety of physical phenomena in the space environment. One of the primary mechanisms through which the Sun interacts directly with various planetary bodies, such as planets, comets and asteroids, is via the solar wind. Originating from the corona, which is the outermost layer of the solar atmosphere, the solar wind is a stream of high-temperature, ionized plasma flowing away from the Sun. The hot plasma emanating from the solar atmosphere also drags the solar magnetic field with them into the interplanetary space, resulting in the interplanetary magnetic field (IMF). *Parker* (1958) is the first to suggest that an equilibrium state does not exist for the solar atmosphere, and the pressure gradients between the solar corona base and the interstellar medium are capable of accelerating the solar wind to supersonic speeds. He also pointed out the existence of the IMF and further predicted that the footprint of the IMF is rooted on the solar surface and rotates slowly with the Sun, which leads to a twisted structure of IMF called the Parker spiral. A schematic illustration of the Parker spiral is shown in Figure 1-1.

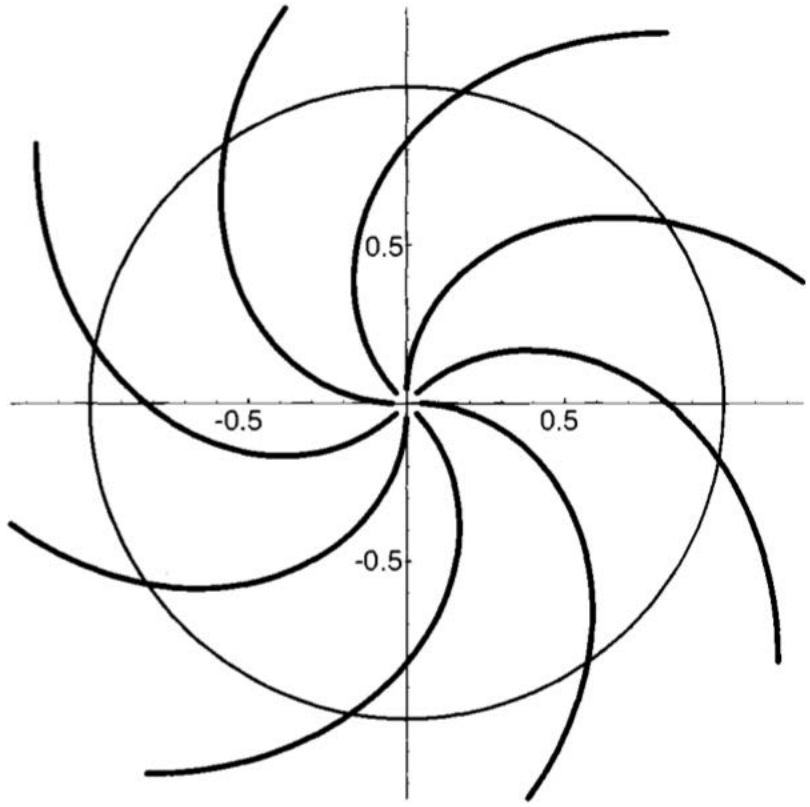

Figure 1-1: A schematic illustration of the spiral shape of the interplanetary magnetic field (IMF). (adapted from *Gombosi*, [1998])

The solar wind can be generally classified into two types based on its composition and speed: the slow wind with a typical speed of 300 ~ 500 km/s and a composition similar to the corona, and the fast wind with a typical speed of about 750 km/s and a composition similar to the photosphere. The speed of the solar wind is primarily controlled by the magnetic field structure and strength in the solar corona. The slow wind originates from the regions called coronal streamers, where the shape of the magnetic field line resembles a loop with its two ends rooted on the Sun, making it difficult for the particles to escape. The fast wind is generated within the regions termed as corona holes, where the field lines are "open" with one end rooted on the solar surface and the other end extended radially outward into the interplanetary space. When the trailing fast solar wind stream approaches the slow solar wind from behind, a spiral compression zone called

corotating interaction region is formed at their interface. The compression results in enhanced plasma pressure and IMF strength, which can cause strong disturbances to planetary magnetospheres.

The plasmas and IMF carried by the solar wind interact with the intrinsic magnetic fields of planets, and such interaction plays a crucial role in the formation and evolution of planetary magnetospheres. In this dissertation, we study the magnetosphere of Mercury and the following subsections give an introduction of its general characteristics.

1.1.2 Mercury's Magnetosphere

Mercury's magnetic field was initially discovered through measurements taken by the magnetometer experiment aboard the Mariner 10 spacecraft during its flybys of Mercury in 1974 and 1975 (*Ness et al*., 1974, 1975). Subsequent and more refined measurements were obtained by the magnetometer aboard the MErcury Surface, Space ENvironment, GEochemistry, and Ranging (MESSENGER) spacecraft, which orbited Mercury from 2011 to 2015. These measurements revealed several key characteristics of Mercury's magnetic field. Specifically, the magnetic field resembles a dipole field aligned with Mercury's spin axis, with a deviation of less than 1°. Additionally, the center of the intrinsic magnetic field is offset to the north relative to the planet's rotational center by approximately 484 km, which is roughly equal to 0.2 Mercury radius (R_M ~ 2437.9 km). The field lines launch from Mercury's southern hemisphere and then re-enter the planet's surface in the northern hemisphere, which is the same as the orientation of Earth's magnetic field. The dipole moment of Mercury's intrinsic field is approximately 190 $nT \cdot R_M^3$ (*Anderson et al*., 2011). Compared to Earth's dipole field, the surface magnetic field at Mercury's magnetic equator is approximately 150 times weaker in strength.

Mercury has a highly eccentric orbit around the Sun, with perihelion and aphelion at ~ 0.31 and 0.47 AU, respectively. Its proximity to the Sun together with its elliptical orbit result in a dynamically changing local plasma environment around Mercury. The fundamental parameters characterizing the solar wind, which exerts strong influence on magnetospheric dynamics, are the IMF, solar wind plasma density, temperature, and bulk flow velocity. Regarding the ambient solar wind, all of these parameters, except for velocity, exhibit notable variations as one moves away from the Sun along the radial direction. It is conventionally assumed that the solar wind has already been accelerated to its average asymptotic speed ~ 430 km/s before passing Mercury's orbit. Table 1-1, which is taken from *Slavin and Holzer* (1981), lists a group of typical solar wind parameters computed at various terrestrial planets with their radial dependencies. These parameters were further evaluated for both Mercury's perihelion and aphelion positions in its orbital path. Notably, the solar wind proton density (n_p) and the IMF strength (B) at perihelion are approximately twice those observed at aphelion. This observation underscores the range of expected variations of Mercury's local plasma environment over the course of its orbital motion around the Sun.

Table 1-1: Typical solar wind conditions scaled from Earth's orbit at 1 AU to the orbit of other terrestrial planets. Solar wind values for perihelion and aphelion of Mercury's highly eccentric orbit were calculated. Basic parameters listed in the table are radial distance of planet's orbit from the sun (R), solar wind velocity (V_{SW}), proton number density (n_p), IMF strength (B), proton and electron temperature (T_p and T_e, respectively). The scaling of each parameter with R is also tabulated in their respectively columns. This table is adapted from *Slavin and Holzer* (1981).

TABLE 1. Interplanetary Conditions

Planet	R, AU	V_{sw}, Km/S	n_p, cm^{-3}	B, nT	T_p, 10^4°K	T_e, 10^4°K
Mercury	0.31	430	73	46	17	22
	0.47	430	32	21	13	19
Venus	0.72	430	14	10	10	17
Earth	1.00	430	7	6	8	15
Mars	1.52	430	3.0	3.3	6.1	13
(Scaling)	•••	R^0	R^{-2}	$R^{-1}(2R^{-2}+2)^{1/2}$	$R^{-2/3}$	$R^{-1/3}$

At Mercury's orbit, its dipole magnetic field constantly interacts with the ambient super-Alfvénic and super-sonic solar wind. The region that is dominated by Mercury's intrinsic magnetic field is called magnetosphere. An illustration of the average state of Mercury's magnetosphere is

shown in Figure 1-2. Due to its weak intrinsic magnetic field and the strong upstream solar wind driving at its orbit, Mercury's magnetosphere is much smaller with respect to the size of the planet compared to Earth's magnetosphere. Nonetheless, Mercury still stands out in our solar system as a unique laboratory for space plasma research due to the presence of its global intrinsic magnetic field. The presence of an appreciable intrinsic field at Mercury sets it apart from the other inner planets, i.e., Mars and Venus, which lack a global intrinsic magnetic field, and Mercury's magnetosphere perhaps represents the closest analog to Earth's in terms of magnetospheric configuration and dynamics, as will be discussed in the following chapters.

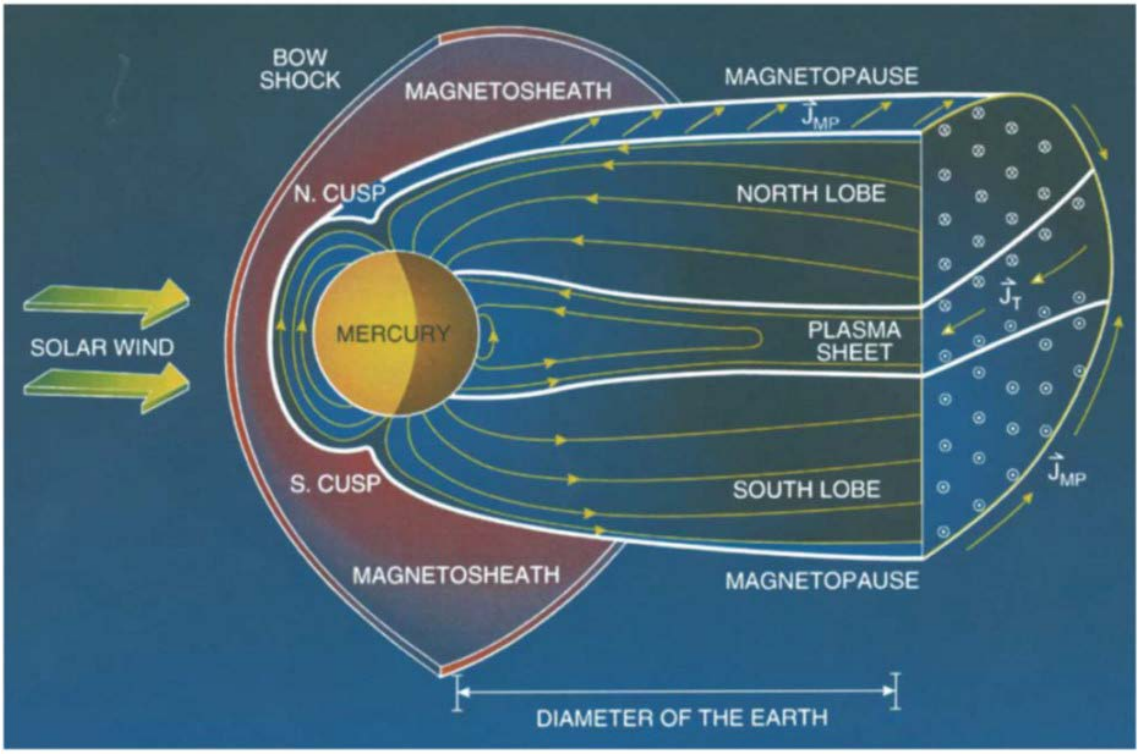

Figure 1-2: An illustration of the nominal state of Mercury's magnetosphere with key regions of the magnetosphere labelled. (adapted from *Slavin* [2004])

Given the super-Alfvénic nature of the solar wind at Mercury's orbit, characterized by an Alfvénic Mach number (M_A) that is larger than unity, a bow shock is formed in front of the magnetosphere. Across the bow shock interface, the solar wind experiences compression, heating,

and deceleration. With respect to Mercury's reference frame, the solar wind's velocity undergoes a transition from super-Alfvénic to sub-Alfvénic. The specific location of the bow shock is dependent upon various factors, including solar wind conditions, as well as the strength of the planet's magnetic field. After crossing the bow shock, the solar wind flow experiences a reduction in speed and continues to flow towards Mercury, where it encounters and interacts with the planet's magnetic field. The interface, where the magnetic pressure exerted by Mercury's dipole field balances the collective pressure of the shocked solar wind, is called the magnetopause. The region situated between the magnetopause and the bow shock is referred to as the magnetosheath. On the dayside of Mercury, the magnetic field dominated by the planetary dipole undergoes compression, while on the nightside, it extends into an elongated shape forming the magnetotail. The magnetotail can be further divided into two segments separated by a cross-tail current sheet: the northern lobe comprises magnetic field lines directed toward Mercury and the southern lobe consists of magnetic field lines directed away from Mercury.

1.1.3 Dungey Cycle

Mercury's magnetosphere is a dynamic system characterized by a global magnetospheric convection known as the Dungey cycle, initially proposed by *Dungey* (1961) to describe the global plasma and magnetic flux circulation at Earth. This convection pattern arises due to the occurrence of magnetic reconnection, a fundamental process capable of transferring energy from the magnetic field to the plasma, at both the dayside magnetopause and in the nightside magnetotail. Figure 1-3 illustrates the successive stages of the Dungey cycle. It starts with the reconnection between closed magnetospheric field lines (depicted in red) and solar wind magnetic field lines (shown in blue), resulting in the formation of "open" field lines tethered to the planet at one end (indicated in purple). These open field lines serve as a channel for the solar wind plasma to enter the

magnetosphere. Then, the plasma and open field lines are transported poleward first through the cusps and then into the magnetotail, causing the accumulation of magnetic flux in the form of open field lines within the magnetotail region. Subsequently, magnetic reconnection occurs across the tail current sheet, resulting in the return of plasma and closed field lines (red) to the dayside and thus completing the Dungey cycle. At Earth, the Dungey cycle typically takes about 1 hour. Since the progression of Dungey cycle is strongly influenced by the dimensions of the planetary magnetosphere and its interaction with the solar wind, the Dungey cycle at Mercury is much faster and more intense compared to that at Earth with a typical duration between 1 - 3 minutes due to the stronger solar wind forcing present at Mercury's orbit.

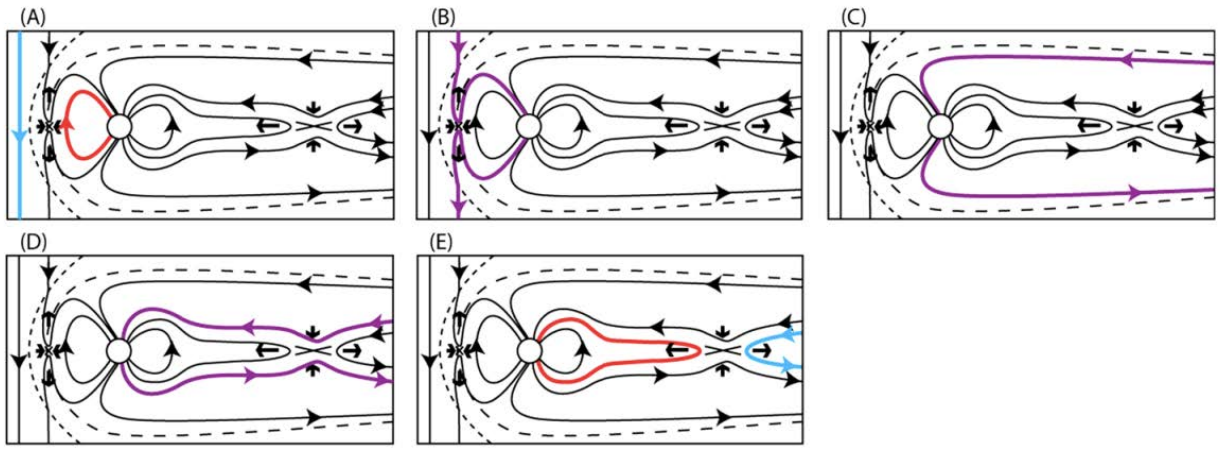

Figure 1-3: A cartoon showing the successive stages of the Dungey cycle. (adapted from *Eastwood et al*. [2015])

1.1.4 Magnetic Reconnection

Magnetic reconnection, as described in the previous subsection, is the key physical process that drives the Dungey cycle at Mercury by reconfiguring the magnetic field topology and converting the free energy stored in magnetic field into particle kinetic and thermal energy. To understand the physics of magnetic reconnection under the magnetohydrodynamic (MHD) framework, we start by introducing a generalized Ohm's law for collisionless plasma:

$$\boldsymbol{E} + \boldsymbol{u} \times \boldsymbol{B} = \eta \boldsymbol{J} + \frac{1}{ne}\boldsymbol{J} \times \boldsymbol{B} - \frac{1}{ne}\nabla \cdot \boldsymbol{P_e} + \frac{m_e}{ne^2}\frac{\partial \boldsymbol{J}}{\partial t}, \quad (1\text{-}1)$$

where $\boldsymbol{E}$ is the electric field, $\boldsymbol{u}$ is the plasma bulk flow velocity, $\boldsymbol{B}$ is the magnetic field, η is the resistivity of the plasma, $\boldsymbol{J}$ is the current density, e is the magnitude of the charge carried by an electron, n is the number density of ions or electrons (charge neutrality is assumed in MHD), m_e is the electron mass, and $\boldsymbol{P_e}$ is the electron pressure tensor. The right-hand-side of Equation (1-1) describes the deviation from ideal MHD in which $\boldsymbol{E} + \boldsymbol{u} \times \boldsymbol{B} = \boldsymbol{0}$. In an ideal MHD fluid, the magnetic field lines move together with the plasma (or are frozen-in to the plasma), and the resultant electric field is always perpendicular to the magnetic field. The magnetic reconnection only occurs when the deviation from ideal MHD becomes significant on scales comparable to electron inertial length. Figure 1-4 shows a two-dimensional schematic view of magnetic reconnection.

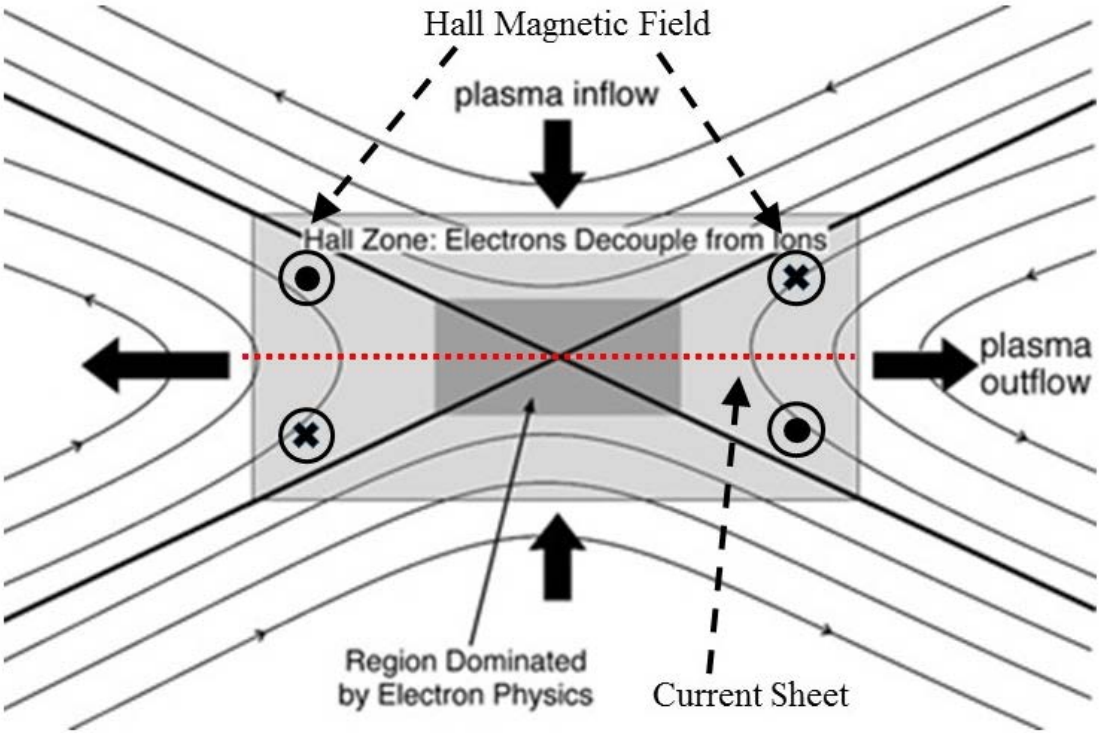

Figure 1-4: A two-dimensional schematic diagram of magnetic reconnection. The outer light shaded box represents the Hall/ion diffusion region and the inner dark shaded box represents the electron diffusion region (URL: http://mms.space.swri.edu/science-3.html).

As shown in Figure 1-4, when two magnetic field lines with opposite orientations approach each other, a current sheet forms in the center due to the Ampere's law. As the thickness of this current sheet becomes smaller than the ion inertial length, the frozen-in condition for ions is violated and the ions are no longer co-moving with the magnetic field lines. This specific region is termed the ion diffusion region, where the magnitude of the Hall term ($\frac{1}{ne}\boldsymbol{J} \times \boldsymbol{B}$) is significantly larger than that of the convection term ($\boldsymbol{u} \times \boldsymbol{B}$) on the left-hand-side of Equation (1-1). By contrast, the electrons are still magnetized to the inflow magnetic field lines because of their smaller gyroradii. The decoupling of ions and electrons within this region leads to the characteristic quadrupolar Hall magnetic field. Subsequently, the inflow magnetic field lines break into two parts and reconnect at the neutral point situated within the electron diffusion region, where the frozen-in condition for electrons is violated and the electrons become demagnetized. In the electron diffusion region, the dominant term on the right-hand-side of Equation (1-1) is the electron pressure gradient term ($-\frac{1}{ne}\nabla \cdot \boldsymbol{P_e}$). The plasmas are then propelled away from the reconnection region at a velocity close to the local Alfvén speed, driven primarily by the parallel component of the electric field with respect to $\boldsymbol{B}$. Note that in Figure 1-4, only an idealized configuration of reconnection geometry is shown. However, it is not a strict requirement for the magnetic field lines to exhibit a perfectly opposing orientation in the inflow region for reconnection to take place. At Mercury, magnetic reconnection has been observed to occur over a wide range of shear angles, which are defined as the angles between the IMF and Mercury's magnetic field (*DiBraccio et al*., 2013).

The MHD theory of magnetic reconnection described above requires the plasma to behave as a charge-neutral fluid in thermal equilibrium (i.e., the particles are in Maxwellian distribution). However, these assumptions may not necessarily be valid at a spatial scale on the order of the

electron skin depth as non-Maxwellian particle distributions have been commonly observed within electron diffusion regions, such as observations by Magnetospheric Multiscale (MMS) mission (*Burch et al.*, 2016). Hence, a kinetic approach that treats plasma as a collection of individual particles, rather than as a continuous fluid, is better suited for understanding the underlying kinetic physics governing magnetic reconnection. A comprehensive discussion of this kinetic description of plasma and the associated numerical method will be provided in Section 2.3 of the next chapter.

1.1.5 Flux Transfer Events and Cusp Filaments

One of the key products of magnetic reconnection occurring at the magnetopause boundary is flux transfer events (FTEs), which were first discovered at the Earth's magnetopause based on magnetic field measurements (*Russell and Elphic*, 1978). FTEs are typically characterized by bipolar variations in the magnetic field component normal to the magnetopause surface and enhanced field strength near the center of the structure. Such magnetic signatures associated with FTEs suggest that their interior structures mostly resemble magnetic flux ropes with helical topology. Figure 1-5 shows schematic views of the internal magnetic field structure of a flux rope and the large-scale geometry of an FTE.

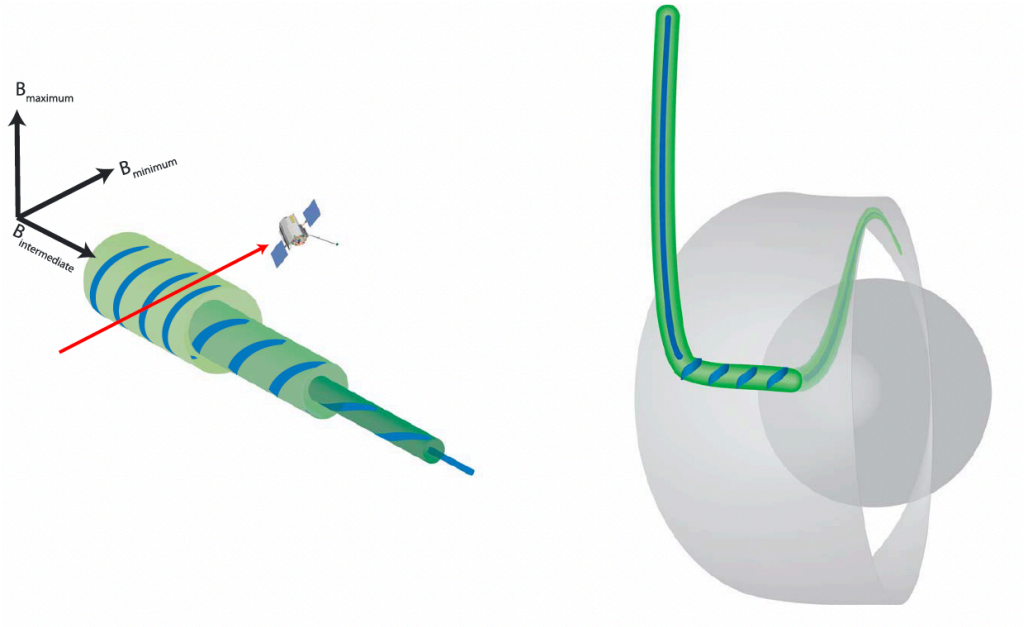

Figure 1-5: Schematic views of (left) the internal magnetic field structure of a flux rope (magnetic field lines through the structure are shown in blue) and (right) the characteristic location and orientation of a newly formed FTE at Mercury's dayside magnetopause. The planet and the magnetopause are represented by the grey-shaded surfaces with the Sun out of the page and to the left of the schematic view. The newly formed FTE is shown in green, and the blue line follows a magnetic field line through the structure. (adapted from *Imber et al*. [2014])

As revealed by MESSENGER observations, FTEs are prevalent at Mercury and consequently considered an important player in driving Mercury's magnetospheric dynamics (e.g., *Slavin et al*., 2010a) and influencing Mercury's exosphere through enhanced surface sputtering (e.g., *Sun et al*., 2022a). Many models have been proposed to explain the formation of FTEs. In this dissertation, we define "FTEs" as flux ropes developing in the magnetopause current layer as a result of multiple X-line reconnection (MXR). Figure 1-6 shows the schematics of the MXR model first introduced by *Lee and Fu* (1985). In this model, two or more X-lines are concurrently or sequentially generated on the magnetopause surface, resulting in the formation of a helical flux rope (i.e., FTE) between each pair of X-lines (as depicted in Figure 1-6a and b). Subsequent to the reconnection event, the pair of FTEs will move in opposite directions due to the external force exerted by magnetosheath plasma flow and the magnetic tension force associated with the curved magnetic field lines (as depicted in Figure 1-6c and d).

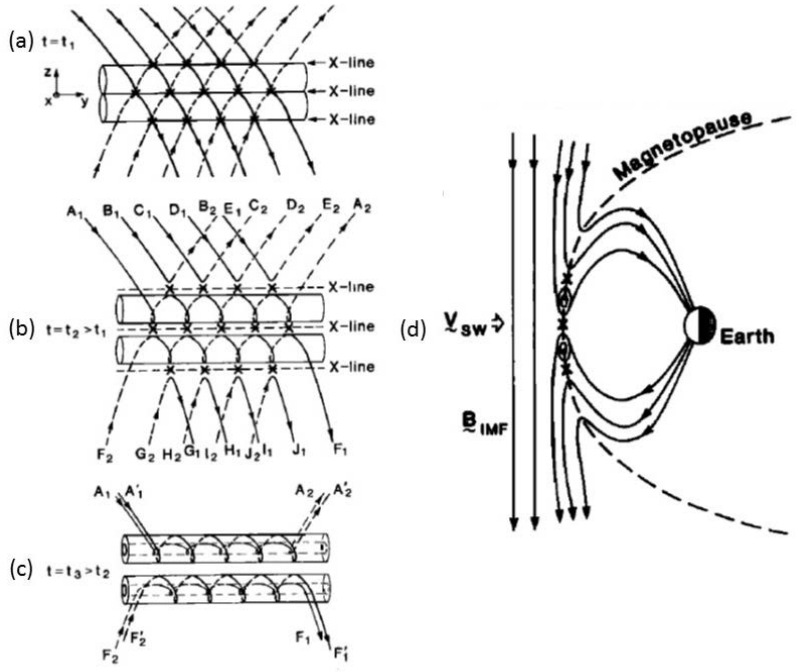

Figure 1-6: (a - c) Schematics illustrating the formation of a pair of flux transfer events (i.e., flux ropes) from multiple X-line reconnection at the dayside magnetopause. (d) Side view of the FTEs forming on the magnetopause surface. (adapted from *Lee and Fu* [1985])

As illustrated in Figure 1-5, the helical magnetic flux making up the FTE are "open" with one end connected to the draped IMF and the other end rooted in Mercury. The additional magnetic flux opened by magnetopause reconnection also fills the regions between the individual flux ropes and helps to pull them away from the quasi-stagnant subsolar regions and toward the cusp and into the outer layers of the northern and southern magnetic lobes of the tail. The total magnetic flux opened by dayside reconnection is therefore the sum of these two sources (e.g., *Sun et al*., 2020). The study by *Slavin et al.* (2012) showed that the time separation between consecutive FTEs can be as brief as only a few seconds, much shorter than typically observed for Earth's FTEs, which is of the order of minutes. The frequent occurrence of FTEs observed at Mercury has motivated a number of observational and theoretical studies to assess the role of FTEs in driving the global convection in Mercury's magnetosphere. In particular, *Imber et al.* (2014) carried out a case study of large-size FTEs observed by MESSENGER and estimated that large FTEs could carry at least

30% of the open flux needed to drive the substorm cycle at Mercury. *Sun et al.* (2020) recently conducted a comprehensive survey of FTE showers observed by MESSENGER, which correspond to clusters of relatively small-size FTEs, and inferred that during FTE shower intervals, FTEs can carry 60% to 85% of the open magnetic flux involved in driving Mercury's Dungey cycle. Drawing an analogy with Earth's FTEs, *Fear et al.* (2019) argued that the amount of magnetic flux opened by FTEs may represent an even greater contribution if one also considers the magnetic flux contained in the post-FTE reconnection exhaust. All of those previous works point to the idea that FTEs could be a major contributor in producing the open flux needed to drive Mercury's Dungey cycle, which is in sharp contrast with the situation at other planetary magnetospheres, such as those of Earth, Jupiter, and Saturn.

Another plasma structure potentially associated with magnetopause reconnection and FTEs is the so-called cusp filaments, whose existence was initially reported by *Slavin et al*. (2014) and subsequently confirmed by *Poh et al*. (2016). The cusp filaments correspond to columns of enhanced plasma density aligned with the local magnetic field, occurring in or around the cusp regions of Mercury. Notably, they are linked to discrete diamagnetic reductions (> 20%) in the magnetic field that last for several seconds. Figure 1-7 shows an example of several cusp plasma filaments recorded by MESSENGER just after and equatorward of the magnetospheric cusp encounter on 23 November 2011.

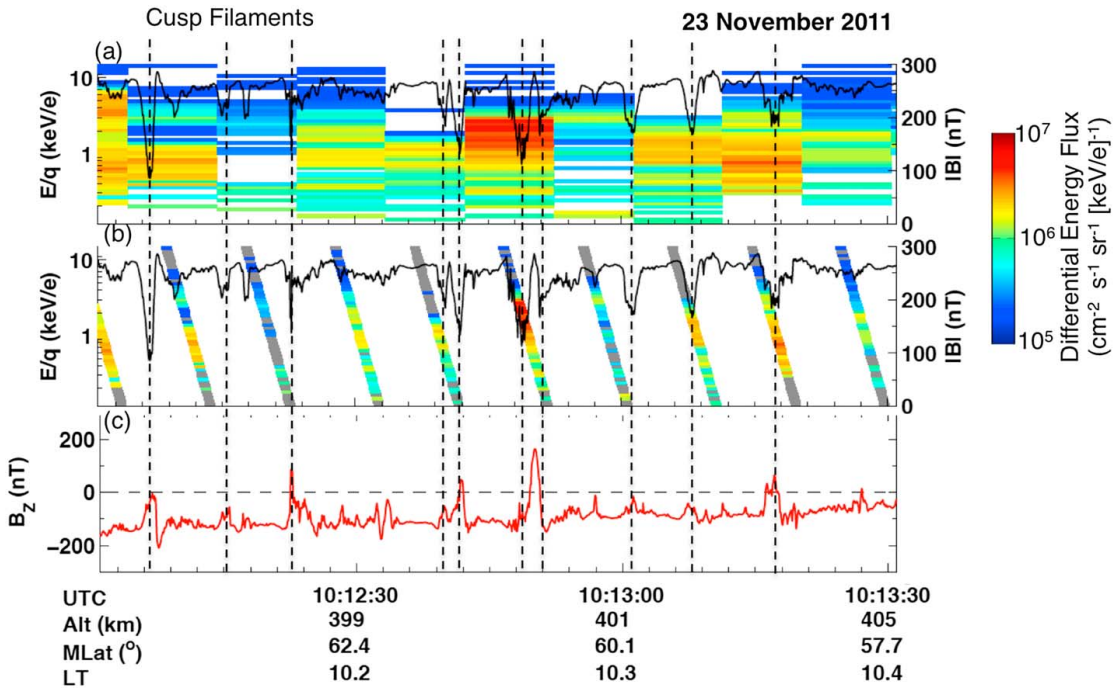

Figure 1-7: An example of cusp filaments (marked by vertical dashed lines) recorded equatorward of the magnetospheric cusp by MESSENGER on 23 November 2011. (a) Proton differential energy flux versus energy per charge and time. The magnitude of the magnetic field is shown in black. (b) Differential flux versus energy per charge plotted at the time of each energy step. The magnetic field strength is again shown in black. (c) The z-component of the magnetic field, Bz, in Mercury Solar Magnetospheric (MSM) coordinates. (adapted from *Slavin et al*. [2014])

It is worth noting that, thus far, the occurrence of cusp filaments is unique to Mercury and has not been found in other planetary cusps. Drawing an analogy with the particle acceleration and transport processes associated with FTEs at Earth, *Slavin et al*. (2014) hypothesized that the cusp filaments at Mercury are of diamagnetic origin and resulted from the injection of magnetosheath plasma into discrete flux tubes due to reconnection at the magnetopause. Based on MESSENGER observations, *Poh et al*. (2016) found that most cusp filaments exhibit a cylindrical flux tube-like structure, characterized by a gradual reduction in magnetic field intensity towards the central axis. However, there is still very limited information available on middle- to high-latitude FTEs and the temporal variability of FTE-filament interaction, primarily due to the limitations of single-point in-situ observations from the MESSENGER spacecraft. Therefore, further investigations through

numerical modeling, which can provide global context of Mercury's magnetosphere, is required to establish the link between FTEs and cusp filaments.

1.1.6 Proton Precipitation

Mercury, unlike Earth and the other terrestrial planets, lacks a well-formed atmosphere. Instead, it harbors an "exosphere," a tenuous envelope primarily composed of heavy neutral particles originating from its surface and held loosely by gravity. These neutral particles mostly follow ballistic trajectories, with some influenced by solar radiation pressure, and their low density results in minimal inter-particle collisions (*Cheng et al*., 1987). The primary constituents of Mercury's exosphere include sodium, potassium, and calcium, with sodium being the most abundant species. Previous studies (e.g., *Sarantos et al*., 2001; *Sun et al*., 2022a) have shown that the sputtered sodium in Mercury's exosphere primarily originates from high latitudes, possibly through the planetary cusps. While some recent works have suggested that a uniform exosphere could explain observed sodium enhancements within a single hemisphere, it fails to account for asymmetric sodium peaks frequently observed in the northern or southern hemisphere at high latitudes (*Killen*, 2022). The exact cause of this global asymmetry remains unclear, partly due to limited sampling of Mercury's southern hemisphere by the MESSENGER spacecraft.

Recent studies have established a strong correlation between cusp proton precipitation rates and significant variations in singly-ionized sodium ion density in Mercury's vicinity (*Sun et al*., 2022a). The study of proton precipitation onto Mercury's surface, a precursor to sodium sputtering, is thus important for understanding the intricate interplay among the neutral, plasma, and radiation environments, as well as heavy ion loss, in Mercury's near-space environment. Despite its significance, only a few investigations into proton precipitation at Mercury have been conducted, resulting in a quite wide range of estimates on the precipitation rate. Specifically, through a

technique called "proton reflectometry" *Winslow et al*., (2014) estimated that the proton precipitation flux in the norther cusp is about 3.7×10^8 $cm^{-2}s^{-1}$. *Poh et al*., (2016) reported that the cusp filaments observed by MESSENGER appear to carry magnetosheath plasma down to the surface with an estimated precipitation flux of 7.8×10^{10} $cm^{-2}s^{-1}$. Most recently, *Raines et al*., (2022) found that the average proton precipitation flux is approximately 1.0×10^7 $cm^{-2}s^{-1}$. However, many aspects regarding the proton precipitation process at Mercury remain poorly understood, i.e., the energy of the precipitating protons, the global precipitation rate, and the spatial distribution over which precipitation primarily occurs. Further investigations aimed at addressing these open questions are warranted.

1.2 Modeling of Mercury's Magnetosphere

Similar to the terrestrial magnetosphere, Mercury's magnetosphere is a complicated system in which various space plasma phenomena occur simultaneously and interact with the ambient plasma environment on different spatial and temporal scales. At Mercury, the global magnetospheric dynamics is primarily driven by magnetopause reconnection. However, the available in-situ measurements, such as those from MESSENGER, were all obtained from single-point observations with limited spatial coverage. As a result, it remains a challenge to develop quantitative understanding of how magnetopause reconnection occurs and its impact on the global dynamics solely based on single spacecraft observations.

Global simulation models, including both magnetohydrodynamic (MHD), hybrid, coupled fluid-kinetic and fully kinetic models, have been developed to provide global context for interpreting measurements obtained in various regions of Mercury's magnetosphere, thereby broadening our understanding of Mercury's magnetospheric environment beyond that derived

from in-situ spacecraft observations. The first ideal MHD model for Mercury's magnetosphere was published by *Kabin* et al. (2000), in which the authors reported that the Hermean magnetosphere exhibits many quantitative differences compared to the terrestrial magnetosphere due to its much smaller size. Later, the same ideal MHD model was used to assess the feasibility of inferring the internal magnetic field of Mercury based on MESSENGER observations (*Kabin et al*., 2008). *Trávníček et al*. (2010) presented two hybrid simulations in the context of MESSENGER's first two encounters with Mercury, and confirmed the existence of many basic structures, including a bow shock, ion foreshock, magnetosheath, magnetopause, etc. A resistive MHD model was applied to Mercury by *Jia et al*. (2015), where they coupled, for the first time, Mercury's interior electrodynamically with the global magnetosphere to investigate the dynamic response of Mercury to time-varying external conditions in a self-consistent manner. Later, they used the same resistive MHD model to further examine the roles of induction-driven shielding and reconnection-driven erosion in controlling Mercury's dayside magnetospheric configuration (*Jia et al*., 2019). Meanwhile, *Fatemi et al*., (2018) presented a GPU-based hybrid model for inferring the solar wind dynamic pressure from magnetic field observations inside Mercury's magnetosphere. A follow-up study (*Fatemi et al*., 2020) using the same hybrid model found that the proton precipitation rate onto the entire surface of Mercury is higher when the IMF has a northward component. The first application of coupled fluid-kinetic model to Mercury's magnetosphere was published by *Chen et al*. (2019), where they embedded a Particle-in-Cell (PIC) code into a fluid model to study the dawn-dusk asymmetries of Mercury's magnetotail. Most recently, *Lapenta et al*. (2022) presented a semi-implicit PIC model for Mercury's magnetosphere and found that the electron physics has significant impact on the reconnection-driven particle energization. *Lavorenti et al*. (2022) applied another semi-implicit PIC model to simulate the

Hermean magnetosphere and revealed that high-energy electrons (up to tens of keV) are generated in Mercury's magnetotail under southward IMF conditions.

Most previous simulation studies have focused on the large-scale configuration and global-scale dynamics of the magnetosphere, and, as such, there have not been many modeling efforts devoted to understanding the dayside magnetopause dynamics at Mercury that is primarily driven by reconnection. It is only recently that a hybrid simulation was conducted by *Lu et al.* (2022) to investigate FTE formation for two IMF configurations (purely northward and purely southward orientation). However, there are still many open questions yet to be answered regarding the FTEs, potential dawn-dusk asymmetries of dayside magnetopause reconnection, cusp filaments, and proton precipitation at Mercury. In this dissertation, we perform a series of global simulations with a range of solar wind and IMF conditions using both the Block-Adaptive-Tree Solarwind Roe Upwind Scheme (BATS-R-US) Hall-MHD and MHD with Adaptively Embedded Particle-in-Cell (MHD-AEPIC) models to study in detail the reconnection-driven magnetopause dynamics at Mercury.

1.3 Outline of the Dissertation

This dissertation work is built upon both Hall-MHD and MHD-AEPIC simulations of Mercury's magnetosphere. Chapter 2 provides a description of the Hall-MHD and MHD-AEPIC models used in this dissertation. Chapter 3 presents the results of Hall-MHD simulations with a focus on the generation and evolution of FTEs under different upstream conditions. The 3D structure and evolution of FTEs as well as the dependences of FTE properties on the solar wind Alfvénic Mach number (M_A) and IMF orientation are also discussed in Chapter 3. Chapter 4 and Chapter 5 show the results of MHD-AEPIC simulations from different perspectives. In particular,

Chapter 4 discusses the kinetic signatures of particle phase space distributions, the dawn-dusk asymmetries of reconnection occurrence on the dayside, and the impact of kinetic effects on the formation and evolution of FTEs. Chapter 5 presents an in-depth investigation of cusp filaments and proton precipitation as modeled by the PIC code, which is embedded adaptively into the global MHD model. The relationship between FTEs and cusp filaments is also discussed in Chapter 5. Lastly, Chapter 6 summarizes the major findings from the work presented in this dissertation and discusses a few potential directions to explore in future research.

Chapter 2 Model Description

In this chapter, we present the models that are used in this dissertation. First, we introduce the **Space Weather Modeling Framework** (**SWMF**) (*Tóth et al*., 2012), which is a comprehensive and versatile computational tool designed for simulating the complex interactions and space weather phenomena occurring in various space environments. Next, we describe the magnetohydrodynamics (MHD) model **BATS-R-US** (**Block Adaptive Tree Solar-wind Roe-type Upwind Scheme**) and its Hall-MHD version, which is used as the global magnetosphere (GM) component in SWMF in our study. Following this, we provide an overview of the particle-in-cell (PIC) simulation method and the energy conserving semi-implicit scheme. Finally, we describe the PIC code **Flexible Exascale Kinetic Simulator** (**FLEKS**) and the **MHD with Adaptively Embedded Particle-in-Cell** (**MHD-AEPIC**) model, which two-way couples FLEKS with the BATSRUS Hall-MHD model.

2.1 Space Weather Modeling Framework

The space weather modeling framework (SWMF) is a software framework consisting of a collection of physics-based numerical models. It is designed to provide a unified platform for running and coupling multiple models simultaneously, thus enabling the simulation of space weather and space plasma processes on a wide range of spatiotemporal scales. A variety of commonly-used utilities, including linear solvers, mesh interpolation algorithms, coordinate transformations and timings are offered by the shared libraries. The models within SWMF can be compiled into separate libraries, and subsequently linked together with the core of the framework

and the shared libraries to generate a single executable file. The information exchange between different models, which is required for the coupling, is efficiently handled by the Message Passing Interface (MPI) library. Additionally, each model in the SWMF can also be compiled into a single executable and used as a stand-alone simulation tool. The general structure of the SWMF is shown in Figure 2-1.

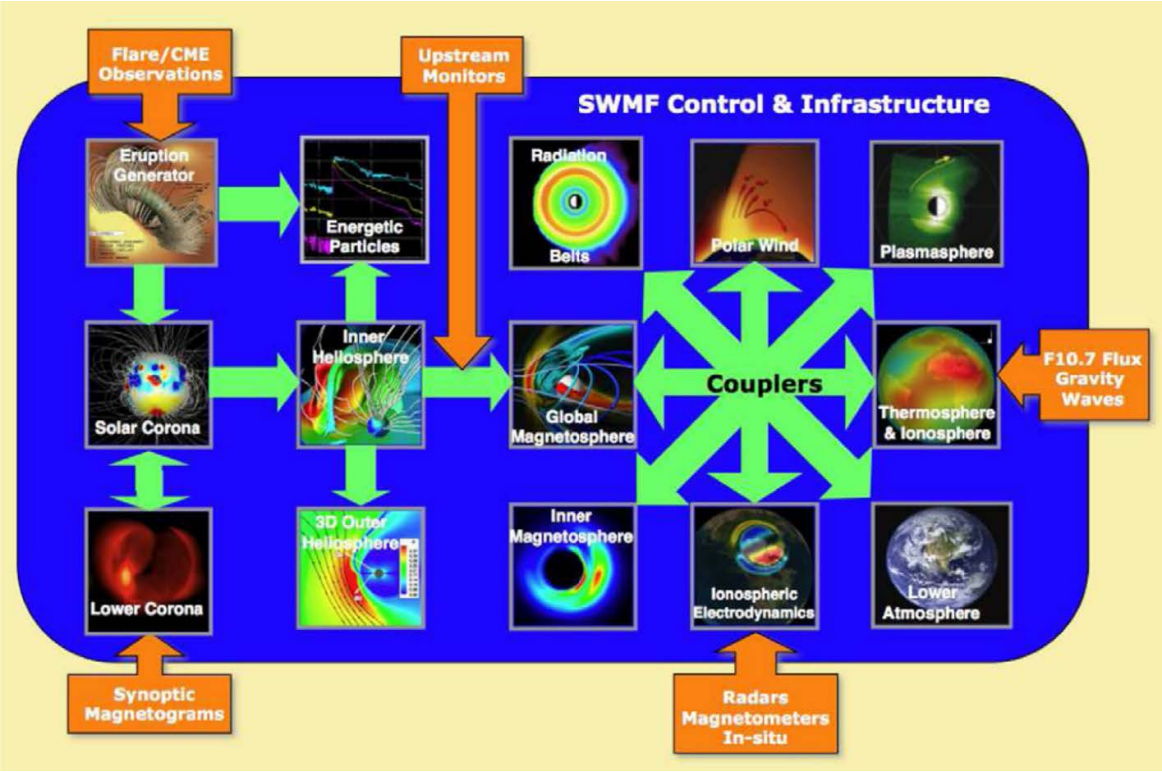

Figure 2-1: Components (boxes) and their couplings (green arrows) in the Space Weather Modeling Framework. External input is indicated by the orange arrows. (adapted from *Tóth et al*. [2012])

2.2 The BATS-R-US Model

The Block-Adaptive-Tree Solarwind Roe Upwind Scheme (BATS-R-US) (*Powell et al*., 1999; *De Zeeuw et al*., 2000) is a robust multi-physics magnetohydrodynamics (MHD) code, primarily written in Fortran 90+. Having been developed and refined at the University of Michigan over two decades, BATS-R-US represents one of the most complex and computationally

demanding components within the SWMF. Its wide-ranging applications span multi-scale space plasma systems, including the solar corona, the heliosphere, planetary magnetospheres, planetary moons, comets, and exoplanets. BATS-R-US was initially designed with adaptive mesh refinement (AMR) and computational efficiency in mind, utilizing a 3D Cartesian block-adaptive mesh structure and Message Passing Interface (MPI) parallelization (*Stout et al*., 1997; *De Zeeuw et al*., 2000). A significant overhaul took place in 2012, replacing the original block-adaptive system with the Block Adaptive Tree Library (BATL) (*Tóth et al*., 2012). BATL excels at creating, adapting, load balancing, and accelerating message-passing for 1D, 2D, or 3D block-adaptive grids in generalized coordinates. This approach offers several advantages, including locally structured grids within each block, cache optimizations due to the relatively compact arrays associated with grid blocks, efficient loop handling for fixed-sized loops over cells within blocks, and simplified load balancing. The choice of block size in 3D simulations typically falls within the range of 4^3 to 16^3 grid cells, with 1-3 layers of ghost cells on each side depending on the numerical scheme's order.

Over time, BATS-R-US has evolved into a comprehensive numerical model, encompassing a broad spectrum of equation sets, from ideal magnetohydrodynamics to advanced six-moment fluid models (*Huang et al*., 2019). Its primary applications revolve around solving diverse formulations of the MHD equations, including resistive, Hall, semi-relativistic, multi-species, and multi-fluid MHD, optionally incorporating features like anisotropic pressure, radiative transport, and heat conduction. Numerous choices for Riemann solvers are available, ranging from the original Roe scheme to various others combined with second-order total variation diminishing (TVD) schemes or fifth-order accurate conservative finite difference schemes (*Chen et al*., 2016). Regarding time discretization, users can choose explicit, point-implicit, semi-

implicit, hybrid between explicit and implicit, or fully implicit approaches. One of BATS-R-US's notable features is the integration of user modules, which provides an interface for users to modify virtually any part of the kernel code without disrupting other modules. This feature grants user substantial control over simulations and there are currently more than 50 distinct user modules provided in the repository. These modules primarily serve to configure specific initial and boundary conditions and introduce user-defined source and loss terms for particular applications.

2.2.1 Hall MHD with Separate Electron Pressure Equation

The equation set of BATS-R-US used in this dissertation is Hall MHD with separate electron pressure equation (*Tóth et al*., 2008). Compared to the ideal/resistive MHD model, Hall MHD decouples the ion and electron motions by keeping the Hall term in the generalized Ohm's law

$$\boldsymbol{E} = -\boldsymbol{u} \times \boldsymbol{B} + \eta \boldsymbol{J} + \frac{1}{ne}\boldsymbol{J} \times \boldsymbol{B} - \frac{\nabla p_e}{ne} \tag{2-1}$$

where the first term on the right-hand-side corresponds to the convection term, the second term is the resistivity term resulted by finite conductivity, the third term is the Hall term which accounts for the Hall effect, and the last term is the electron pressure gradient term. As an approximation, the divergence of electron pressure tensor is reduced to the gradient of scalar pressure.

Equations (2-2) – (2-8) describe the full set of equations solved in all the simulations of Mercury's magnetosphere presented in this dissertation, where the primitive variables are plasma mass density, plasma bulk velocity (which is approximately the ion bulk velocity), magnetic field, ion pressure and electron pressure (ρ, u, B, p, p_e), $\bar{I}$ indicates the identity matrix. A separate electron pressure equation is added into typical Hall MHD equation set to obtain the values of electron scalar pressure. Other derived quantities include the current density, $J = \nabla \times B/\mu_0$, and the electron bulk velocity $u_e = u - J/ne$, where n is the plasma number density. In Equation

(2-8), e represents the total energy density, which is the sum of the hydrodynamic energy density and the magnetic energy density, and γ is the ratio of specific heats set to be 5/3.

$$\frac{\partial \rho}{\partial t} = -\nabla \cdot (\rho \boldsymbol{u}) \tag{2-2}$$

$$\frac{(\partial \rho \boldsymbol{u})}{\partial t} = -\nabla \cdot \left[\rho \boldsymbol{u}\boldsymbol{u} + (p + p_e)\bar{I} + \frac{\boldsymbol{B}^2}{2\mu_0}\bar{I} - \frac{\boldsymbol{B}\boldsymbol{B}}{\mu_0}\right] \tag{2-3}$$

$$\frac{\partial e}{\partial t} = -\nabla \cdot \left[(\varepsilon + p)\boldsymbol{u} + (\varepsilon_e + p_e)\boldsymbol{u}_e + \boldsymbol{u}_e \cdot \left(\frac{\boldsymbol{B}^2}{\mu_0}\bar{I} - \frac{\boldsymbol{B}\boldsymbol{B}}{\mu_0}\right) - \boldsymbol{B} \times \eta \boldsymbol{J}\right] \tag{2-4}$$

$$\frac{\partial \boldsymbol{B}}{\partial t} = \nabla \times \left[\boldsymbol{u} \times \boldsymbol{B} - \frac{\boldsymbol{J}}{ne} \times \boldsymbol{B} - \eta \boldsymbol{J} + \frac{\nabla p_e}{ne}\right] \tag{2-5}$$

$$\frac{\partial p_e}{\partial t} + \nabla \cdot (p_e \boldsymbol{u}) = -(\gamma - 1) p_e \nabla \cdot \boldsymbol{u}_e \tag{2-6}$$

$$\boldsymbol{u}_e = \boldsymbol{u} - \frac{\boldsymbol{J}}{ne} \tag{2-7}$$

$$e = \frac{1}{2}\rho \boldsymbol{u}^2 + \frac{1}{\gamma - 1}p + \frac{1}{\gamma - 1}p_e + \frac{\boldsymbol{B}^2}{2\mu_0} \tag{2-8}$$

In solving the set of Hall-MHD equations above, we have used a second-order finite-volume scheme with a HLLE (Harten-Lax-van Leer-Einfeldt) Riemann solver (*Einfeldt et al*., 1991) and Koren's third-order limiter (*Koren*, 1993). The time stepping is done in a semi-implicit manner, where the resistive term $\eta \boldsymbol{J}$ and the Hall term $-(\boldsymbol{J} \times \boldsymbol{B})/(ne)$ in the induction equation (Equation (2-5)) are advanced with an implicit scheme, while all the other terms are advanced using explicit time stepping (*Tóth et al*., 2012). The advantage of using a semi-implicit scheme is that it helps to reduce the stiffness of the system without limiting the timestep of the explicit time-stepping, thereby allowing us to achieve affordable computational costs for running multiple global Hall-MHD simulations. To maintain the divergence-free property of the magnetic field, we have combined the eight-wave scheme and the hyperbolic cleaning scheme to remove excess $\nabla \cdot \boldsymbol{B}$ from the simulation domain (*Tóth*, 2000). Furthermore, azimuthal smoothing is applied to cell-centered values near the pole axis to reduce discontinuities around the axis of symmetry of the spherical grid used for the simulation, thereby increasing the allowable timesteps.

2.3 Particle-in-Cell Method

To a good approximation, space plasmas can be considered as collisionless plasma, given that the direct Coulomb interaction between particles is negligible. Therefore, they can be described as the Vlasov-Maxwell system. The Vlasov equation is:

$$\frac{\partial \mathrm{f_s}}{\partial \mathrm{t}} + \mathbf{v} \cdot \frac{\partial \mathrm{f_s}}{\partial \mathbf{x}} + \frac{\mathrm{q_s}}{\mathrm{m_s}} (\mathbf{E} + \mathbf{v} \times \mathbf{B}) \frac{\partial \mathrm{f_s}}{\partial \mathbf{v}} = 0, \tag{2-9}$$

where $f_s(\mathbf{x}, \mathbf{v}, t)$ is the phase space density of particles of species *s* with velocity **v** at the spatial location **x**; q_s and m_s represent the particle charge and mass, respectively; **B**(**x**, t) and **E**(**x**, t) are the magnetic and electric fields, whose spatial and temporal evolutions are governed by Maxwell's equations:

$$\nabla \cdot \mathbf{E} = \frac{\rho_q}{\epsilon_0} \tag{2-10}$$

$$\nabla \cdot \mathbf{B} = 0 \tag{2-11}$$

$$\frac{\partial \mathbf{B}}{\partial \mathrm{t}} = -\nabla \times \mathbf{E} \tag{2-12}$$

$$\frac{1}{\mathrm{c}^2} \frac{\partial \mathbf{E}}{\partial t} = \nabla \times \mathbf{B} - \mu_0 \boldsymbol{J} \tag{2-13}$$

where ρ_q is the charge density; ϵ_0, μ_0, and c are constants representing electric permittivity, magnetic permeability, and speed of light, respectively. To solve the Vlasov equation with reduced complexity, the particle-in-cell (PIC) method samples the particle phase space distribution and treat many physical particles that are close to each other in the phase space as a single macro-particle. The majority of the PIC codes employ prescribed shapes of macro-particles in space to reduce numerical collisions (e.g., *Birdsall and Langdon,* [1991]) and the most widely used one is the cloud-in-cell scheme, in which a macro-particle is represented by either a flat-top function or a linear function. The statistical noise caused by the macro-particle approximation is on the order

of $\frac{1}{\sqrt{N}}$, where N is the number of macro-particles per computational cell. To reduce this noise while keeping the computational cost affordable, N is typically set to fall within the range of a few dozens to several thousands. Maxwell's equations in the PIC method are differenced in space on a staggered Cartesian grid. The magnetic field **B** and charge density ρ_q are stored/evaluated at the center of each cell, while the electric field **E** and the current density ***J*** are stored/evaluated on vertices of the grid. An example of the structure of one cell with index (i, j, k) in a staggered Cartesian grid is shown in Figure 2-2.

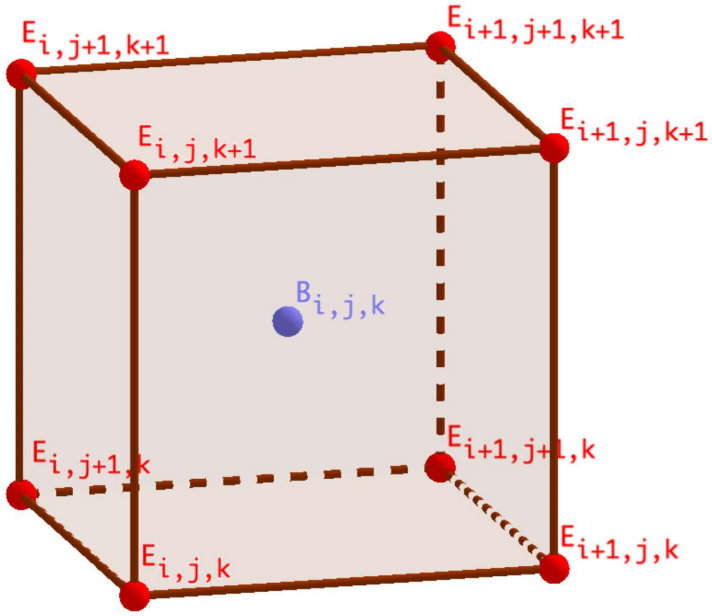

Figure 2-2: Staggered field storage in the PIC method for cell index (i, j, k). The magnetic field **B** and charge density ρ_q are stored at the center of each cell, while the electric field **E** and the current density ***J*** are stored on vertices of the grid.

The temporal advancing of PIC method can be separated into two major parts. First, the macro-particles are pushed by the electromagnetic fields:

$$\frac{d\mathbf{x}_p}{dt} = \mathbf{v}_p \tag{2-14}$$

$$\frac{d\mathbf{v}_p}{dt} = \frac{q_s}{m_s}\left(\mathbf{E}_p + \mathbf{v}_p \times \mathbf{B}_p\right) \tag{2-15}$$

where $\mathbf{x}_p$ and $\mathbf{v}_p$ are macro-particle's position and velocity, respectively; $\mathbf{E}_p$ and $\mathbf{B}_p$ are interpolated electric and magnetic fields at the macro-particle's position. Secondly, Maxwell's equations (Equation (2-10) - (2-13)) are solved on the staggered grid to get updated electromagnetic fields. It's worth noting that the charge density ρ_q and current density $\boldsymbol{J}$ appearing in Maxwell's equations are obtained by interpolating from macro-particles to the grid cells based on the prescribed particle shape.

2.3.1 Gauss's Law Satisfying Energy Conserving Semi-Implicit Method

Many PIC codes employ explicit time discretization schemes, such as the widely used leap-frog algorithm. These explicit PIC codes require grid resolution at or below the Debye length to avoid finite grid instability and the allowable timestep is limited by the plasma frequency and the speed of light, as demonstrated in previous works (e.g., *Birdsall and Langdon,* [1991]; *Lapenta,* [2012]). In an effort to relax these stability constraints, for decades researchers have explored implicit particle methods, which utilize implicit schemes for solving the equations (*Mason*, [1981]; *Brackbill and Forslund*, [1982]; *Markidis et al*., [2010]). Implicit PIC codes are linearly unconditionally stable and allow the application of larger cell sizes and time steps when compared with explicit PIC methods. In this dissertation, we employ the Gauss's Law satisfying Energy Conserving Semi-Implicit Method (GL-ECSIM) designed by *Chen and Tóth* (2019) to solve the PIC equations. Compared to its predecessor, Energy Conserving Semi-Implicit Method (ECSIM) published in *Lapenta* (2017), GL-ECSIM has several major improvements with better stability, charge conservation, and load-balancing algorithm. Here we present the key steps in GL-ECSIM.

The positions and velocities of macro-particles are updated explicitly through solving the equations below:

$$\mathbf{x}_p^{n+1/2} = \mathbf{x}_p^{n-1/2} + \Delta t \mathbf{v}_p^n, \tag{2-16}$$

$$\mathbf{v}_p^{n+1} = \mathbf{v}_p^n + \frac{q_p \Delta t}{m_p}\left[\mathbf{E}^{n+\theta} + \frac{\mathbf{v}_p^n + \mathbf{v}_p^{n+1}}{2} \times \mathbf{B}^n\right], \tag{2-17}$$

where the position $\mathbf{x}_p$ and velocity $\mathbf{v}_p$ are staggered in time in a leapfrog fashion, the electric field is measured at time level $n + \theta$ and the magnetic field is evaluated at time step n (*Lapenta*, 2017).

The electromagnetic fields are updated implicitly via:

$$\frac{\mathbf{B}^{n+1} - \mathbf{B}^n}{\Delta t} = -c\nabla \times \mathbf{E}^{n+\theta}, \tag{2-18}$$

$$\frac{\mathbf{E}^{n+1} - \mathbf{E}^n}{\Delta t} = c\nabla \times \mathbf{B}^{n+\theta} - 4\pi\bar{\mathbf{J}}, \tag{2-19}$$

where $\bar{\mathbf{J}}$ is the predicted current density at time level $n + \theta$ and it depends on the unknown electric field $\mathbf{E}^{n+\theta}$ (*Lapenta*, 2017). The fields information at level $n + \theta$ is defined as the linear interpolations between time steps n and n + 1:

$$\mathbf{E}^{n+\theta} = (1 - \theta)\mathbf{E}^n + \theta\mathbf{E}^{n+1}, \tag{2-20}$$

$$\mathbf{B}^{n+\theta} = (1 - \theta)\mathbf{B}^n + \theta\mathbf{B}^{n+1}, \tag{2-21}$$

Upon substituting Equations (2-20), (2-21) into Equations (2-18), (2-19), we obtain a second order implicit equation containing only $\mathbf{E}^{n+\theta}$:

$$\mathbf{E}^{n+\theta} + (c\theta\Delta t)^2\left[\nabla\left(\nabla \cdot \mathbf{E}^{n+\theta}\right) - \nabla^2\mathbf{E}^{n+\theta}\right] = \mathbf{E}^n + c\theta\Delta t\left(\nabla \times \mathbf{B}^n - \frac{4\pi}{c}\bar{\mathbf{J}}\right), \tag{2-22}$$

Theoretically, the exact energy conserving occurs at $\theta = 0.5$ if the spatial discretizations are handled properly. However, *Chen and Tóth* (2019) found that in practice numerical waves may still be present in simulations even with $\theta = 0.5$. Thus $\theta = 0.51$ is used for the simulations presented in this dissertation such that the robustness can be significantly improved. After the update of electromagnetic fields, the particles' positions are adjusted slightly to correct the newly-created numerical error in Gauss's law. Since the position adjustment algorithm is designed in a

way such that electromagnetic fields and particle velocities are not changed after the adjustment, the total energy of the system is still conserved.

2.4 MHD with Adaptively Embedded Particle-in-Cell model

MHD models are proven to be efficient in simulating global magnetospheric phenomena. However, these models are limited by the MHD approximation, which is inadequate for describing phenomena governed by kinetic physics, such as magnetic reconnection. In contrast, PIC methods are able to resolve the kinetic physics on much smaller scales, but they are computationally much more demanding, which makes it exceptionally challenging to apply PIC to global magnetosphere simulations (*Lapenta*, 2012). In this section, we describe the PIC model used in this dissertation and the approach employed to combine the computational efficiency of MHD model with the accuracy of the PIC code (*Daldorff et al*., 2014).

2.4.1 FLexible Exascale Kinetic Simulator

The PIC code used in this dissertation is the FLexible Exascale Kinetic Simulator (FLEKS) (*Chen et al*., 2023), which implements the GL-ECSIM algorithm. FLEKS offers a variety of features that can be used to improve the computational efficiency and accuracy of the simulation results. One of the most important features of FLEKS is the adaptive grid capability, which allows user to run the PIC simulation in a 3D non-rectangular region with curved boundaries. In many of the previous coupled fluid-kinetic simulations of planetary magnetospheres, only a box-shaped PIC domain was available for modeling the dayside magnetosphere (e.g., *Chen et al., 2017*; *Zhou et al*., 2019). However, a box-shaped domain cannot cover the entire magnetopause surface as the PIC boundaries are not allowed to cut through the planet. Furthermore, a rectangular PIC box

inevitably spends a lot of computational resources on simulating regions where kinetic effects are not important. In contrast, the FLEKS code supports the utilization of a flexible PIC domain with arbitrary boundaries, which allows a more complete coverage of the magnetopause surface and significantly reduces the overall computational costs. In addition to the flexible boundaries, the PIC grid in FLEKS can also dynamically switch on/off a portion of its cells such that the resultant active PIC region only covers the locations where magnetic reconnection could potentially occur. This dynamically adjusted PIC grid has been demonstrated to provide an efficient means for simulating the flapping motion of Earth's magnetotail current sheet during a geomagnetic storm (*Wang et al*., 2022).

To achieve the adaptive grid capability, FLEKS uses the parallel data structure offered by the AMReX library (*Zhang et al*., 2021). Although FLEKS still requires that the full PIC grid be a box-shaped uniform Cartesian grid, it divides the entire computational domain into multiple patches, each containing N cells along each dimension. Since two layers of ghost cells are required to couple FLEKS with the MHD model, N has to be greater than 1 such that ghost cells from distinct patches do not overlap with each other. In our coupled fluid-kinetic simulation, the status of these patches is set by the MHD model based on geometric or physics-oriented criteria. Through the Message Passing Interface (MPI), the MHD model sends a bit-wise patch status array to FLEKS to dynamically adjust the geometry of the active PIC region by setting each patch to be either active or inactive. An example of an adaptive PIC grid with two active PIC patches in different shapes is presented in Figure 2-3.

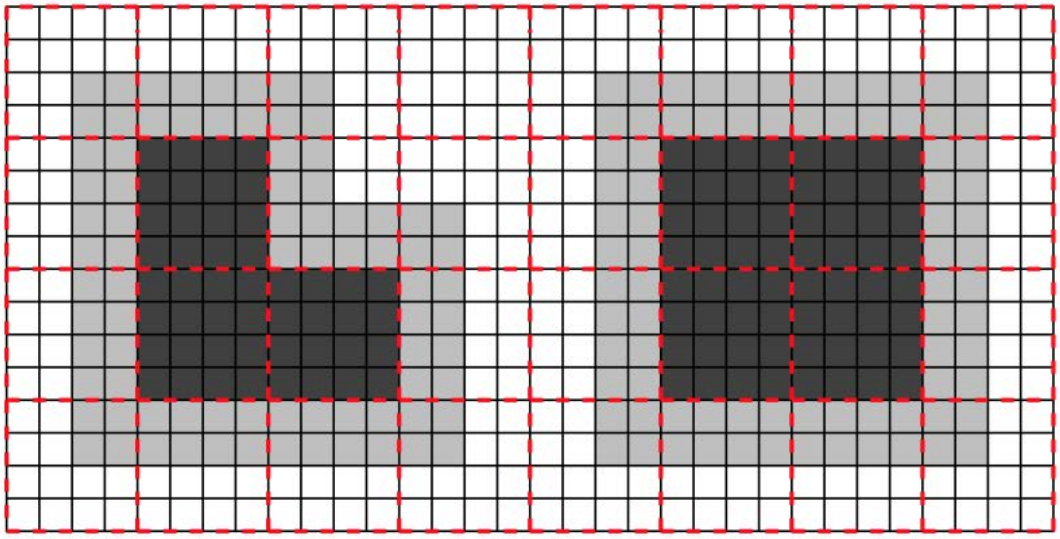

Figure 2-3: An adaptive PIC grid with two active PIC patches in different shapes. The black lines represent the PIC cells. The red dashed lines show the patches, and one patch contains 4 × 4 cells in this figure. The active patches/cells are colored by dark gray, and light gray area represents the ghost cells of the active PIC regions. (adapted from *Chen et al*. [2023])

2.4.2 Coupling between MHD Model and PIC Code

The BATS-R-US Hall MHD model and FLEKS are coupled through the SWMF to form the MHD-AEPIC model. The temporal discretization of the MHD-AEPIC coupling algorithm is shown in Figure 2-4. At the start of the coupling process, BATS-R-US sends the information of plasma density, bulk velocity, thermal pressure, and the magnetic field to FLEKS. Subsequently, FLEKS initializes the electric field using the generalized Ohm's law (Equation (2-1)) and creates macro-particles assuming Maxwellian distribution according to the received fluid properties. This initialization step ensures that FLEKS and BATS-R-US share the same plasma density, velocity, and pressure within the active PIC region at the initial time step. Following the PIC initialization, both the MHD and PIC models advance in time independently with their own time steps. The coupling frequency between these two models can be set to a prescribed value Δt_{couple} as both the MHD and PIC models automatically adjust their time steps so that they can reach the prescribed coupling times ($t = k\Delta t_{couple}$, where k is a positive integer) precisely. At the time of coupling,

FLEKS calculates various moments of the particle distribution function, including density, velocity, and pressure. These values, together with the magnetic field solved by the PIC model, are then used to overwrite the information stored on the MHD cells that overlap with the active PIC region. In exchange, BATS-R-US provides the particle and electromagnetic field boundary conditions for FLEKS. Concerning the particle boundary conditions, FLEKS removes all particles within the boundary cells and subsequently generates new particles based on the fluid properties received from BATS-R-US. Before the next coupling time, FLEKS uses the latest boundary conditions obtained from BATS-R-US for every time step. More details about the MHD-AEPIC coupling algorithm can be found in *Daldorff et al*. (2014), *Shou et al*. (2021), and *Wang et al*. (2022).

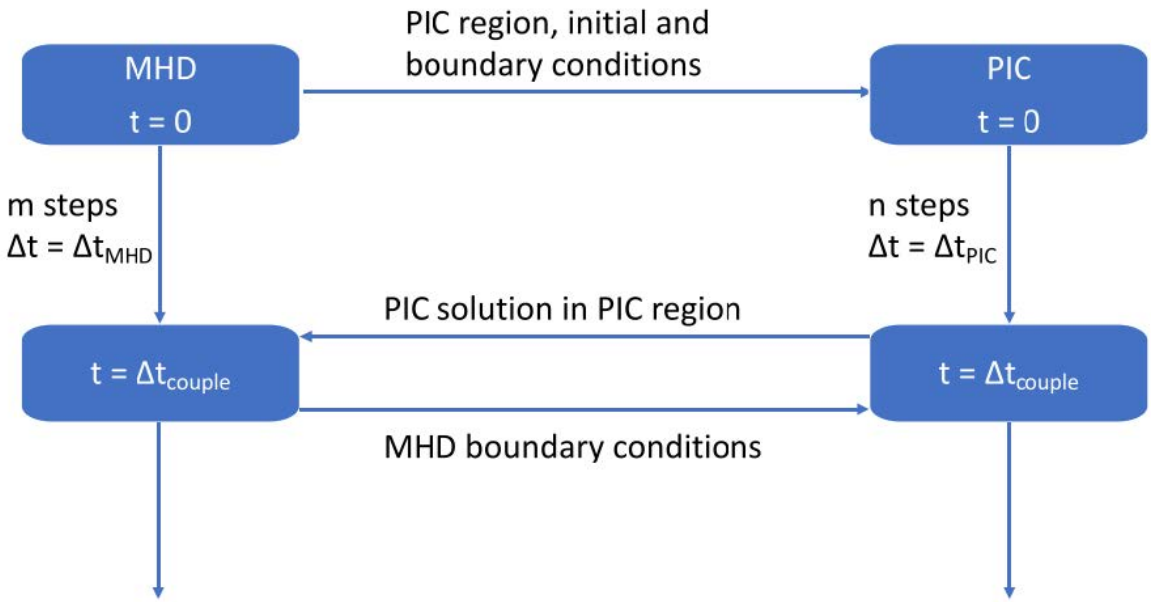

Figure 2-4: Temporal discretization of the MHD-AEPIC coupling algorithm, based on Figure 1 in *Daldorff et al*. (2014).

Chapter 3 Global Hall MHD Simulations of Mercury's Magnetopause Dynamics and Flux Transfer Events Under Different Solar Wind and Interplanetary Magnetic Field Conditions[1]

3.1 Introduction

As described in Chapter 1, FTEs play an important role in driving Mercury's Dungey cycle. However, many outstanding questions still remain unanswered regarding FTEs at Mercury, such as their 3D structure, time evolution and overall contribution to the global dynamics as well as how those FTE characteristics vary depending on the external conditions. A systematic modeling study is warranted in order to obtain global context for addressing those open questions related to Mercury's FTEs.

In this chapter, we employ the BATS-R-US global Hall MHD model (*Tóth et al*., 2008) to simulate Mercury's magnetosphere with a focus on understanding the generation and characteristics of FTEs under a variety of solar wind and IMF conditions. As demonstrated by previous numerical studies (e.g., *Birn et al*., 2001; *Liu et al*., 2022), by allowing separate bulk motions of plasma ions and electrons Hall-MHD is capable of producing fast reconnection with reconnection rates comparable to those seen in fully kinetic simulations and it is also computationally cheaper compared to fully kinetic models. These properties make Hall-MHD a suitable tool for our modeling study, in which we aim to conduct multiple simulations to

[1] This chapter has been published in *Li et al*. (2023) Global Hall MHD Simulations of Mercury's Magnetopause Dynamics and FTEs Under Different Solar Wind and IMF Conditions, *Journal of Geophysical Research: Space Physics*, *128*(5), e2022JA031206, https://doi.org/10.1029/2022JA031206.

systematically investigate the effects of different upstream conditions on FTEs. The external parameters we focus on in this work are the solar wind Alfvénic Mach number and the IMF orientation, which have been found through MESSENGER observations to have significant influences on Mercury's FTEs (e.g., *Sun et al*., 2020).

The details of our numerical model, simulation setup and input parameters are described in Section 3.2. Section 3.3 introduces an automated algorithm that we have developed to automatically identify FTEs in our simulations as well as various analysis techniques used to extract key FTE properties from the model. Results of the simulated FTEs, including their physical properties and statistics, are also presented in Section 3.3 and further discussed in Section 3.4. Section 3.5 provides a summary and conclusions. The work presented in this chapter has been published in *Li et al*. (2023).

3.2 Methodology

In this work, the interaction between Mercury's magnetosphere and the solar wind is simulated using a 3D global Hall-MHD model based on the BATSRUS (Block Adaptive Tree Solar wind Roe-type Upwind Scheme) code. The BATSRUS Hall MHD model and the full set of equations to solve are described in detail in Chapter 2. Here, we focus on the key aspects of the simulation model adapted for Mercury, including the model configuration and the structure of the numerical grid specifically designed to capture the dayside magnetopause dynamics.

The simulation domain covers a rectangular box with dimensions of $-64R_M < X < 8R_M$, $-128R_M < Y < 128R_M$, $-128R_M < Z < 128R_M$, where $R_M = 2440$ km is Mercury's mean radius. Here, X, Y, Z are defined in MSO (Mercury Solar Orbital) coordinates, where the +X-axis is pointing

from Mercury to the Sun, the +Z-axis is perpendicular to Mercury's equatorial plane and is pointing northward, and the Y-axis completes the right-handed system with positive pointing in the direction opposite to Mercury's orbital motion. A Hall factor of 4 has been multiplied to the plasma ion mass-to-charge ratio in the MHD equations, which in effect scales up the ion inertial length by a factor of 4. As shown by *Tóth et al.* (2017), scaling the ion kinetic scale length using this approach results in considerable reduction in the computational costs required to resolve the ion kinetic physics without significantly changing the behavior of the global simulation provided that the scaled ion inertial length is still well separated from the global scale, which is the case here for Mercury. We have used a stretched spherical grid with up to three levels of adaptive mesh refinement near the dayside magnetopause, resulting in a grid resolution of 20 km (or 0.008 R_M), which is about one sixth of the effective ion inertial length (d_i) at the magnetopause after scaling. Such a high grid resolution ensures that the ion scale physics is well resolved in our simulations.

A key difference of this modeling work from the previous MHD simulations of Mercury's magnetosphere is the use of Hall-MHD, which has been shown to be able to enable fast reconnection with reconnection rates comparable to those seen in fully kinetic simulations (e.g., *Birn et al.*, 2001; *Liu et al*., 2022). The Hall term in the induction equation (Equation (2-5)) becomes important only in regions of strong electric currents, which, in Mercury's case, lie in the magnetopause and magnetotail regions. Therefore, we have chosen to turn on the Hall term in a rectangular box ($-8\ R_M < X < 2\ R_M$, $-4\ R_M < Y < 4\ R_M$, $-4\ R_M < Z < 4\ R_M$) that covers the entire dayside magnetosphere and the majority of the nightside magnetotail. To save computational costs, the Hall term is switched off outside this box and inside the sphere of radius of 1.15 R_M where there are no significant plasma currents (and hence the Hall effect) present.

Mercury possesses a large-size conducting core with a radius of ~ 0.8 R_M, which has been shown to play an important role in governing the structure of Mercury's magnetosphere (e.g., *Slavin et al*., 2014, 2019; *Jia et al*., 2015, 2019; *Heyner et al*., 2016). To account for the induction effect of Mercury's conducting core, we have followed the approach used in previous Mercury simulations by *Jia et al.* (2015, 2019) to include Mercury's interior in our global Hall-MHD simulations. Specifically, the planetary interior is assumed to consist of a conducting core of radius 0.8 R_M and a resistive mantle (between 0.8 and 1.0 R_M) characterized by a prescribed resistivity profile according to *Jia et al*. (2015). For the interior, the MHD primitive variables (except the magnetic field) are set to constants and only the magnetic field is solved for and updated inside Mercury's interior using the induction equation that allows the magnetic field to diffuse in time into the planet according to the prescribed resistivity profile. At the core-mantle boundary (r= 0.8 R_M), we apply a zero magnetic field perturbation boundary condition so that below this boundary the magnetic field is fixed to Mercury's intrinsic field, which is represented as a dipole aligned with the Z-axis with an equatorial surface strength of 195 nT and a northward offset of 0.2 R_M (*Anderson et al.,* 2011). Outside of the planet (r > 1.0 R_M) the full set of MHD equations described above are solved, and, therefore, boundary conditions need to be prescribed at the planet's surface for the plasma density, velocity and pressure. For the plasma ion and electron pressure, we apply a floating boundary condition, that is the values in the ghost cell are set to be equal to those in the physical cell inside the simulation domain ($p_{ghost} = p_{physical}$). In terms of the plasma density, we apply different treatments based on the direction of the plasma bulk velocity in the physical cell right next to the boundary: (1) if the plasma is flowing towards the surface, then we apply a floating boundary condition $\rho_{ghost} = \rho_{physical}$, which allows the incoming plasma to be absorbed by the surface; (2) if the plasma flow has a radially outward component, then we fix the

plasma density to a relatively small value, $\rho_{ghost} = 5\ amu/cc$. For the simulations presented in this work, the total source rate of outflowing plasma from the surface boundary into the magnetosphere ranges between 1 – 6 x10^{24} amu/s, consistent with the idea that Mercury's surface acts as a very weak source of plasma (e.g., *Raines et al.*, 2015). Finally, we use a magnetic field-based boundary condition to set the plasma velocity in the ghost cell in which the parallel component of velocity with respect to magnetic field in physical cell is reversed ($\boldsymbol{u}_{ghost} \cdot \boldsymbol{B} = -\boldsymbol{u}_{physical} \cdot \boldsymbol{B}$) from the parallel component in the physical cell and the perpendicular component is kept the same ($\boldsymbol{u}_{ghost} \times \boldsymbol{B} = \boldsymbol{u}_{physical} \times \boldsymbol{B}$). The idea of this approach is to set the plasma velocity at the surface $\boldsymbol{u}_{surface} = \left(\boldsymbol{u}_{ghost} + \boldsymbol{u}_{physical}\right)/2$ to be perpendicular to the local magnetic field as described in detail in *Zhou et al.* (2019).

For the simulation outer boundaries, we specify the boundary conditions using idealized solar wind and IMF conditions at the upstream boundary (X=8 R_M) and apply floating boundary conditions to all the other five boundaries of the rectangular simulation domain to allow the super-magnetosonic solar wind to leave the system freely. For all the simulations performed in this study, the upstream conditions (see Table 3-1) are fixed in time. Because we aim to investigate how Mercury's magnetopause reconnection depends on the upstream conditions, specifically the solar wind Alfvenic Mach number (M_A) and the IMF orientation, the simulations presented here can be divided into two groups: one with M_A= 6, which may be considered nominal solar wind driving, and another with M_A= 2, which can be deemed as strong driving. Each Mach number group then consists of three simulations with the same IMF strength but different orientations characterized by the clock angle (i.e., the angle of the IMF vector in the YZ plane relative to the +Z axis measured counter-clockwise when viewed from the Sun) resulting in three different shear angles between the IMF and Mercury's magnetospheric field at the low-latitude dayside magnetopause, i.e., 90°,

135° and 180°. As shown in Table 3-1, the solar wind density, velocity and temperature chosen for the simulations fall within the typical ranges observed at Mercury. The design of the solar wind input parameters enables us to make systematic comparisons between (1) simulations with the same IMF orientation but different Alfvenic Mach number and (2) simulations with the same Mach number but different IMF orientations, which will be described in detail in the following sections.

3.3 Simulation Analysis and Results

In this section, we present our simulation results for different upstream conditions listed in Table 3-1 focusing on the formation and properties of FTEs and their role in driving the global dynamics. Section 3.3.1 gives an overview of the typical structure and properties of the FTEs formed in our Hall-MHD simulations. Section 3.3.2 describes the quasi-automated algorithm we have developed to identify FTEs and extract their properties from the simulations. Section 3.3.3 shows the statistical results on the identified FTEs. In Section 3.3.4, we assess the contribution of FTEs to Mercury's Dungey cycle and how this contribution varies depending on the upstream conditions.

3.3.1 Spatial structure and temporal evolution of simulated FTEs

To illustrate the 3D structure of the FTEs seen in our simulations, we show in Figure 3-1 an example of FTE extracted from Run #2 (in Table 3-1), which corresponds to M_A= 6 and IMF clock angle of 135°. The magnetopause surface is extracted from the simulation based on the analytical magnetopause model first introduced in *Shue et al.* (1997). The colors on the surface indicate the normal component of the magnetic field (B_n) with respect to the modeled magnetopause surface (red colors indicate magnetic fields pointing away from the Mercury and

blue colors indicate the opposite direction) and the black lines show magnetic field lines traced from locations within the FTE. Rope-like structure and resultant bipolar B_n signature of FTE can be seen clearly from Figure 3-1. In addition to providing global context for the example FTE in 3D, the Shue magnetopause model presented here is also used in our quasi-automated algorithm to identify FTEs whose detail will be discussed in the next section (Section 3.3.2).

Figure 3-2 shows a snapshot of B_y contours in X-Z plane with magnetic field lines superimposed to delineate the magnetospheric configuration from another simulation, Run #1 (M_A=6, IMF clock angle = 180°). The magenta ellipses outline the boundaries of two identified FTEs whose cross-section areas are fitted with 2D ellipses that are used for evaluating the amount of magnetic flux carried by FTEs (see detailed discussion later in the text). Both FTEs seen in this example not only have a loop-like magnetic geometry (as shown by the field lines) but also exhibit enhancements in the axial component of the magnetic field (as indicated by the colors), which is pointing in the -Y direction in this case.

While Figure 3-1 and Figure 3-2 provide single snapshots of the 2D and 3D structure of simulated FTEs, those FTEs, once formed in our simulations, all undergo substantial changes as they interact with the surrounding plasma and magnetic field. To illustrate how FTEs evolve in time, we show in Figure 3-3 and Figure 3-4 a series of snapshots of B_y contours with sampled magnetic field lines in X-Z plane in a similar format as in Figure 3-2. The results shown here were extracted from two simulations with Figure 3-3 from Run #1 where M_A= 6 and Figure 3-4 from Run #4 where M_A= 2. In both runs, the IMF clock angle is kept at 180°. The time separation between consecutive frames is 2 seconds. Mercury's conducting core is shown as black filled half-circle capped at 0.8 R_M and its surface is represented by the red half-circle at r = 1 R_M. FTEs in Figure 3-3 and Figure 3-4 show up as concentric magnetic loops with a significant out-of-plane

magnetic component (B_y). In the M_A= 6 case (Figure 3-3), initially at the start of the series (T= 36 s), there are five FTEs present over a large range of latitudes on the magnetopause: one each near the northern and southern cusp and another three at low latitudes. Following the labeled FTEs through the various snapshots shows that they typically go through a growth phase first in which their size and core field strength keep increasing, and then experience a decay phase in which they gradually dissipate while passing through the cusp region. During the time interval of ~ 15 seconds shown in Figure 3-3, four new FTEs are observed to form and they essentially follow a similar evolution from growth to decay. For the M_A= 2 case (Figure 3-4), FTEs typically are found to have smaller size than that seen in the M_A= 6 case (Figure 3-3). The series of snapshots start with 3 FTEs initially (T= 28 s), but six additional FTEs are formed over the course of 15 seconds, suggesting a more frequent occurrence of FTEs compared to the M_A= 6 case in Figure 3-3. In both the M_A= 6 and M_A= 2 cases shown here for the IMF clock angle of 180°, most FTEs initially form close to the noon-midnight meridian (i.e., LT = 12 plane) and near the magnetic equator. Once formed, the FTEs propagate mostly along ±Z direction (either northward or southward). In contrast, as the IMF clock angle decreases (e.g., to 90° and 135°), the locations where most FTEs form in our simulation start to shift away from the noon-midnight meridional plane as well as in the north-south direction. This is because FTEs typically form near the primary reconnection X-line where the reconnection electric field peaks. As will be shown later in Section 3.4, the geometry of the reconnection X-line in our simulations exhibits a clear dependence on the IMF orientation, and as such the primary locations of where FTEs form are also dependent on the IMF orientation. Detailed statistics on various properties of the simulated FTEs will be presented and compared among different simulations in Section 3.3.3.

Another notable feature in Figure 3-3 and Figure 3-4 is the common presence of multiple X-lines on the magnetopause surrounding FTEs, suggesting that multiple X-line reconnection is the underlying mechanism responsible for the formation of FTEs in our Hall-MHD simulations. To confirm this point, we have repeated Run #1 using an ideal MHD simulation model while keeping all the simulation setup and input parameters the same. We find that the magnetopause boundary in the ideal MHD simulation appears very quiescent with relatively steady reconnection arising from single X-line on the magnetopause. As a result, there are no FTEs formed in the ideal MHD simulation. The behavior observed in the ideal MHD simulation is in sharp contrast with the unsteady nature of reconnection and the presence of multiple X-lines on the magnetopause seen in the Hall MHD simulations.

The global model also allows us to extract plasma and magnetic field signatures associated with FTEs at fixed spatial locations, which makes it possible to compare directly with spacecraft measurements. As an example, Figure 3-5 shows the time series of key physical parameters, including plasma density, pressure and magnetic field vector components and magnitude, extracted from Run #1 at a virtual satellite located at [X, Y, Z] = [1.26, 0, 0.93] R_M in MSO coordinates. The position of this satellite, being on the magnetopause north of the equator, gives us a clear view of the perturbations caused by FTEs as they pass by in the simulation. The red vertical intervals correspond to identified FTEs based on bipolar B_n signature, the detail of which will be discussed in the next section. One notable feature that immediately stands out in Figure 3-5 is that the typical duration of FTEs as seen by a virtual observer is quite short, on the order of a few seconds, which is consistent with MESSENGER observations of FTEs at Mercury (e.g., *Slavin et al*., 2012; *Sun et al*., 2020). As will be shown later, the short duration of FTEs is a result of their small scale size and the relatively fast speeds at which they move along the magnetopause. Furthermore, FTEs are

separated by a few to a couple of tens of seconds, indicating a quite frequent occurrence. Figure 3-6 is similar to Figure 3-5 but for results extracted from Run #4, which differs from Run #1 in the solar wind M_A used. Comparing Figure 3-5 with Figure 3-6, we find that for Run #4, which corresponds to a lower M_A condition, the spacing between neighboring FTEs is smaller, the typical duration of FTEs is shorter and consequently the number of identified FTEs is larger compared to Run #1. This comparison clearly shows that lower M_A solar wind and IMF conditions lead to a more dynamic dayside magnetopause and more frequent formation of FTEs, which is in general agreement with previous MESSENGER observations (e.g., *Sun et al*. [2020]).

3.3.2 Automated method for FTE identification

Given the large number of FTEs formed in our simulations, we have developed an automated method to consistently identify FTEs in the simulations and extract the physical properties of FTEs (e.g., size, speed, magnetic flux content, etc.) that will be used later in our statistical analysis of the simulated FTEs. When the IMF has a significant southward component, because of the small size of Mercury's magnetosphere, almost all the FTEs formed in the simulation cut across the noon-midnight meridional plane (XZ plane). Such a behavior allows us to identify FTEs along the intersection of the magnetopause with the noon-midnight meridian for cases when the IMF has a significant southward component (or large shear angle). For small shear angle cases, magnetopause reconnection sites and resultant FTEs tend to occur away from the noon-midnight meridian, and for those cases we sample meridional planes at both morning and afternoon local times to capture FTEs, which will be explained later. In general, because of the rope-like structure of FTEs, the magnetic field component normal to the magnetopause (B_n, where a positive value corresponds to magnetic field pointing toward the magnetosheath) is expected to have a bipolar pattern associated with each FTE, which means that pairs of positive-negative B_n

on the magnetopause surface can be used as a selection criterion for identifying potential FTEs. Since Mercury's intrinsic magnetic field points from south to north near the equator, an FTE will always have positive B_n for the upper half of the magnetic loop and negative B_n for the lower half. The clear ordering of positive-negative B_n in the latitudinal direction gives another criterion to identify FTEs in our automated algorithm. The existence of FTEs and its dynamic nature presents a challenge to determine the exact location and shape of the magnetopause boundary that separates the magnetosphere and magnetosheath. In a previous modeling study of Ganymede's magnetosphere, *Zhou et al*. (2020) used time-averaged $B_z = 0$ surface as an estimation for Ganymede's magnetopause. However, such an approach is less ideal for Mercury because (1) Mercury has a very dynamic magnetopause such that the actual magnetopause at a given timestep could deviate significantly from the time-averaged $B_z = 0$ surface, and (2) the presence of FTEs creates indentations/bulges on the $B_z = 0$ surface and the resultant irregular shape makes it difficult to identify FTEs based on bipolar B_n signatures. Considering these factors, in this study we employ the empirical magnetopause model by *Shue et al.* (1997) as an approximation to determine the normal component of magnetic field B_n on the magnetopause. By analyzing the MESSENGER observations of magnetopause crossings, *Winslow et al*. (2013) have shown that the Shue model works reasonably well for Mercury. The analytical form of the Shue model is given as:

$$r = r_0 \left(\frac{1}{1 + cos\,\theta} \right)^{\alpha}, \tag{3-1}$$

where r is the radial distance from the center of the planet's dipole and θ is the angle between the radial direction and the +X direction in MSO coordinates. Both r_0 and α are free parameters used to determine the shape of the empirical magnetopause. Specifically, r_0 is the subsolar magnetopause standoff distance and α is a parameter that decides the level of tail flaring. We

adjust r_0 and α to match the Shue magnetopause model with the simulated magnetopause for every timestep on which the simulation results were saved such that the constantly changing shape and motion of the magnetopause are accounted for. The approach we used to determine r_0 and α for every timestep is as follows: (1) Launch multiple horizontal lines (Z = constants) in the meridional plane of interest, and then identify the magnetopause boundary locations as the points where large plasma density jumps are observed, (2) Use the Z = 0.2 horizontal line (corresponding to the magnetic equator) to determine the magnetopause subsolar standoff distance r_0 . Take r_0 determined from the previous step to calculate α using Equation (3-1) for the other horizontal lines at different Z distances and then take the average value to be α for this particular timestep. As a demonstration, Figure 3-7 shows the result of our dynamically fitted Shue model (magenta line) for Run #2 in the XZ at Y= 0 plane for two different timesteps. Sampled magnetic field lines are shown as black stream traces in Figure 3-7 to illustrate the topology of dayside magnetic field. The background colors in Figure 3-7 represent contours of B_z, where the B_z= 0 contour (white color) provides a crude indication of where the magnetopause is. As can be seen, by dynamically adjusting the values of r_0 and α in the Shue empirical model we are able to obtain reasonably good fits to the simulated magnetopause as it varies with time. This dynamic fitting approach, compared to time-averaged $B_z = 0$ surface, not only addresses the unsteady nature of Mercury's magnetopause but also yields a relatively smooth transition of the magnetopause normal direction between different timeframes.

By applying the magnetopause fitting procedure to the simulation output we can then extract physical parameters of interest along the magnetopause boundary from different timesteps and then examine the time evolution of the extracted parameters to identify FTEs and determine their physical properties, such as spatial size, speed of motion and the amount of magnetic flux

contained. A useful way to visualize the extracted simulation results is to construct a time-latitude (t-θ) map as shown in Figure 3-8, which corresponds to Run #2 (M_A= 6, IMF clock angle = 135°). The extracted parameters shown as color contours in this particular example are (a) plasma pressure (P), (b) perturbations to the magnetic field strength, (c) FTE core field (B_c), and (d) the normal component of the magnetic field (B_n). Note that for panel (b), the perturbation to the magnetic field magnitude is measured with respect to the average value of |B| in a 5-second sliding window. The method we use to calculate the core field (B_c) shown in panel (c) will be described in detail in Section 3.3.3.

Figure 3-9 is similar to Figure 3-8 but for Run #3 (M_A= 6, IMF clock angle = 90°). For this IMF configuration, most FTEs do not form near the noon-midnight meridian, but instead they are produced primarily in the northern-dawn and southern-duck quadrants of the magnetopause. Once the FTEs have formed, their subsequent motion tends to follow the direction of the reconnection outflow, which is generally perpendicular to the X-line. As such, the FTEs formed under this IMF configuration propagate mostly in a direction that deviates from the ±Z-direction and has a significant Y-component (almost along the diagonal direction in the YZ-plane). Therefore, instead of using the LT=12 meridian as described above for larger IMF clock angle cases, for simulations with 90° IMF clock angle (Runs #3 and #6) we identify FTEs in two meridional planes corresponding to LT= 09 and LT= 15, and then add the results together to obtain the total number of unique FTEs. Figure 3-9 shows the results from the LT = 15 cut for Run #3. We have verified that no FTE in our simulation extends in the azimuthal direction to intersect with both the LT= 09 and 15 cut planes, which ensures that no FTE is counted twice in our statistics.

As explained above, potential FTEs would show up in the time-latitude map as pairs of positive-negative B_n (red and blue stripes in Figure 3-8d and Figure 3-9d). Based on this expected

B_n signature associated with FTEs, we have developed an automated identification method consisting of the following steps: (1) Identify the points between red and blue stripes that correspond to $B_n = 0$, (2) Measure the minimum and maximum values of B_n along the vertical (latitudinal) direction, (3) Apply a 20 nT threshold on the absolute values of B_n extrema to filter out ineligible red-blue stripes, (4) Visually check the 3D magnetic topology of all candidate FTEs and remove those that do not exhibit a rope-like structure. The 20 nT threshold applied in our identification algorithm was inspired by a previous study of Earth's FTEs (*Sun et al.,* 2019), which used 5-10 nT as the threshold. However, in Mercury's case we have found that using 5 or 10 nT yields many false positive detections. For example, when using 10 nT as the criterion in our automated method we found that about 40% of those identified FTEs with desired positive-negative B_n pairs are false positives for Run #1 after manually checking their 3D magnetic field lines. This is likely due to the fact that intense reconnection occurring at Mercury's magnetopause causes large, local variations in the magnetopause shape in the simulation that results in significant B_n fluctuations. We have tested different thresholds of B_n and determined that 20 nT works reasonably well for our analysis in that the set of selection criteria combined are robust to capture the vast majority of FTEs in our simulations and at the same time conservative enough to filter out most of the false positives.

We have applied the automated algorithm to the output from all six simulations at 0.2 second cadence to identify FTEs. Note that the total duration of the model output that enters our analysis varies case by case ranging from ~ 150 to 200 seconds, which is comparable to the typical timescale of Mercury's Dungey cycle. The total number of unique FTEs identified is tabulated in Table 3-2 for all six simulations. One apparent trend that can be noticed in Table 3-2 is that the number of FTEs formed in the simulation increases with decreasing solar wind M_A and increasing

IMF clock angle, which is consistent with the findings from the recent MESSENGER survey of FTE showers at Mercury (*Sun et al*., 2020). Detailed statistics of simulated FTE properties and comparisons with observations will be presented in Section 3.3.3.

To follow the time evolution of FTEs that will feed into our statistical analysis later on, we also need to determine the centers of the FTEs, which can be readily identified in the B_n time-latitude map (e.g., Figure 3-8d and Figure 3-9d) as B_n= 0 points (magenta dots). Tracking the centers of FTEs in time allows us to directly estimate their speed of motion as well as other properties of FTEs, which will be presented in the next section. By overplotting the FTE centers onto the other panels of Figure 3-8 and Figure 3-9, we can cross-compare different physical parameters that provide useful insight into the structure of FTEs. For instance, panels (a-c) in Figure 3-8 and Figure 3-9 indicate that most FTEs seen in our simulations show enhancements in plasma pressure, core field and total magnetic field strength near the FTE center, which are typical characteristics of FTEs observed at Mercury (e.g., *Slavin et al*., 2012; *Sun et al*., 2020). Another interesting feature in Figure 3-8b and Figure 3-9b is that most FTEs have trailing regions where the magnetic field is depressed compared to the background. Similar modeling results have been reported previously by *Kuznetsova et al*. (2009) who found magnetic field cavities in the wake of FTEs from their high-resolution simulations of Earth's FTEs.

The black dots in Figure 3-8 and Figure 3-9 represent the locations on the magnetopause where the plasma flow speed reaches its minimum value. As a good approximation, those black dots can be deemed as flow diverging points that separate northward and southward moving plasma flows on the magnetopause. In the examples shown here for two different IMF orientations, we find that the flow diverging point in the simulation is, in general, located very close to Mercury's magnetic equator with some fluctuations caused by reconnection outflows, which is

consistent with the general expectation that the large-scale structure of the solar wind-magnetosphere interaction is controlled primarily by symmetries associated with the planetary internal field. Figure 3-8, which corresponds to IMF clock angle of 135°, the northward and southward moving FTEs are generally well divided by a separatrix close to the magnetic equator and hence the flow diversion region, consistent with the geometry of the primary X-line expected for this particular IMF orientation (see Figure 3-13 and associated discussions in Section 3.5). In contrast, in Figure 3-9 that corresponds to 90° IMF clock angle case, the separatrix between northward and southward moving FTEs is shifted to the south (~ 30° southern latitude) in the dusk meridian and shifted to the north in the dawn meridian (not shown). Again, such a behavior can be readily understood in terms of the geometry of the primary X-line expected for an IMF configuration with a dominant y-component (see Figure 3-13 and associated discussions in Section 3.5). Because the flow diversion region is still located near the magnetic equator, FTE formation and their subsequent motion are restricted almost exclusively to the south of the flow diverging points on the dusk side. A similar pattern is seen on the dawn side but with most FTEs seen north of the flow diversion region. These simulation results suggest it is important to take into account both the reconnection geometry and large-scale plasma flows, especially the magnetosheath flow, in considering FTE formation and propagation.

3.3.3 Statistical survey of simulated FTEs

Here we present a statistical analysis on the simulated FTEs identified by our automated method. The primary properties of FTEs we focus on in this work are their occurrence rate, spatial size, traveling speed, core field strength and magnetic flux content.

The FTE occurrence rate can be readily obtained based on the total number of FTEs identified within the duration of the simulation output, which is given in Table 3-2. For the external

conditions considered in our work, FTEs are formed in the simulation every few seconds, with occurrence rates ranging from 2 to 9 seconds. Comparing the occurrence rates across different runs reveals a clear trend that FTEs are formed more frequently in the simulation with smaller solar wind Alfvénic Mach number, which leads to lower plasma beta in the magnetosheath, and larger IMF clock angle, which corresponds to stronger magnetic shear across the magnetopause boundary. Both the FTE occurrence rate and its dependence on the solar wind M_A and IMF orientation found in our Hall-MHD simulations are in good agreement with the results reported in a recent MESSENGER survey of FTE shower events at Mercury (*Sun et al*., 2020).

The statistical results of other FTE properties, including size, traveling speed, core field strength and magnetic flux content, are shown as histograms in Figure 3-10 - Figure 3-12. To facilitate comparison, we have paired the results from simulations with the same IMF clock angle but different solar wind M_A into one figure, i.e., Figure 3-10 for 180° clock angle, Figure 3-11 for 135° and Figure 3-12 for 90°. Determining those FTE properties shown in Figure 3-10 - Figure 3-12 from the simulation requires further analysis beyond the automated indemnification method described in Section 3.3.2, which we explain in the following.

First, we measure the size of an FTE as its characteristic scale length in the latitudinal direction along the magnetopause surface. Because of the loop-like structure of FTE's cross-section, the magnetic field normal component, B_n, normally would exhibit a bi-polar variation along the latitudinal direction. For a given timestep, we first find the maximum (positive) and minimum (negative) values of B_n associated with a particular FTE. The northern and southern outer boundaries of the FTE are then defined as the locations where B_n has decayed by 1/e (one e-folding distance) from its maximum and minimum values. The distance between the northern and southern boundary points approximately represents the length along the semi-major axis of the

FTE's cross-section in the particular LT cut in which we identify the FTE. However, the FTE size we aim to quantify should be measured in the cross-section orthogonal to the axis of the FTE, whose orientation varies depending on the IMF clock angle. For example, for 180° IMF clock angle cases, the axes of FTEs formed in the simulations are approximately aligned with the Y-axis. However, when the IMF clock angle is smaller than 180°, the axes of FTEs are slanted with respect to the equatorial plane (see the example shown in Figure 3-1) at an angle that can be readily related to the IMF clock angle. To correct for this geometric effect, we define the FTE size to be the length measured in the LT multiplied with a factor $\cos(\theta_{FTE})$, where θ_{FTE} is the angle between the normal direction of the LT cut used to identify FTEs and the FTE axis. The value of θ_{FTE} is taken empirically as 0°, 22.5°, 45° when the IMF clock angle is 180°, 135°, 90°, respectively. Moreover, since the size of an FTE changes in time as it interacts with the surrounding plasma and field, for each identified FTE we repeat the above procedure for every timestep (0.2 s cadence), and then average over 5 timesteps evenly sampled through its entire evolution to obtain the mean FTE size, which enters our statistical analysis. Panels (a) and (e) in Figure 3-10 - Figure 3-12 show the distributions of average FTE size for simulations using different solar wind M_A. There is a wide spread in the size distribution for all simulations, with average FTE sizes ranging from < 100 km to ~ 2000 km. Comparing the results (shown in the legends of panels (a) and (e)) seen in different simulations reveals that the average FTE size is comparable between 180° and 135° IMF clock angle cases and becomes significantly larger in 90° IMF clock angle simulations. When the IMF clock angle is 180° or 135°, there is a higher percentage of small-size FTEs in M_A= 2 than in M_A= 6, and as a result, the average FTE size decreases with decreasing M_A. However, the 90° clock angle simulations do not appear to follow the same trend and the average FTE size increases with decreasing M_A.

The traveling speed of an FTE along the magnetopause can be determined from the aforementioned time-latitude maps (e.g., Figure 3-8 and Figure 3-9) by tracking the slope of the curve connecting the identified FTE centers (magenta dots). Note that positive and negative slopes correspond to northward and southward motion, respectively, which are reflected in the sign of FTE traveling velocity shown in our statistics. It is evident from the examples shown in Figure 3-8 and Figure 3-9 that the slope is not a constant for most FTEs, suggesting that FTEs commonly travel at varying speeds as they evolve in time, just like the size of FTEs discussed above. To account for this feature in our statistics, we calculate an average velocity for each FTE by taking the mean value of the estimated velocities from 5 timesteps evenly sampled through its lifetime. In estimating the FTE traveling velocity using the time-latitude maps, we have also taken into account the aforementioned geometric effect arising from projecting slanted FTEs onto LT cut planes by multiplying the speed extracted from a given LT plane with the same "$\cos(\theta_{FTE})$" as used in calculating the FTE size. The distributions of average FTE traveling velocities are shown in panels (b) and (f) of Figure 3-10 - Figure 3-12. For all six simulations, both northward (positive velocities) and southward (negative velocities) moving FTEs are present and the respective total numbers are roughly equal, consistent with the expectation based on the result discussed in Section 3.3.2 that symmetries in the planetary internal field predominantly control the global structure of the magnetospheric interaction and associated large-scale plasma flows. Overall, the average FTE traveling speeds seen in the various simulations have a wide distribution ranging between a few tens of km/s to a few hundred km/s with peak distributions around 200 - 400 km/s, which are comparable to the typical value of 300 km/s assumed for FTE travelling speed in previous MESSENGER investigations of FTEs (e.g., *Imber et al*., 2014; *Sun et al.*, 2020). There is also the tendency that for the same IMF clock angle the distribution becomes wider for M_A= 2 cases

compared to M_A= 6, indicating a more dynamic magnetopause under lower M_A solar wind conditions. By averaging over all FTEs seen in a given simulation, which is shown in the legends of panels (b) and (f), we find a consistent trend across all three pairs of simulations using the same IMF clock angle that the average FTE traveling speed increases with decreasing solar wind M_A. This result is consistent with theoretical expectation considering that FTE's traveling speed along the magnetopause largely depends on the flow speed in the reconnection outflow region, which scales directly with the Alfvén speed in the reconnection inflow region. Solar wind with lower M_A tends to result in higher Alfvén speed in the magnetosheath, thereby leading to faster reconnection outflows. When comparing the FTE speeds for simulations with the same M_A but different IMF clock angles, we find that the speed in general decreases with decreasing clock angle, with the exception from the case of M_A= 2 and clock angle= 90° (Figure 3-12f) where the average speed lies somewhere between the 135° and 180° cases. The general trend can be well understood in terms of how reconnection outflow speed depends on the reconnection magnetic field components on the two sides of the magnetopause (e.g., *Cassak and Shay,* 2007), which generally become weaker for smaller IMF clock angle with the same field magnitude.

The core field strength and magnetic flux content of FTEs are obtained through additional modeling of the structure of individual FTEs. In order to determine the total flux content carried by an FTE, we need to first identify its cross-section, which requires knowledge of the outer boundary of the FTE. While the latitudinal extent of an FTE can be determined using the method described above in the discussion of FTE size, the radial extent of an FTE can be estimated using a similar method. We first measure the maximum plasma pressure (P_{max}) along the ray path going radially through the FTE's center (see the red lines in Figure 3-2), and then identify the inward and outward boundary locations of the FTE in the radial direction as the points along the radial ray

where the plasma pressure has fallen off by *1/e*. Note that here we have used the plasma pressure, instead of B_n, as a criterion to search for the boundary locations in the radial direction mainly because B_n almost always vanishes along the radial ray passing through an FTE's center. Knowing the four boundary points of a given FTE in the latitude and radial directions, we then fit the FTE's cross-section as an ellipse (see the magenta ellipses in Figure 3-2), whose semi-minor axis and semi-major axis are equal to one half of the lengths in the radial and latitudinal directions, respectively. The total amount of magnetic flux carried by an FTE can then be obtained by integrating the out-of-plane magnetic field component (B_{out}) over the area of the ellipse representing the FTE's cross-section. The core field of an FTE (B_c) can also be estimated directly from the out-of-plane magnetic field component (B_{out}). Similar to the consideration in calculating the FTE size, we also take into account the geometric effect in our estimation of the FTE core field, which is defined as $B_c = B_{out}/\cos(\theta_{FTE})$, where B_{out} is the magnetic field component perpendicular to the LT cut used to identify FTEs and θ_{FTE} is the angle between the normal direction of the LT cut and the FTE axis. The value of θ_{FTE} is chosen to be 0°, 22.5°, 45° for IMF clock angles of 180°, 135°, 90°, respectively. Since the core field strength is non-uniform within the cross-section of an FTE and typically peaks near the center, we use the maximum core field in our statistics.

Similar to what is done for the other FTE parameters, we also take averages of the calculated magnetic flux content and core field over 5 evenly sampled timesteps through its lifetime for every identified FTE, whose distributions are shown in panels (c, g) and (d, h) of Figure 3-10 - Figure 3-12. For the 180° IMF clock angle cases, FTEs' core fields can have either positive or negative polarity with respect to the dawn-dusk direction. In contrast, when the IMF has a significant B_y component, such as in the 90° and 135° clock angle simulations, the core fields

associated with the vast majority of FTEs show the same polarity as that of the IMF B_y. This result is consistent with previous observations of FTEs at Earth. For instance, *Kieokaew et al*. (2021), found a similar trend in the FTEs observed by the Magnetospheric MultiScale (MMS) mission and suggested that the polarity of FTE's core field is controlled mainly by the orientation of the guide field (e.g., IMF B_y) in the context of multiple X-line reconnection. The average core field strength ranges from ~ 50 nT to 170 nT in the six simulations, which is entirely consistent with that observed by MESSENGER during FTE shower events (*Sun et al*., 2022a). For 180° and 135° clock angle simulations, the average core field strength shows significant increases (~ 70%) as the solar wind M_A decreases from 6 to 2. The 90° simulations show a somewhat different trend in that the average core field strength exhibits a modest decrease of ~ 15% between M_A= 6 and M_A= 2 cases.

As shown in panels (d) and (h), the average magnetic flux carried by individual FTEs ranges between 0.005 MWb and 0.03 MWb, which is consistent with the range of values estimated by *Sun et al.* (2020) for the FTE shower events observed by MESSENGER. Furthermore, the upper end of the simulated FTE flux content of 0.03 MWb, which is a rare occurrence in the simulation, is comparable to the mean flux content (0.06 MWb) estimated for single "large" FTEs encountered by MESSENGER (*Slavin et* al., 2010a; *Imber et al.*, 2014). Comparing the simulation results for different IMF clock angle cases shows that under purely southward IMF conditions (180° cases), FTEs tend to carry less flux compared to the cases when the IMF contains a large B_y (135° and 90° cases). Furthermore, the average FTE flux content is comparable between the 135° and 90° clock angle cases, which is in general agreement with the result of very weak dependence on IMF clock angle identified in the *Sun et al.* (2020) MESSSENGER survey. For the same IMF clock angle, individual FTEs on average carry a larger amount of open flux under lower solar wind M_A

conditions, which is, again, in agreement with the trend found in the *Sun et al.* (2020) MESSENGER study.

3.3.4 FTE contributions to global dynamics

Previous studies based on MESSENGER observations (e.g., *Slavin et al*., 2012; *Imber et al.*, 2014; *Sun et al*., 2020) and theoretical arguments (e.g., *Fear et al*., 2019) have suggested that FTEs at Mercury could make a much more significant contribution to the global Dungey cycle compared to the situation at Earth. Here we assess the importance of FTEs in contributing to the global circulation of magnetic flux in our simulations. In this analysis, we use the cross polar cap potential (CPCP) as a measure of the solar wind-magnetosphere coupling through magnetopause reconnection. The CPCP is calculated using the same approach described in detail by *Zhou et al.* (2020) from the simulation by integrating the convectional electric field along the dawn-to-dusk direction between the boundary points of the polar cap in the terminator plane. As discussed in *Zhou et al*. (2020), the CPCP calculated in this manner essentially can be viewed, as an approximation, the amount of magnetic flux per unit time opened through dayside magnetopause reconnection. We have verified that CPCP values are the same for the northern and southern hemispheres in our simulations, which is expected considering conservation of magnetic flux. However, it is worth noting that the northern and southern polar caps differ significantly in their size and shape because of the northward offset of Mercury's internal dipole.

With the statistics introduced previously on FTE occurrence rate and the average amount of magnetic flux carried by individual FTEs, we can evaluate the overall contribution of FTEs (C) to open flux generation on the dayside as follows:

$$C = \frac{\Phi_{avg} * N_{FTE}}{CPCP * T} \tag{3-2}$$

where Φ_{avg} is the average FTE open flux content presented in Figure 3-10 - Figure 3-12, N_{FTE} is the total number of identified FTEs within the duration T of the simulation output that has been used in our statistical analysis. The results of CPCP and estimated contribution of FTEs to open flux generation are presented in the last two rows of Table 3 for all six simulations. For the various external conditions used in the simulation, the CPCP ranges between 28 kV and 119 kV, representing nominal and strong solar wind driving cases. The CPCP is found to increase with increasing IMF clock angle and decreasing solar wind M_A, which is consistent with the expectation based on how the reconnection rate depends on the upstream Alfvén speed and the shear angle across the magnetopause. As shown by the bottom row of Table 3-3, FTEs contribute about 3% - 13% of the total magnetic flux opened through dayside reconnection for the upstream conditions considered in our study. These values indicate that FTEs at Mercury carry a significant portion of the open flux that participates in the Dungey cycle, which is in line with the finding reached in previous studies based on MESSENGER observations (e.g., *Slavin et al*., 2012; *Imber et al*., 2014; *Sun et al*., 2020). Our simulation also reveals that the percentage contribution of FTEs to open flux generation increases with decreasing IMF clock angle, whereas it increases with decreasing solar wind M_A although the dependence on M_A is relatively weak compared to that on clock angle. The trend seen in the overall contribution of FTEs to the dayside open flux generation as function of IMF clock angle may imply that under large IMF clock angle conditions, more open flux is generated through single X-line reconnection, instead of multiple X-line reconnection that produces FTEs.

3.4 Discussion

In Section 3.3, we have presented the techniques used to identify FTEs from the various simulations and the properties of simulated FTEs extracted using those techniques. Here we summarize the key statistics of simulated FTEs in Table 3-3 for all six simulations. To obtain a better understanding of how the characteristics of FTEs depend on the upstream conditions, we have also evaluated the reconnection geometry and intensity at the magnetopause in order to place our FTE results into context. The main parameter of interest here is the reconnection electric field (E_{rec}), which can be estimated according to the following formula proposed by *Cassak and Shay* (2007) for asymmetric reconnection.

$$E_{rec} = 2kV_{out}\left(\frac{B_{msh}B_{msp}}{B_{msh}+B_{msp}}\right) \tag{3-3}$$

Here, B_{msh} and B_{msp} represent the reconnecting magnetic field component on the magnetosheath and magnetospheric side adjacent to the magnetopause boundary, respectively. k is the dimensionless reconnection rate, which is related to the aspect ratio of the diffusion region. Numerous previous studies have attempted to determine k for various reconnection scenarios in space plasmas and the commonly found order-of-magnitude value for k is 0.1 (e.g., *Cassak et al*., 2017; *Liu et al.*, 2017), which is assumed in our calculation. V_{out} in the equation for E_{rec} represents the reconnection outflow flow speed, which can be obtained as follows:

$$V_{out} = \left[\frac{B_{msh}B_{msp}(B_{msh}+B_{msp})}{\mu_0(\rho_{msp}B_{msh}+\rho_{msh}B_{msp})}\right]^{\frac{1}{2}} \tag{3-4}$$

, where ρ_{msh} and ρ_{msp} are the plasma mass density on the magnetosheath and magnetospheric side adjacent to the magnetopause boundary, respectively. Clearly, calculation of E_{rec} requires knowledge of the plasma and magnetic field conditions on both sides of the magnetopause boundary, which we extract from the simulation using a similar approach as used for identifying FTEs. After having determined the magnetopause surface based on the *Shue et al*. (1997) empirical

model for each timestep, we scale the fitted magnetopause surface radially inward into magnetosphere and outward into magnetosheath by multiplying the previously determined "r_0" parameter in Equation (3-1) with a coefficient of 0.9 and 1.1, respectively. The plasma density and magnetic field are then extracted from these two surfaces to calculate V_{out} and E_{rec} according to the equations above. Note that in this procedure we have to first determine from the extracted magnetic field vectors the reconnecting components between the magnetospheric and magnetosheath magnetic fields, which are the components that are anti-parallel to each other. The reconnection electric field is calculated for each timestep from the simulation and the mean electric field strength, which is averaged over all timesteps, is projected onto the magnetopause surface in Figure 3-13 to illustrate the large-scale geometry and intensity of the dayside magnetopause reconnection. It should be pointed out that the onset conditions for reconnection were not evaluated in this analysis, and our intention with estimating E_{rec} is to investigate how strong the reconnection electric field would be in each simulation using a different set of upstream conditions when reconnection occurs on the magnetopause. It is clear from Figure 3-13 that the reconnection electric field varies systematically in its strength and spatial distribution in response to changes in the external conditions. In particular, the overall strength of E_{rec} increases with decreasing solar wind M_A and increasing IMF clock angle, consistent with the expectation that these two parameters primarily control the Alfvén speed in the reconnection inflow region and the magnetic shear across the magnetopause boundary. The region where strong reconnection electric fields are present in each simulation, which can be deemed as a proxy for identifying the location of the primary X-line on the magnetopause, correlates closely with the IMF orientation imposed. For instance, the strongest $|E_{rec}|$ is concentrated in a horizontal belt near the magnetic equator in the 180° IMF clock angle simulations, whereas similar belts containing strong $|E_{rec}|$ are also present in the 135° and

90° IMF clock angle simulations but are tilted relative to the equatorial plane. The tilt angle is roughly 22.5° for the 135° cases and 45° for the 90° cases, which explains our choices of the "θ_{FTE}" parameter in the estimation of the FTE size and core field presented in Section 3.3.3.

With the results on the reconnection electric field as a global context, we now return to Table 3-3 to further discuss some of the general trends of our simulation results. We first examine the effects of solar wind M_A on FTEs by comparing each pair of columns color-coded with the same color in Table 3-3, for which the only difference between the simulations is the upstream solar wind M_A. For all three IMF orientations tested in our experiment, the occurrence rate of FTEs is consistently higher for M_A= 2 than for M_A= 6, which is in agreement with the MESSENGER observations reported by *Sun et al.* (2020). The more frequent FTE occurrence in lower M_A cases is a direct result of the enhanced reconnection electric field with decreasing solar wind M_A, as shown in Figure 3-13. Similarly, there is also a consistent trend in the average FTE traveling speed between different M_A simulations using the same IMF clock angle. That is the average speed increases with decreasing solar wind M_A, which, as we discussed previously, arises from the dependence of the reconnection outflow speed on the Alfvén speed in the reconnection inflow region. The other properties of FTEs appear to show somewhat different trends for different IMF clock angles. For example, for 180° and 135° clock angles, the average FTE size decreases by 10-25% between M_A= 6 and M_A= 2 simulations, whereas it increases by ~ 10% for 90° IMF clock angle. Similarly, the average FTE core field increases significantly by ~ 70% when M_A decreases from 6 to 2 for 180° and 135° clock angle simulations, while it shows a slight decrease (~15%) for 90° clock angle simulations. Nonetheless, the average magnetic flux carried by FTEs consistently shows an increase with decreasing solar wind M_A for all IMF clock angles, although the relative increase is much larger for 180° and 135° cases than for 90° case.

Next, we examine the effects of the IMF orientation on the simulated FTE properties. The occurrence rate of FTEs increases monotonically with the IMF clock shear angle for both sets of simulations using the same solar wind M_A. This result is consistent with the trend identified in the MESSENGER observations of FTEs (*Sun et al.*, 2020). The average FTE size in the latitudinal direction is comparable between the 180° and 135° cases, whereas it is significantly larger under 90° IMF clock angle conditions. Because the latitudinal scale lengths of FTEs largely depend on the spacing between neighboring reconnection X-lines, the size difference among different clock angle simulations can be partially attributed to the reconnection electric field shown in Figure 3-13. For 180° and 135° clock angles, both the average reconnection electric field strength (Figure 3-13) and the resultant CPCP (Table 3-3) are comparable to each other, while the reconnection electric field strength and CPCP become significantly smaller for 90° simulations.

Finally, we discuss the CPCP values determined for our simulations in comparison to prior work based on in-situ observations. As shown in Table 3-3, the CPCP in our simulations ranges from 28 kV to 119 kV, representing nominal and strong solar wind driving conditions used in the model. Various previous studies have estimated the CPCP based on MESSENGER data. For example, *Slavin et al*., (2009) estimated that the CPCP of Mercury's magnetosphere during MESSENGER's second close flyby (M2), which corresponds to nominal solar wind driving conditions, is around 30 kV. A subsequent work by *DiBraccio et al*., (2015) showed similar values (23 kV and 29 kV) from two plasma mantle case studies. *Sun et al*., (2020) analyzed stronger solar wind driving cases and found that the CPCP during the impact of a coronal mass ejection (CME) could increase to ~ 45 kV. While the CPCP values seen in our M_A= 6 simulations (28 kV to 57 kV) are in line with the range of CPCPs inferred by the previous observational work, the CPCP in our M_A=2 simulations are significantly higher (69 to 119 kV), which deserves further discussion.

It is important to note that the IMF field strength we chose for the M_A= 2 simulations is 69 nT, which is larger than the high end (~ 45 nT) of the range of IMF strengths typically observed at Mercury (*Sun et al*., 2022b). As a result, stronger reconnection electric field and consequently larger CPCP are expected in the simulation. Therefore, the large CPCP values seen in the M_A=2 simulations can be attributed in part to the relative strong IMF used in driving our simulation. To confirm if this is the case, we have also estimated the CPCP values analytically following the method adopted by *Sun et al.* (2022b) based on the formula first proposed by *Kivelson and Ridley* (2008) [their Eq. 13] for explaining the CPCP saturation phenomenon at Earth.

$$CPCP = 10^{-7}u_x^2 + 0.1\pi R_{mp}B_{sw,yz}u_x sin^2\left(\frac{\theta}{2}\right)\frac{2\Sigma_A}{(\Sigma_A + \Sigma_P)} \quad (3\text{-}5)$$

, where u_x is the solar wind speed in m/s, R_{mp} is the subsolar magnetopause standoff distance in m, $B_{sw,yz}$ is the magnitude of the IMF component (in T) in the YZ plane, and Σ_A and Σ_P are the Alfven conductance (in S) of the solar wind and the Pedersen conductance (in S) of the conducting region associated with the planet. As shown above, the formula to calculate CPCP requires knowledge of the upstream solar wind (u_x) and IMF ($B_{sw,yz}$) conditions, all of which are known as input parameters in our simulations, as well as the length of the reconnection X-line at the dayside magnetopause, for which we follow the typical assumption of using "$0.1\pi R_{mp}$" as an approximation (R_{mp} is determined directly from the simulation by taking the average of r_0 in Equation (3-1) over all timesteps). Furthermore, the calculation also needs to know the Alfvén conductance of the solar wind $\Sigma_A = 1/(\mu_0 v_A)$, where v_A is the Alfvén speed in the upstream solar wind and μ_0 is the magnetic permeability in free space, as well as the Pedersen conductance (Σ_P) associated with any conductive region the planet may possess near its surface. Since Mercury lacks an appreciable ionosphere, the Pedersen conductance (Σ_P) can be deemed as the effective conductance in the planetary mantle (the layer immediately below the surface). Using the

resistivity profile assumed in our simulations (e.g., *Jia et al*., 2015, 2019), we obtain $\Sigma_P \sim 0.05$ S, which is negligible compared to the Alfvén conductance (Σ_A) of the solar wind (of the order of a few S). Considering the 180° IMF clock angle cases as an example, putting the upstream conditions and the R_{mp} extracted from the simulation into Equation (3-5) yields a CPCP of 50 kV for $M_A = 6$ and 94 kV for $M_A = 2$. It can be seen that the CPCP values determined for our simulations are quite consistent with the theorical predictions, which suggests that the seemingly high CPCPs seen in the $M_A = 2$ cases are most likely due to the stronger-than-typical IMF used in the model.

3.5 Summary and Conclusions

Motivated by the extensive observations of Mercury's magnetopause dynamics from MESSENGER, we have carried out a simulation study to investigate how the formation of FTEs and their contribution to the global dynamics are affected by external conditions. In this work, we employ the BATSRUS Hall MHD model (*Tóth et al*., 2008) with coupled planetary interior (*Jia et al*., 2015, 2019) to simulate Mercury's magnetosphere and use a high-resolution grid with resolution of ~ 20 km (or 0.008 R_M) near the magnetopause to well resolve the Hall effect that enables fast reconnection in the global simulation. A series of six global Hall MHD simulations have been conducted by using different sets of idealized upstream conditions designed to represent a range of solar wind and IMF conditions that could potentially be experienced by Mercury. The main external parameters of interest in this study are the solar wind Alfvénic Mach number and the IMF clock angle, for which several representative values ($M_A = 2$ and 6, IMF clock angle= 90°, 135°, 180°) were chosen for our numerical experiment.

In all simulations, which were driven by fixed upstream conditions, Mercury's magnetopause reconnection is found to occur in a non-steady fashion resulting in FTEs with rope-

like magnetic topology. To identify the large number of FTEs in the simulations, we have developed an automated algorithm that takes into consideration key characteristics of FTEs, such as the bi-polar variation of B_n associated with flux ropes. Important properties of FTEs, including their occurrence rate, size, traveling speed, core field strength and magnetic flux content, and their time histories were then extracted from all simulations and compared among different simulations to gain insight into the control of FTE properties by the solar wind. Below we summarize the key findings from our analysis.

FTEs are found to form frequently in all of the Mercury simulations with a new FTE born every 3 to 9 seconds for the external conditions used. The FTE occurrence rate shows a clear dependence on the solar wind M_A and the IMF orientation. Smaller solar wind M_A or larger IMF clock angle leads to more frequent occurrence of FTE. Both the range of FTE occurrence rate and its dependence on the upstream conditions are consistent with the results reported in the recent MESSENGER survey of FTE shower events at Mercury (*Sun et al*., 2020).

FTEs formed in the simulations have a wide range of sizes, from < 100 km to ~ 2000 km. As FTEs evolve in time, their sizes also change due to their interaction with the surrounding plasma and magnetic field. In comparing the results from different simulations, we find that the average FTE size is comparable between 180° and 135° IMF clock angle cases, while FTEs in the 90° IMF clock angle cases have significantly larger size. A smaller solar wind M_A typically results in FTEs with smaller size under 180° and 135° IMF clock angle conditions, while producing FTEs with larger size under 90° IMF clock angle conditions.

By tracking the time history of FTE locations, we have also determined the traveling speeds of identified FTEs. FTEs formed in our simulations typically travel at speeds ranging between 200 - 400 km/s, which is close to the value previously assumed in various MESSENGER data analysis

of FTEs. It is also found that the average FTE traveling speed generally becomes higher in lower solar wind M_A cases and in larger IMF clock angle cases. Such dependencies are consistent with the expectation of how reconnection outflow speed varies depending on the inflow Alfven speed and magnetic shear angle at the magnetopause. The motion of FTEs is also significantly affected by the interplay between the geometry of magnetopause reconnection and large-scale plasma flows near the magnetopause.

The average core fields of FTEs seen in the simulations have a range from 50 - 170 nT for the external conditions used in this study, and the average magnetic flux content associated with FTEs falls in the range of 0.005 MWb to 0.03 MWb. Overall, we find that individual FTEs normally carry more magnetic flux when the IMF clock angle is smaller or when the solar wind M_A is smaller. By comparing the aggregate magnetic flux carried by FTEs with the cross polar cap potential, which provides a measure of the global coupling efficiency, we find that FTEs contribute about 3% - 13% of the open flux created at the dayside magnetopause that eventually participates in the global circulation of magnetic flux. This result is in general agreement with the previous findings obtained through analysis of MESSENGER data that FTEs at the magnetopause play a significant role in driving the Dungey cycle at Mercury.

In summary, we have used a global Hall MHD model to simulate Mercury's magnetopause dynamics focusing on the generation and evolution of FTEs under different external conditions. The main characteristics of our simulated FTEs agree generally well with the observations of FTEs by the MESSENGER spacecraft. In addition to confirming many of the previous observational findings, our simulations provide further insight into the 3D structure and motion of FTEs and how FTE properties are influenced by the solar wind and IMF. Our model results should provide useful context for interpreting in situ observations of Mercury's magnetosphere from spacecraft missions,

such as MESSENGER and Bepi-Colombo, which is currently en route to Mercury with a scheduled arrival time of late 2025 (*Millilo et al*., 2020).

Table 3-1: Solar wind and IMF parameters used for the simulations presented in this chapter

Run #	**M_A**	**IMF clock angle (°)**	$B_y(nT)$	$B_z(nT)$	$U_x(km/s)$	ρ**(amu/cc)**	$T(K)$
1	6	180	0	-23	-500	36	8.7e4
2	6	135	-16	-16	-500	36	8.7e4
3	6	90	-23	0	-500	36	8.7e4
4	2	180	0	-69	-500	36	8.7e4
5	2	135	-49	-49	-500	36	8.7e4
6	2	90	-69	0	-500	36	8.7e4

Table 3-2: Total number of unique FTEs and average occurrence rate for different simulations. *Note that for the 90° IMF clock angle cases we have identified FTEs in two meridional planes (LT= 09 and 15), so the corresponding column gives the number of FTEs in different planes and the total count.

		IMF clock angle					
		180°		**135°**		**90°**	
Solar wind Alfvénic Mach number	**M_A = 6**	Total No.: **52**	Occur. Rate: **1 FTE every 3.4 s**	Total No.: **42**	Occur. Rate: **1 FTE every 4.2 s**	LT=09: 8 LT=15: 15 Total No.: **23**	Occur. Rate: **1 FTE every 8.7s**
	M_A = 2	Total No.: **68**	Occur. Rate: **1 FTE every 2.6 s**	Total No.: **60**	Occur. Rate: **1 FTE every 2.7 s**	LT=09: 33 LT=15: 16 Total No.: **49**	Occur. Rate: **1 FTE every 3.2 s**

Table 3-3: Comparison of simulated FTE properties for different solar wind M_A and IMF clock angles

Upstream Conditions / **FTE Properties**	**$M_A = 6$**			**$M_A = 2$**		
	Clock angle 180° (Run #1)	**Clock angle 135°** (Run #2)	**Clock angle 90°** (Run #3)	**Clock angle 180°** (Run #4)	**Clock angle 135°** (Run #5)	**Clock angle 90°** (Run #6)
Simulation duration	176 s	178 s	200 s	175 s	159 s	158 s
Total number of FTEs	52	42	23	68	60	49
Average recurrence rate (or temporal spacing)	1 FTE every 3.4 s	1 FTE every 4.2 s	1 FTE every 8.7 s	1 FTE every 2.6 s	1 FTE every 2.7 s	1 FTE every 3.2 s
Average size	746 km	772 km	920 km	673 km	587 km	1002 km
Average speed	253 km/s	200 km/s	126 km/s	360 km/s	304 km/s	326 km/s
Average core field	46 nT	100 nT	110 nT	77 nT	170 nT	94 nT
Average flux content	0.005 MWb	0.016 MWb	0.025 MWb	0.010 MWb	0.030 MWb	0.028 MWb
Cross Polar Cap Potential	57 kV	50 kV	28 kV	119 kV	106 kV	69 kV
FTE contribution to open flux circulation	2.7%	7.5%	10.4%	3.1%	10.6%	12.7%

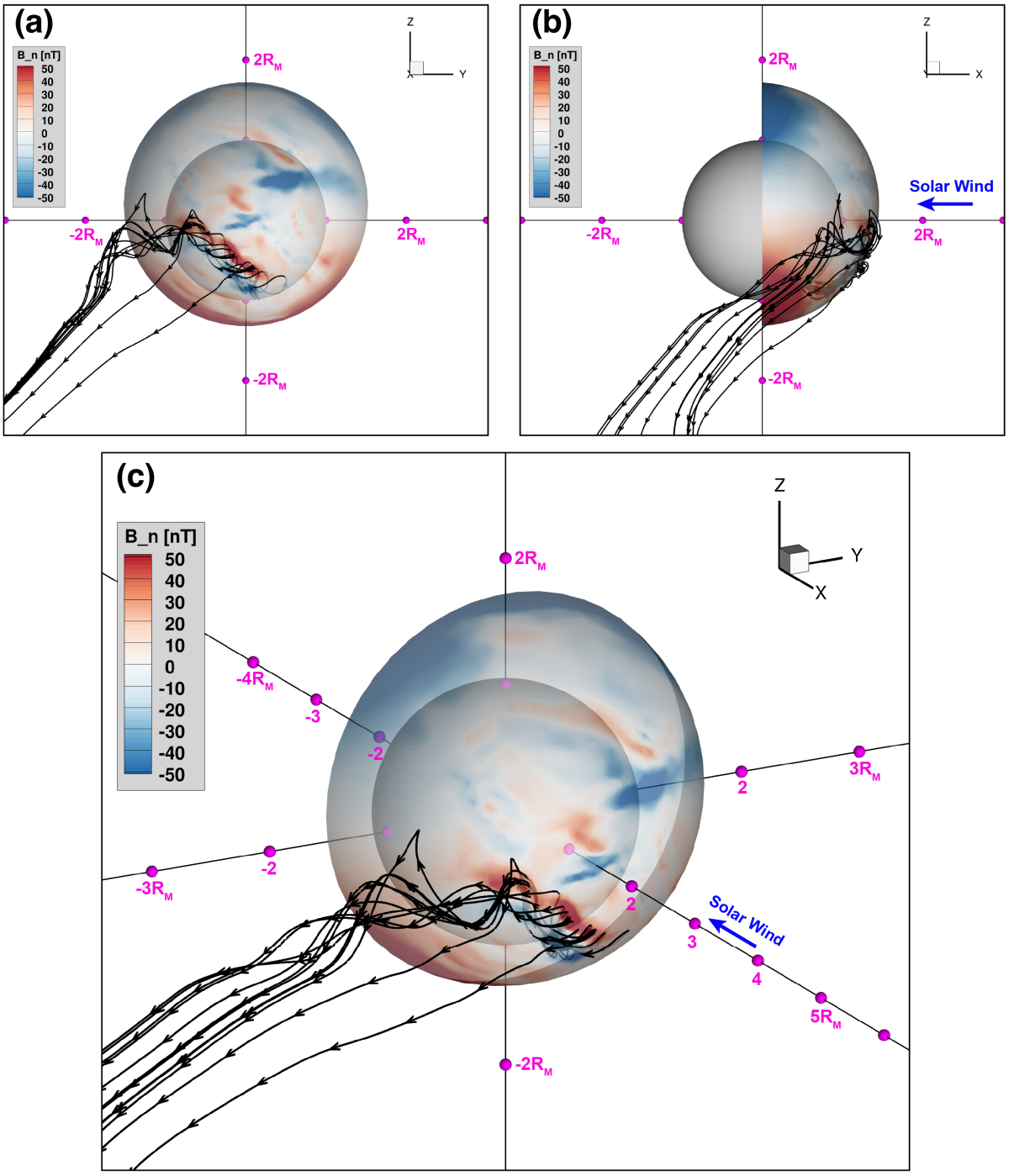

Figure 3-1: An FTE example from Run #2 corresponding to M_A = 6 and IMF clock angle of 135°. The three panels show the FTE structure as viewed from different perspectives: (a) YZ plane as viewed from the solar wind; (b) XZ plane as viewed from the dawn side; (c) 3D view. In all three panels, color contours of B_n (the magnetic field component normal to the magnetopause) are shown on the magnetopause surface extracted from the simulation. Red colors indicate magnetic field pointing outward away from Mercury and blue colors indicate inward-pointing magnetic field. The black lines with arrows are sample field lines with one end connected to Mercury and the other end connected to the solar wind. Mercury is represented by a grey sphere with a radius of 1 R_M in the center. The FTE shown here is clearly characterized by rope-like magnetic topology and bipolar B_n signatures.

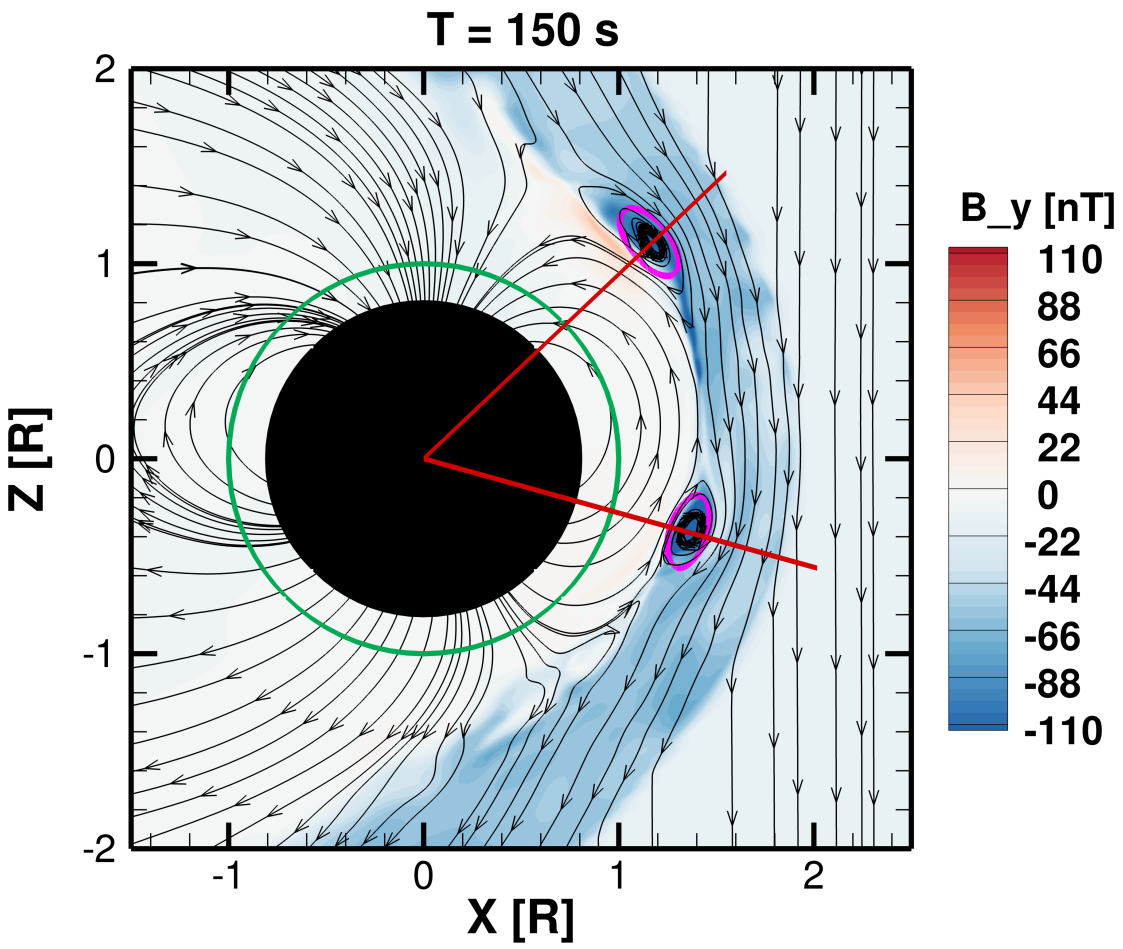

Figure 3-2: Snapshot of B_y contour in X-Z plane with magnetic field lines overplotted as black arrowed lines. The magenta ellipses outline the outer boundaries of two identified FTEs, whose cross-sections are modeled as 2D ellipse in this study to quantify their magnetic flux. Two red straight lines going through the center of the FTE are used to measure FTE's size in the radial direction.

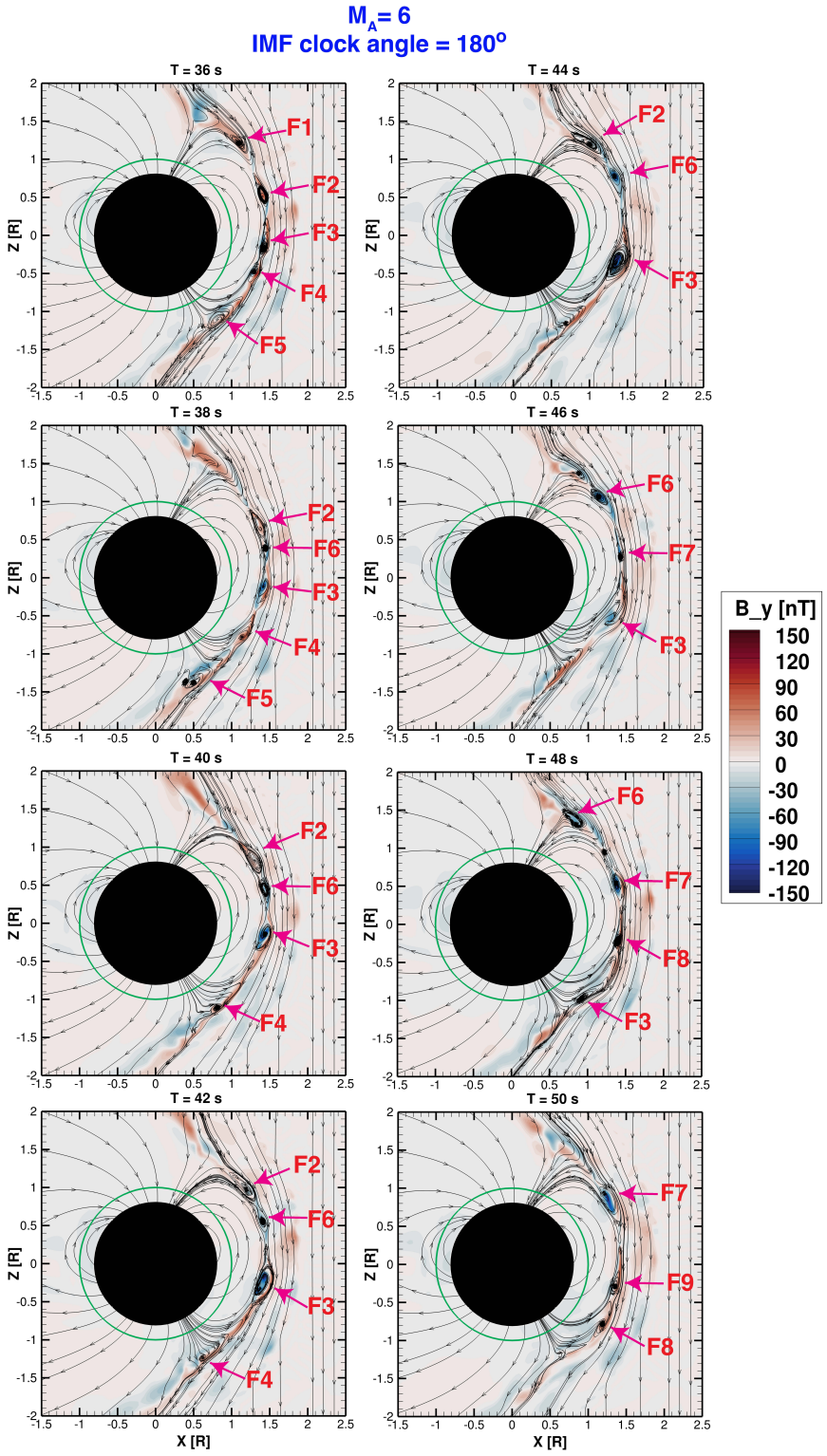

Figure 3-3: Multiple snapshots of B_y contours and sample magnetic field lines in the X-Z plane extracted from two simulations for comparison. The results are extracted from Run #1 (M_A= 6, IMF clock angle= 180°) at a time cadence of 2 seconds. The green circle represents Mercury's surface at r= 1R_M and the black filled disk represents Mercury's core with an assumed radius of 0.8 R_M. Labels and arrows are added to each panel to track individual FTEs.

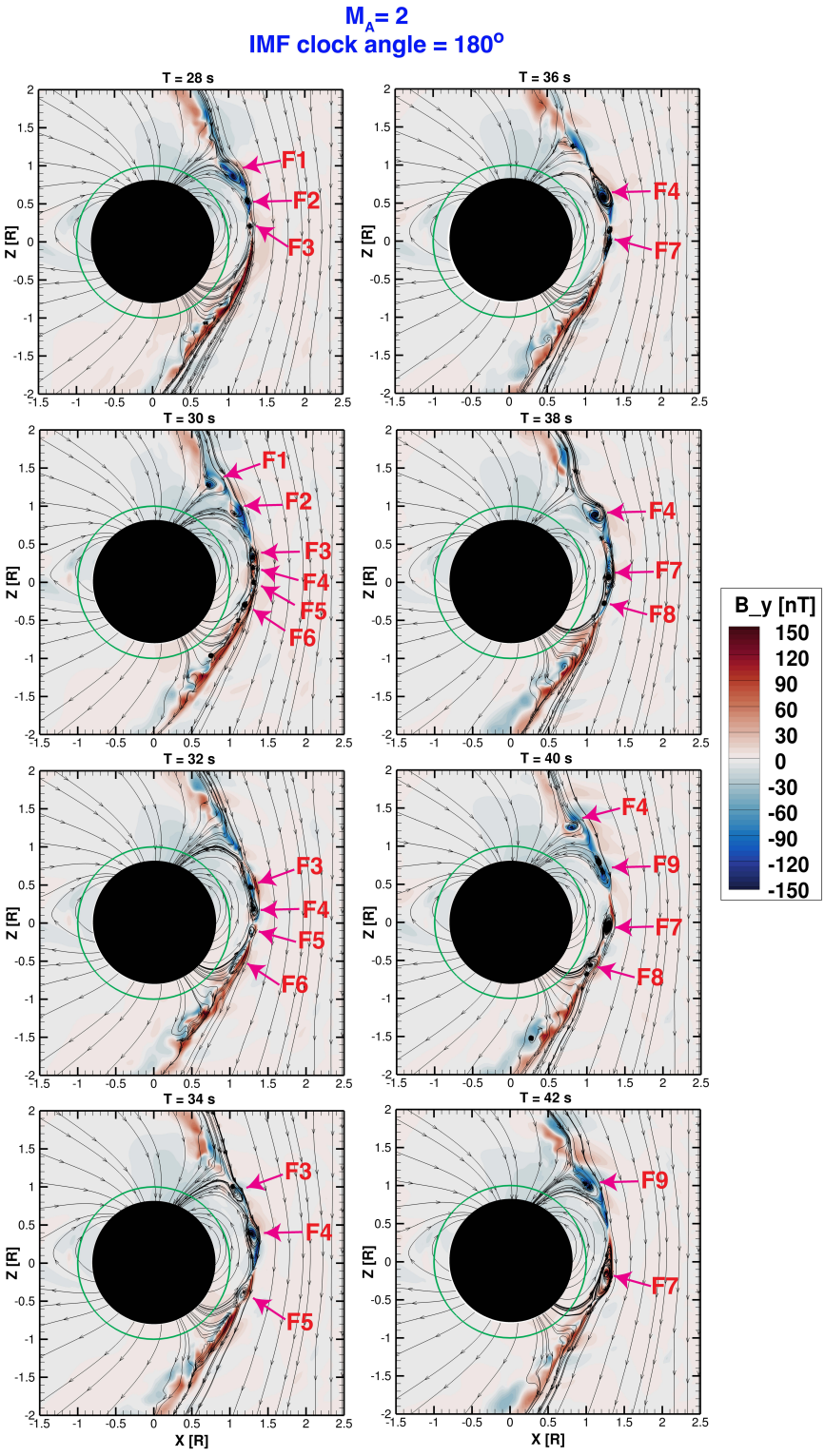

Figure 3-4: Same as Figure 3-3 but for Run #4 (M_A= 2, IMF clock angle = 180°).

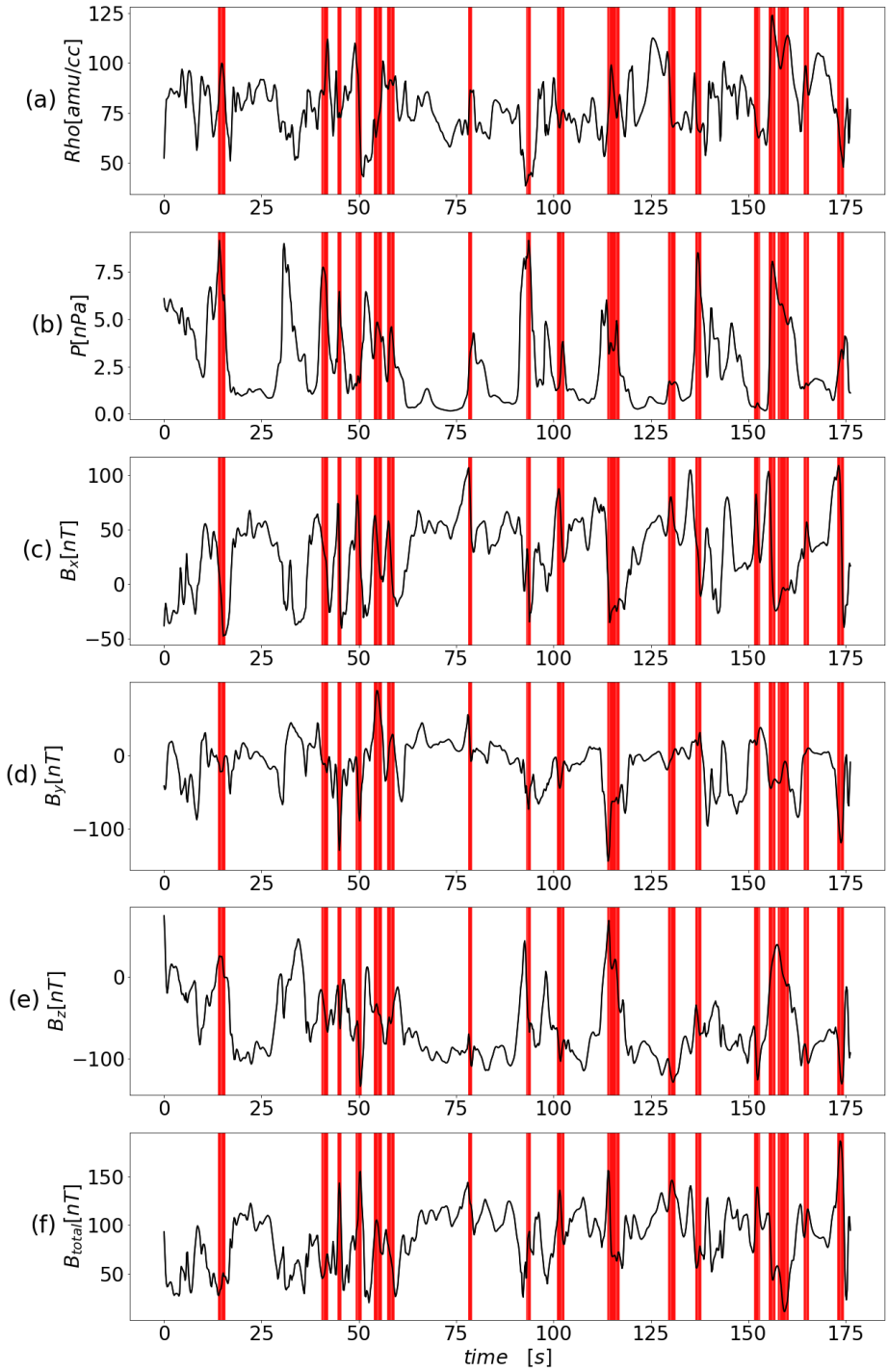

Figure 3-5: Time series of simulated physical parameters (a) plasma density, (b) plasma pressure, (c) – (e) Bx, By, Bz, and (f) magnetic field strength, observed by a virtual satellite located at [X, Y, Z]= [1.26, 0, 0.93] R_M from Run #1 (M_A= 6, IMF clock angle= 180°). The red vertical intervals correspond to identified FTEs based on bipolar $\boldsymbol{B_n}$ signature.

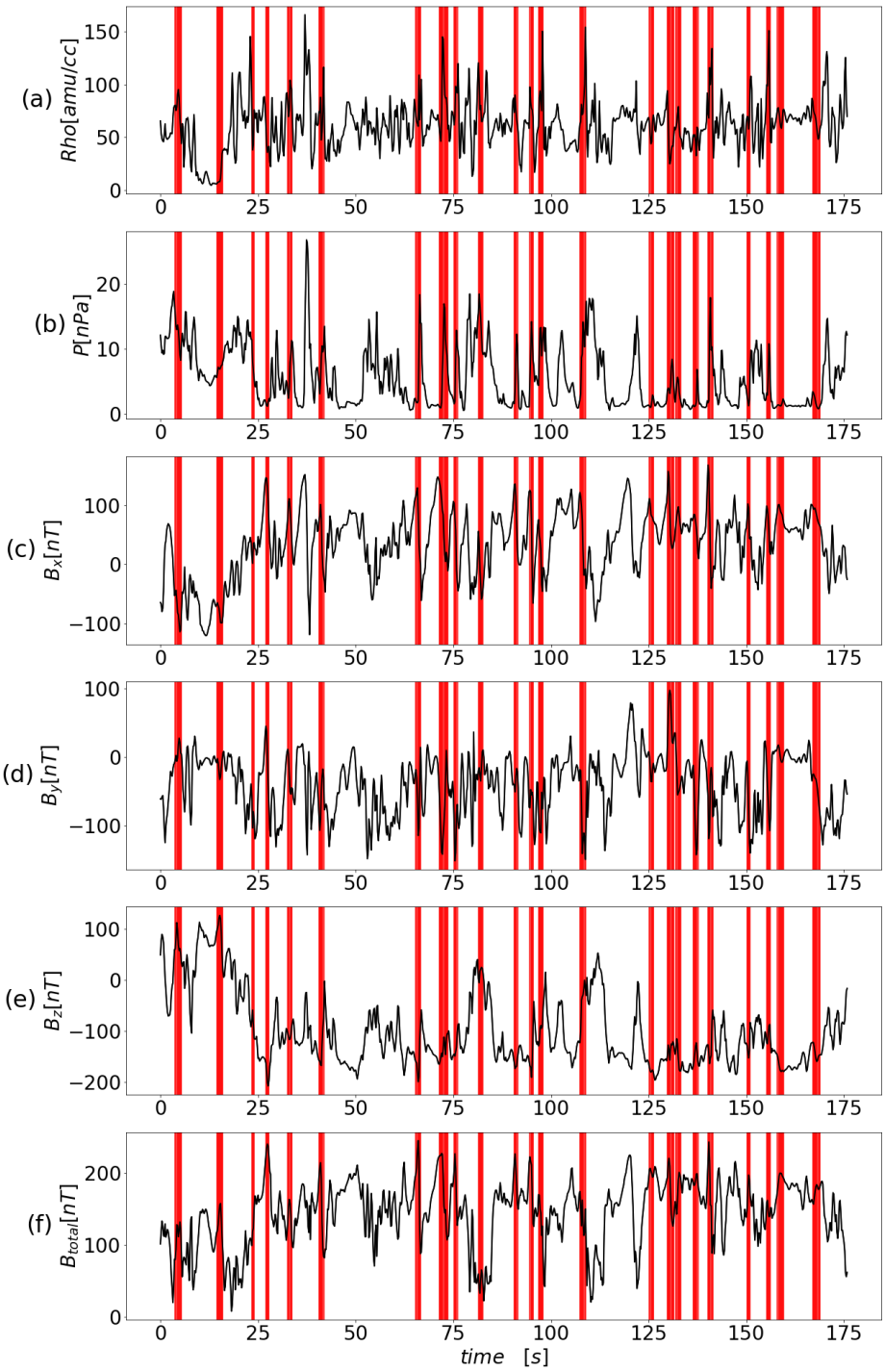

Figure 3-6: Same as Figure 3-5 but for results extracted from Run #4 (M_A= 2, IMF clock angle= 180°) at a virtual satellite located at [X, Y, Z]= [1.16, 0, 0.87] R_M, which is also on the sheath side of the magnetopause boundary.

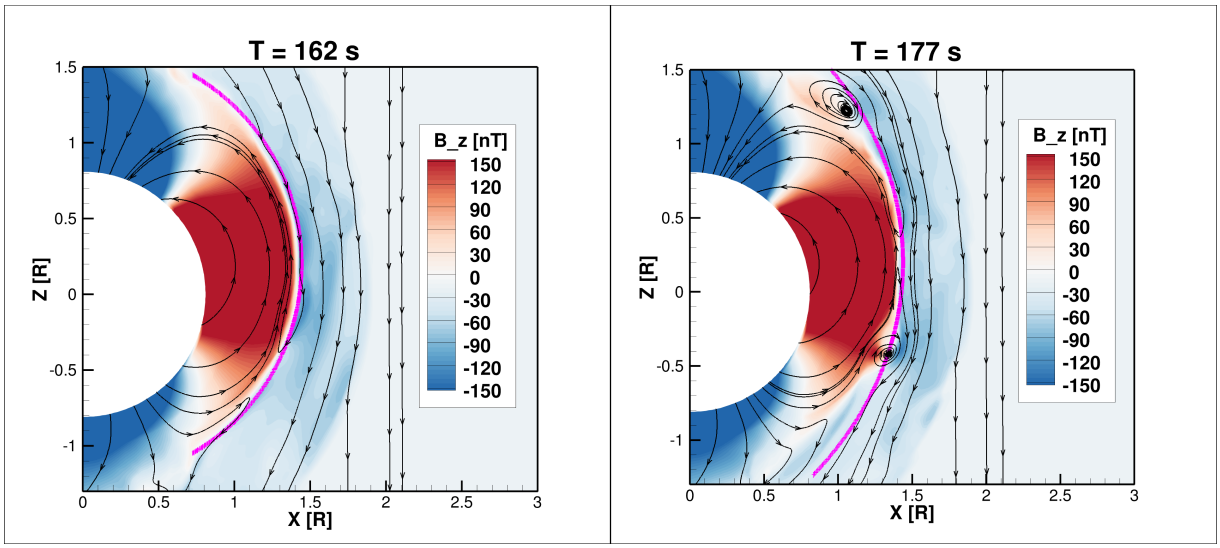

Figure 3-7: Demonstration of fitting the Shue et al. empirical model to the simulated magnetopause boundary. The two panels show results from two timesteps (T= 162 s and 177 s) extracted from Run #2 (M_A= 6, IMF clock angle= 135°) with sampled magnetic field lines in the X-Z plane. The background colors show B_z contours in the XZ plane and the magenta curve shows the fitted magnetopause model.

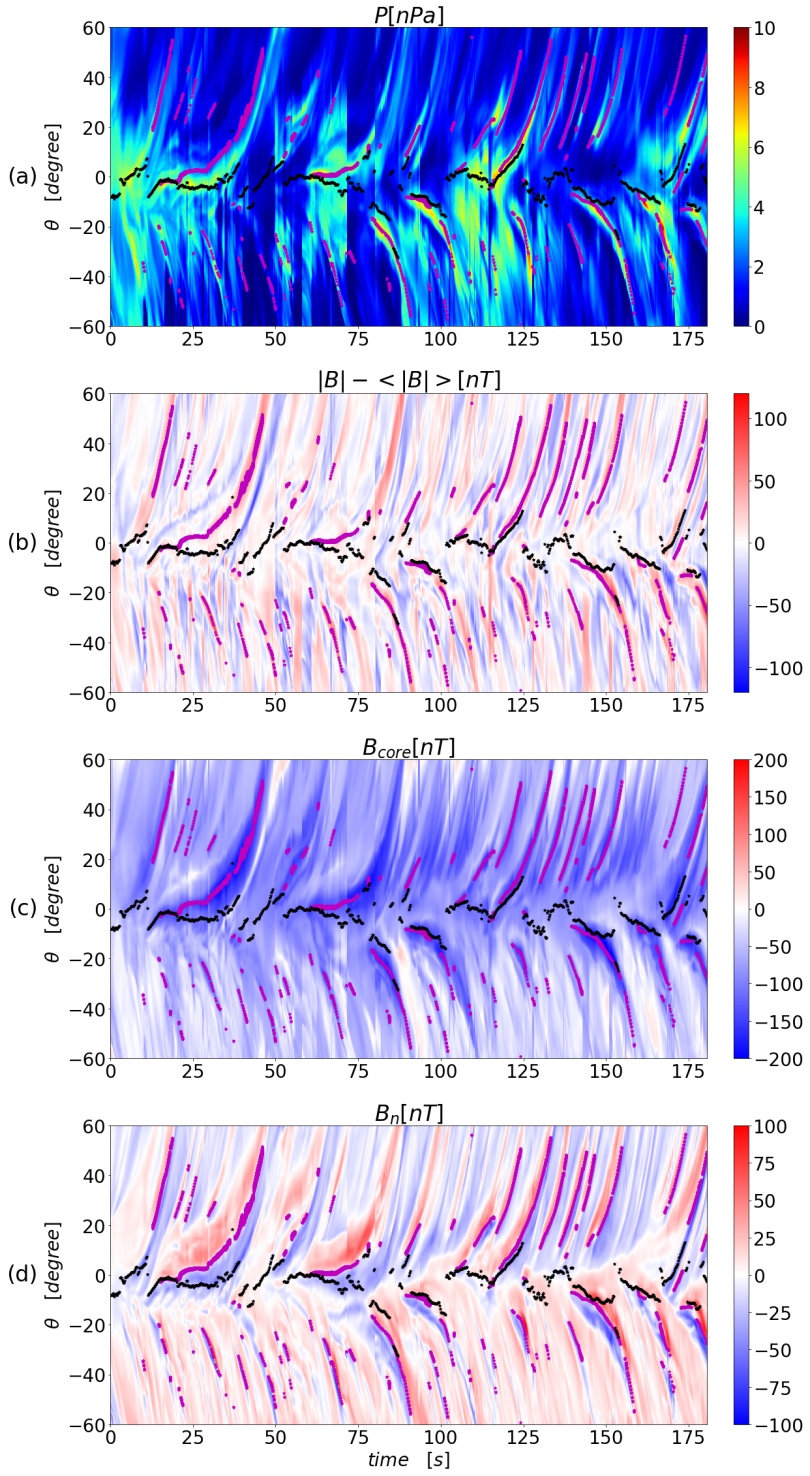

Figure 3-8: Time-latitude map to characterize the temporal variation of physical parameters along the magnetopause in the noon-midnight meridian (LT= 12) for Run #2 (M_A= 6, IMF clock angle= 135°). The extracted physical parameters shown here as the background colors are: (a) Plasma pressure P, (b) Perturbations to the magnetic field strength, (b) FTE core field, B_c and (d) Magnetic field component normal to the magnetopause, B_n. The magenta dots superimposed on each panel represent the centers of those identified FTEs and the black dots mark the flow diverging points near the magnetopause. The X-axis shows the simulation time in seconds and the Y-axis represents the magnetic latitude in degrees.

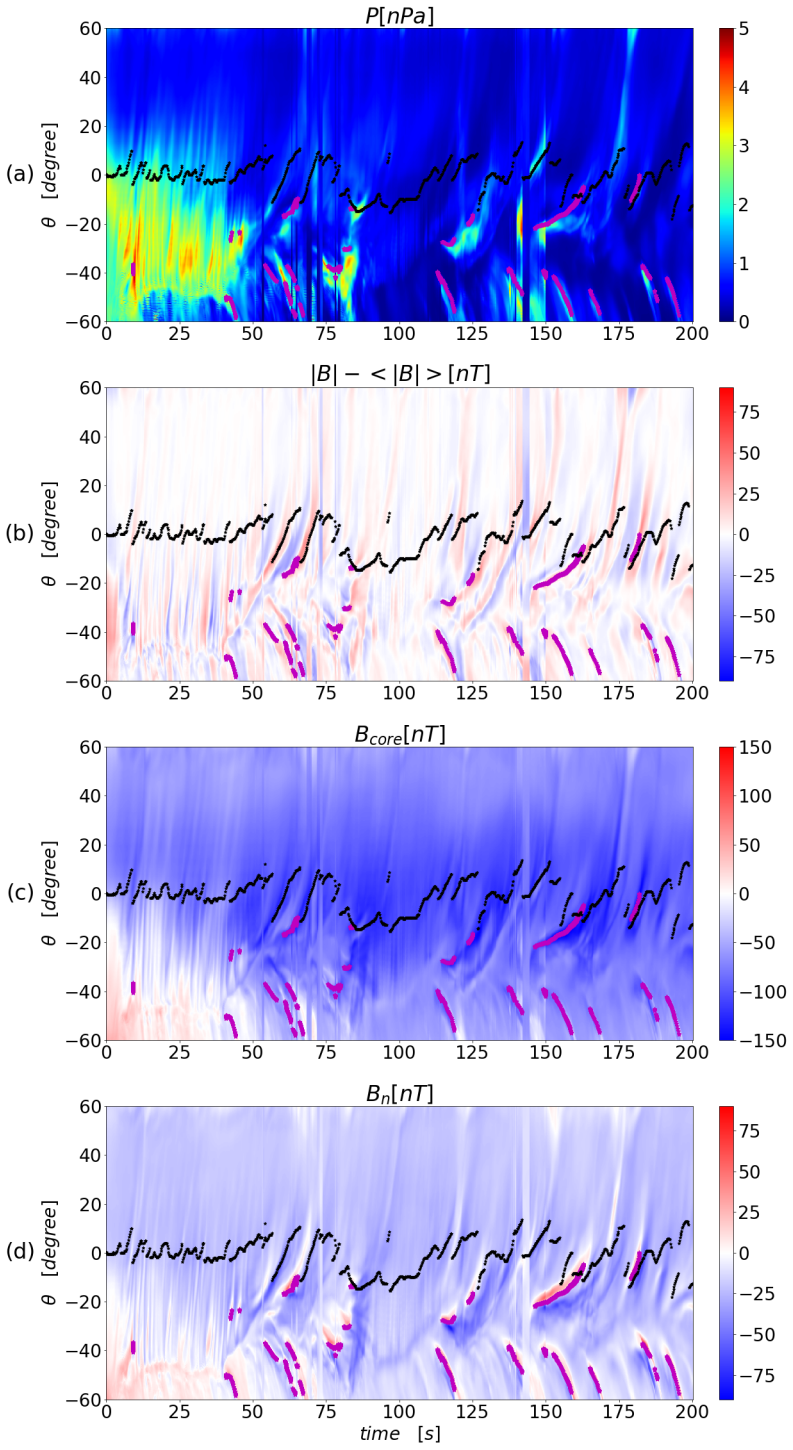

Figure 3-9: Same as Figure 3-8, but for Run #3 (M_A= 6, IMF clock angle= 90°). The results shown here are extracted from the LT= 15 meridian on the dusk side.

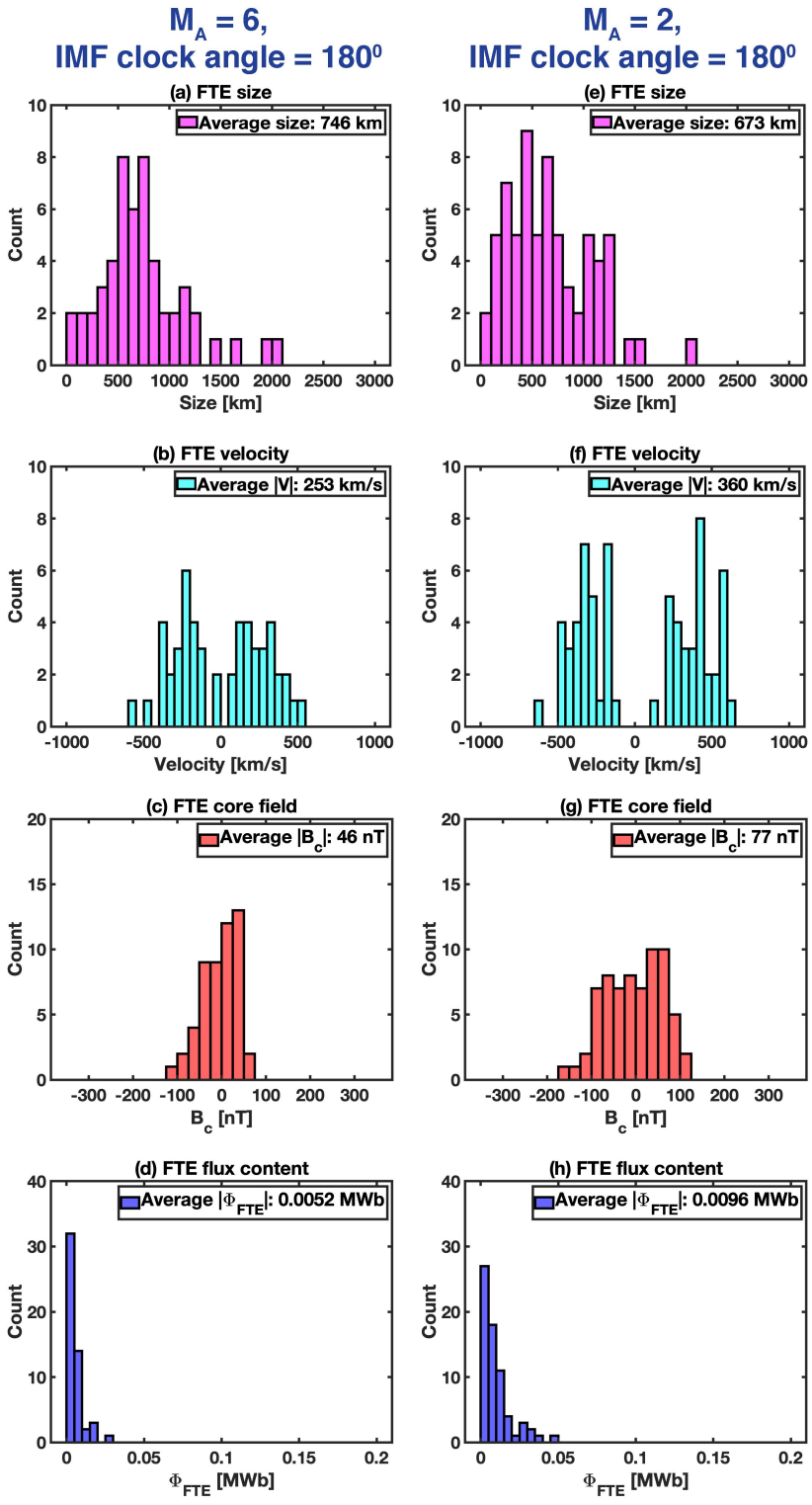

Figure 3-10: Histograms of various FTE properties for 180° IMF clock angle cases. (a) and (e) Average FTE size. (b) and (f) Average FTE velocity in the latitudinal direction. (c) and (g) Core field strength. (d) and (h) Magnetic flux carried by FTE. The left column corresponds to M_A= 6 and the right column is for M_A= 2.

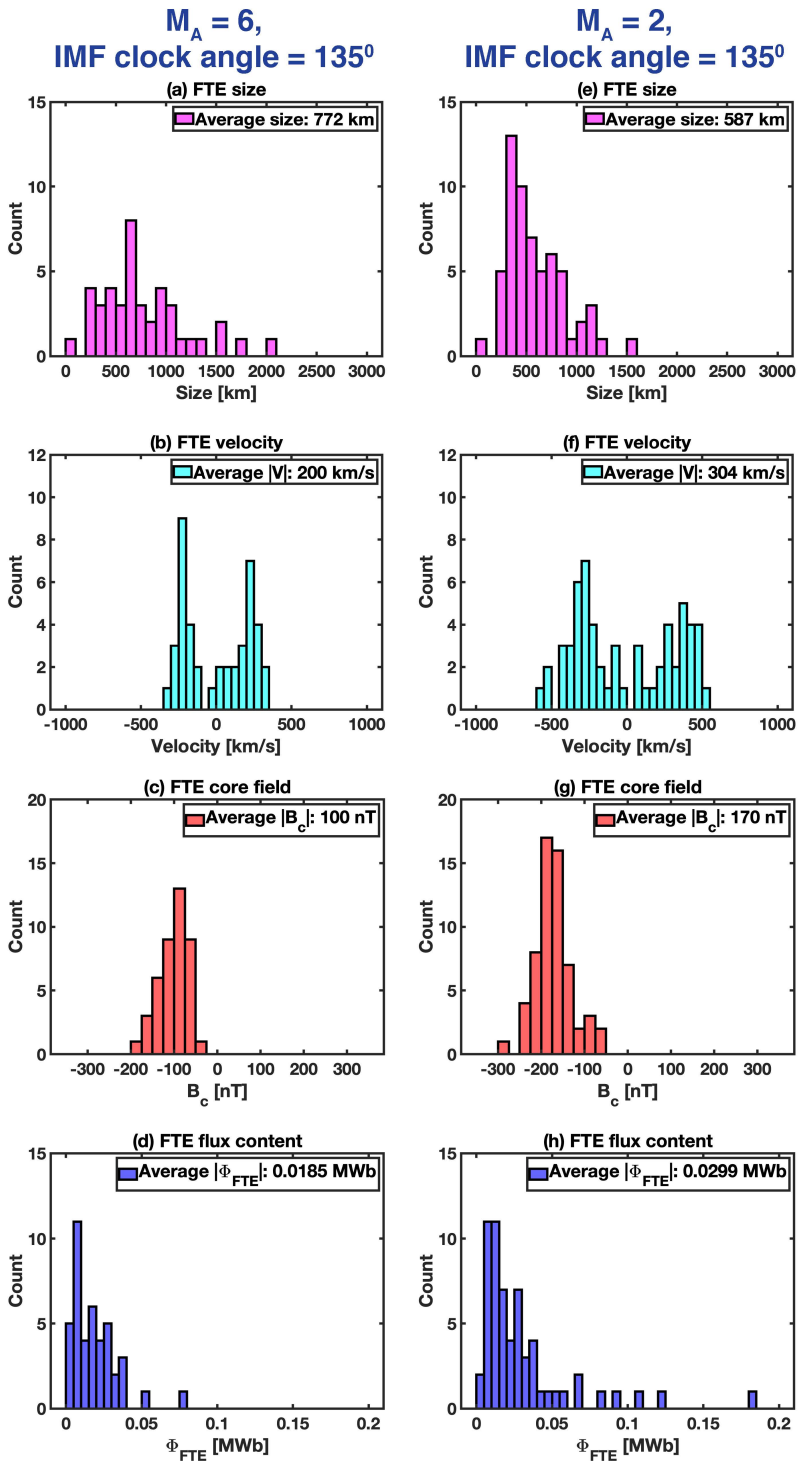

Figure 3-11: Same as Figure 3-10, but for 135° IMF clock angle cases.

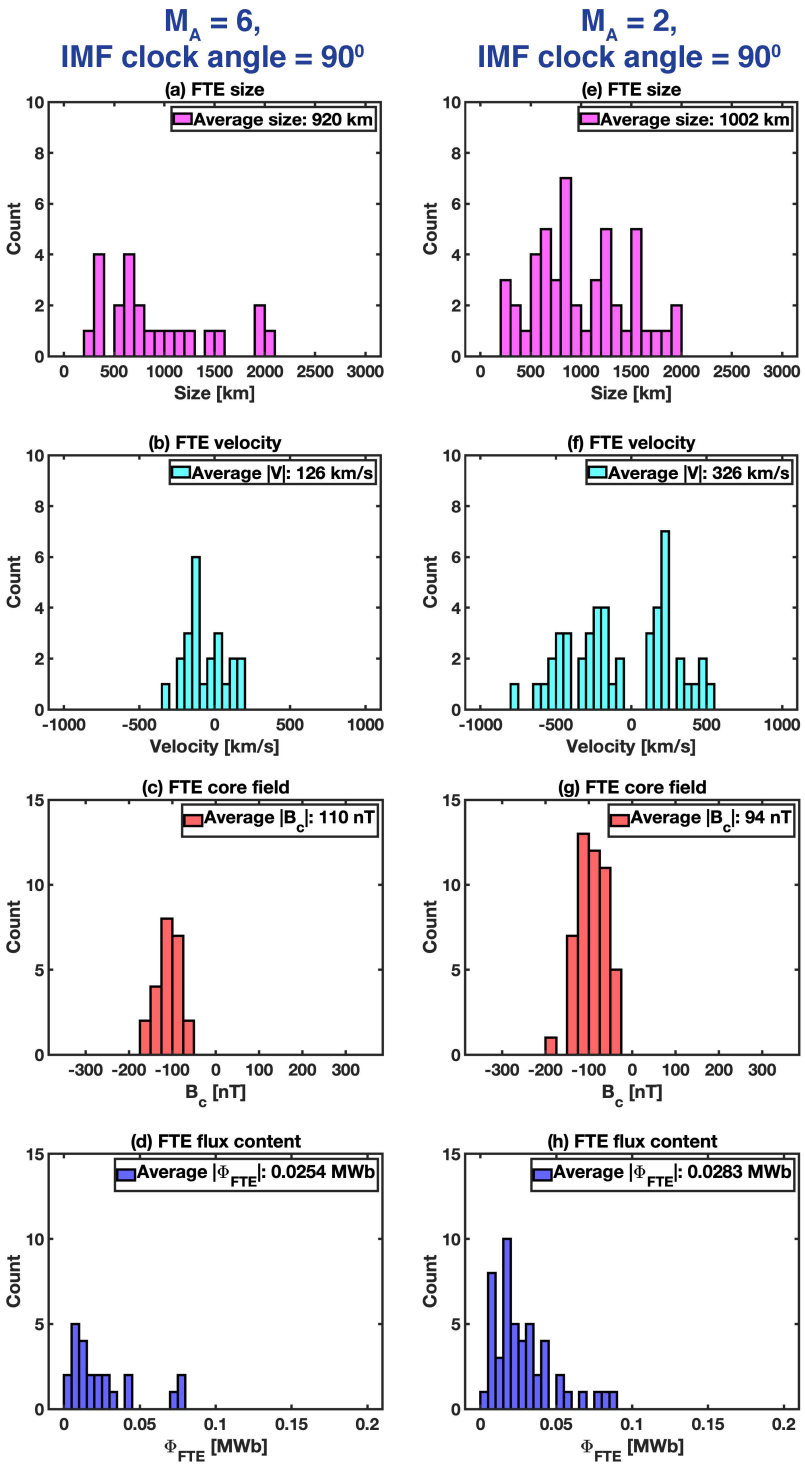

Figure 3-12: Same as Figure 3-10, but for 90° IMF clock angle cases.

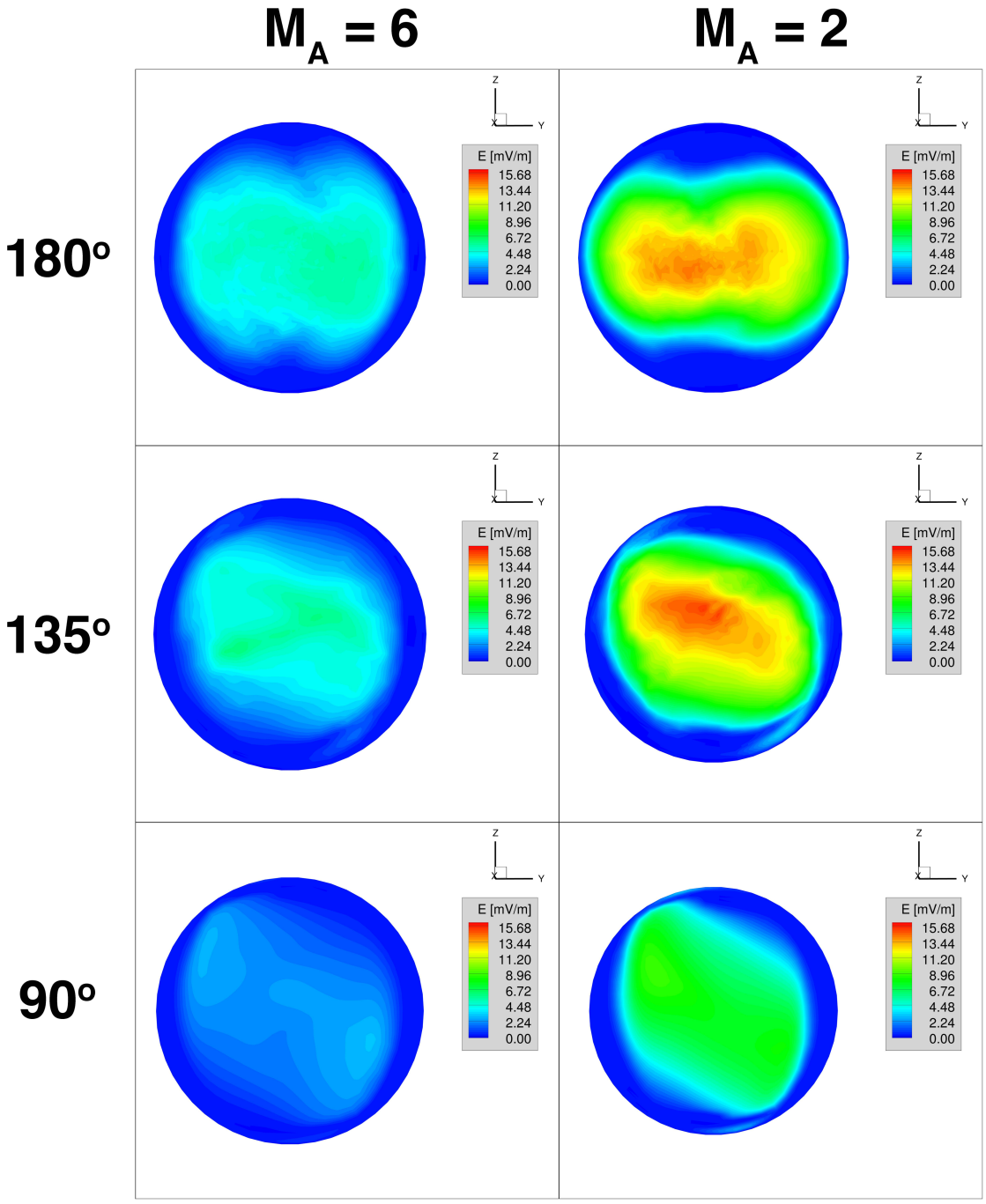

Figure 3-13: Time-averaged reconnection electric field on the magnetopause for the six simulations. The electric field is calculated according to the formula proposed by *Cassak and Shay* (2007) for asymmetric reconnection using the plasma and magnetic field conditions extracted on the magnetospheric and magnetosheath sides of the simulation, and then averaged over all timesteps to show the large-scale structure. The results are shown as contours projected onto the dayside magnetopause surface as viewed from the Sun.

Chapter 4 Kinetic Signatures, Asymmetries, and FTEs Associated with Mercury's Dayside Magnetopause Reconnection from 3D MHD-AEPIC Simulations[2]

4.1 Introduction

The Hall-MHD model used in the previous chapter includes the Hall effect by allowing separate bulk motion of ions and electrons. However, because Hall-MHD treats both plasma ions and electrons as fluids, it could not fully capture the behavior of plasma at kinetic scales, especially in regions where kinetic effects play an important role, such as near reconnection sites.

In order to study plasma phenomena in Mercury's magnetosphere involving kinetic processes, such as magnetic reconnection and formation of FTEs, a numerical model that incorporates kinetic physics is required. To that end, hybrid models, which consider ions as kinetic particles and electrons as a fluid, has been employed to simulate the interaction between solar wind and Mercury's magnetosphere (e.g., *Trávníček et al.*, 2010; *Muller et al*., 2012; *Exner et al*., 2018; *Fatemi et al*., 2018; *Lu et al*., 2022). However, because electrons are still modeled as a fluid in hybrid simulations, they lack electron kinetic physics, which is believed to play an important role in reconnection physics. In contrast, Particle-in-Cell (PIC) codes treat both ions and electrons as interacting kinetic particles, thereby allowing for a more accurate description of kinetic processes, including electron-scale dynamics. Coupled fluid-PIC (*Chen et al*., 2019) and fully-implicit PIC (*Lapenta et al*., 2022; *Lavorenti et al*., 2022) simulations have been conducted previously to study

[2] This chapter has been submitted to *Journal of Geophysical Research* as *Li et al*. (2023b) Kinetic signatures, asymmetries, and FTEs associated with Mercury's dayside magnetopause reconnection from 3D MHD-AEPIC simulations, *Journal of Geophysical Research: Space Physics*, e2023JA032129

the large-scale configuration and global-scale dynamics of Mercury's magnetosphere. But, there have not been dedicated simulation efforts based on a kinetic modeling approach devoted to understanding the occurrence and kinetic signatures of Mercury's magnetopause reconnection, as well as the impact of kinetic physics on the formation and evolution of FTEs.

Inspired by the previous coupled fluid-PIC simulations performed by *Chen et al*. (2019), where a rectangular PIC box was placed near the tail plasma sheet to model reconnection-driven dynamics in Mercury's magnetotail, in this chapter we use the newly developed Magnetohydrodynamics with Adaptively Embedded Particle-in-Cell (MHD-AEPIC) model (*Wang et al*., 2022) to simulate Mercury's magnetosphere under various solar wind and IMF conditions with a focus on the kinetic signatures, asymmetries, and FTEs associated with the reconnection at Mercury's dayside magnetopause. Recent advances in model development and computational capability allow us to place a non-rectangular PIC region with high-resolution grid to cover the entire dayside magnetopause such that we can resolve the kinetic physics on a scale comparable to the electron skin depth and study the reconnection process from a kinetic perspective. Insights into the effects of kinetic physics on FTE characteristics and global magnetospheric dynamics can also be obtained by comparing the results from MHD-AEPIC with our previous Hall-MHD simulations presented in Chapter 3 (*Li et al*., 2023).

The structure of this chapter is as follows: Section 4.2 provides a detailed description of our numerical model, simulation setup, and input parameters. In Section 4.3, we present the kinetic signatures associated with dayside magnetopause reconnection and introduce a novel metric and algorithm developed for the automatic identification of reconnection sites in our MHD-AEPIC simulations. Furthermore, we present the asymmetries in reconnection occurrence and properties of simulated FTEs in Section 4.3 and conduct a detailed discussion of these results in Section 4.4.

Finally, Section 4.5 presents a summary of our work with concluding remarks. The work presented in this chapter is adapted from a manuscript currently under review by the *Journal of Geophysical Research: Space Physics*.

4.2 Methodology

The coupled fluid-kinetic model, MHD-EPIC (MHD with Embedded Particle-in-Cell), has been successfully applied to investigate the interaction between Jupiter's magnetospheric plasma and Ganymede's magnetosphere (*Zhou et al*., 2019; *Zhou et al.*, 2020), Mercury's magnetotail reconnection (*Chen et al*., 2019), and Earth's dayside reconnection-driven dynamics (*Chen et al*., 2017). The Mercury simulations presented in this paper were performed with the newly developed MHD-AEPIC model (*Wang et al*., 2022). The global magnetosphere is simulated by the BATSRUS Hall-MHD model (*Powell et al*., 1999; *Tóth et al.,* 2008), and the entire dayside magnetopause is covered by a semi-implicit, particle-in-cell code (PIC) called Flexible Exascale Kinetic Simulator (FLEKS), which allows for a proper treatment of the kinetic effects of magnetic reconnection. The MHD and FLEKS models are two-way coupled (*Daldorff et al*., 2014) through the Space Weather Modeling Framework (*Tóth et al*., 2012; *Gombosi et al*., 2021) by exchanging information periodically at prescribed timesteps. For all the simulations conducted for this work, we first ran the BATSRUS Hall-MHD model in local time stepping mode to establish a quasi steady-state magnetosphere, and then switch to time-accurate mode and start the coupling between the MHD and PIC codes. The simulation setup for both BATSRUS and FLEKS are described in the following subsections.

4.2.1 Global Hall-MHD Model: BATSRUS

The Mercury MHD model used in this work is based on the work of *Jia et al*. (2015), who adapted BATSRSU to Mercury by modeling the planet as a resistive body consisting of a perfectly conducting core of radius 0.8 R_M (R_M= 2440 km is Mercury's mean radius) surrounded by a highly resistive mantle (between 0.8 R_M and 1 R_M). The resistivity profile used in our MHD-AEPIC simulations is identical to that used in *Jia et al*. (2015, 2019). To account for the induction effect of Mercury's conducting core, a zero magnetic field perturbation boundary condition is applied at the core-mantle boundary (0.8 R_M), whereas boundary conditions for other MHD primitive variables (plasma density, velocity, and pressure) are prescribed at Mercury's surface (1 R_M). Inside the planet, only a reduced Faraday's law (Equation (4-1)) is solved to model the diffusion of magnetic field through Mercury's interior.

$$\frac{\partial \boldsymbol{B}}{\partial t} = -\nabla \times (\eta \boldsymbol{J}), \tag{4-1}$$

where $\boldsymbol{B}$ is the magnetic field vector, $\boldsymbol{J}$ denotes the current density and η is the resistivity prescribed according to *Jia et al.* (2015, 2019).

The BATSRUS Hall MHD model used in this work includes a separate equation for the electron pressure, as well as the corresponding electron pressure gradient term in the generalized Ohm's law used to advance the induction equation for the magnetic field. The set of Hall-MHD equations and the layered inner boundary conditions are described in detail in Chapter 2 and Chapter 3, respectively. A semi-implicit scheme (*Tóth et al*., 2012), which relaxes the stiffness arising from the Hall term and the resistivity term without limiting the timestep, is used to reduce the computational costs.

The simulations are performed in MSO (Mercury Solar Orbital) coordinates. The entire simulation domain is a rectangular box with dimensions of $-64R_M < X < 8R_M$, $-128R_M < Y < 128R_M$, $-128R_M < Z < 128R_M$ cut out of a spherical grid. A scaling/Hall factor (*Tóth et al*., 2012)

of 4, which was shown to work reasonably well in our previous global Hall MHD simulations (*Li et al*., 2023), is used to scale up the kinetic length by a factor of 4 by artificially increasing the ion mass-to-charge ratio. A stretched spherical grid with up to three levels of adaptive mesh refinement near the dayside magnetopause is used for all simulations, resulting in a grid resolution of 20 km or 0.008 R_M, which is equal to 1/6 of the ion inertial length after scaling. Figure 4-1a shows the structure of the numerical grid in the XZ plane with the background colors representing the plasma density contours.

The outer boundary conditions at six faces of the simulation box are set as follows. At the upstream face, an inflow boundary condition is imposed to allow the solar wind with prescribed parameter to flow into the simulation domain. For the other five faces, we have used a zero-gradient floating boundary condition such that the super-magnetosonic plasma flow can leave the simulation domain freely.

In total, we have conducted six MHD-AEPIC simulations with different solar wind and IMF conditions (see Table 4-1). The upstream conditions used in this work are the same as those used in Chapter 3, which allows us to make direct comparisons of simulation results between the coupled fluid-kinetic model and the Hall MHD model.

4.2.2 PIC Model: FLEKS

FLEKS is a semi-implicit, particle-in-cell (PIC) code developed by *Chen et al*. (2023). It uses Gauss's law satisfying energy-conserving semi-implicit method (GL-ECSIM) (*Chen and Tóth*, 2019) to resolve the kinetic physics in the PIC domain. FLEKS employs an adaptive Cartesian grid which allows changing the simulation domain dynamically by turning on and off selected computational cells. In this work, we have used an active PIC region that is fixed in time to cover the entire dayside magnetopause. The PIC box has a uniform mesh covering the region

between $0 < X < 2\ R_M$, $-2.25\ R_M < Y < 2.25\ R_M$, and $-2\ R_M < Z < 2\ R_M$ with a grid resolution of $1/96\ R_M$ in all directions. As shown in Figure 4-1b and Figure 4-1c, the inner and outer boundaries of active PIC region are prescribed by two elliptic paraboloids. The nose of the PIC inner boundary is placed in the $Z= 0\ R_M$ plane for the $M_A= 6$ simulations (Runs #1, #2, #3) and in the $Z= 0.05\ R_M$ plane for the $M_A= 2$ simulations (Runs #4, #5, #6). We have shifted the inner boundary of the PIC domain for the $M_A = 2$ simulations slightly northward to avoid statistical noise caused by small electron pressure values near Mercury's surface. The nose of the PIC outer boundary is placed in the $Z = 0\ R_M$ plane for all simulations. 64 macroparticles per cell per particle species are used to initialize the active PIC region. To reduce the computational cost and make the simulations affordable, we have assumed the proton-to-electron mass ratio (m_p/m_e) to be 100 and artificially reduced the speed of light (c) by an order of magnitude to 30,000 km/s.

The PIC grid resolution of $1/96\ R_M$ is about 1/5 of the ion inertial length or twice the electron skin depth after applying the scaling factor of 4 (see Section 4.2.1) and the artificially increased proton-electron mass ratio of 100. Although such choice of cell size cannot fully resolve the electron-scale physics, it was proven to work reasonably well in producing the correct reconnection rate, reconnection outflows, and the Hall magnetic field (*Chen and Tóth*, 2019) as well as capturing the large-scale dynamics accurately (*Chen et al*., 2019). Our test results also suggest that a grid resolution of $1/96\ R_M$ achieves a desired balance between computational cost and the need for resolving kinetic scales.

4.2.3 Coupling Between BATSRUS and FLEKS

BATSRUS and FLEKS are coupled through the Space Weather Modeling Framework (SWMF) (*Tóth et al*., 2012; *Gombosi et al*., 2021). Both models run simultaneously on the same processors with different time steps and they are set to exchange information every 0.01 s for all

of the six MHD-AEPIC simulations we have performed. At T= 0 s, FLEKS assumes a Maxwellian distribution in initializing the macro particles according to the plasma bulk properties (e.g., plasma density, bulk flow velocity, and temperature) output from the Hall MHD that has been run in localtime stepping model to reach a quasi-steady state magnetosphere. A coupler is employed to handle the interpolation and communication of variables between the two models. At the coupling timestep, FLEKS overwrite the Hall-MHD solution with the PIC results in the region covered by the PIC code, and takes the latest information (e.g., plasma bulk properties and the magnetic field) from the BATSRUS Hall-MHD code to set the boundary conditions at the PIC outer boundary. Then, the two models advance individually with their own timesteps until reaching the next coupling time. For the simulations presented here, the MHD-AEPIC model was run for 200 s in physical time, which is comparable to the typical timescale of Mercury's Dungey cycle, resulting in a total of 20,000 couplings between BATSRUS and FLEKS.

4.3 Simulation Analysis and Results

In this section, we present the results of our simulations for different upstream conditions listed in Table 4-1, with a focus on the kinetic signatures and asymmetries associated with the dayside magnetopause reconnection and the properties of FTEs. Section 4.3.1 discusses the reconnection-driven kinetic signatures of ion and electron distributions modeled by PIC. Section 4.3.2 describes the metric and algorithm we have developed to automatically identify the reconnection sites in our simulations. Section 4.3.3 presents dawn-dusk asymmetries in the distribution of identified reconnection sites and the associated reconnection electric field as predicted by our MHD-AEPIC model. Lastly, in Section 4.3.4, we provide a statistical survey of

key properties of FTEs simulated by PIC, which will be compared to the results from our previous work based on Hall-MHD simulations.

4.3.1 Kinetic Signatures Associated with Mercury's Magnetopause Reconnection as Simulated by PIC

Since the PIC model, FLEKS, uses a grid resolution comparable to the electron skin depth, we can directly investigate the kinetic signatures of ions and electrons associated with dayside magnetopause reconnection by studying their phase space distributions. To facilitate interpretation of the simulation results, we present the velocity distributions of ions and electrons in a field-aligned coordinate system constructed based on the ambient magnetic field (**B**) and plasma bulk flow (**U**) directions. Specifically, $V_{//}$ denotes the component of the particle velocity parallel to the local magnetic field, $V_{\mathbf{B}\times\mathbf{U}}$ represents the component parallel to $\mathbf{B} \times \mathbf{U}$, and V_{perp} completes the right-handed system.

Figure 4-2 shows selected ion and electron phase space distribution functions on the magnetosheath side of a reconnection site from Run #4 (M_A = 2, IMF clock angle = 180°). Both the ion and electron distributions were extracted from a sphere centered at X = 1.2 R_M, Y = 0 R_M, Z = 0.8 R_M with a radius of 0.05 R_M. As shown in Figure 4-2d, the ion phase space distribution exhibits a clear crescent-like shape in the plane perpendicular to the local magnetic field. The electron distribution in the same plane, depicted in Figure 4-2g, also exhibits a crescent-shaped pattern, albeit with less prominent signature compared to the ion distribution. We have also checked the ion and electron distributions on the magnetospheric side of the same reconnection site but found no crescent-like distributions for both species. The result that crescent-shaped distributions are found on the magnetosheath side of the reconnection site in our simulations contrasts with the observations from the Magnetospheric Multiscale (MMS) mission at the Earth's

magnetopause (*Burch et al*., 2016) and previous MHD-EPIC simulations of Ganymede's magnetopause reconnection (*Zhou et al*., 2019), where crescent-shaped distributions were found to form predominantly on the magnetospheric side. Such a difference may be attributed to the higher temperatures of ions and electrons inside Mercury's magnetosphere in our simulation, in comparison to those in the magnetosheath. Consequently, more energetic magnetospheric particles are able to penetrate the magnetopause and enter the magnetosheath via their meandering motion through the reconnection diffusion region, resulting in the crescent distribution observed in our MHD-AEPIC simulation. The relatively high plasma temperature within Mercury's dayside magnetosphere is likely due to the presence of return plasma flows resulting from magnetotail reconnection as part of the Dungey cycle. At Mercury, the absence of a plasmasphere, which typically acts as a source of cold plasma in the terrestrial magnetosphere, is another contributing factor that could lead to the relatively high temperature seen in our simulation. At Earth or Ganymede, the temperatures are generally higher inside the magnetosheath compared to those in the magnetosphere which leads to crescent-shaped distributions on the magnetospheric side. The penetration of energetic electrons from the magnetosphere into the magnetosheath via meandering motion has also been invoked to successfully explain the rare observation of crescent-shaped distribution on the magnetosheath side at Earth (*Norgren et al*., 2016).

In addition to the crescent-shaped distribution, the electron phase space distributions exhibit preferential heating along the magnetic field direction, which is approximately aligned with the reconnection outflow direction at the sampling location shown here. Such heating results in notable temperature anisotropies, which are evident from the elongated shapes in the distributions shown in panels (e) and (f) of Figure 4-2. In contrast, such temperature anisotropy is not observed in the ion distributions, possibly due to their larger mass compared to electrons. Within the

sampling region, the cross product of the magnetic field and the plasma bulk velocity directions ($\mathbf{B} \times \mathbf{U}$) is roughly along +Y direction pointing to the dusk side. As shown in panels (b) and (e) of Figure 4-2, the ions and electrons exhibit drifts toward the duskside and dawnside, respectively, which are consistent with the direction of the out-of-plane magnetopause currents (in -Y direction in MSO coordinates).

Figure 4-3 shows the phase space distributions for ions and electrons sampled in the mid-latitude southern cusp region from the same run as shown in Figure 4-2 (Run #4), but at a different time (T= 65 s). The sampling region is a sphere with radius of 0.05 R_M centered at X= 0.85 R_M, Y= 0 R_M, Z= -0.8 R_M (Figure 4-3a). As shown in panels (b) and (c) of Figure 4-3, the ion phase space distributions exhibit a clear signature of counter-streaming particle populations, characterized by the presence of two groups of particles traveling along the parallel (radially outward) and anti-parallel (radially inward) directions relative to the local magnetic field. In contrast, the electrons show a Maxwellian-like distribution in all three planes, and do not display a similar counter-streaming signature. The direction of the plasma bulk velocity in the vicinity of Mercury's surface within the southern cusp region around T= 65 s is pointing radially inward, suggesting that Mercury's surface is not a significant source of plasma in the simulation. Therefore, the outgoing ions seen in panes (b) and (c) correspond to particles that are reflected at mirror points above the planetary surface within the cusp region. Both the precipitating and mirrored particles originate from the magnetopause, where reconnection accelerates particles to speeds of hundreds of km/s travelling along the field line into the cusp region. A fraction of those precipitating particles (with pitch angles outside of the loss cone) are reflected back towards high altitudes due to the mirror force, forming the outcoming ion population seen in the phase-space distribution. The occurrence of counter-streaming ions suggests that reconnection processes taking place on the

dayside magnetopause of Mercury can potentially lead to plasma instabilities and wave generation in the cusp region, a prediction that may be verified by in-situ observations from future missions, such as the Bepi-Colombo mission.

Figure 4-4 presents the ion and electron distribution functions measured by two virtual satellites (S1 and S2) at T= 119 s from Run #5 (M_A= 2, IMF clock angle= 135°). Both satellites sample the particles within a sphere of radius 0.05 R_M. Satellite S1 is located at X=1.15 R_M, Y= 0 R_M, Z= 0.77 R_M, which is near the center of an FTE. Within this FTE, both the ion and electron distributions show significant deviations from Maxwellian distribution, and they display notable temperature anisotropies, which are associated with particle heating resulting from magnetic reconnection. Satellite S2 is situated at X= 0.75 R_M, Y= 0 R_M, Z= -1.0 R_M, which is near the southern cusp region. In the plane perpendicular to the magnetic field, both ion and electron distributions are observed to exhibit crescent-like shape as shown in the bottom plots of Figure 4-4d and Figure 4-4e. Close inspection of the magnetic field topology around this time suggests that the virtual satellite S2 is located on the magnetosheath side of a high-latitude X-line. The presence of high-latitude reconnection sites has also been reported at Earth by *Burkholder et al*. (2020) based MMS observations. However, it is worth noting that in *Burkholder et al*. (2020), the crescent-shaped distributions were found on the magnetospheric side of the reconnection sites, which, as we discussed earlier for Figure 4-2, is likely due to the higher ion and electron temperatures in Earth's magnetosheath. Furthermore, as shown in Figure 4-4d and Figure 4-4e, crescent-shaped distributions are also present for both ions and electrons in the other two planes that involve the parallel direction (along $\boldsymbol{B}$), indicating the transition from a perpendicular crescent to a field-aligned flow. This transition serves as strong evidence for the opening of magnetic field lines, as previously suggested by *Burch et al*. (2016) based on MMS observations.

4.3.2 Method for Identifying Reconnection X-lines

While the examples presented in the previous sections are extracted from 2D planes to illustrate kinetic signatures associated with reconnection, magnetopause reconnection occurs over a wide range of locations in the 3D space around the magnetopause. To obtain a global picture of Mercury's magnetopause reconnection, we have developed a novel metric and algorithm to facilitate automated identification of reconnection X-lines in the MHD-AEPIC simulation. Previous studies have employed various metrics to identify reconnection sites and electron diffusion regions (EDRs). Some examples of those metrics are: (1) $\boldsymbol{E} + \boldsymbol{V} \times \boldsymbol{B}$, which quantifies the degree of violation of the frozen-in condition, (2) Nongyrotropy measures that assess particle distribution function's deviation from circular symmetry around the magnetic field direction, and (3) Local energy dissipation rate. We have conducted extensive tests on our simulations using multiple metrics and evaluated their correlation with reconnection X-lines identified based on magnetic topology. Among these metrics, we have found four quantities that demonstrate robust capabilities in helping to locate the reconnection sites in Mercury's magnetopause environment. They are: (1) Lorentz reconnection indicator: $\boldsymbol{L} = \boldsymbol{log_{10}}\left(\boldsymbol{c}\frac{|\boldsymbol{E}\times\boldsymbol{B}|}{\boldsymbol{E^2}}\right)$ (*Lapenta,* 2021), (2) Electron dissipation measure: $\boldsymbol{D_e} = \boldsymbol{J'}\cdot\boldsymbol{E'} = \boldsymbol{J}\cdot(\boldsymbol{E}+\boldsymbol{V_e}\times\boldsymbol{B}) - (\boldsymbol{n_i}-\boldsymbol{n_e})\boldsymbol{V_e}\cdot\boldsymbol{E}$ (*Zenitani et al*., 2011), (3) Nongyrotropy measure: $\boldsymbol{A\varnothing}$ (*Scudder and Daughton.* 2008), and (4) Another nongyrotropy measure: $\boldsymbol{Q}$ (*Swisdak,* 2016). The frame-independent definitions of $\boldsymbol{A\varnothing}$ and $\boldsymbol{Q}$ are given in Appendix: Nongyrotropy Measures. The Lorentz reconnection indicator $\boldsymbol{L}$ has been found to decrease significantly near the reconnection site, where the in-plane component of the magnetic field is much reduced (*Lapenta,* 2021). Both $\boldsymbol{A\varnothing}$ and $\sqrt{\boldsymbol{Q}}$ represent the nongyrotropy of the electron pressure tensor in the plane perpendicular to the magnetic field, and they were previously

observed to peak near the electron diffusion region in Ganymede's MHD-EPIC simulations (*Zhou et al*., 2020).

All the parameters involved in calculating the various quantities described above can be obtained directly from the output of the PIC code in our simulation. As an example, Figure 4-5 shows a snapshot of the various quantities in the noon-midnight meridional cut taken from Run #1 (M_A= 6, IMF clock angle= 180°). Note that the background colors are only plotted within the active PIC region. Panels (a) – (c) in Figure 4-5 show the ion density, out-of-plane magnetic field component or equivalently the core field (B_y), and ion scalar pressure (P), respectively. Notably, at this particular timestamp, three FTE-type flux ropes, separated by multiple reconnection X-lines, are present on the magnetopause. Each of these flux ropes exhibits notable enhancements in ion density, B_y and thermal pressure. The subsequent panels, (d)-(g) in Figure 4-5, show the four reconnection metrics $\boldsymbol{L}$, $\boldsymbol{D_e}$, $\boldsymbol{A\varnothing}$, and $\sqrt{\boldsymbol{Q}}$, respectively. We note that panel (d) employs a reversed rainbow colormap, with the minimum and maximum values represented by red and blue colors, respectively. The first reconnection metric, $\boldsymbol{L}$, exhibits a notable decrease near the electron diffusion region and within the cross-section area of the FTE located in the southern hemisphere. The second reconnection metric, $\boldsymbol{D_e}$, peaks near the reconnection X-lines but also shows elevated values inside all three FTEs. The third reconnection metric, $\boldsymbol{A\varnothing}$, demonstrates the best performance at this selected timestamp, with its value increasing significantly at three reconnection sites (Z ~ 0.7R_M, -0.1R_M, -0.7R_M) on the magnetopause surface compared to neighboring regions. Lastly, the final reconnection metric, $\sqrt{\boldsymbol{Q}}$, behaves similarly to $\boldsymbol{A\varnothing}$ in that it peaks around the three X-lines. However, it also shows enhanced values at the outer edge of the FTE near the northern cusp.

We have examined the aforementioned reconnection metrics for all the six simulations (Runs #1-6) and found that the effectiveness of individual reconnection metrics in identifying reconnection X-lines varies over different timesteps. Such variability, which was previously reported in *Zhou et al*. (2020), can be attributed to the complex nature of the kinetic reconnection processes. For example, *Shay et al*. (2016) also found that the violation of the frozen-in condition and nongyrotropic distributions themselves do not uniquely define the electron diffusion region at the X-line and suggested that complementary approach is required for more precise identification. To address the issue pertaining to varying performance of reconnection metrics ($\boldsymbol{L}$, $\boldsymbol{D_e}$, $\boldsymbol{A\varnothing}$, and $\sqrt{\boldsymbol{Q}}$) over different timesteps, we have designed a synthesized reconnection score $\boldsymbol{S}$ in this work to consistently identify the X-lines in our MHD-AEPIC simulation. The synthesized reconnection score $\boldsymbol{S}$ is defined as follows and evaluated at each timestep.

$$\boldsymbol{S} = 10^{\frac{1}{4}*\frac{3-\boldsymbol{L}}{3-min(\boldsymbol{L})}} + 10^{\frac{1}{4}*\frac{\boldsymbol{D_e}}{max(\boldsymbol{D_e})}} + 10^{\frac{1}{4}*\frac{\boldsymbol{A\varnothing}}{max(\boldsymbol{A\varnothing})}} + 10^{\frac{1}{4}*\frac{\sqrt{\boldsymbol{Q}}}{max(\sqrt{\boldsymbol{Q}})}} \quad (4\text{-}2)$$

where min($\boldsymbol{L}$) is the minimum value of $\boldsymbol{L}$ inside the active PIC region for a given timestep, and max($\boldsymbol{D_e}$), max($\boldsymbol{A\varnothing}$), max($\sqrt{\boldsymbol{Q}}$) are the maximum values of $\boldsymbol{D_e}$, $\boldsymbol{A\varnothing}$, and $\sqrt{\boldsymbol{Q}}$, respectively. Instead of averaging the normalized reconnection metrics linearly, each term on the righthand side (RHS) of Equation (4-2) is amplified exponentially to increase the separation between regions with and without active reconnection. The theoretical lower bound and upper bound of $\boldsymbol{S}$ are 2 and $4 * 10^{1/4}$ (~ 7.11), respectively. Based on the definition in Equation (4-2), it is expected that $\boldsymbol{S}$ peaks near the X-lines and EDRs. We also note that our design of *S* is flexible and can be easily extended to include more reconnection metrics by adjusting their weights (constant coefficient of exponent in each term on the RHS of Equation (4-2)) correspondingly. Figure 4-5h shows the values of $\boldsymbol{S}$ in Y = 0 plane at T= 102 s from Run #1. The calculated reconnection score exhibits prominent enhancements in the close vicinities of the three X-lines (Z ~ $0.7R_M$, $-0.1R_M$, $-0.7R_M$) on the

magnetopause and remains relatively small within the FTEs. Such behaviors of *S* are consistent with our expectations. We also observe that *S* increases at the edges of the FTE near the northern cusp, which is due to the enhancement of $\sqrt{\boldsymbol{Q}}$ in the same regions.

To determine whether reconnection is present at a given location, we have set an ad hoc threshold of 4.9 to filter the synthesized reconnection score, $\boldsymbol{S}$, and the outcome is shown in Figure 4-5i. The yellow colors ($\boldsymbol{S} > 4.9$) indicate that reconnection is active (or present) at that location, while the blue colors ($\boldsymbol{S} < 4.9$) indicate absence of reconnection. We have tested 7 different thresholds from 4.7 to 5.0 with a step size of 0.05 and determined that 4.9 works reasonably well for all of our simulations in that this threshold is able to capture the vast majority of X-lines and, at the same time, is conservative enough to filter out most of the false positives, making it a judicious choice for the purpose of our analysis. As shown in Figure 4-5i, the X-lines at $Z \sim 0.7R_M$ and -0.1 R_M are clearly marked by two yellow stripes, the other X-line at $Z \sim -0.7R_M$ is marginally discernible by a small area of yellow coloring due to our conservative choice of the threshold. These results suggest that our approach, which involves the calculation of synthesized reconnection score $\boldsymbol{S}$ followed by a filtering process, is highly effective in identifying the precise locations of X-lines in the meridional cut of the active PIC region.

The performance of our reconnection X-line identification algorithm has also been validated for the 3D PIC domain. Figure 4-6 shows a series of snapshots of ion density isosurfaces (orange surfaces corresponding to $\rho_i = 180\ amu/cc$) and reconnection score isosurfaces (red surfaces corresponding to $score\ \boldsymbol{S} = 4.9$) in 3D taken at different timesteps from Run #1. Since the red surfaces are defined as $\boldsymbol{S} = 4.9$, they effectively indicate the identified X-lines in 3D geometry. Mercury is represented by the gray sphere in the center. Ion density contours in the Y = 0 and Z = 0 planes are also given in Figure 4-6 to provide global context. As indicated by the

sampled magnetic field lines (black arrowed lines), the enhanced density regions are located mostly within the flux ropes, suggesting that FTEs carry a dense population of plasmas while moving along the magnetopause surface. In Figure 4-6a, there are two FTEs: one large FTE (labeled as F1) located near the equatorial plane and another small FTE (labeled as F2) located in the northern dusk sector of the magnetopause. Each of the two FTEs is accompanied by two X-lines situated to its north and south. Twelve seconds later, as shown in Figure 4-6b, F2 has evolved into a medium-size FTE with well-developed twisted magnetic field lines enveloping the corresponding ion density isosurface. In Figure 4-6c, two smaller FTEs have formed in addition to the primary FTE F1 seen in Figure 6a: one in the southern dawn sector (labeled as F3) and another in the northern dusk sector (labeled as F4). Both FTEs are observed to locate between two identified reconnection X-lines, indicating that the FTEs were generated by multiple X-line reconnection in the simulation. The presence of such geometry, which is characterized by FTEs surrounded by two adjacent X-lines, is also clearly reflected in Figure 4-6d, 6e, and 6f, suggesting that our set of selection criteria for X-lines not only have reliable performance for the 2D meridional plane but also are robust in capturing reconnection sites in 3D.

The varying intensity of reconnection can also be captured appropriately by applying our automated identification algorithm. As depicted in Figure 4-6e, there are three FTEs observed in close proximity to the equatorial plane. In particular, the first FTE is positioned in the dawn sector (labeled as F5), the second FTE traverses the meridional plane (labeled as F8), and the third FTE resides within the dusk sector (labeled as F9). Seven seconds later (Figure 4-6f), F5 has moved in both the -Y and -Z directions from its previous position, while F8 and F9 remain situated near the equatorial plane. However, all three FTEs undergo significant changes in their sizes as they interact with the surrounding plasma and magnetic field. Specifically, FTE F5 exhibits a reduction in its

cross-section area while preserving its length in the Y direction, and the signature of identified X-lines surrounding F5 becomes weaker from Figure 4-6e to 6f. In contrast, both FTEs F8 and F9 have expanded in the axial direction (which is roughly aligned with the Y-axis for 180° clock angle IMF) and cross-sectional direction, and their corresponding adjacent X-lines display significant broadening in both Y- and Z-direction. These observations indicate that, in our simulations, The growth and decay of FTEs are typically associated with enhanced and reduced reconnection intensity, respectively, which is consistent with previous observations from Magnetospheric MultiScale (MMS) mission (*Akhavan-Tafti et al*., 2019a) and the general expectation that the plasmas carried by FTEs are supplied primarily by reconnection outflows (*Akhavan-Tafti et al*., 2019b).

4.3.3 Dawn-dusk Asymmetries in Magnetopause Reconnection Occurrence and Electric Field

The spatial distribution of reconnection occurrence in Mercury's tail plasma sheet has been investigated extensively in prior works. Previous studies from both MESSENGER observations (*Sun et al*., 2016) and global embedded PIC simulations (*Chen et al.,* 2019) have demonstrated the presence of a dawn-dusk asymmetry in tail reconnection occurrence. Specifically, it has been shown that the reconnection events tend to happen preferentially in the dawn sector (or the post-midnight region) of the tail. With our MHD-AEPIC simulations that used an active PIC region to cover the dayside magnetopause, our analysis in this study will, instead, focus on investigating the distribution of reconnection occurrence at the dayside magnetopause. To quantify the distribution of reconnection occurrence, we have made a 2D rectangular graph for each simulation showing the aggregated reconnection probability in Magnetic Local Time (MLT) and geographic latitude coordinates and the results for all six simulations are summarized in Figure 4-7.

The method we used to calculate aggregated reconnection probability is outlined as follows: Firstly, we compute the synthesized reconnection score $\boldsymbol{S}$ within the 3D active PIC domain for every timestep for which the simulation results were saved (i.e., every 1 second). Secondly, we count the number of times where a given grid point exhibits a value of $\boldsymbol{S}$ exceeding the designated threshold of 4.9 across all timesteps. These aggregated counts are subsequently linked to their corresponding grid points. Each grid point is then projected onto the two-dimensional MLT and latitude coordinates depicted in Figure 4-7. Lastly, we partition the two-dimensional MLT-latitude coordinates into discrete bins (or boxes), each measuring 0.1 MLT × 3° of latitude in size. The aggregated reconnection probability is then calculated by dividing the value within each box by the total sum of values across all boxes.

Comparing all the panels in Figure 4-7 indicates that there is a close correlation between the primary locations of reconnection X-lines on the magnetopause and the IMF clock angle in the upstream solar wind. For instance, the locations of X-lines in the 180° clock angle IMF cases (top row) are primarily concentrated in a horizontal band centered around the magnetic equator, which is slightly above the geographic equator due to Mercury's offset dipole. When the IMF clock angle is 135° or 90°, the primary X-line locations are tilted with respect to the equatorial plane. The tilt angle is roughly 22.5° for the 135° IMF cases (middle row) and 45° for the 90° IMF cases (bottom row). Such correlation is consistent with the expectation that reconnection tends to occur at places of maximum magnetic shear, i.e., where the magnetic fields in the magnetosphere and magnetosheath are anti-parallel to each other.

The results shown in Figure 4-7 further reveal some intriguing dawn-dusk asymmetries in the reconnection occurrence predicted by our MHD-AEPIC simulation. In all six cases, the distribution of reconnection probability exhibits a more diffusive pattern on the dawnside,

characterized by a larger area in which reconnection can potentially occur. To assess the distribution of identified reconnection events in a more quantitative manner, we have calculated the probabilities of reconnection (*P*) occurring on the dawn side (MLT < 12) and on the dusk side (MLT > 12). The results are shown as white texts inside each panel in Figure 4-7. Across all six cases, the probability of reconnection occurring on the dawn side ranges from 56% to 72%, indicating a notable dawn-dusk asymmetry. For simulations with the same IMF orientations, the dawn-dusk asymmetry becomes more prominent for solar wind $M_A = 2$ compared to $M_A = 6$, possibly due to the increased strength of the IMF set in the simulation. We will return to this point later in the Discussion section. For simulations with identical M_A numbers, the 90° IMF cases exhibit the strongest dawn-dusk asymmetry when compared to the 180° and 135° cases, with approximately 70% of reconnection events occurring on the dawn side. In all six cases, magnetopause reconnection appears to show a consistent preference for occurring on the dawn side. Such a dawn-dusk asymmetry, as predicted by our MHD-AEPIC simulations, would suggest that the upstream solar wind plasma may enter Mercury's magnetosphere via reconnection preferentially on the dawn side, and the resultant energetic particle precipitation into Mercury's cusps is then expected to also exhibit preference towards dawn. Possible explanations for such dawn-dusk asymmetry in reconnection occurrence will be discussed in the Discussion section.

Given that parallel electric field plays a central role in magnetic reconnection, where it facilitates the conversion of magnetic energy to particle energy by accelerating particles along the field line direction (*Schindler et al*., 1988), we have conducted further analysis to investigate the spatial distributions of the reconnection electric field simulated by the MHD-AEPIC model. In our analysis, the reconnection electric field $\boldsymbol{E}_{rec}$ is defined as the parallel component of the electric field in the electron's co-moving frame, given by the following expression:

$$\boldsymbol{E}_{rec} = (\boldsymbol{E} + \boldsymbol{V}_e \times \boldsymbol{B}) \cdot \frac{\boldsymbol{B}}{|\boldsymbol{B}|} \tag{4-3}$$

where $\boldsymbol{E}$ represents the electric field, $\boldsymbol{V}_e$ denotes the electron bulk velocity, and $\boldsymbol{B}$ represents the magnetic field. For this analysis, we have calculated $\boldsymbol{E}_{rec}$ on the magnetopause surface for each timestep. The magnetopause surface in the simulation was determined based on the *Shue et al.* (1997) empirical model (which was shown to work reasonably well for Mercury by *Winslow et al*. [2013]), with dynamically adjusted parameters involved in the empirical model at each timestep to account for the temporarily varying shape and location of the simulated magnetopause, following the same approach as described in Chapter 3. Figure 4-8 presents the distributions of time-averaged $\boldsymbol{E}_{rec}$ for all six simulations, following the same format as Figure 4-7. The MLT-latitude graphs shown in Figure 4-8 clearly demonstrate that the reconnection electric field exhibits systematic variations in both its strength and spatial distribution in response to changes in the upstream solar wind conditions. Specifically, the strength of $\boldsymbol{E}_{rec}$ shows a consistent trend of increasing magnitude with decreasing solar wind M_A and increasing IMF clock angle, consistent with the expected influence of these two parameters on the reconnection intensity as they primarily control the magnetosheath plasma β and the magnetic shear across the magnetopause boundary. The spatial distribution of $\boldsymbol{E}_{rec}$ exhibits a similar pattern as that of the corresponding primary X-line, as observed in Figure 4-7. Such a behavior is consistent with the expectation that the reconnection electric field tends to peak in close proximity to the primary X-line. In addition, the spatial distribution of $\boldsymbol{E}_{rec}$ displays a noticeable dawn-dusk asymmetry similar to that observed in the aggregated reconnection score distribution. In all six simulations, there is a clear shift in the center of the $\boldsymbol{E}_{rec}$ distribution towards the dawn side of the magnetopause. Moreover, the magnitude of this shift is found to correlate with the probability of reconnection occurring on the dawn side (P[dawn] shown in Figure 4-7). The asymmetric spatial distributions of $\boldsymbol{E}_{rec}$ and

reconnection probability suggest that there is an inherent dawn-dusk asymmetry in reconnection occurrence in our simulations. We will further discuss this point in the Discussion section by suggesting possible mechanisms that may account for such an asymmetry.

4.3.4 Statistical Properties of FTEs as Simulated by PIC

As seen in the examples shown in previous sections, FTEs with rope-like magnetic topology are formed frequently in our MHD-AEPIC simulation. They arise as a result of multiple X-line reconnection and carry solar wind plasma and open magnetic flux into the magnetosphere, which eventually participate in the global circulation of plasma and magnetic flux, or the so-called "Dungey-cycle". It is, therefore, of interest to characterize the properties of FTEs and quantitively assess their contribution to the global convection and dependence on the upstream conditions based on our simulation results. The properties of FTEs we focus on here are their temporal spacing (or equivalently, recurrence rate), spatial size, traveling speed, core field strength, plasma density, magnetic flux content, and overall contribution to open flux generation in the magnetosphere. In our statistical analysis presented below, we have utilized the maximum values of plasma density and core field strength across the cross-section of an FTE to represent its characteristic density and core field strength, acknowledging that their distributions within the FTE typically are non-uniform. The meanings of other properties are as follows: temporal spacing refers to the time interval between the centers of neighboring FTEs; traveling speed denotes the average speed at which an FTE traverses along the magnetopause surface; FTE size is characterized by its length in the latitudinal direction multiplied by a geometric factor $\cos(\theta_{FTE})$, where θ_{FTE} is the angle between the horizontal direction and the FTE axis. Further details regarding the techniques employed for extracting the characteristics of FTEs can be found in Chapter 3.

Figure 4-9 - Figure 4-11 present histograms of FTE size, traveling speed, core field strength, and magnetic flux content extracted from our MHD-AEPIC simulations for different solar wind and IMF conditions. To facilitate effective comparison, simulations with the same IMF clock angles but different solar wind M_A are grouped into a single figure (Figure 4-9 for 180° IMF clock angle, Figure 4-10 for 135° clock angle, and Figure 4-11 for 90° clock angle). We have taken the average of FTE size over its entire evolution to obtain the mean FTE size, which is shown in panels (a) and (e) in Figure 4-9 - Figure 4-11. Across all simulations, the FTE size ranges from ~ 300 km to ~ 2700 km and the breadth of the size distribution exceeds 1000 km, suggesting that even under constant upstream conditions, FTEs formed on Mercury's magnetopause can exhibit considerable range in their spatial sizes. For the three IMF clock angles investigated in this paper, the average FTE size (shown in the legends of panels (a) and (e)) is found to increase monotonically with decreasing IMF clock angle but appear to be less sensitive to changes in the solar wind M_A, i.e., the average size is comparable between different M_A numbers for the same IMF clock angle.

The distributions of FTE traveling speed are shown in panels (b) and (f) of Figure 4-9 - Figure 4-11, with the positive and negative values corresponding to northward and southward propagation, respectively. The traveling speeds of FTEs fall into a range spanning from -500 km/s to 600 km/s. For all IMF clock angles, the average traveling speeds follow an upward trend as the solar wind M_A decreases. Additionally, there is a roughly even distribution of FTEs traveling in the northward and southward directions, except for the 90° clock angle simulations where FTEs appear to favor southward propagation. This deviation from the general trend may be attributed to the presence of dawn-dusk asymmetry in reconnection probability, which has been presented in Section 4.3.3. This asymmetry results in higher occurrence of multiple X-line reconnections in the

dawn sector, which consequently leads to an increased number of FTEs originating in the dawn sector, specifically to the south of the primary reconnection X-line (the geometry of which has been shown in Section 4.3.3). These FTEs inherit the dominant southward motion driven by the reconnection outflow upon formation, thereby resulting in a preference for southward propagation.

Panels (c) and (g) in Figure 4-9 - Figure 4-11 show the distributions of FTE core field strength for all simulations. The mean core field strength falls within the range of 66 - 212 nT, which is consistent with the findings reported by *Sun et al.* (2020) for FTE shower events observed by MESSENGER. The polarity of the FTE core field indicates its alignment with respect to the dawn-dusk direction (Y-axis). In simulations with an IMF clock angle of 180°, both positive and negative core fields are present for the FTEs formed in the simulation with an approximately even distribution. In contrast, in the presence of a significant B_y component in the upstream IMF (i.e., 135° and 90° clock angle simulations), almost all FTEs exhibit a negative polarity in their core fields, which is the same direction as the ambient IMF B_y. This dependence of FTE core field polarity on the upstream B_y component of the IMF is consistent with previous findings from our Hall MHD simulations (*Li et al*., 2023) and observations of FTEs at the Earth's magnetopause by the Magnetospheric MultiScale (MMS) mission (*Kieokaew et al*., 2021). Both our simulation results and in situ observations suggest that the orientation of the reconnection guide field, which largely depends on the upstream IMF in the case of Mercury (and Earth), plays a crucial role in establishing the polarity of the FTE core field. Furthermore, the average core field strength of FTEs increases with decreasing solar wind M_A and with decreasing IMF clock angle. These findings are entirely consistent with the observed dependence of FTE core field strength reported by *Sun et al*. (2020).

The distributions of FTE magnetic flux content are shown in panels (d) and (h) of Figure 4-9 - Figure 4-11. The average open flux carried by FTEs under different solar wind and IMD conditions ranges from 0.01 MWb to 0.12 MWb. The maximum amount of open flux carried by FTEs seen in our simulations is ~ 0.36 MWb (see Figure 4-11h), which is very close to the upper limit of ~ 0.4 MWb reported from MESSENGER observations (*Sun et al*., 2022b). *Imber et al*. (2014) conducted a survey of MESSENGER magnetic data and identified 17 "large" FTEs. By modeling the FTEs as force-free flux ropes, they estimated the average flux content of these 17 "large" FTEs to be 0.06 MWb, which closely aligns with our simulation results, especially those for Run #3 and #5. However, the higher end of simulated average FTE flux content (seen in Run #6) is about twice the estimate by Imber et al., suggesting that our M_A= 2, 90° IMF clock angle simulation may represent a scenario of stronger solar wind driving than considered by the Imber et al. study. Our simulation results also show that when considering the same IMF clock angle, individual FTEs transport approximately twice the amount of open flux for solar wind M_A = 2 compared to M_A = 6. For both M_A = 6 and M_A = 2 simulations, the average magnetic flux carried by FTEs follows a consistent, increasing trend as the IMF clock angle decreases, which is in good agreement with the trend found in the statistical study of MESSENGER FTE shower events by *Sun et al*. (2020).

To summarize the results, we compare in Table 4-2 key statistics pertaining to simulated FTEs as well as the total open flux content in the polar cap and the cross polar cap potential (CPCP) for all six simulations. The latter two quantities (i.e., total open flux and CPCP) provide a global measure of the solar wind-magnetosphere coupling, which can be used as context to evaluate the contributions of FTEs in driving the global convection and dynamics. The methodology used to calculate CPCP is described in detail in *Zhou et al*. (2020), which has also been successfully

applied to our previous Hall-MHD simulations of Mercury's magnetosphere (*Li et al*., 2023). As can be seen from Table 4-2, the temporal separation between adjacent FTEs spans from 4.1 s to 8.7 s. Comparing the results among simulations using different upstream conditions reveals the following trends regarding the temporal spacing: (1) For the same IMF orientation, the spacing is smaller in simulations with solar wind $M_A = 2$ compared to those with $M_A = 6$. (2) The spacing decreases with increasing IMF clock angle in simulations with the same solar wind M_A. Both the range and trend of the FTE temporal spacing derived from our simulations exhibit good agreement with the MESSENGER observations during FTE shower events (*Sun et al*., 2020). These results together suggest that FTEs at Mercury tend to occur more frequently when the upstream solar wind driving is more favorable for reconnection onset, i.e., low M_A solar wind and large shear angle IMF.

As indicated in Table 4-2, the time-averaged peak plasma density within FTEs varies between 77 - 139 amu/cm^3. In both $M_A = 6$ and $M_A = 2$ simulations, the FTE density is found to decrease with decreasing IMF clock angle. For all three IMF clock angles investigated in this study, the characteristic FTE density is found to decrease with decreasing solar wind M_A. The reduced plasma density under smaller solar wind M_A could be accounted for by the dependence of the properties of the magnetosheath on the solar wind conditions. That is, solar wind with lower M_A leads to a thicker magnetosheath with less dense plasma compared to higher M_A solar wind. The changes in the magnetosheath thickness and plasma density can be clearly observed by comparing Figure 4-1a with Figure 4-2a.

The average polar cap open flux content and average CPCP in the simulations range from 2.65 MWb to 4.38 MWb and 25 kV to 130 kV, respectively. Both quantities increase with decreasing solar wind M_A and increasing IMF clock angle. Such a trend is consistent with the

expectation that reconnection occurring at the dayside magnetopause tends to favor a low plasma β environment and an anti-parallel configuration of the magnetic field. By comparing the flux content associated with all FTEs with the total open flux in the polar cap, we find that, on average, approximately 0.28% to 3.97% of the total open flux content within the polar cap is contributed by FTEs, which is in accordance with the previously reported ranges in *Sun et al* (2022b).

To further determine the role of FTEs in driving the Dungey-cycle at Mercury, we estimate FTEs' overall contribution to the open flux generation on the dayside by calculating $(\Phi_{avg} * N_{FTE})/(CPCP * T)$, where Φ_{avg} is the average open flux carried by FTEs as shown in the legends of panels (d) and (h) in Figure 4-9 - Figure 4-11, N_{FTE} is the total number of identified FTEs in the simulation, T represents the duration of the simulation, which is 200 s for all six cases. The numerator $\Phi_{avg} * N_{FTE}$ denotes the total amount of magnetic flux transported by FTEs during the simulation, and the denominator $CPCP * T$ indicates the total amount of open flux generated at the dayside magnetopause, which presumably includes contributions from FTEs resulting from multiple X-line reconnection as well as single X-line reconnection that also produces open flux but not FTEs. As indicated in Table 4-2, about 2.9% to 36.4% of the dayside open flux is generated through FTEs. These numbers are in agreement with the previous estimates based on MESSENGER observations (*Slavin et al*., 2012; *Imber et al*., 2014). For all three IMF clock angles (180°, 135°, and 90°), our results reveal that a higher percentage of open flux is generated by FTEs in simulations with $M_A = 2$ compared to $M_A = 6$. However, the contribution of FTE to the open flux generation appears to be primarily controlled by the IMF clock angle, as indicated by the exponentially increasing values shown in the bottom row of Table 4-2.

4.4 Discussion

4.4.1 Potential mechanisms causing dawn-dusk asymmetries in Mercury's magnetopause reconnection

In Section 4.3.3, we have presented simulation evidence of dawn-dusk asymmetry in magnetopause reconnection occurrence and electric field, both of which exhibit preference for the dawn side. Here we discuss several processes that could account for the dawn-dusk asymmetry found in our simulations. One of the prominent features of 3D dayside reconnection observed at Earth's magnetopause is the spreading of the X-lines in the direction perpendicular to the plane of reconnection (*Zou et al*., 2018), which we think could also operate at Mercury. *Shepherd and Cassak* (2012) suggested that X-line spreading is mainly driven by two processes: one associated with the motion of the current carriers and another caused by the propagation of Alfvén waves along the out-of-plane (guide field) direction. Correspondingly, the speeds of X-line spreading in the directions of electron and ion out-of-plane flows are expressed as follows:

$$V_{Xe} = max\{V_{eg}, C_{Ag}\} \tag{4-4}$$

$$V_{Xi} = max\{V_{ig}, C_{Ag}\} \tag{4-5}$$

where V_{eg} and V_{ig} represent the out-of-plane flow speeds of electrons and ions contributing to carrying the electric currents, and C_{Ag} denotes the Alfvén speed based on the guide field, given by

$$C_{Ag} = \frac{B_g}{\sqrt{\mu_0 \rho}} \tag{4-6}$$

where B_g is the strength of the guide field and ρ is the plasma density near the reconnection site. We have sampled multiple reconnection sites in the six simulations and used Equations (4-4) - (4-6) to calculate the characteristic values of V_{Xe} and V_{Xi} in each simulation. For electrons, their flow direction in the dayside magnetopause current sheet is towards the dawnside, and as such

they tend to spread the X-line towards the dawn side. We find that the spreading speed due to electron motion, V_{Xe}, varies from 937 km/s to 1551 km/s. It is worth noting that V_{Xe} is equivalent to V_{eg} across all six simulations, as the electron flow speed is significantly greater than the Alfvén speed C_{Ag}. In contrast, the ion flow tends to cause the X-line to spread towards the dusk side and the spreading speed, $V_{Xi,}$ falls within the range of 81 km/s to 451 km/s. We note that V_{Xi} is primarily determined by the Alfvén speed C_{Ag}, except in cases with 180° IMF clock angle, where the guide field is almost absent. Comparing the calculated spreading speeds from our simulations indicates that at Mercury's dayside magnetopause, the dawnward spreading speed (V_{Xe}) of X-lines is significantly larger than the duskward spreading speed (V_{Xi}). Such difference in spreading speeds offers a plausible explanation for the observed dawn-dusk asymmetry in the reconnection occurrence and electric field, as shown in Figure 4-7 and Figure 4-8. Furthermore, our calculations show that, when the IMF clock angle is the same, the X-line spreading speed for electrons consistently exhibits larger values in $M_A = 2$ simulations compared to $M_A = 6$ simulations, which is consistent with the increased strength of the magnetopause currents seen in $M_A = 2$ cases. This enhanced dawnward X-line spreading speed in $M_A = 2$ simulations provides an explanation for the results presented in Section 4.3.3, which shows that the dawn-dusk asymmetry becomes more prominent in $M_A = 2$ simulations compared to $M_A = 6$ simulations for the same IMF orientations.

Another possible contributing process to the dawn-dusk asymmetry associated with the magnetopause reconnection seen in our simulations is the Hall effect. Previous study by *Liu et al*. (2019) demonstrated the presence of a suppression region near the reconnection site in their 3D PIC simulations, which arises due to the Hall effect in three-dimensional configuration. The spatial extent of this suppression region is of the order $10d_i$ (d_i is the ion inertial length), leading to an "internal" asymmetric structure of the X-line which is notable only in systems with sizes

comparable to that of the suppression region. Given that the dawn-dusk width of Mercury's tail current sheet is ~ 37d_i (*Poh et al*., 2017; *Sun et al*., 2016), this internal asymmetry has been invoked to explain various dawn-dusk asymmetries observed by MESSENGER in Mercury's magnetotail (*Liu et al*., 2019). Here we examine if the same Hall effect could also be present at Mercury's dayside magnetopause. In our MHD-AEPIC model, the proton density near the magnetopause reconnection sites is found to fall in the range of ~60 cm^{-3} to ~90 cm^{-3}. After applying the scaling factor of 4, as described in Section 4.2.1, the effective ion inertial length d_i at the dayside magnetopause in our simulation is estimated to be around 100 km ~ 120 km. The dayside magnetopause current sheet in our simulation extends in the Y direction over a distance of ~ 2 R_M, which is equivalent to ~ 40 d_i. Therefore, the dawn-dusk extent of the magnetopause current sheet in our simulation is comparable to the dimension of the suppression region, similar to the situation for the magnetotail current sheet. Therefore, it is reasonable to expect that the internal asymmetry resulting from the Hall effect in 3D may also contribute to the dawn-dusk asymmetries in Mercury's dayside magnetopause reconnection observed in our simulations.

4.4.2 Large FTEs and their contribution to global convection and dynamics

In the statistical results of FTE properties presented in Section 4.3.4 and Figure 4-9 - Figure 4-11, we find that FTEs formed in the simulation come with a range of sizes, including some that have scale lengths in the cross-section exceeding ~ 1000 km, which we term as "large" FTEs. Various previous works have studied large FTEs based on MESSENGER data. For instance, *Slavin et al*. (2010b) identified six FTEs encountered during MESSENGER's first two flybys of Mercury (M1 and M2) and estimated that a single large FTE may carry an axial magnetic flux content of ~ 0.2 MWb and contribute ~ 30 kV to the cross polar cap potential (CPCP). *Imber et al*. (2014) further studied 58 large FTEs observed by MESSENGER and found that, on average, a large FTE

carries ~ 0.06 MWb of flux content and contribute ~ 25 kV to CPCP, which suggests that large FTEs play an important role in driving global convection. Here we examine the properties of those large FTEs seen in our simulations and compare them with MESSENGER observations. The large FTEs of interest correspond to those appearing near the tail end of the FTE flux content distributions (panels (d) and (h) in Figure 4-9 - Figure 4-11). Figure 4-12 shows one example of large FTE from Run #5 (M_A = 2, IMF clock angle= 135°). This particular FTE, as highlighted by the magenta box, is situated slightly south of the equatorial plane characterized by twisted magnetic field lines and enhanced plasma density within the FTE. Notably, the cross-section area of this FTE is significantly expanded in both the latitudinal and radial directions, resulting in a substantial compression to both the magnetospheric and magnetosheath plasmas adjacent to the magnetopause. The open flux carried by this large FTE is estimated to be Φ = 0.15 MWb, which corresponds to 3.86% of the total polar cap flux content found in the simulation (3.95 MWb). The transfer of this magnetic flux from the dayside to the nightside magnetosphere will contribute to the CPCP by an amount $\Phi/\Delta T$, as proposed by *Slavin et al*. (2010b), where $\Delta T \equiv$ (FTE size) / (FTE speed) is the time required for the FTE's open flux to merge into the polar cap. For this FTE, the value of ΔT is ~ 21 s, which results in a CPCP contribution of ~ 7 kV. We have performed the same analysis for all large FTEs found in the six simulations, and found that the magnetic flux carried by individual large FTEs varies between 0.05 MWb and 0.36 MWb, which is about 1.3% - 11.9% of the total open flux in the polar cap. This result is in general agreement with the previous estimate of 8.8% obtained by *Imber et al*. (2014) through analysis of MESSENGER data. The contribution of individual large FTEs to the CPCP falls in the range between 4 kV and 29.8 kV in our simulation, which is also in line with the finding reached in previous studies based on MESSENGER observations (e.g., *Slavin et al*., 2010b; *Imber et al*., 2014). The percentage

contribution of a large FTE to the CPCP is about 7% to 47.6%, which is consistent with the results reported in *Sun et al.* (2022b) that individual FTEs can contribute up to ~ 40% of the CPCP. Overall, we find that the properties of large FTEs simulated by our MHD-AEPIC model agrees very well with the results obtained in previous studies based on in-situ observations. Comparing the six simulations using different upstream conditions further reveals that large FTEs tend to carry more magnetic flux when the solar wind M_A is smaller or when the IMF clock angle is smaller.

4.4.3 Comparison between MHD-AEPIC and Hall-MHD simulations

Finally, we discuss the effects of the kinetic physics on the characteristics of both simulated FTEs and reconnection X-lines. As mentioned in Section 4.2.1, the upstream conditions employed in this work are the same as those used in our previous global Hall-MHD simulations (*Li et al*., 2023), allowing us to make a direct comparison of simulation results between coupled fluid-kinetic model (i.e., MHD-AEPIC) and pure Hall MHD code. Figure 4-13 shows a comparison of various FTE properties and CPCP simulated by MHD-AEPIC and Hall-MHD models. The horizontal axis in each panel corresponds to the IMF clock angle in decreasing order. As shown, the majority of the quantities of interest extracted from MHD-AEPIC and Hall-MHD simulations display similar dependencies on the upstream solar wind M_A and IMF clock angle, with only few exceptions in FTE size, travelling speed, and core field strength. Furthermore, the observed dependencies on the upstream conditions are consistent with the findings reported in the recent MESSENGER survey of FTE shower events at Mercury (*Sun et al*., 2020). For instance, the temporal spacing between FTEs increases with increasing M_A number and decreasing IMF clock angle in both MHD-AEPIC and Hall-MHD simulations. Consequently, the occurrence of FTEs is most frequent when $M_A = 2$ and IMF clock angle = 180°.

Having evaluated the overall trends of various quantities shown in Figure 4-13, we now discuss the similarities and differences between MHD-AEPIC and Hall-MHD shown in Figure 4-13. We first focus on the impact of kinetic physics on CPCP, FTE speed, spacing, and density. As illustrated in Figure 4-13g, the CPCP values modeled by MHD-AEPIC and Hall-MHD are nearly identical, suggesting that kinetic effects do not significantly alter the global efficiency of the coupling between the solar wind and the magnetosphere. However, some differences can be observed in other FTE characteristics between the Hall-MHD and MHD-AEPIC models. For example, under the same upstream driving, the FTE speeds in the MHD-AEPIC model are generally smaller compared to those in the Hall-MHD model. The relatively slower FTE speeds in the MHD-AEPIC model would imply that FTEs can stay for a longer period on the dayside magnetopause (e.g., some FTEs and X-lines last for more than 20 s as shown in Figure 4-6). The FTE spacing is, in general, larger in the MHD-AEPIC model in comparison with Hall-MHD, suggesting that the generation of new X-lines occurs less frequently in the PIC model. This observed difference in FTE spacing is consistent with the result that individual X-line's lifetime on the dayside magnetopause is longer in the PIC model. We note that this decrease in the occurrence rate of FTEs, as simulated by the embedded PIC model, has also been reported previously in simulations of Ganymede's magnetosphere (*Zhou et al*., 2020). The FTE density consistently exhibits higher values in MHD-AEPIC simulations, which may be attributed to the result that the longer lifetime of FTE and reconnection X-line seen in the PIC model naturally lead to an increased injection of plasmas into the interior of FTE through reconnection outflow.

Next, we examine how the modeled FTE size, core field strength, magnetic flux content, and their overall contribution to open flux generation are affected when kinetic effects associated with reconnection are included in the simulation. As shown by Figure 4-13c and Figure 4-13e, the

modeled FTE size and core field strength in the MHD-AEPIC simulations are, in general, very comparable to those seen in the Hall-MHD simulations using the same upstream conditions, with only a couple of exceptions. Particularly, in the $M_A = 2$ and IMF clock angle = 135° case, the average FTE size is smaller in Hall-MHD results, while for the case with $M_A = 2$ and IMF clock angle = 90°, the average FTE core field strength is lower in the Hall-MHD simulation compared to MHD-AEPIC simulation. In contrast, the average magnetic flux contents of FTE modeled by MHD-AEPIC are approximately twice those modeled by Hall-MHD under the same upstream driving. At a first glance, this discrepancy in FTE flux content seems to contradict with the result of comparable FTE size and core field strength observed in MHD-AEPIC and Hall-MHD simulations. However, our further analysis indicates that this result is due to the following two factors: (1) The standard deviations of the FTE size distribution in MHD-AEPIC simulations are smaller compared to Hall-MHD, suggesting that medium-size FTEs are more prevalent in MHD-AEPIC runs, and (2) the large-size FTEs seen in MHD-AEPIC tend to fall into the higher end of the core field strength distribution, resulting in well-formed FTEs carrying a substantial amount of open flux (which were termed as "large" FTEs previously in Section 4.4.2). We note that such correlation between large FTE size and strong core field is not seen in the Hall-MHD simulations. The FTE contribution to open flux generation in the MHD-AEPIC simulations shows a considerable increase when compared to Hall-MHD, especially for the 90° IMF clock angle case. In particular, for $M_A = 6$ and IMF clock angle = 90° cases, the FTE contribution is 26.2% in MHD-AEPIC and 10.4% in Hall-MHD, while for $M_A = 2$ and IMF clock angle = 90° cases, the corresponding values are 36.4% for MHD-AEPIC and 12.7% for Hall-MHD. The substantial increase in FTE contributions to open flux generation in the MHD-AEPIC model at 90° IMF clock angle may have resulted from the differences in the evolution of individual FTEs, which is

predominantly controlled by characteristics of the local reconnection that is modeled by PIC method.

4.5 Summary and Conclusions

Taking advantage of the recent development on coupled fluid-kinetic simulations, we have conducted a series of global simulations of Mercury's magnetosphere to investigate the kinetic signatures, dawn-dusk asymmetries, and FTEs associated with the dayside magnetopause reconnection. For this study, we have utilized the MHD-AEPIC model (*Wang et al*., 2022; *Chen et al*., 2023) coupled with planetary interior (*Jia et al*., 2015, 2019) to simulate Mercury's magnetosphere and adaptively placed a non-rectangular PIC region to cover the entire dayside magnetosphere where reconnection is expected to occur. Six simulations were performed to study how Mercury's magnetosphere responds to different upstream parameters, specifically focusing on the impact of the solar wind Alfvénic Mach number and the IMF clock angle. Below we summarize the key results from our simulations.

The application of a fully kinetic approach to treat both ions and electrons in the embedded PIC model unveils distinct features in the plasma phase space distributions that result from magnetopause reconnection at Mercury. In particular, our results reveal crescent-shaped phase space distributions for both ions and electrons on the magnetosheath side of the reconnection sites. Additionally, near reconnection sites, electron phase space distributions exhibit signatures of preferential heating along the magnetic field direction, aligning with the reconnection outflow direction. In the cusp region, ion distributions exhibit counter-streaming behavior with two populations traveling in opposite directions relative to the magnetic field. Such counter-streaming particle distribution may potentially lead to plasma instabilities and wave generation in the cusp

region. Inside the FTEs, both ion and electron distributions are found to deviate from the Maxwellian distribution, showing notable signatures of temperature anisotropies due to magnetopause reconnection.

In all six simulations, where the upstream solar wind and IMF conditions are maintained at constant values, Mercury's magnetopause reconnection is found to occur in a non-steady manner resulting in FTEs with flux-rope like magnetic topology. In order to identify the reconnection X-lines in the 3D simulations, we have explored various published metrics used in studying reconnection physics, and come up with a synthesized reconnection score, *S*, based on four reconnection metrics that works reasonably well for all of our simulations in identifying the locations of X-lines. By projecting the identified reconnection sites onto the MLT-latitude coordinates, we found that the distribution of reconnection occurrence at Mercury's dayside magnetopause exhibits significant dawn-dusk asymmetries in all six simulations, with the probability of reconnection events occurring on the dawnside ranging from 56% to 72%. The dawn-dusk asymmetry appears to be more pronounced in simulations with lower solar wind M_A and smaller IMF clock angle (or equivalently, IMF with larger B_y component). Potential processes that may have contributed to the dawn-dusk asymmetry seen in our simulations include X-line spreading preferentially towards dawnside due to the large flow speeds associated with the current-carrying electrons and suppression of reconnection on the duskside due to the Hall effects in 3D reconnection.

An automated algorithm previously developed by *Li et al*. (2023) has been used to identify the large number of FTEs in the MHD-AEPIC simulations. The simulated FTEs are found to form frequently in our simulations with occurrence rates ranging from 4 to 9 seconds. Key properties of the FTEs, including their density, size, traveling speed, core field strength, and magnetic flux

content were extracted from the simulations and compared with the results extracted from previous Hall-MHD simulations, which were driven by the same set of upstream conditions listed in Table 4-1. In both MHD-AEPIC and Hall-MHD simulations, the properties of simulated FTEs generally exhibit the same dependencies on the solar wind M_A and IMF clock angle, and the observed dependencies are consistent with the findings reported in previous observational studies based on MESSENGER data (e.g., *Sun et al*., 2020). However, some characteristics of FTEs seen in the MHD-AEPIC simulations differ from those in the Hall-MHD simulations, likely due to kinetic effects, which are absent in the Hall-MHD model. Specifically, the FTEs and their associated reconnection X-lines, as modeled by PIC, tend to stay for a longer period of time on the magnetopause surface compared to their counterparts in Hall-MHD. The longer lifetime of FTEs and X-lines leads to slower FTE traveling speeds, slightly less frequent FTE occurrence, and higher FTE densities in the MHD-AEPIC model. The average magnetic flux content carried to FTEs simulated by MHD-AEPIC is approximately twice as high as those modeled by Hall-MHD, primarily due to the formation of greater number of "large" FTEs in the MHD-AEPIC simulation. These "large" FTEs in the MHD-AEPIC simulations carry about 1.3% - 11.9% of the total polar cap flux and contribute 7% to 47.6% of the average CPCP, which confirms the finding from previous MESSENGER work (e.g., *Imber et al*., 2014) that they play an important role in driving the global convection and dynamics in Mercury's magnetosphere.

In summary, we have employed a coupled fluid-kinetic model to investigate several aspects of reconnection-driven dynamics in Mercury's magnetosphere, including the kinetic signatures observed in particle distributions, the dawn-dusk asymmetry of reconnection occurrence on the dayside, and the effect of kinetic physics on the formation and evolution of FTEs. The findings obtained through our simulations are expected to be useful for the interpretation of in situ

measurements collected by spacecraft missions, such as MESSENGER and Bepi-Colombo, the latter scheduled to arrive at Mercury in late 2025 (*Milillo et al*., 2020).

4.6 Appendix: Nongyrotropy Measures

The two nongyrotropy measures presented in this chapter are both scalar quantities that are invariant with respect to the coordinate system. These measures can be computed locally on each grid point of the PIC model using the following equations. It is important to note that in the following equations the electron subscripts have been omitted in the expressions of the pressure tensor.

The first measure $\boldsymbol{A\emptyset}$ is defined as

$$\mathbf{A\emptyset} = 2\frac{|\mathrm{P}_{\perp 1} - \mathrm{P}_{\perp 2}|}{\mathrm{P}_{\perp 1} + \mathrm{P}_{\perp 2}}, \tag{4-7}$$

where the subscripts 1 and 2 represent the two directions perpendicular to the magnetic field. *Scudder and Daughton* (2008) showed that in any coordinate system defined by (XYZ), by defining

$$\mathrm{N_{xx}} = \mathrm{b_y b_y P_{zz}} - 2\mathrm{b_y b_z P_{yz}} + \mathrm{b_z b_z P_{yy}} \tag{4-8}$$

$$N_{xy} = -b_y b_x P_{zz} + b_y b_z P_{xz} + b_z b_x P_{yz} - b_z b_z P_{xy} \tag{4-9}$$

$$N_{xz} = b_y b_x P_{yz} - b_y b_y P_{xz} - b_z b_x P_{yy} + b_z b_y P_{xy} \tag{4-10}$$

$$N_{yy} = b_x b_x P_{zz} - 2b_x b_z P_{xz} + b_z b_z P_{xx} \tag{4-11}$$

$$N_{yz} = -b_x b_x P_{yz} + b_x b_y P_{xz} + b_z b_x P_{xy} - b_z b_y P_{xx} \tag{4-12}$$

$$N_{zz} = b_x b_x P_{yy} - 2b_x b_y P_{xy} + b_y b_y P_{xx}, \tag{4-13}$$

and

$$\alpha = N_{xx} + N_{yy} + N_{zz} \tag{4-14}$$

$$\beta = -\left(N_{xy}^2 + N_{xz}^2 + N_{yz}^2 - N_{xx}N_{yy} - N_{xx}N_{zz} - N_{yy}N_{zz}\right), \tag{4-15}$$

$\boldsymbol{A\varnothing}$ can be rewritten as

$$\boldsymbol{A\emptyset} = 2\frac{\sqrt{\alpha^2 - 4\beta}}{\alpha} \tag{4-16}$$

The second nongyrotropy measure, $\boldsymbol{Q}$, is proposed by *Swisdak* (2016), which is defined as

$$\boldsymbol{Q} = 1 - 4\frac{I_2}{(I_1 - P_{\|})(I_1 + 3P_{\|})}, \tag{4-17}$$

where $I_1 = P_{xx} + P_{yy} + P_{zz}$ is the trace of the electron pressure tensor and $I_2 = P_{xx}P_{yy} + P_{xx}P_{zz} + P_{yy}P_{zz} - \left(P_{xy}P_{yx} + P_{xz}P_{zx} + P_{yz}P_{zy}\right)$ is the principle minor of the electron pressure tensor.

Table 4-1: Solar wind and IMF parameters used for the simulations presented in this chapter

Run #	**M_A**	**IMF clock angle (°)**	$B_y(nT)$	$B_z(nT)$	$U_x(km/s)$	**ρ(amu/cc)**	$T(K)$
1	6	180	0	-23	-500	36	8.7e4
2	6	135	-16	-16	-500	36	8.7e4
3	6	90	-23	0	-500	36	8.7e4
4	2	180	0	-69	-500	36	8.7e4
5	2	135	-49	-49	-500	36	8.7e4
6	2	90	-69	0	-500	36	8.7e4

Table 4-2: Comparison of simulated FTE properties, polar cap open flux, and CPCP for different solar wind M_A and IMF clock angles

Upstream Conditions / FTE Properties	$M_A = 6$			$M_A = 2$		
	Clock angle 180° (Run #1)	**Clock angle 135°** (Run #2)	**Clock angle 90°** (Run #3)	**Clock angle 180°** (Run #4)	**Clock angle 135°** (Run #5)	**Clock angle 90°** (Run #6)
Simulation duration	200 s	200 s	200 s	200 s	200 s	200 s
Total number of FTEs	33	28	23	49	38	34
Average recurrence rate (or temporal spacing)	1 FTE every 6.1 s	1 FTE every 7.5 s	1 FTE every 8.7 s	1 FTE every 4.1 s	1 FTE every 5.3 s	1 FTE every 5.9 s
Average density	139 amu/cc	111 amu/cc	93 amu/cc	132 amu/cc	102 amu/cc	77 amu/cc
Average size	719 km	758 km	876 km	705 km	777 km	930 km
Average speed	197 km/s	147 km/s	123 km/s	230 km/s	210 km/s	179 km/s
Average core field	66 nT	89 nT	142 nT	94 nT	169 nT	208 nT
Average flux content	0.010 MWb	0.029 MWb	0.057 MWb	0.023 MWb	0.061 MWb	0.120 MWb
Average polar cap open flux content	3.51 MWb	3.45 MWb	2.65 MWb	4.38 MWb	3.95 MWb	3.02 MWb
Cross Polar Cap Potential	56 kV	50 kV	25 kV	130 kV	101 kV	56 kV
FTE contribution to open flux circulation	2.9%	8.1%	26.2%	4.3%	11.5%	36.4%

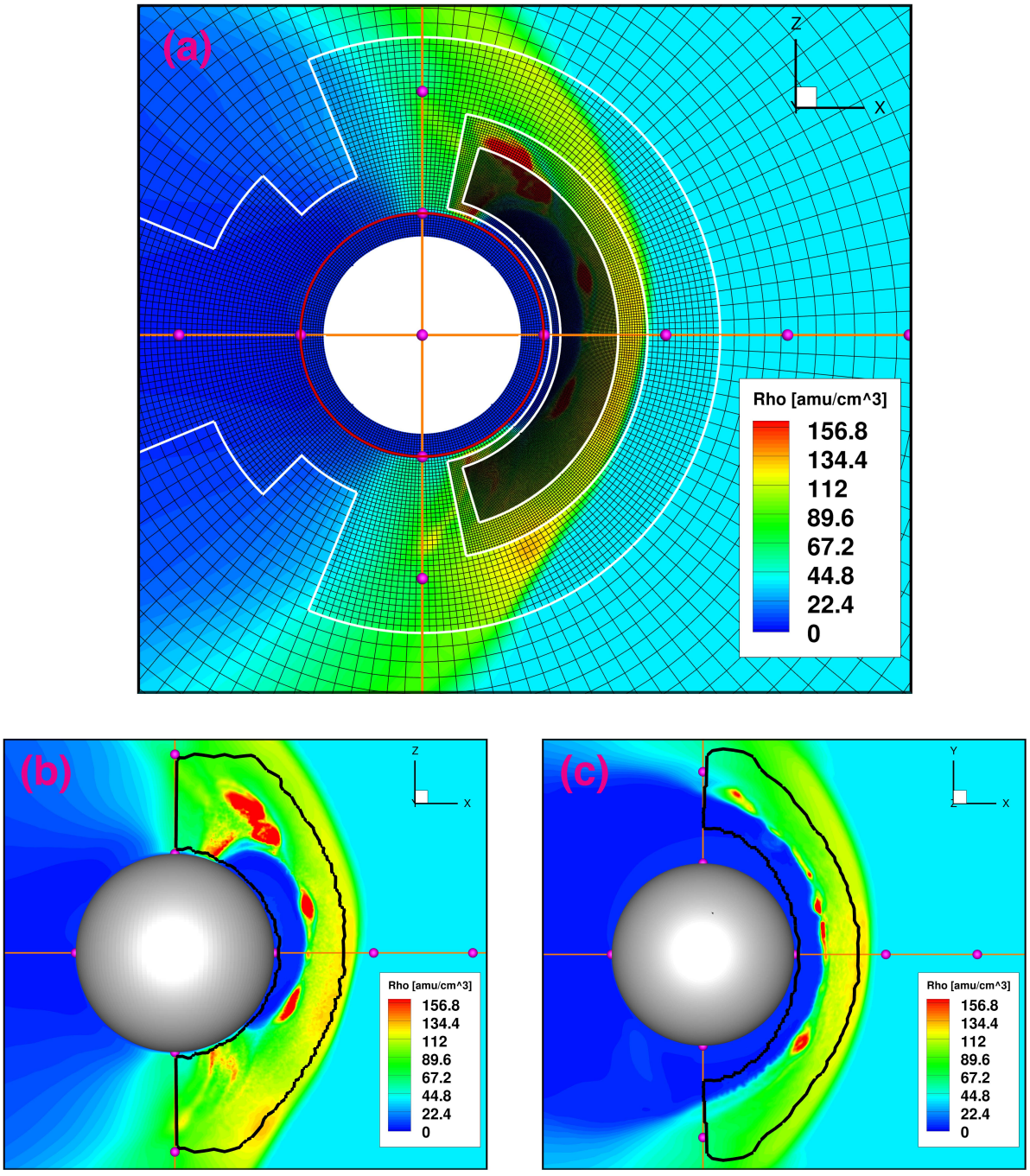

Figure 4-1: The structure of the BATSRUS Hall-MHD grid and the active PIC region. (a) Stretched spherical grid (in black) used by the BATSRUS Hall-MHD model with three levels of adaptive mesh refinement (AMR) at the dayside magnetopause, as viewed in the XZ plane. The boundaries between successive AMR levels are indicated by the white curves. The red circle centered at the origin with radius of 1 R_M represents the surface of Mercury and the centered white-filled disk represents Mercury's conducting core with an assumed radius of 0.8 R_M. (b) and (c) The boundaries of the active PIC region (marked by the black curves) in the XZ and XY planes, respectively. Mercury is represented by a grey sphere with a radius of 1 R_M in the center. The background colors in all panels show the plasma density (ρ) contours. For illustration purposes, the density contours were extracted from Run #1 (M_A= 6, IMF clock angle= 180°) and the distance between neighboring magenta balls on the axes is 1 R_M.

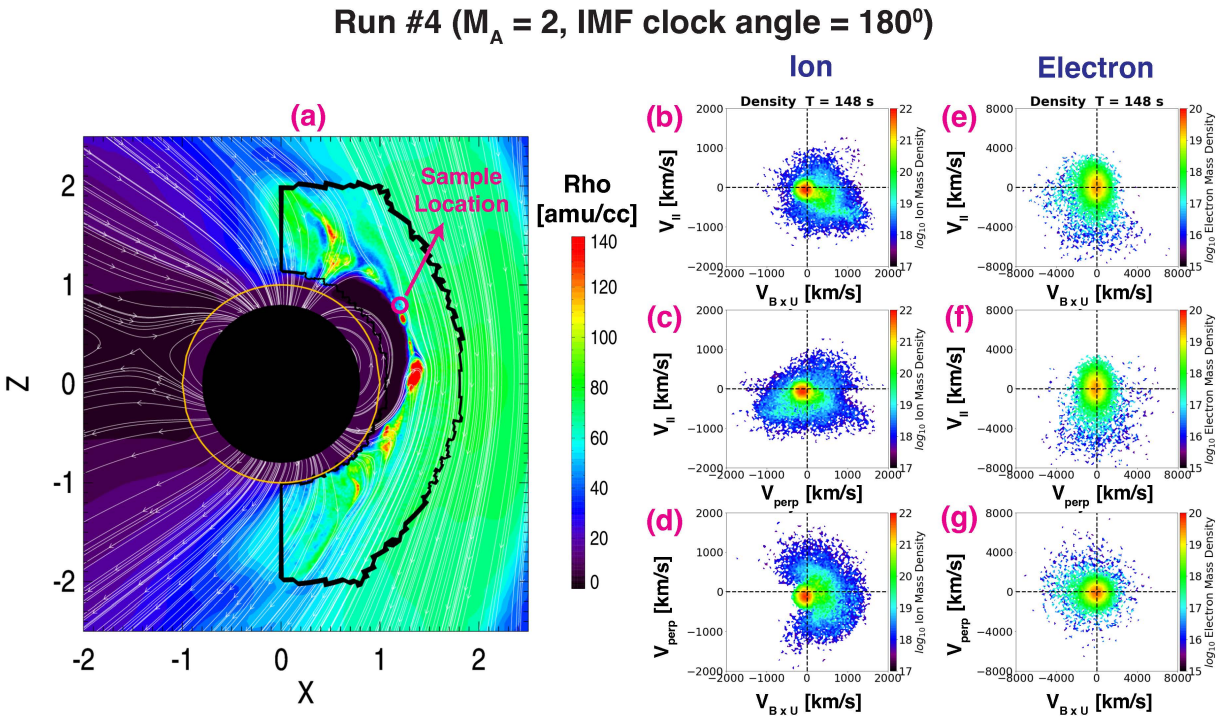

Figure 4-2: Ion and electron phase space distributions in logarithmic scale on the magnetosheath side of a reconnection site from Run #4 at T= 148 s. (a) Contours of plasma density in the XZ plane with sample magnetic field lines overplotted as white arrowed lines showing the global configuration of the simulated magnetosphere. The yellow circle with radius 1 R_M shows Mercury's surface and the black-filled disk with radius 0.8 R_M represents its conducting core. The black curve marks the boundary of the active PIC region. The magenta circle near the magnetopause boundary indicates the sampling location used to extract the ion and electron phase space distributions. Panels (b-d) and (e-g) show the phase space distributions for ions and electrons, respectively. The distributions are displayed in a field-aligned coordinate system with the parallel direction along the ambient magnetic field (**B**), one perpendicular direction along the direction of **B** × **U** (**U** is the plasma bulk flow velocity) and the other perpendicular direction completing the right-handed system. The unit of phase space density is amu*s^2/km^2.

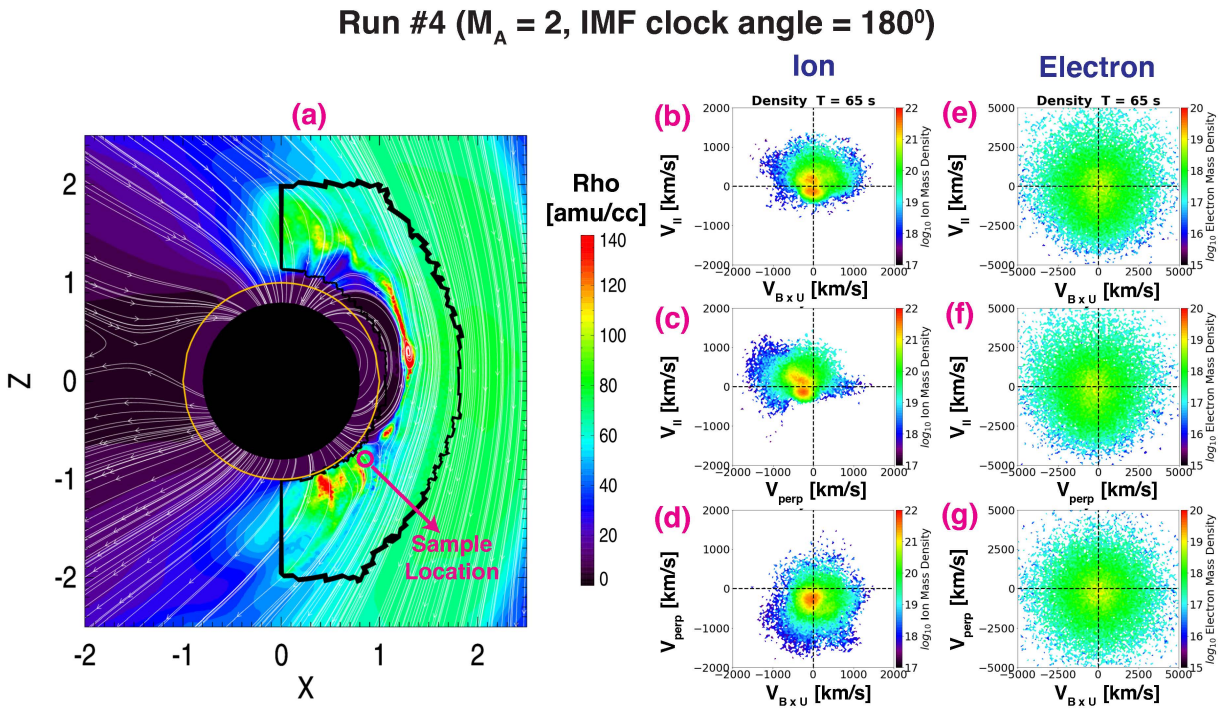

Figure 4-3: Same as Figure 4-2 but for a sampling location positioned in the southern cusp region at X= 0.85 R_M, Y= 0 R_M, Z= -0.8 R_M. The ion and electron distributions were extracted from Run #4 at T= 65s. Counter-streaming ion distribution associated with precipitating and mirrored particles in the cusp can be clearly seen in panels (b) and (c).

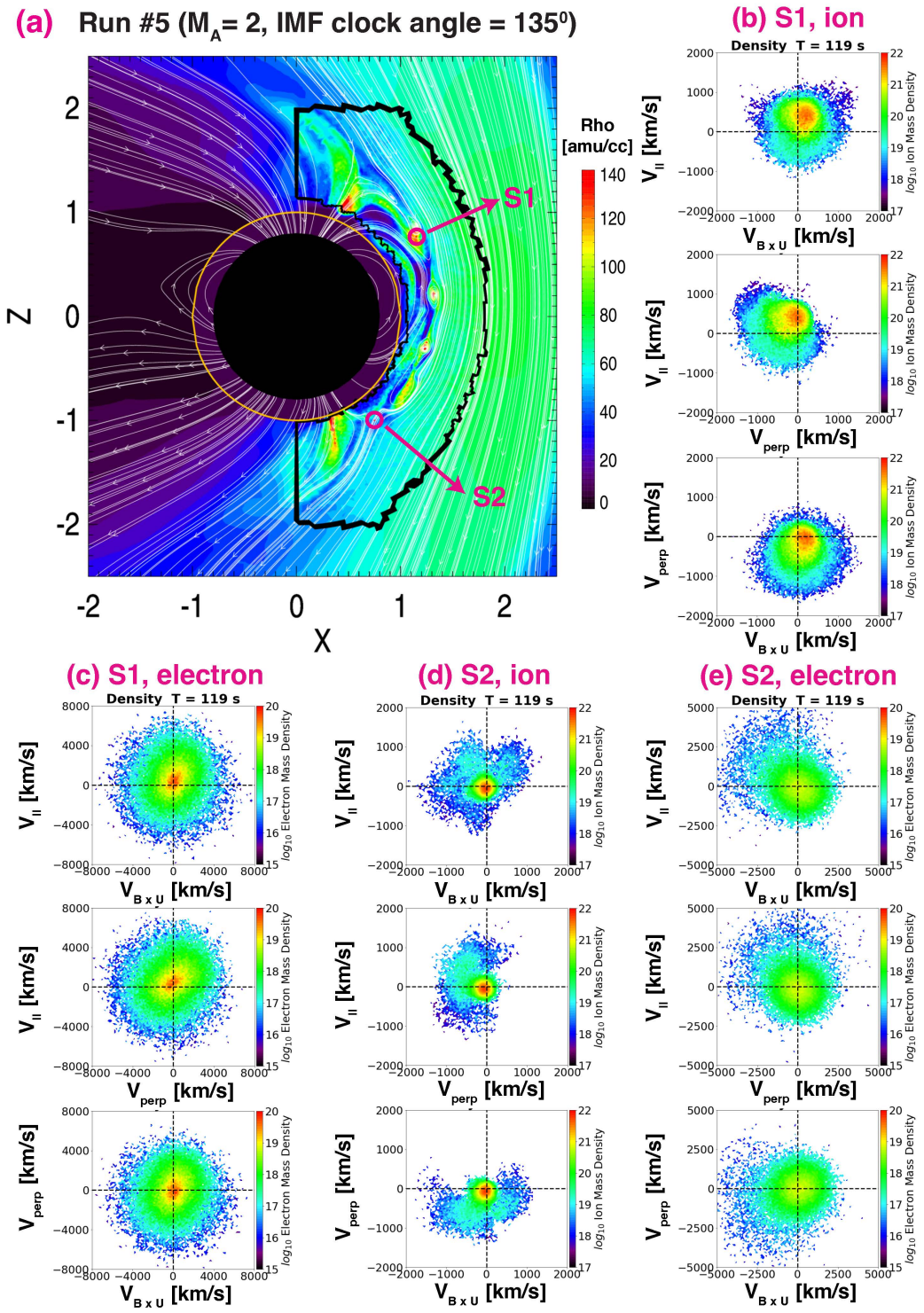

Figure 4-4: Phase-space distributions for ions and electrons extracted from Run #5 (M_A= 2, IMF clock angle= 135°) at T= 119 s. Panel (a) shows the global configuration of the simulated magnetosphere in the XZ plane. The red circles mark the locations of two virtual satellites placed in the simulation to sample distribution functions. Virtual satellite S1, at X = 1.15 R_M, Y = 0 R_M, Z = 0.77 R_M, is located within an FTE and satellite S2, at X = 0.75 R_M, Y = 0 R_M, Z = -1.0 R_M, lies in the southern cusp. Panels (b) and (c) show the ion and electron distributions extracted at S1, respectively, whereas panels (d) and (e) show the distributions extracted at S2.

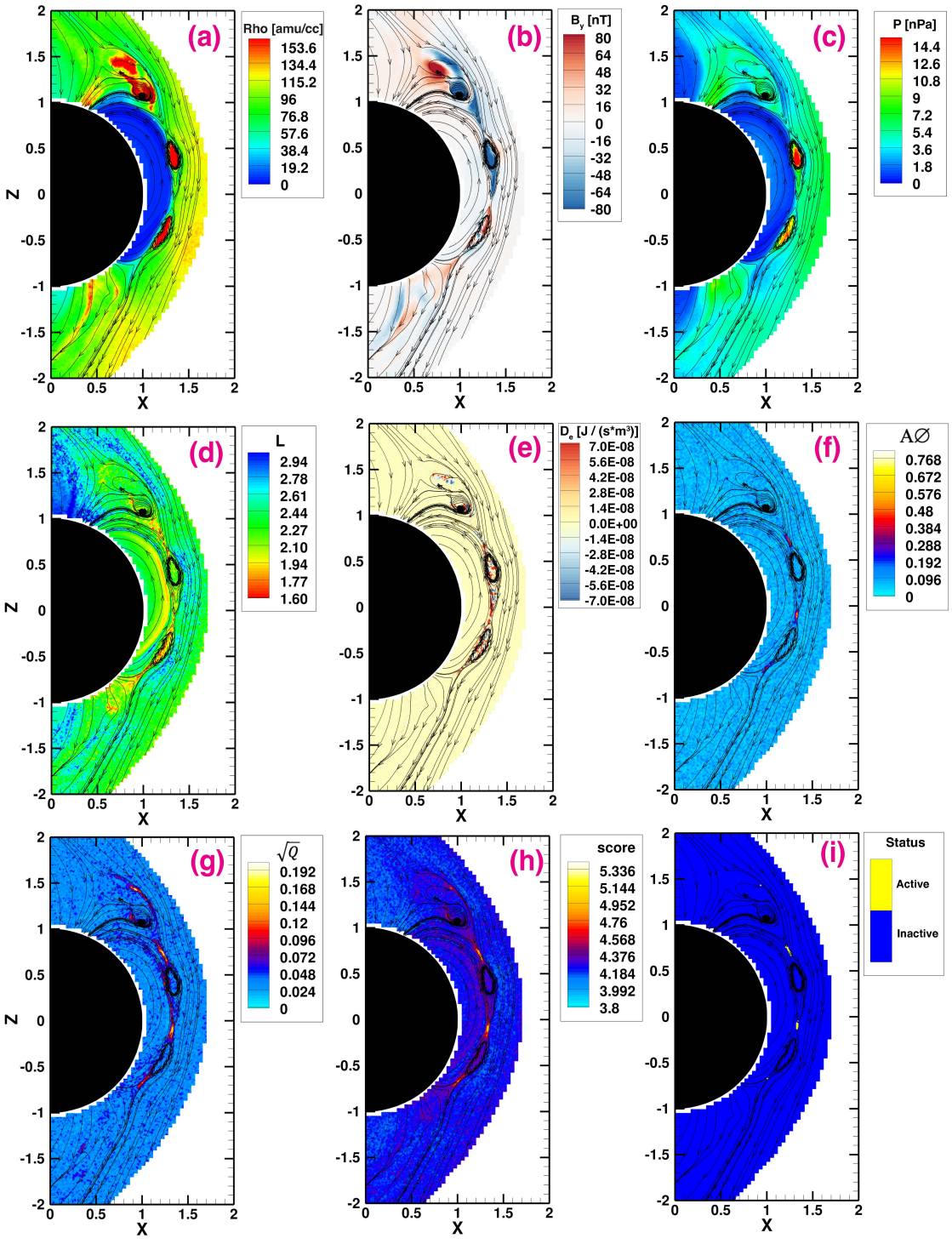

Figure 4-5: Snapshot of various quantities relevant to reconnection in the meridional cut (Y = 0) through the PIC domain taken from Run #1 (M_A = 6, IMF clock angle = 180°) at T = 102 s. Mercury is represented by the solid black disk. Sampled magnetic field lines are overplotted as black arrowed lines to delineate the magnetospheric configuration. The background colors in different panels are (a) Ion density, (b) B_y, (c) Ion pressure P, (d) Lorentz reconnection indicator L, (e) Electron dissipation measure D_e, (f) and (g) Nongyrotropy measures $A\varnothing$ and $\sqrt{Q}$, (h) Synthesized reconnection score S, (i) Status of active reconnection obtained by filtering the synthesized score.

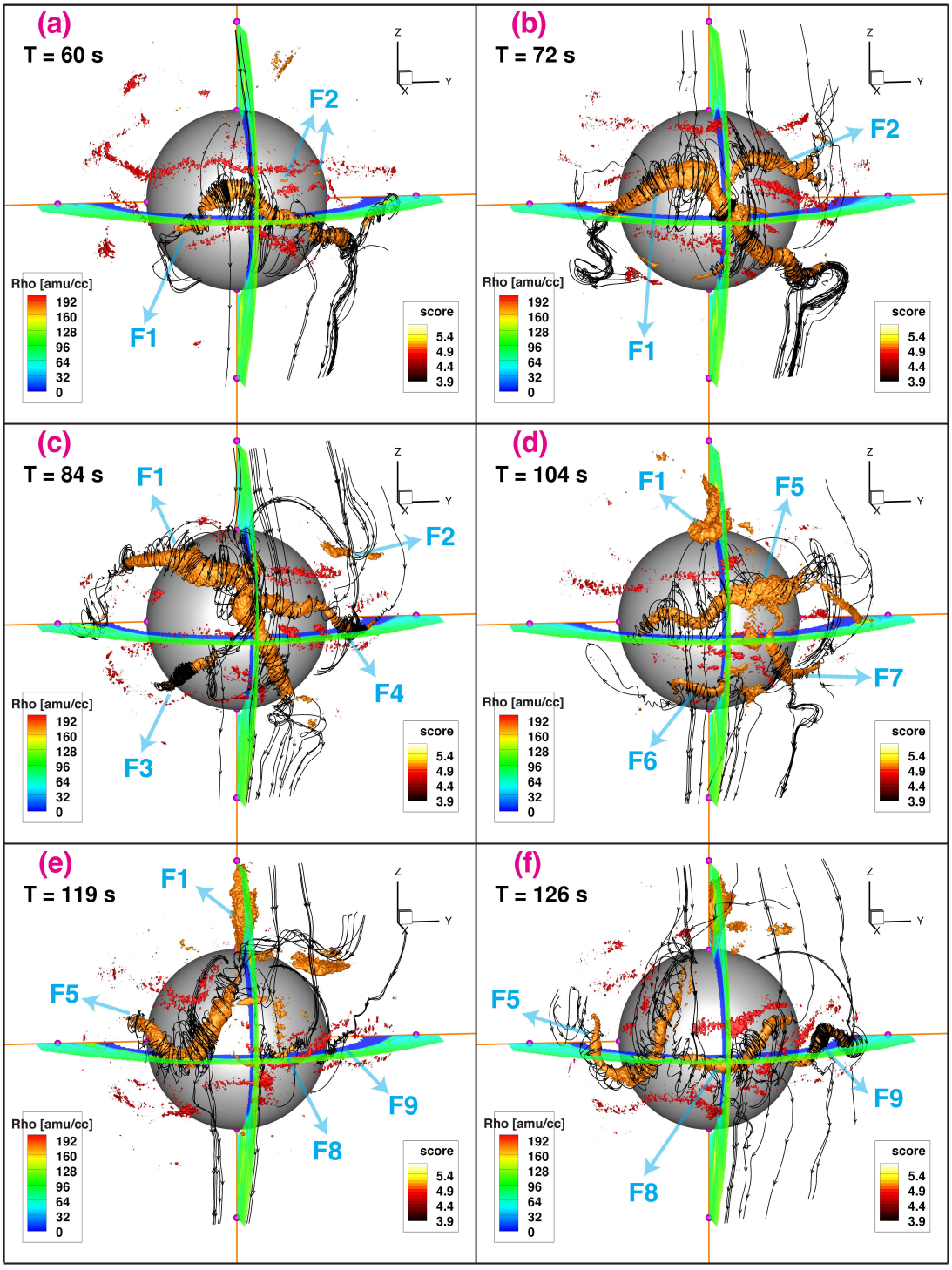

Figure 4-6: 3D geometry of FTEs and reconnection sites identified in the simulation as shown by multiple snapshots of ion density isosurfaces (orange surfaces corresponding to $\rho_i = 180\ amu/cc$) and synthesized reconnection score isosurfaces (red surfaces corresponding to $S = 4.9$). The results were extracted from Run #1 (M_A= 6, IMF clock angle= 180°). Sampled magnetic field lines are plotted as the black arrowed lines to show the geometry of the magnetic field. Color contours of ion density in both Y = 0 and Z = 0 cuts of the PIC region are overplotted to illustrate the spatial orientation and location. Labels and arrows are added to denote FTEs. Mercury is represented by the gray sphere in the center. The distance between neighboring magenta balls along the axes in each panel is 1 R_M.

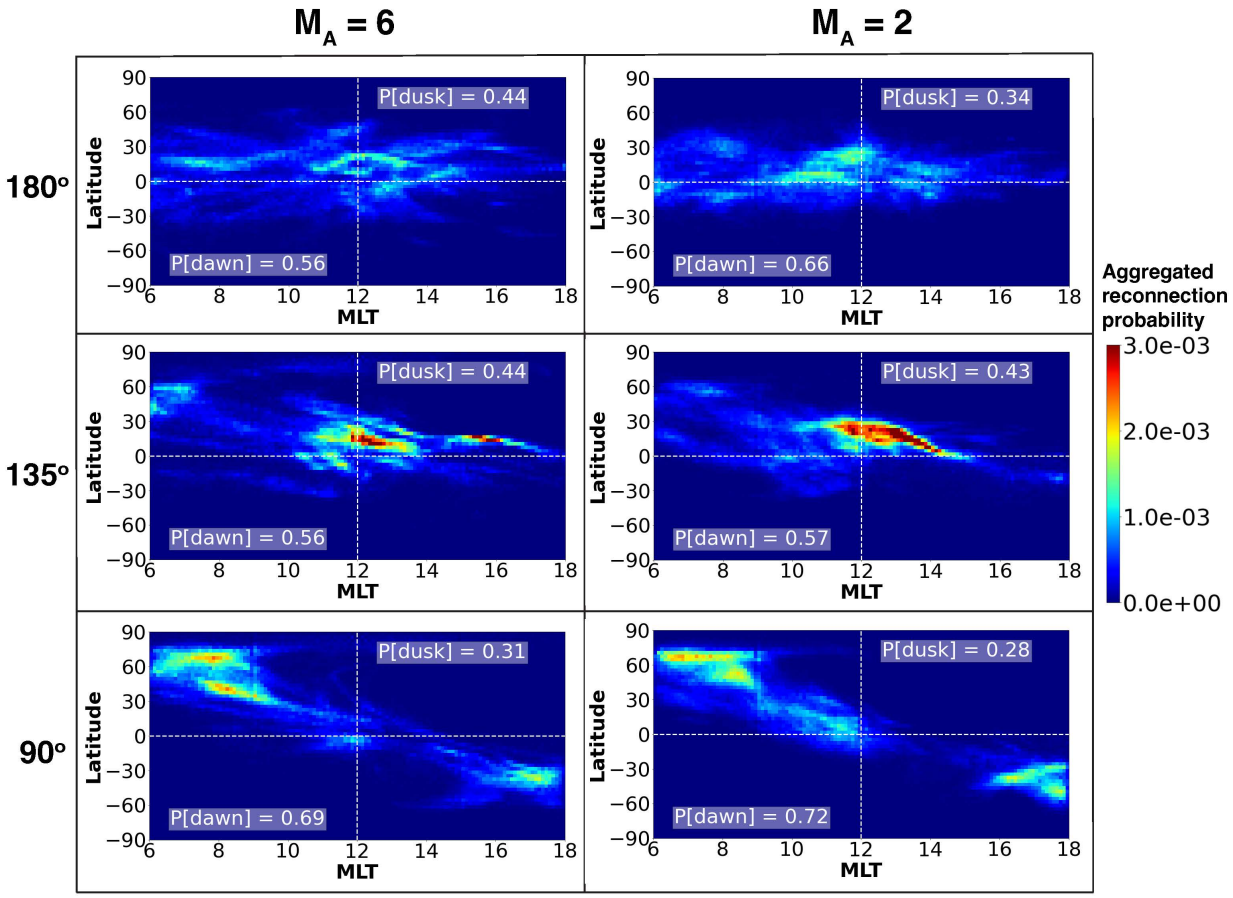

Figure 4-7: Aggregated dayside reconnection probability shown in 2D MLT-latitude coordinates for all six simulations. The method used for calculating the aggregated reconnection probability is described in detail in Section 3.3. The legends located in the bottom-left and top-right corners of each panel display the probabilities of reconnection occurring on the dawnside (MLT < 12) and duskside (MLT > 12), respectively.

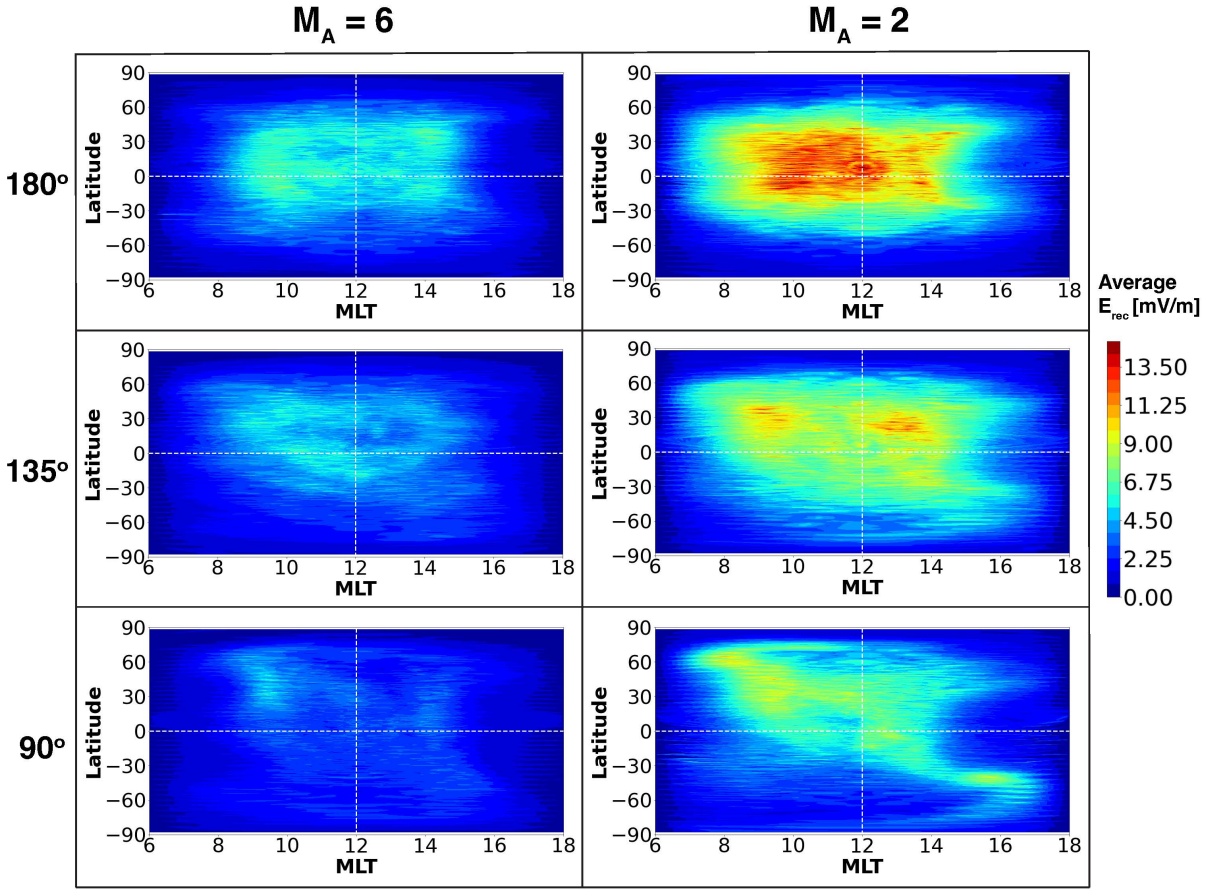

Figure 4-8: Time-averaged reconnection electric field E_{rec} shown in 2D MLT-latitude coordinates for all six simulations. E_{rec} is defined as the parallel component of the electric field in the electron's co-moving frame.

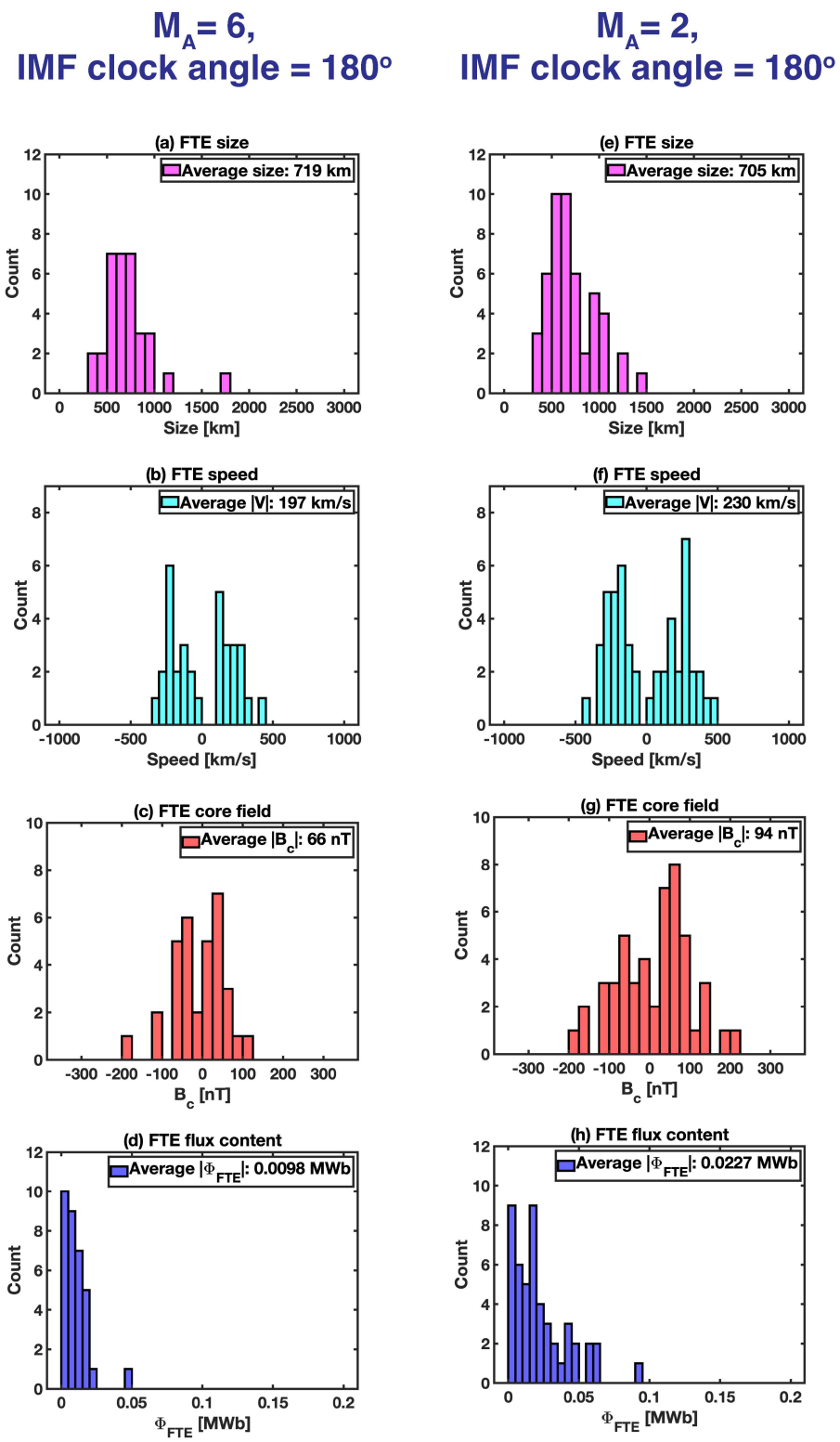

Figure 4-9: Histograms of FTE properties for the 180° IMF clock angle cases with different solar wind M_A. (a) and (e) Average FTE size. (b) and (f) Average FTE speed along the direction perpendicular to its axis. (c) and (g) Core field strength. (d) and (h) Magnetic flux carried by FTE. The left column corresponds to M_A= 6 and the right column is for M_A= 2.

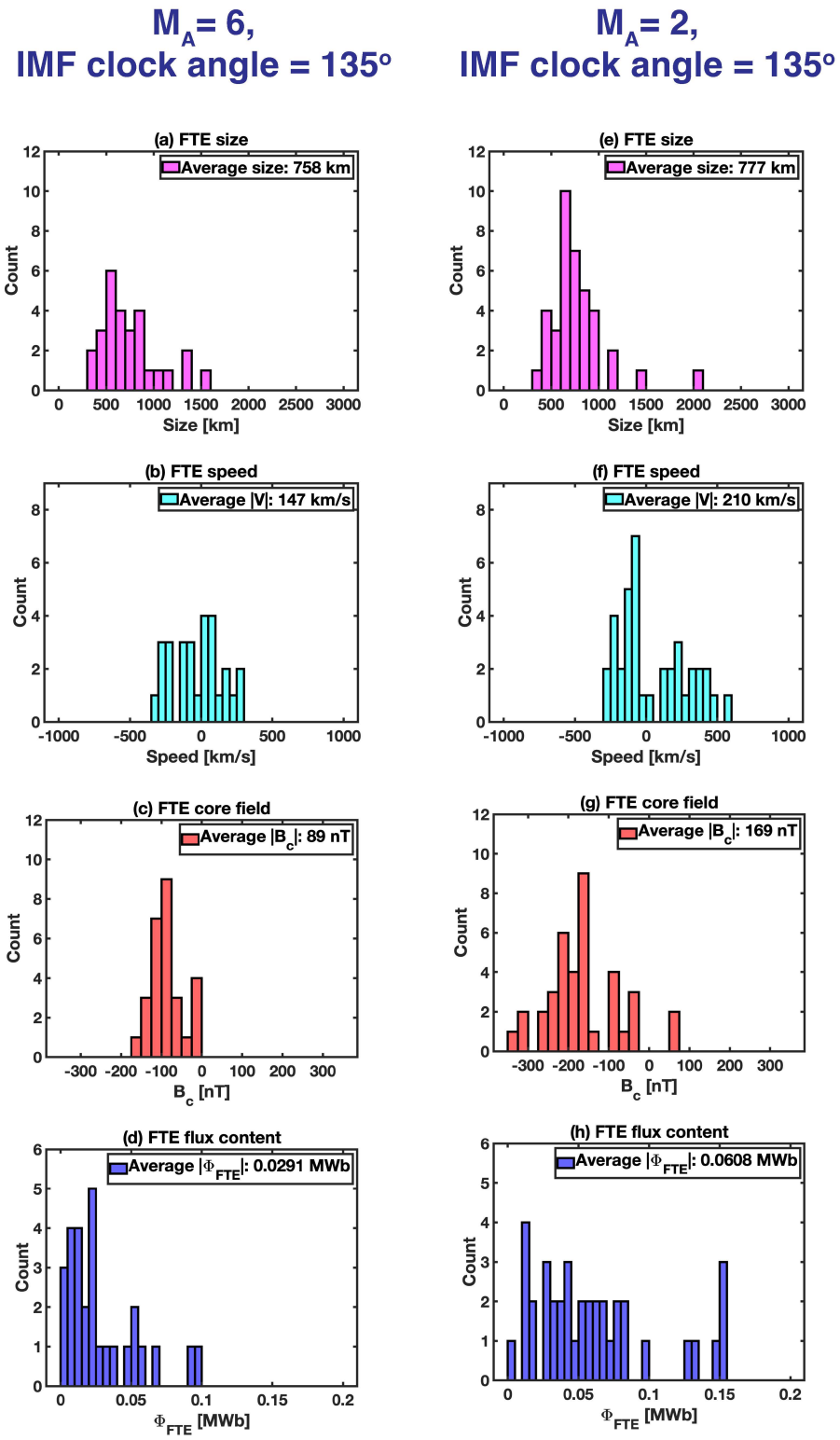

Figure 4-10: Histograms of FTE properties for the 135° IMF clock angle cases with different solar wind M_A. (a) and (e) Average FTE size. (b) and (f) Average FTE speed along the direction perpendicular to its axis. (c) and (g) Core field strength. (d) and (h) Magnetic flux carried by FTE. The left column corresponds to M_A= 6 and the right column is for M_A= 2.

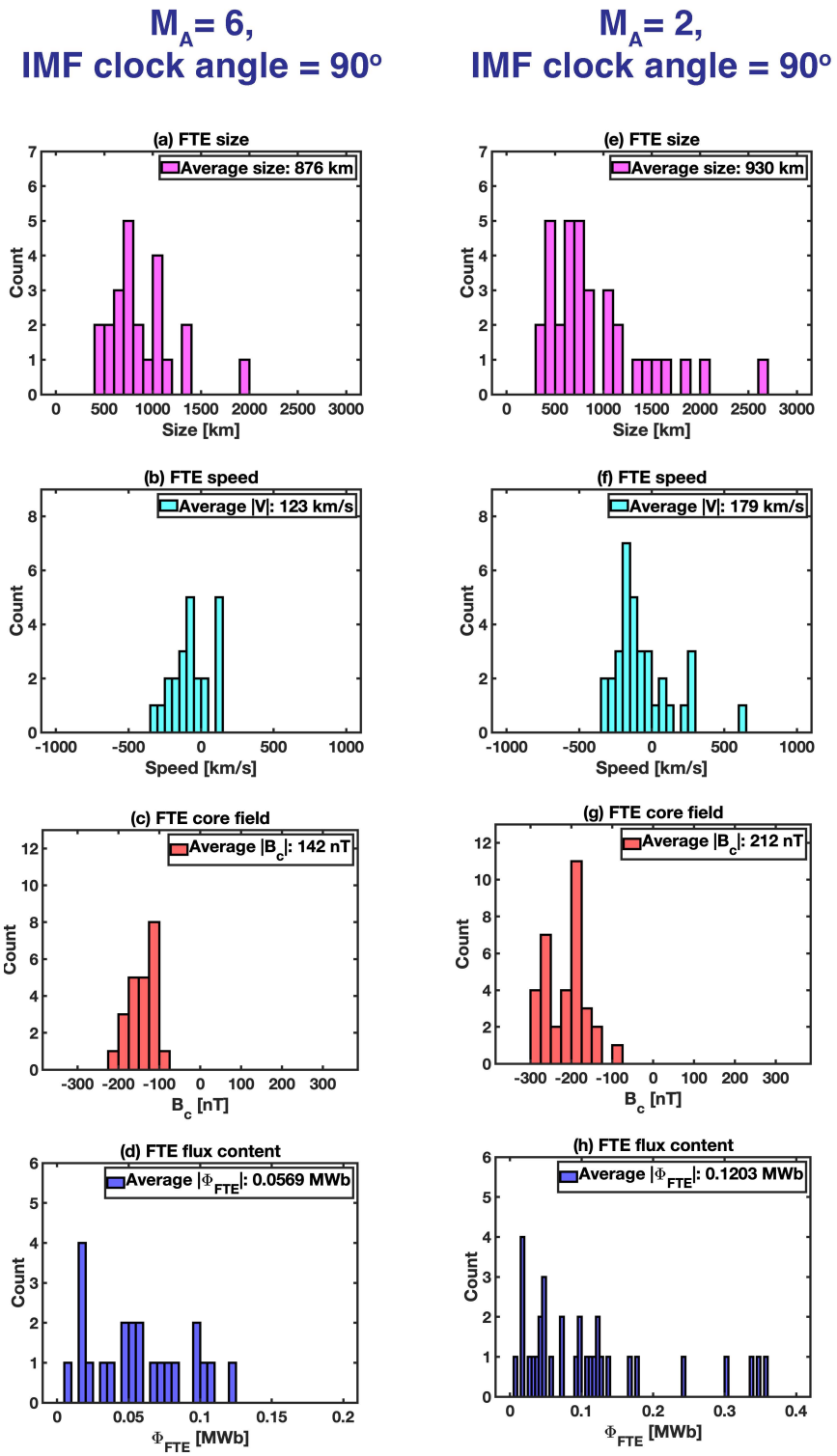

Figure 4-11: Same as Figure 4-9, but for 90° IMF clock angle cases.

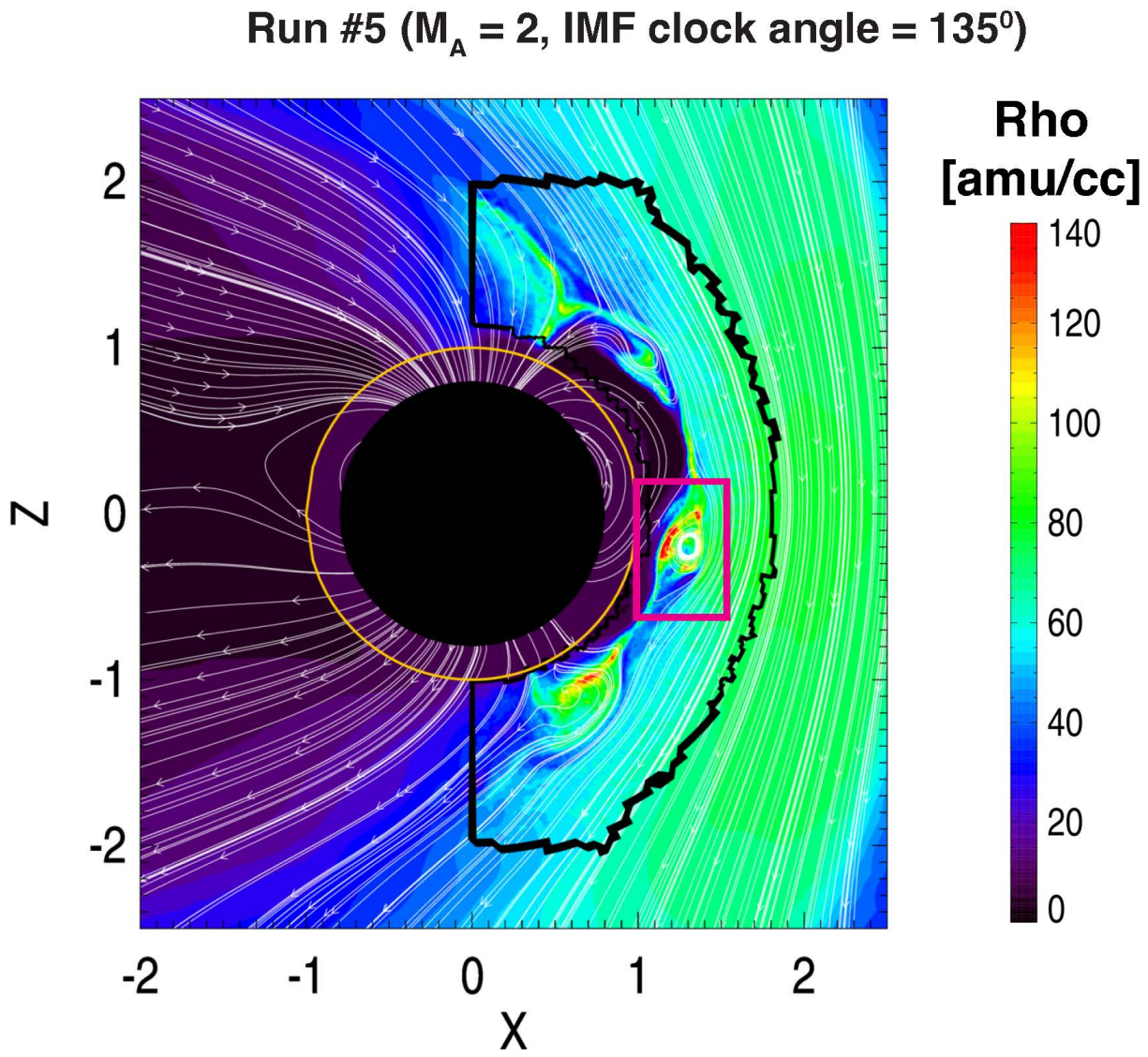

Figure 4-12: Snapshot of plasma density (ρ) contour in meridional plane with sample magnetic field lines overplotted as white arrowed lines. A large FTE associated with density enhancements, highlighted by the magenta box, is positioned slightly south to the equatorial plane at this particular time. The data shown in this figure is extracted at T = 185 s in Run #5.

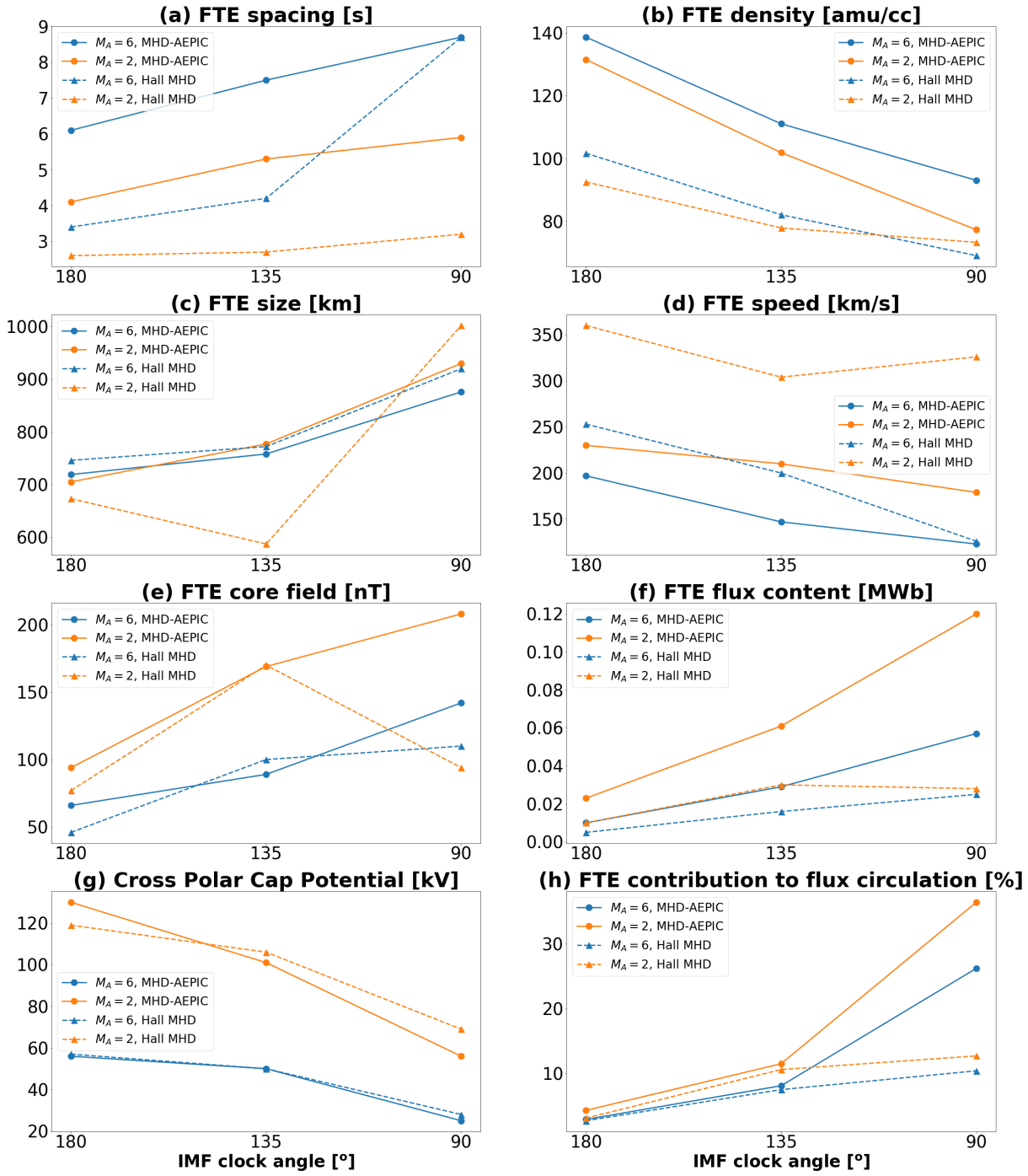

Figure 4-13: Comparison of various FTE properties and CPCP extracted from MHD-AEPIC and Hall-MHD simulations. The same set of upstream solar wind and IMF conditions were used as input to drive both models. The horizontal axis in each panel represents the IMF clock angles used in the simulations. The data points with the same M_A number are connected with solid and dashed lines for MHD-AEPIC and Hall-MHD simulations, respectively. The $M_A = 6$ simulations are represented by blue curves and the $M_A = 2$ simulations are indicated by orange curves. The quantities shown in panels (a) – (f) are FTE spacing, density, size, traveling speed, core field strength, magnetic flux content, CPCP, and FTEs' overall contribution to open flux generation, respectively.

Chapter 5 Cusp Filaments and Proton Precipitation in Mercury's Cusp Regions from 3D MHD-AEPIC Simulations

5.1 Introduction

Building on the preceding chapter that studies the kinetic signatures, asymmetries, and FTEs associated with Mercury's dayside magnetopause reconnection, in this chapter we further analyze the results of our global MHD-AEPIC simulations with emphasis on cusp filaments and proton precipitation in Mercury's cusp regions.

The impact of solar wind ions and electrons in Mercury's northern magnetospheric cusp has been considered to be an important source to the planet's tenuous exosphere (*Killen et al*., 2007; *Milillo et al*., 2005). The primary mechanism for the solar wind plasma to enter the cusp region is thought to be the reconnection process occurring at Mercury's dayside magnetopause. Following magnetopause reconnection, solar wind ions and electrons become energized and subsequently travel along the newly reconnected field lines towards the cusp region. Depending on their pitch angles, these particles can either precipitate onto the planetary surface or undergo reflection via magnetic mirroring. Notably, the surface sputtering process, resulting mainly from precipitating ions, is believed to act as a significant source to Mercury's exosphere (*Killen et al*., 2022). Hence, the investigation into ion precipitation onto the surface is of great importance in achieving a better understanding of the source process for the neutral exosphere at Mercury.

Initially identified by *Slavin et al*. (2014) in Mercury's northern cusp, cusp filaments are plasma structures characterized by discrete field decreases. Subsequent studies based on MESSENGER observations (e.g., *Poh et al*., 2016) revealed that these cusp filaments correspond

to cylindrical flux tubes and are associated with significant diamagnetic depression and enhanced plasma density aligned with the local magnetic field. *Poh et al*. (2016) demonstrated that cusp filaments likely extend down to Mercury's surface and the occurrence-rate-normalized integrated proton precipitation rate onto the surface from all filaments is approximately 2.7×10^{25} s^{-1}, comparable to the global precipitation rate observed by MESSENGER. These results suggest that cusp filaments have important implications for surface sputtering and space weathering within the cusp regions of Mercury.

In this chapter, we continue to analyze the MHD-AEPIC simulations described in Chapter 4 by examining the signatures of cusp filaments and particle energization associated with Mercury's magnetopause reconnection. The layout of this chapter is as follows: Section 5.2.1 presents our simulation results on cusp filaments and their relationship with FTEs, particle energization associated with FTEs, and the similarities and differences between filaments in the northern and southern cusps. The modeled proton precipitation flux, precipitation rate, and their dependences on upstream solar wind conditions are presented in Section 5.2.2. Section 5.3 discusses our simulated precipitation flux and its comparisons with observations made by MESSENGER. Finally, Section 5.4 provides a summary and conclusions.

5.2 Results and Analysis

5.2.1 Cusp Filaments Associated with FTEs

In this section, we first present the main characteristics of cusp filaments as simulated by the PIC model and examine the relationship between FTEs and these filaments. Figure 5-1 and Figure 5-2 show two examples of simulated cusp filaments at t = 173 s and t = 190 s in MHD-AEPIC Run #1 (M_A = 6, IMF clock angle = 180°) and the corresponding particle phase space distributions. The sampling region used for extracting the ion and electron velocity distributions

is a 3D sphere centered at X = 0.45 R_M, Y = 0 R_M, Z = 1.25 R_M with a radius of 0.05 R_M. As shown in panel (a) of both Figure 5-1 and Figure 5-2, near the sampling location, the plasma exhibits enhanced densities along the ambient magnetic field lines and forms filamentary structures with one end connected to Mercury's surface and the other to the solar wind. Within these cusp filaments, the ion distribution exhibits a significant population of precipitating particles as indicated by the positive $V_{//}$ in panel (b) of both Figure 5-1 and Figure 5-2. In contrast, the electron distribution is roughly isotropic with no discernible enhancements in the parallel direction toward the surface, as depicted in panel (e) of Figure 5-1 and Figure 5-2.

The ion energy spectrum, pitch angle distribution, total magnetic field strength, plasma density, and pressure in the sampling region from t = 0 s to t = 200 s are displayed in panels (a) - (d) of Figure 5-3. The white curve in panel (a) of Figure 5-3 represents the time series of the total proton precipitation rate (fluence) in unit of s^{-1} measured in the northern cusp. The approach we used to calculate the proton precipitation rate will be discussed in detail in Section 5.2.2. As shown in Figure 5-3a, the peaks in the time series of proton precipitation rate tend to coincide with increases in the energetic ion counts. The ions exhibit notable precipitating behavior as evidenced in Figure 5-3b where more particles are found in the bottom half (pitch angle < 90°) of the pitch angle distribution. The magnetic field strength, plasma density and pressure are observed to show significant temporal variations inside the sampling region as shown in panels (c) and (d) of Figure 5-3. A zoomed-in view of Figure 5-3 from t = 165 s to t = 200 s is provided in Figure 5-4. At both t = 173 s and t = 190 s, we observe a significant reduction (> 20%) in the total magnetic field strength within the sampling sphere in comparison to its baseline value of approximately 200 nT. This observation is in line with the reported average 22% reduction of the magnetic field intensity inside a filament from the MESSENGER observational analysis (*Poh et al*., 2016). In contrast, the

plasma density and pressure both exhibit significant enhancements at t = 173 s and t = 190 s, consistent with the findings reached in *Poh et al*. (2016) that cusp filaments are diamagnetic in nature due to the increased population of hot plasma ions. Figure 5-4a and Figure 5-4b show that the ion (proton) northern cusp precipitation rates at t = 173 s and t = 190 s correspond to two local peaks and are associated with (1) enhancement of energetic ions at around 0.6 keV, and (2) a shift of ion pitch angle distribution toward the direction parallel to the local magnetic field, i.e., inward towards Mercury in the northern cusp. These results are in excellent agreement with the observational work of *Poh et al*. (2016), who observed an increase in ion counts in the energy range of ~ 0.4 - 1 keV and the pitch angle range of ~ 0 - 90° during cusp filament events.

Slavin et al. (2014) first hypothesized that the filaments were caused by the FTE-associated injections of magnetosheath plasma. However, establishing a clear correlation between FTEs and cusp filaments through in-situ MESSENGER observations proves challenging due to insufficient time resolution and lack of direct observations of FTEs at mid- to high-latitudes (*Slavin et al*., 2014; *Poh et al*., 2016). Unlike in-situ observations, our MHD-AEPIC simulations can provide a global context of Mercury's magnetosphere that allows us to obtain a better understanding of the relationship between FTEs and cusp filaments by tracking their temporal evolutions near the cusp region. Figure 5-5 presents a series of snapshots of plasma density contours in the Y = 0 plane (noon-midnight meridian) leading up to the occurrence of the cusp filament event at t = 190 s. The temporal spacing between neighboring frames is 3 seconds. During this selected time interval, three FTEs are present on the dayside magnetopause. One of these FTEs, labeled as F1 in Figure 5-5, shows a direct connection with the cusp filament at t = 190 s. Zoomed-in views of F1 before it enters the northern cusp are provided in the insets of the top two panels in Figure 5-5. Initially, the apparent length of F1 in the radial direction exhibits a noticeable reduction at t = 184 s in

comparison to that at t = 181 s. Next, at t = 187 s when F1 has already entered the cusp region, it no longer shows signatures of rope-like structure. Additionally, the plasma ions carried by F1 become concentrated along the magnetic field lines forming field-aligned bands of enhanced plasma densities. Finally, at t = 190 s, F1 has completely transformed into several filamentary structures characterized by significant diamagnetic depression and enhanced plasma density and pressure. The temporal evolutions of F1 and the associated filamentary field-aligned density structures, as simulated by our MHD-AEPIC model, support the hypothesis proposed by *Slavin et al*. (2014) that the cusp filaments map to FTEs at the dayside magnetopause. It is also worth noting that the cusp filaments were not observed in our pure Hall-MHD simulations. Given the comparable grid resolutions of the MHDA-EPIC and Hall-MHD simulations near the magnetopause boundary, this result implies that the cusp filaments are likely caused by kinetic effects, which are absent in the Hall-MHD model.

After having presented evidence showing that the cusp filaments are high-latitude extensions of FTEs, we proceed to examine the effects of those FTEs on particle energization by analyzing the properties of those energetic particles transported into the cusp filaments. Figure 5-6 presents the energy spectrum and pitch angle distributions for both ions and electrons at t = 181 s and 190 s within the sampling region shown in Figure 5-5. As depicted in Figure 5-5, t = 181 s corresponds to a relatively quiet state of the northern cusp, where the plasma density stays approximately at its baseline level, while t = 190 s marks the occurrence of a cusp filament event associated with the FTE labeled as F1. Figure 5-6c and Figure 5-6g show the energy spectrum at t = 181 s and 190 s for both the ions and electrons. At the time when the simulated filament passed by the sampling location, both the ion and electron spectrum exhibits signatures of energization. Specifically, the ion populations exhibit a decrease in counts in the energy range below 0.3 keV

and a noticeable increase in the range between 0.3 - 3 keV, relative to their values at t = 181 s. Notably, the energy at which the ion count shows the peak enhancement is about 1 keV, which is consistent with the results reported by *Slavin et al*. (2014) based on measurements obtained from MESSENGER's Fast Imaging Plasma Spectrometer (FIPS). In contrast, the electron populations reduce in count rate slightly in the energy range below 70 eV and increase significantly above 70 eV. The ion and electron pitch angle distributions at t = 181 s and 190 s are shown in Figure 5-6d and Figure 5-6h. For both ions and electrons, the pitch angle distributions at t = 181 s are approximately symmetric around 90°, while the distributions at t = 190 s are asymmetric with a larger particle count in the pitch angle range between 0 - 90°, although the degree of asymmetry is somewhat weaker for electrons than for ions. Furthermore, as discussed for Figure 5-2b, the enhancement in precipitating ions (pitch angle < 90°) within the cusp filament at t = 190 s corresponds to the increased population of energetic ions in the energy range of 0.3 - 3 keV. Such a correspondence suggests that the enhancement of proton precipitation rate at t = 190 s is related to the dayside magnetopause reconnection, which results in FTEs and accelerates charged particles along the field-aligned direction.

Finally, we present a comparison between the filaments seen within the northern and southern cusps, as simulated by the PIC model. Shown in Figure 5-7 are two snapshots displaying the plasma density contours and particle velocity distributions at different timesteps in Run #4 (M_A = 2, IMF clock angle = 180°). The sampling sphere is placed in the southern cusp, with its center positioned at X = 0.85 R_M, Y = 0 R_M, Z = -0.8 R_M. Panels (a) - (g) correspond to t = 105 s, at which time an incoming FTE is approaching the southern cusp, while panels (h) - (n) represent t = 108 s when the FTE has evolved into a cusp filament situated at the same location as the sampling sphere. Figure 5-8 shows the energy spectrum and pitch angle distributions for both ions and electrons at

t = 105 s and 108 s within the sampling sphere in the southern cusp. As shown in panel (a) of Figure 5-8, the proton precipitation rate in the southern cusp reaches its local peak value around the same time as the occurrence of the cusp filament event at t = 108 s. Such concurrence is very similar to that seen in the northern cusp as discussed previously, suggesting that a significant fraction of the ions within the filament move along the magnetic field lines, as depicted in Figure 5-7i and Figure 5-8d, due to the acceleration by dayside magnetopause reconnection. At t = 108 s, noticeable changes in the ion population are observed in comparison to that at t = 105 s. Specifically, the ion counts exhibit minor decreases in the energy range < 0.3 keV but notable increases in the range > 0.3 keV. The maximum enhancement in ion counts occurs at around 1 keV, very similar to the result obtained for the northern cusp. In contrast, the electron counts at t = 108 s experience increases across almost the entire range of sampled energy levels (3 eV - 3 keV), which is different from the result observed in the northern cusp. Panels (d) and (h) of Figure 5-8 show that the number of ions and electrons that travel towards the surface increase significantly at t = 108 s when the filament passes by the sampling location. Such enhanced precipitations of both ions and electrons are also found inside the filament within the northern cusp. Furthermore, it is observed that the pitch angle distributions of both ions and electrons within the filament located in the southern cusp are more symmetric around 90°, compared to those in the northern cusp. Such a difference in the shape of the pitch angle distribution during filament events is due in part to the difference in altitude between the sampling locations in southern cusp and northern cusp.

5.2.2 Proton Precipitation in Mercury's Cusp Regions

In this section, we first utilize the simulation outputs from the PIC model to calculate the flux of proton precipitation onto the dayside surface of Mercury. Subsequently, the results from

this calculation are used to evaluate the global spatial distribution of precipitation flux, quantify the total precipitation rate integrated over the whole cusp region, and study the impact of upstream solar wind and IMF conditions on proton precipitation.

The dayside proton precipitation flux in this work is defined as nV_R, where n represents the ion number density, and V_R corresponds to the radial component of the ion bulk velocity. The proton precipitation flux distribution is extracted from a hemispherical surface situated slightly above Mercury's dayside surface. In order to minimize the distance between the sampling hemispherical surface and the inner boundary of active PIC region, thereby ensuring that the ion number density and velocity are modeled by the PIC code, slightly different hemispherical surfaces are employed for the $M_A = 6$ simulations and the $M_A = 2$ simulations. Specifically, for the $M_A = 6$ simulations, the hemispherical surface used for extracting the proton precipitation flux is centered at the origin with a radius of 1.05 R_M, while in the case of $M_A = 2$ simulations, the hemispherical surface is centered at X = 0, Y = 0, Z = 0.05 R_M with a radius of 1.1 R_M.

Figure 5-9 shows the distributions of time-averaged proton flux, extracted from the sampling surfaces, in a 2D MLT-latitude plane for all six MHD-AEPIC simulations. The first 20 s of the simulation, which represent the transition period from steady-state Hall-MHD simulation to time-accurate MHD-AEPIC, has been excluded from the calculation of average proton flux. The positive fluxes (red colors) correspond to precipitating protons, whereas negative fluxes (blue colors) represent protons leaving Mercury's surface into the simulation domain. As presented in Figure 5-9, the distribution of proton precipitation is primarily concentrated within two high-latitude bands in the northern and southern hemispheres, corresponding to the respective cusp regions. While the peak precipitation fluxes in these northern bands and southern bands are comparable, the southern band exhibits a broader and more diffusive spatial distribution, consistent

with the observed weaker surface magnetic field in the southern cusp based on the MESSENGER data (e.g., *Winslow et al*., 2014). The peak precipitation flux ranges from 0.4×10^9 cm^{-2} s^{-1} to 1.2×10^9 cm^{-2} s^{-1} across all six simulations, which is comparable to the previous estimation of 0.5 - 1.0×10^9 $cm^{-2}s^{-1}$ from hybrid simulations (*Fatemi et al*., 2018, 2020). To quantitatively assess the dawn-dusk asymmetry in the overall proton precipitation, we have calculated the time-averaged total cusp precipitation rate, defined as the average number of protons impacting the dayside surface of Mercury per second, and subsequently determined the percentages of proton precipitation occurring on the dawnside and duskside, respectively. The results are displayed in a pair of legends in each panel of Figure 5-9 for all six simulations. We observed that in simulations with IMF clock angles of 135° and 90°, the number of precipitating protons on the dawnside is notably larger than that on the duskside, which is consistent with the expectation that if magnetopause reconnection occurrence shows the kind of dawn-dusk asymmetries as we found in the MHD-AEPIC simulation, then that should result in asymmetric distribution of proton precipitation in the dawn-dusk direction. In particular, Run #3 (M_A = 6, IMF clock angle = 90°) exhibits the most significant dawn-dusk asymmetry of proton precipitation, where 75.4% of precipitating protons are located on the dawnside. In contrast, for 180° IMF clock angle cases, about 45.6% - 48.2% of the proton precipitation occurs on the dawnside, slightly smaller than the corresponding figures on the duskside.

Figure 5-10 shows the temporal evolution of the global cusp precipitation rate in panel (a) and a scattered plot of its time-averaged value (excluding the initial 20 s transition period) in panel (b) for all six MHD-AEPIC simulations. In Figure 5-10a, each of the six curves representing the temporal evolution of the global precipitation rate displays an increasing trend within the first 20 s, corresponding to the transition from steady-state to time-accurate mode. Following this initial

period, the global precipitation rate demonstrates oscillatory behavior around its mean value in all six simulations. Notably, the amplitude of these oscillations is larger in simulations with $M_A = 2$, as compared to those with $M_A = 6$, suggesting that solar wind with smaller M_A (and effectively stronger IMF strength) may lead to increased dayside magnetopause reconnection rate with stronger temporal variations. As illustrated in Figure 5-10b, the time-averaged global precipitation rate ranges from 0.7×10^{25} s^{-1} to 2.5×10^{25} s^{-1}, aligning closely with the prior estimations derived from MESSENGER observations (*Slavin et al*., 2014; *Raines et al*., 2022). We observe that the average simulated precipitation rate exhibits an increasing trend with decreasing solar wind M_A number, likely due to the enhanced dayside magnetopause reconnection rate in $M_A = 2$ simulations. Additionally, in simulations with the same M_A number, the average precipitation rate is found to increase as the IMF clock angle decreases. As demonstrated in previous chapters, when IMF clock angle decreases from 180° to 90°, the primary dayside magnetopause reconnection sites are expected to shift towards the two cusp regions. Given that the proton velocity distribution is more aligned with the ambient magnetic field direction closer to the reconnection sites, the observed correlation between precipitation rate and IMF clock angle is thus consistent with the changes in the locations of the primary reconnection sites. Lastly, we note that the dependences of simulated precipitation rate on the upstream solar wind M_A and IMF clock angle are in good agreement with the findings recently reported in a study of 2760 MESSENGER cusp crossings (*Raines et al*., 2022).

5.3 Discussion

In Section 5.2.2, we have presented the simulation results on the spatial distribution of proton precipitation flux and the integrated precipitation rate, and also analyzed their dependences

on solar wind M_A and IMF clock angle. Given that magnetopause reconnection at Mercury occurs in a non-steady fashion, as shown in previous chapter, particle precipitation onto Mercury's surface also undergoes temporal variations even under fixed upstream conditions. Here, we discuss the distribution of the mean and peak proton precipitation flux within the two cusp regions under various upstream solar wind conditions, which are shown as histograms in Figure 5-11 for all six MHD-AEPIC simulations. As depicted in Figure 5-11a, the mean precipitation flux in the northern magnetospheric cusp ranges from 4.4×10^7 $cm^{-2}s^{-1}$ to 3.1×10^8 $cm^{-2}s^{-1}$, with an average flux of ~ 1.2×10^8 $cm^{-2}s^{-1}$. The peak precipitation flux falls within the range of 3.3×10^8 $cm^{-2}s^{-1}$ to 3.8×10^9 $cm^{-2}s^{-1}$, with a mean of 1.4×10^9 $cm^{-2}s^{-1}$. Both the mean and peak fluxes are highly variable, each spanning approximately one order of magnitude. Furthermore, the whole distribution of the peak flux is shifted by almost an order of magnitude from the mean flux distribution, indicating that precipitation flux exhibits a strong spatial variation within the northern cusp (see Figure 5-9).

A previous statistical survey of proton precipitation flux based on MESSENGER observations within Mercury's northern cusp estimated that the peak flux ranges from 9.8×10^4 $cm^{-2}s^{-1}$ to 1.4×10^9 $cm^{-2}s^{-1}$, with an average of ~ 3.7×10^7 $cm^{-2}s^{-1}$ (*Raines et al*., 2022). The observed minimum and average values of the peak flux appear to be significantly lower than those seen in our MHD-AEPIC simulations. We suggest that the discrepancies between our model results and the MESSENGER observations may be attributed to a few factors. Firstly, the MESSENGER measurements of the precipitation flux were obtained as single-point observations along the path of the spacecraft through the cusp region, which may or may not be representative of the precipitation flux over the entire cusp, while our global simulations allow us to determine the precipitation flux within the entire northern cusp via the approach described in Section 5.2.2. The difference in spatial coverage naturally could result in the differences in the minimum and

average peak fluxes between our model results and the observations. Secondly, the IMF strength used in our $M_A = 2$ simulations, as discussed previously in Chapter 3, are stronger than those typically encountered by MESSENGER. As we showed in Chapter 3 and Chapter 4, the global reconnection rate at the magnetopause tends to increase with increasing IMF strength. Therefore, the increase in the maximum precipitation flux seen in our simulations (3.8×10^9 $cm^{-2}s^{-1}$), which used $M_A = 2$, compared to MESSENGER observations (1.4×10^9 $cm^{-2}s^{-1}$) at least results in part from the much stronger IMF assumed in our simulation.

In addition to the northern cusp results that can be directly compared with MESSENGER observations, we also present in Figure 5-11b predictions for the occurrence frequencies of mean and peak proton precipitation fluxes in the southern cusp, which was not accessible to MESSENGER because of its orbital geometry. The histograms of mean and peak precipitation fluxes in the southern cusp exhibit similar shapes as those found in the northern cusp, albeit with a two-fold increase in magnitude. This increase can be attributed to the significantly weaker surface magnetic field in Mercury's southern cusp due to the large northward offset of the planetary internal dipole, resulting in a considerably expanded proton loss cone (*Winslow et al*., 2014). The ratio between the precipitation flux within the southern cusp and the northern cusp in our simulations is also in line with the result reached by *Fatemi et al*. (2020) based on their hybrid simulations.

5.4 Summary and Conclusions

Following the analysis of the MHD-AEPIC simulation results on reconnection signatures and FTEs in Chapter 4, this chapter presents a detailed investigation of cusp filaments and proton precipitation in both the northern and southern cusps of Mercury, based on the results of six MHD-

AEPIC simulations driven by various solar wind and IMF conditions. The key findings from our analyses are summarized below.

The filamentary structures observed in our simulations are characterized by substantial decrease (> 20%) in the total magnetic field strength, enhancements in plasma density and pressure, and maximized fluxes of proton precipitation onto Mercury's surface. These distinct features associated with the filamentary structures present in our simulation correspond very well to the cusp filaments observed by MESSENGER spacecraft. By tracking the temporal evolutions of simulated FTEs and subsequent filaments, we find that the cusp filaments are indeed the high-latitude extensions of FTEs and the embedded density and pressure enhancements are due to the plasma injections resulting from dayside magnetopause reconnection. While the cusp filaments are commonly found in MHD-AEPIC simulations, they were absent in our pure Hall-MHD simulations, suggesting that the kinetic effects play an important role in the formation of cusp filaments.

Our analysis of ion and electron energy spectrums and pitch angle distributions sampled within the cusp regions indicates significant energization of the ions and electrons injected into the cusps by FTEs. Notably, the ion count rates in the northern cusp exhibit the most significant increase at energies around 1 keV, consistent with the findings from previous observational works (*Slavin et al*., 2014; *Poh et al*., 2016). The electron count rates in the northern cusp is found to increase notably above 70 eV. In the southern cusp, the ion count rates exhibit similar behavior to those observed in the northern cusp, whereas the electron count rates increase over a broad energy range (almost the entire range of sampled energy levels) during the filament events, in comparison to those in the northern cusp.

The proton precipitation fluxes are found to concentrate within high-latitude bands corresponding to the cusp regions in both hemispheres. While the peak precipitation fluxes in the northern and southern bands are comparable, the southern band exhibits a broader spatial distribution due to the weaker surface field. A dawn-dusk asymmetry in the proton precipitation rate is also observed, plausibly associated with the dawn-dusk asymmetry in the dayside reconnection occurrence discussed in Chapter 4. Specifically, the integrated precipitation rate on the dawnside is notably larger than that on the duskside in simulations with 135° and 90° IMF clock angles, while for 180° IMF clock angle cases, the precipitation rate on the dawnside is comparable to that on the duskside.

For all six MHD-AEPIC simulations, the time-averaged global precipitation rate ranges from 0.7×10^{25} s^{-1} to 2.5×10^{25} s^{-1}, in line with the estimates obtained from MESSENGER observations (*Slavin et al*., 2014; *Raines et al*., 2022). Furthermore, the simulated global precipitation rate is found to increases with decreasing solar wind Mach number and decreasing IMF clock angle, consistent with the findings reached in a previous observational study (*Raines et al*., 2022).

Our statistical analysis of the mean and peak proton precipitation fluxes, extracted at multiple timesteps from all six MHD-AEPIC simulations, reveals that the mean precipitation flux in the northern cusp ranges from 4.4×10^{7} $cm^{-2}s^{-1}$ to 3.1×10^{8} $cm^{-2}s^{-1}$, with an average value of 1.2×10^{8} $cm^{-2}s^{-1}$, while the peak precipitation flux falls within the range of 3.3×10^{8} $cm^{-2}s^{-1}$ to 3.8×10^{9} $cm^{-2}s^{-1}$, with a mean of 1.4×10^{9} $cm^{-2}s^{-1}$. An order-of-magnitude difference between the mean and peak fluxes indicates that the proton precipitation within Mercury's northern cusp is highly variable in space. Additionally, the mean and peak fluxes in the southern cusp are found to

be about two times larger than those in the northern cusp, as a result of the weaker surface field in Mercury's southern hemisphere due to the northward offset of the internal dipole.

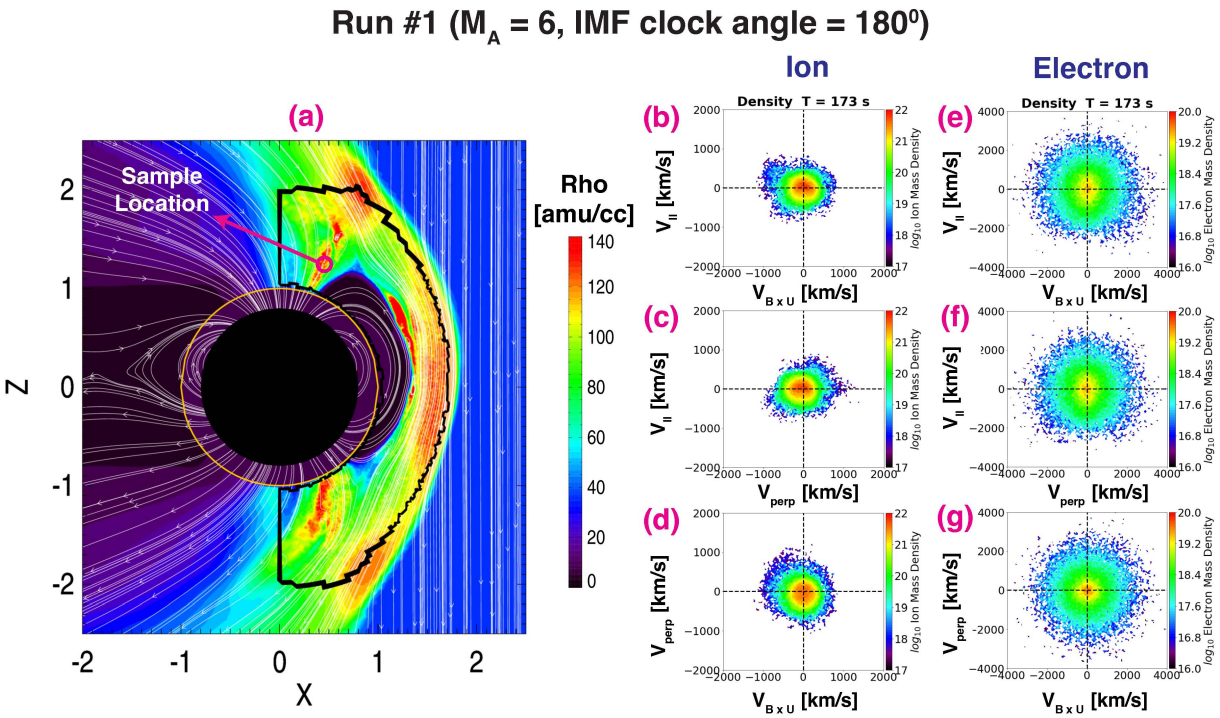

Figure 5-1: Ion and electron velocity distributions in log scale within a cusp filament structure from Run #1 at t = 173 s. The colored contours on the left show the plasma density ρ in Y = 0 plane with sample magnetic field lines overplotted as white arrowed lines. The center yellow circle with radius 1 R_M shows Mercury's surface and the black-filled disk with radius 0.8 R_M represents its conducting core. The black curve marks the boundary of the active PIC region. The magenta circle in the northern cusp indicates the sample location used to extract the ion and electron velocity distributions. The sample location is a sphere centered at X = 0.45 R_M, Y = 0 R_M, Z = 1.25 R_M with a radius of 0.05 R_M. Distributions of ion and electron in velocity space are displayed in a field-aligned coordinate system with one perpendicular direction parallel to B × U (U is the plasma bulk velocity) and the other perpendicular direction completes the right-handed system. The unit of velocity is km/s and the unit of phase space density is amu*s^2/km^2.

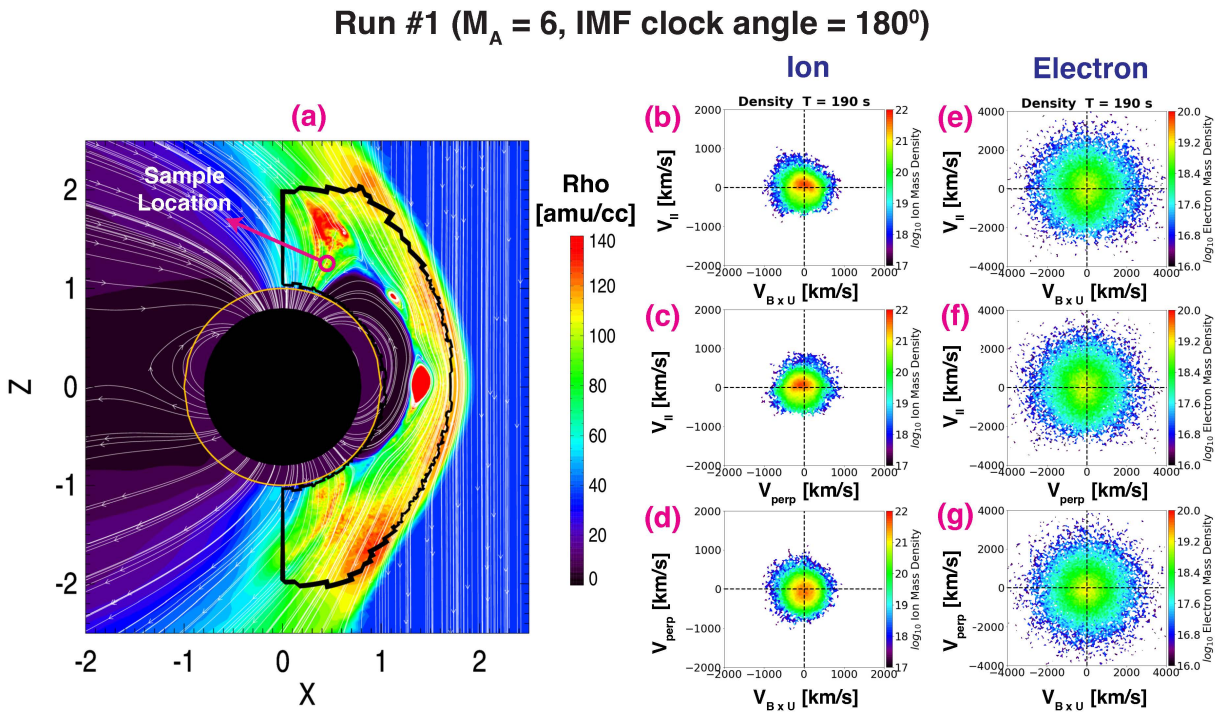

Figure 5-2: Same as Figure 5-1, but at t = 190 s from Run #1.

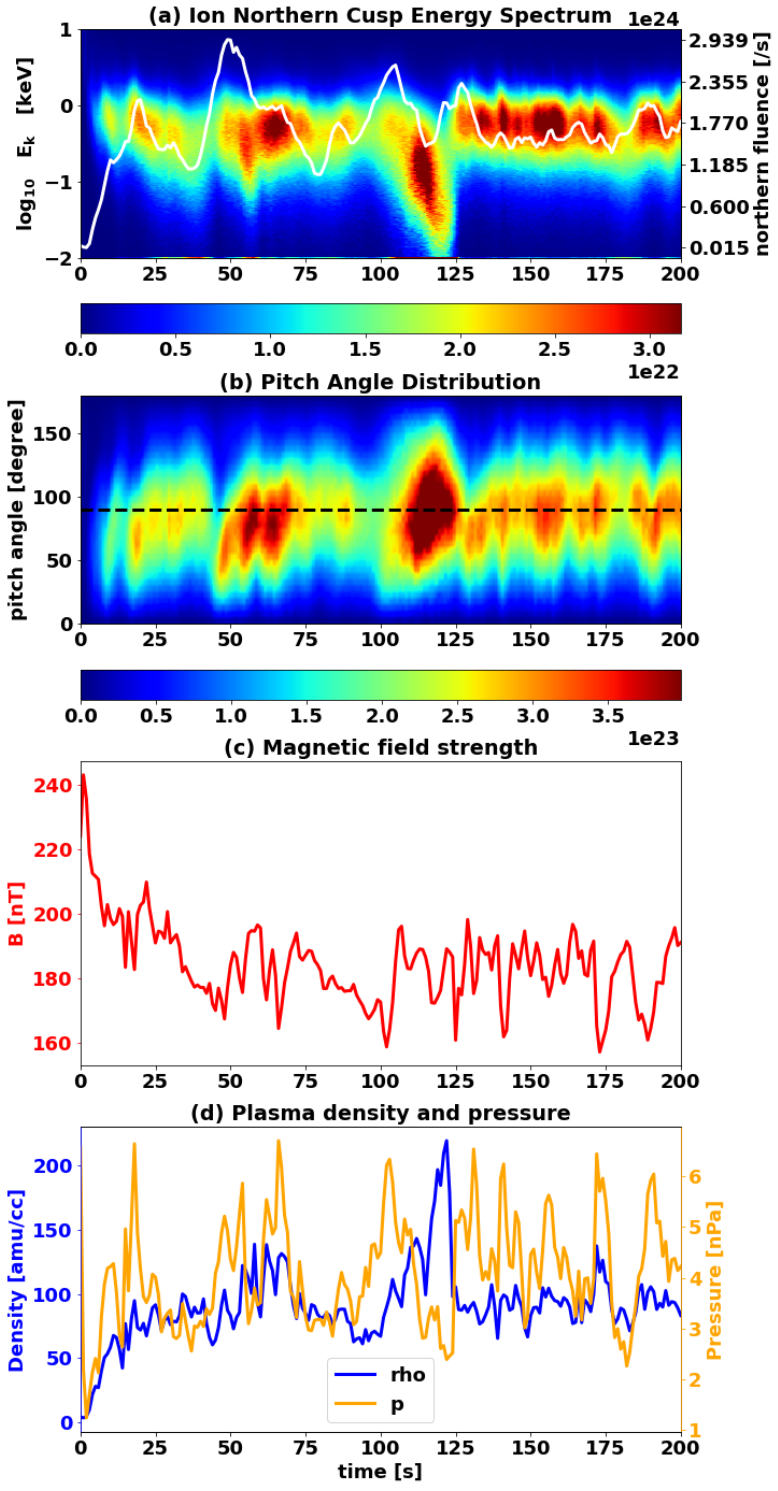

Figure 5-3: (a) Ion energy spectrum, (b) ion pitch angle distribution, (c) total magnetic field strength, and (d) plasma density and pressure from t = 0 s to t = 200 s within the sample location shown in Figure 5-1 and Figure 5-2. The colors in panel (a) and (b) represent the ion count in the sampling sphere binned by its kinetic energy and pitch angle, respectively. The white solid curve in panel (a) shows the time series of proton northern cusp precipitation rate (fluence).

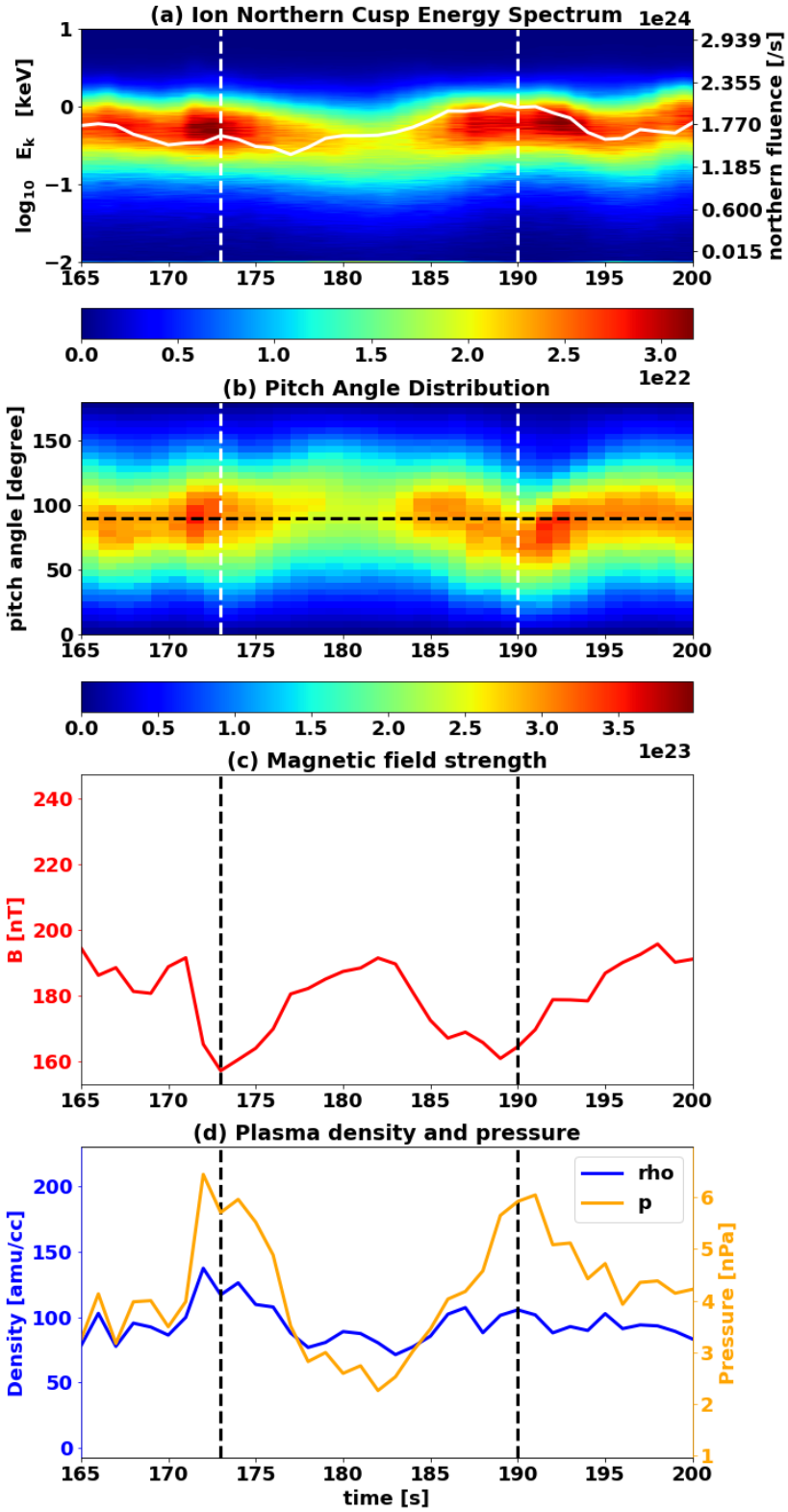

Figure 5-4: A zoomed-in view of Figure 5-3 from t = 165 s to t = 200 s. The two vertical white/black dashed lines in each panel correspond to t = 173 s and t = 190 s, respectively.

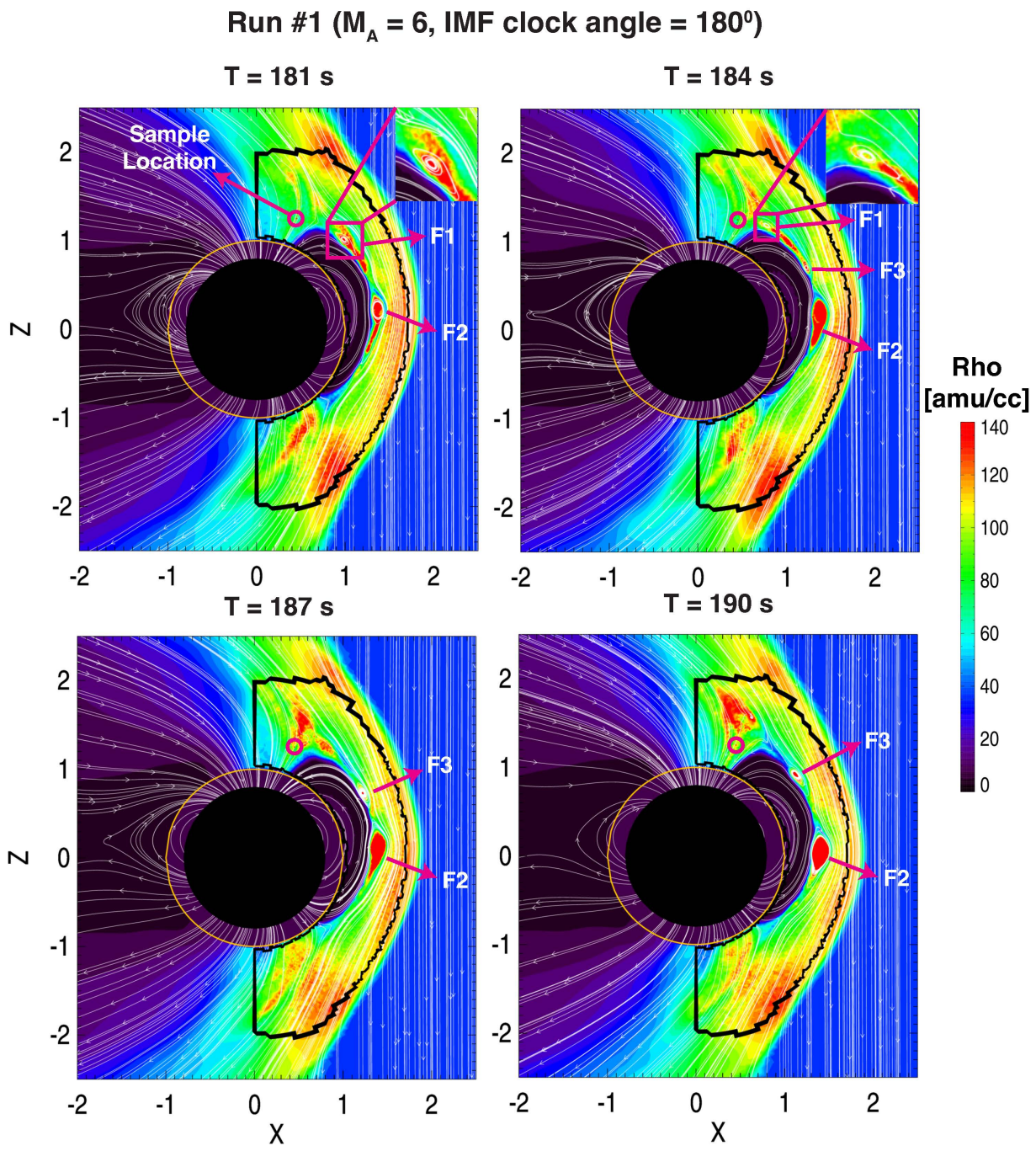

Figure 5-5: Multiple snapshots of density contours and sample magnetic field lines in the X-Z plane from MHD-AEPIC Run #1 (M_A = 6, IMF clock angle = 180°) at a time cadence of 3 seconds. The magenta circle in the northern cusp indicates the position of sample location. The yellow circle represents Mercury's surface at r = 1 R_M and the black filled disk represents Mercury's core with an assumed radius of 0.8 R_M. The black curves mark the boundaries of the active PIC region in the simulation. Labels (in white) and arrows (in magenta) are added to each panel to track individual FTEs. The magenta boxes in the top two panels highlight the FTE (F1), which leads to the formation of cusp filament at *t* = 190 s.

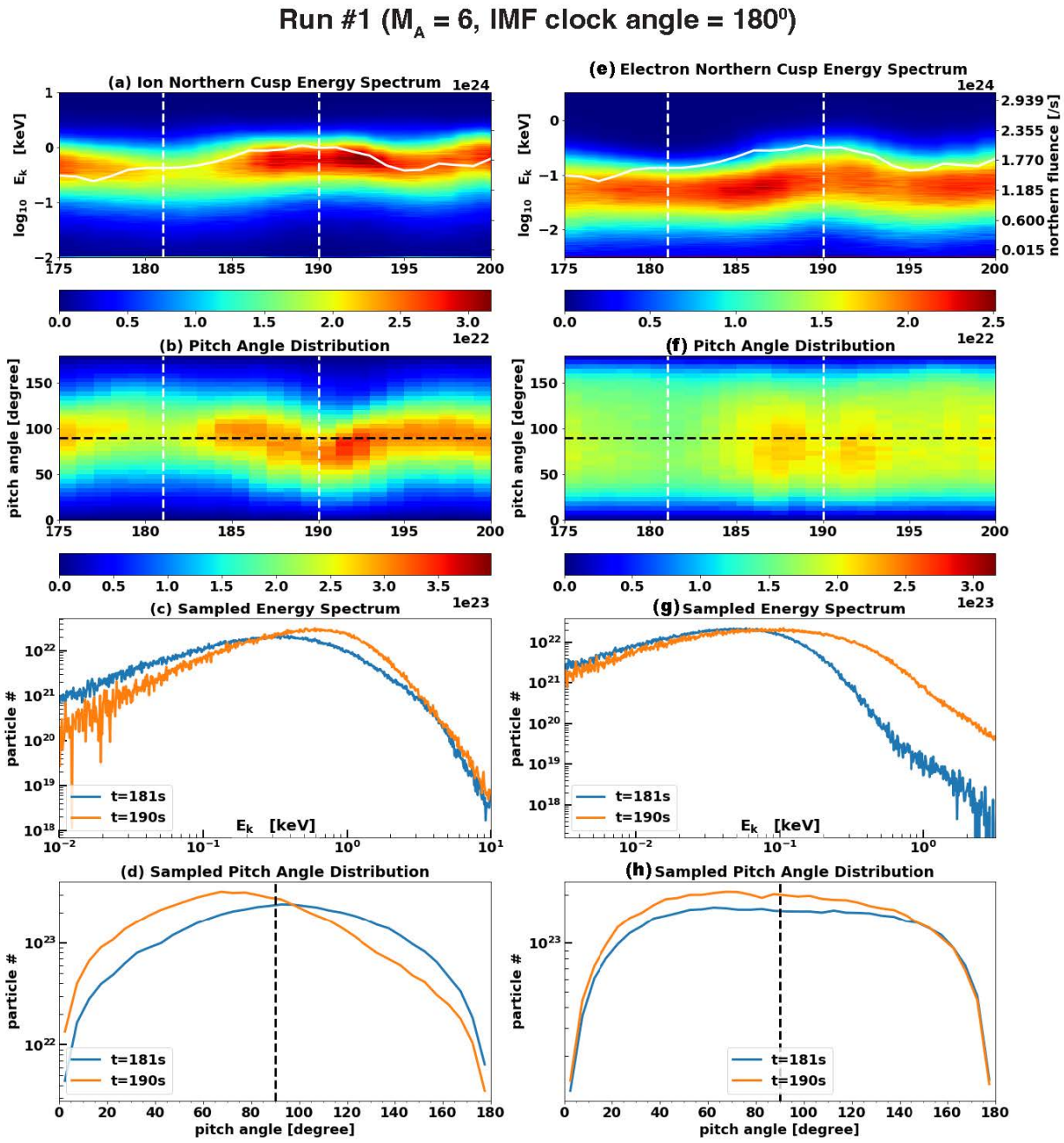

Figure 5-6: Panels (a) and (b) show the ion energy spectrum and pitch angle distribution from t = 175 s to t = 200 s within the sample location shown in Figure 5-5. The colors in panels (a) and (b) represent the ion count in the sampling sphere binned by its kinetic energy and pitch angle, respectively. The white solid curve in panel (a) shows the time series of proton northern cusp precipitation rate (fluence) and the two vertical white dashed lines in panels (a) and (b) correspond to t = 181 s and t = 190 s, respectively. (c) and (d) show the detailed views of energy spectrum and pitch angle distribution at t = 181 s and 190 s in log scale. Panels (e) - (h) are the same as panels (a) - (d) but display the information of electrons.

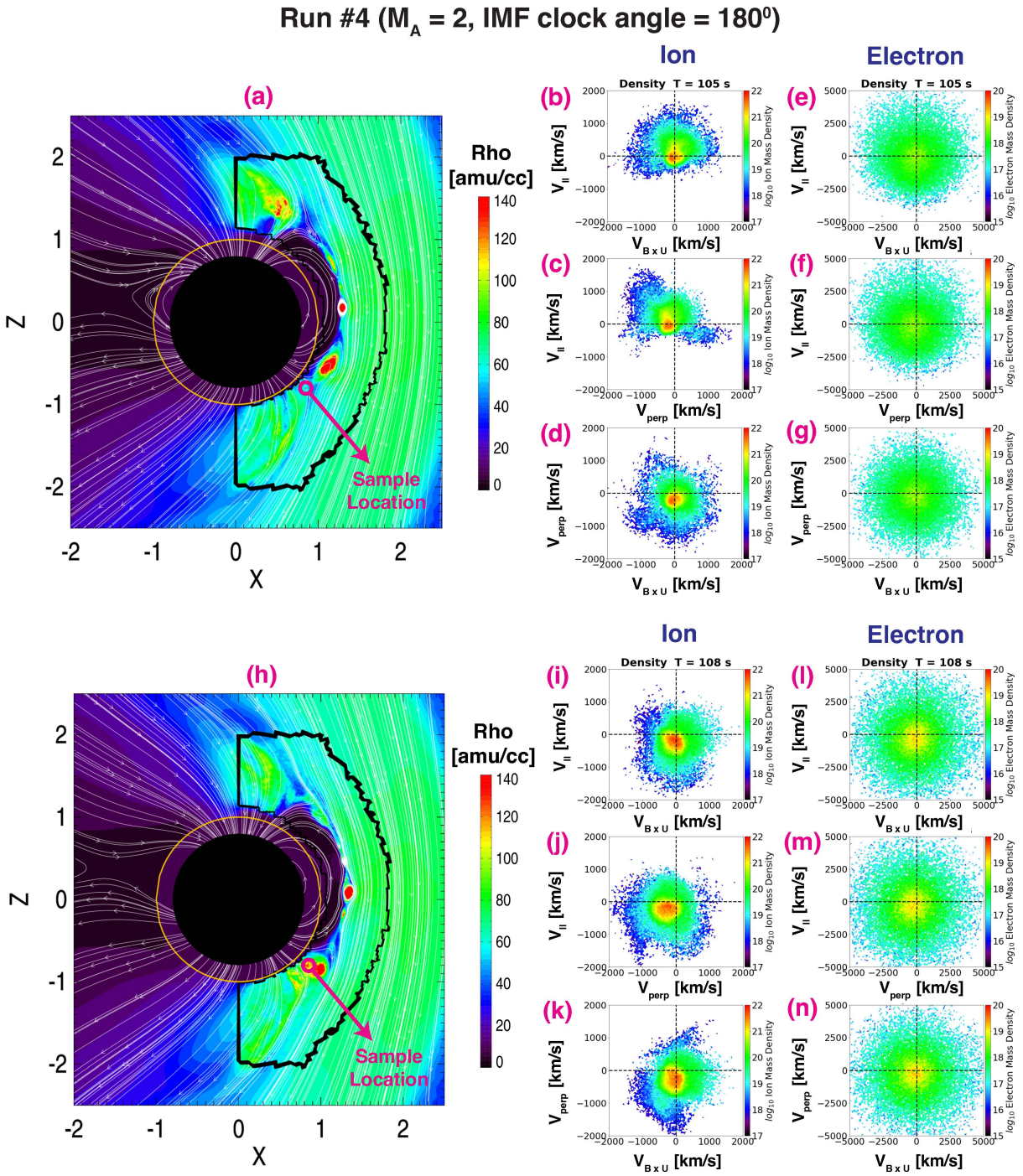

Figure 5-7: (a) - (g): Same as Figure 5-1, but at t = 105 s from Run #4, the sample location is in the southern cusp and is centered at X = 0.85 R_M, Y = 0 R_M, Z = -0.8 R_M. (h) - (n): Same as (a) - (g), but at t = 108 s when the high-latitude extension of FTE (or, cusp filament) passed by the sample location.

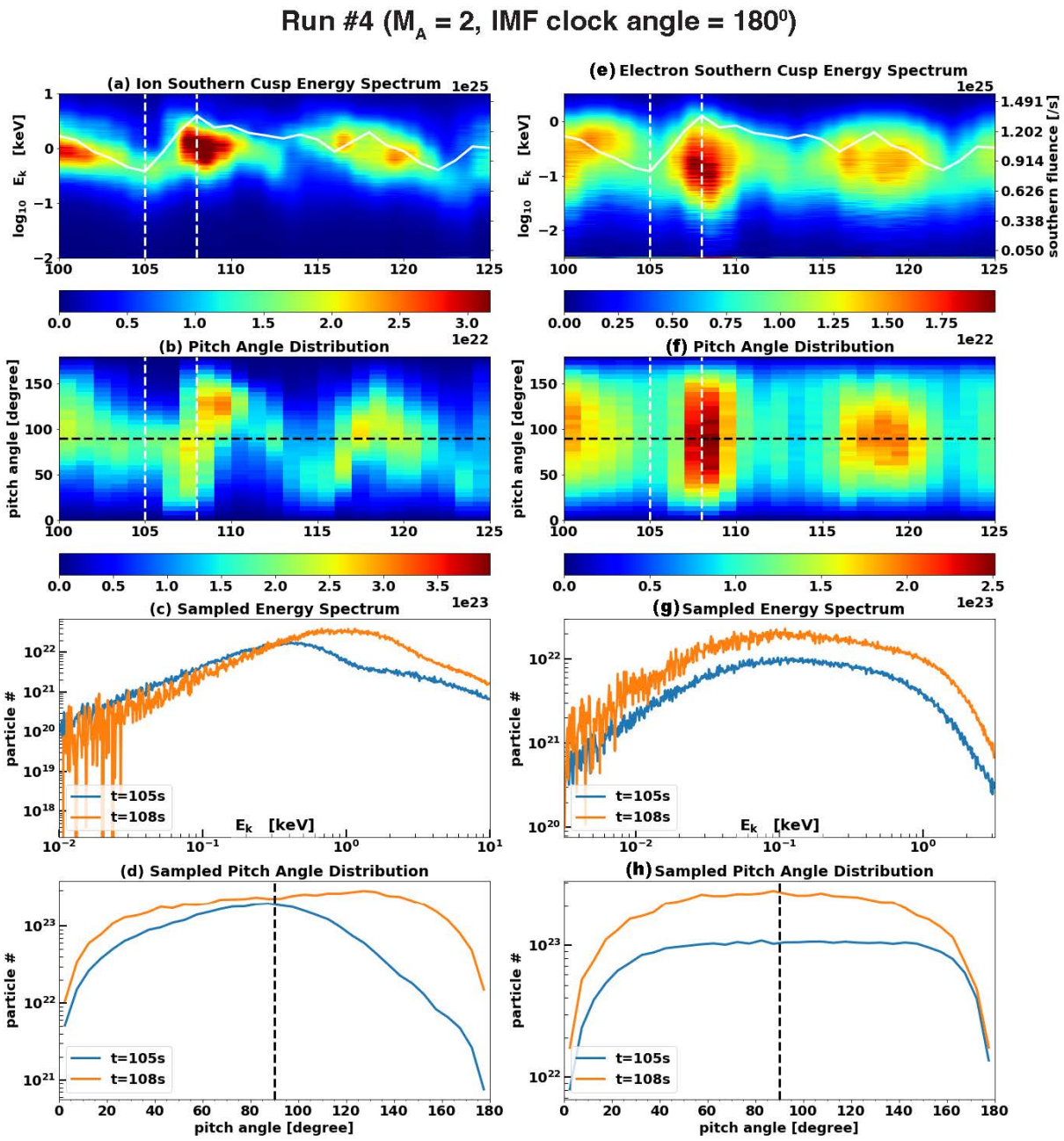

Figure 5-8: Same as Figure 5-6, but for information within the southern cusp sample location in Run #4 (see Figure 5-7a). The white solid curves in (a) and (e) are the time history of the proton southern cusp precipitation rate (fluence). The two timestamps selected for comparison are t = 105 s and 108 s, which correspond to quiet state and filament event, respectively.

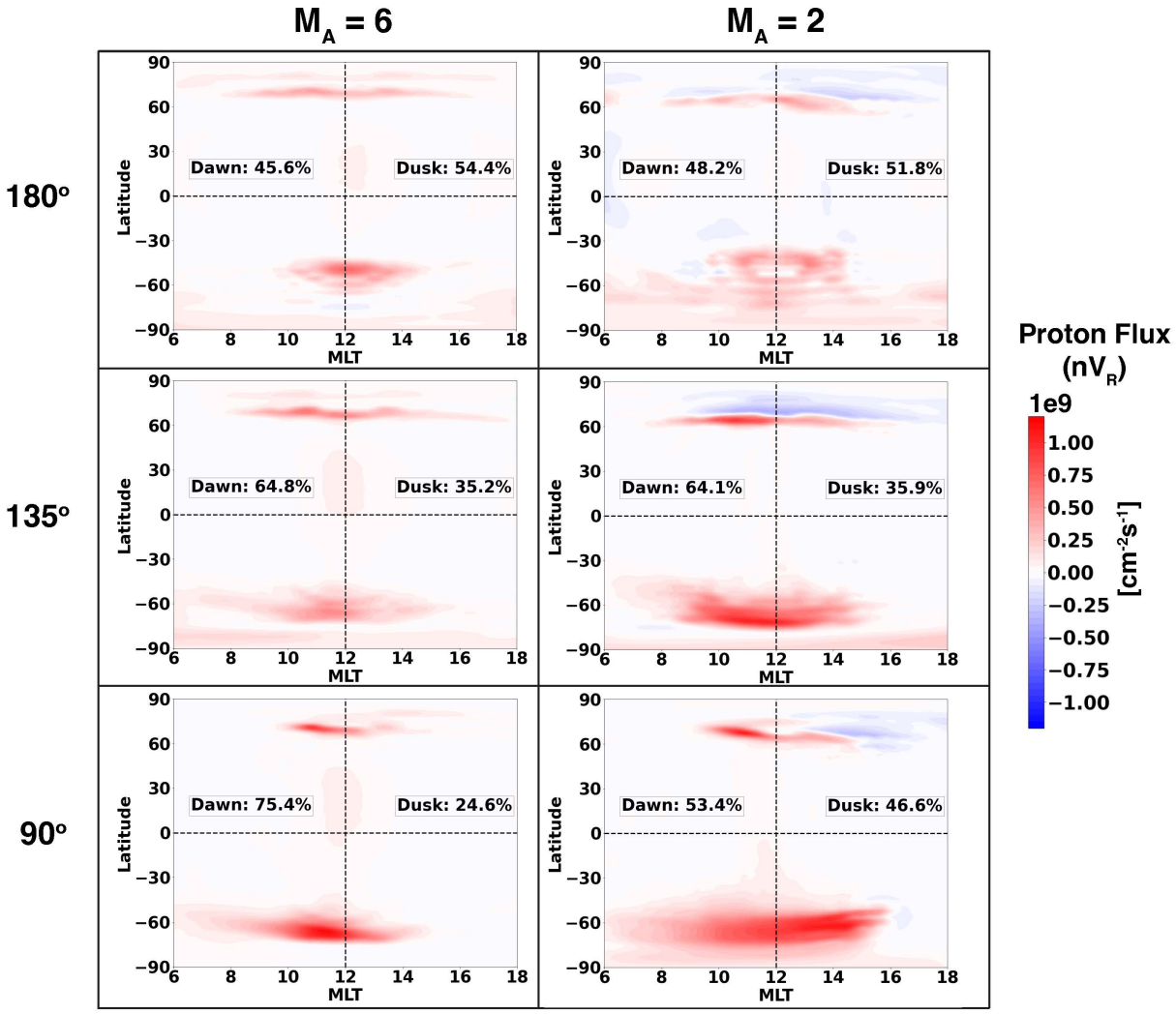

Figure 5-9: Spatial distribution of time-averaged (excluding first 20 s of the time accurate mode) proton flux shown in 2D MLT-latitude graph for all six MHD-AEPIC simulations. The positive and negative values represent the protons that are moving towards and leaving Mercury's surface, respectively. Two legends positioned to the center-left and center-right of each panel show the percentage-wise contribution to total cusp precipitation rate on dawnside (MLT < 12) and duskside (MLT > 12), respectively.

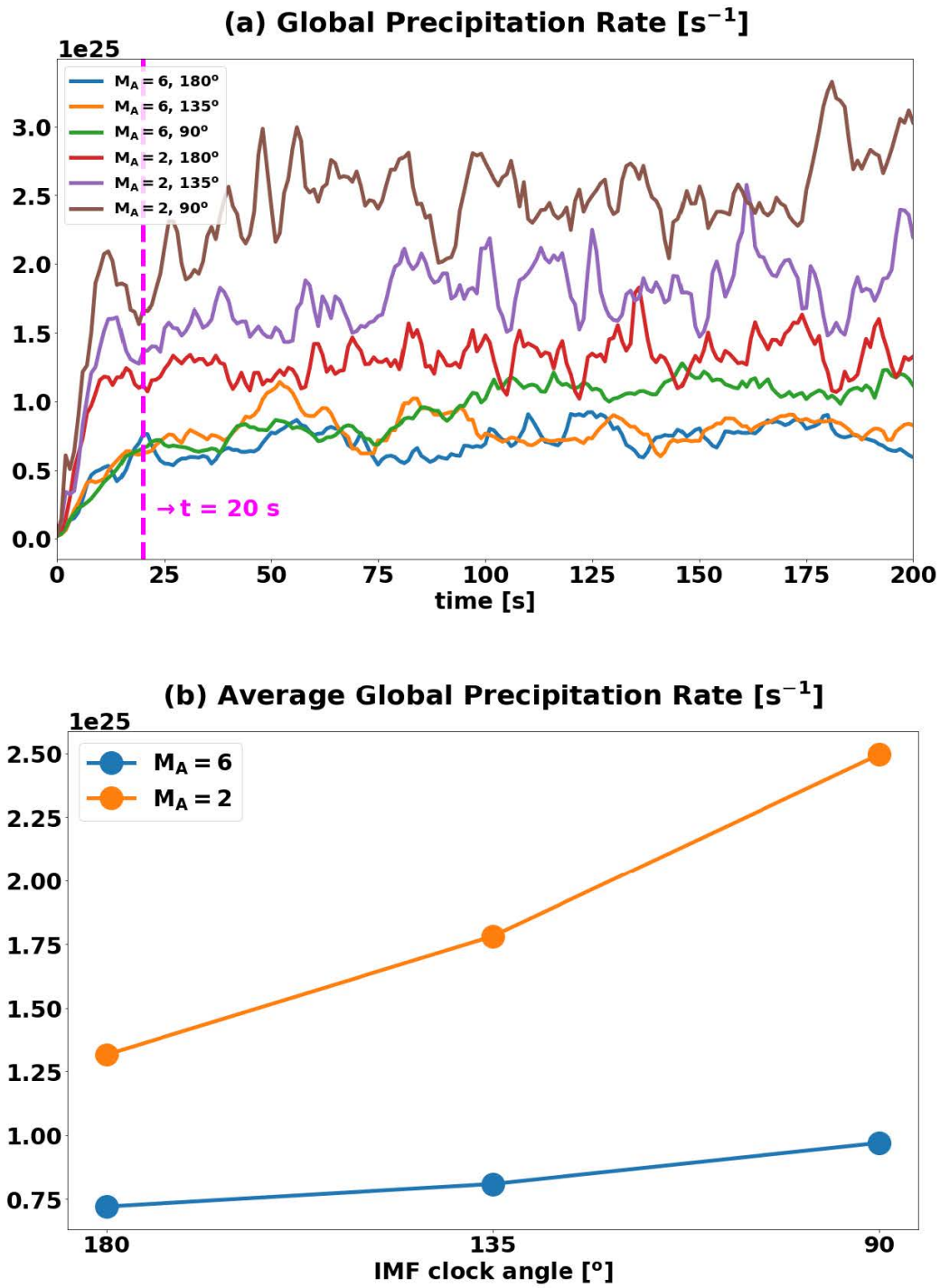

Figure 5-10: (a) Time series of global precipitation rate for all six MHD-AEPIC runs, with each simulation denoted by a unique color. The magenta vertical line to the left marks t = 20 s. (b) Scattered plot of time-averaged (excluding first 20 s) global precipitation rate for all six simulations. The horizontal axis represents the IMF clock angles in decreasing order. M_A = 6 simulations are represented by blue curves and data points and the M_A = 2 simulations correspond to orange curves and data points.

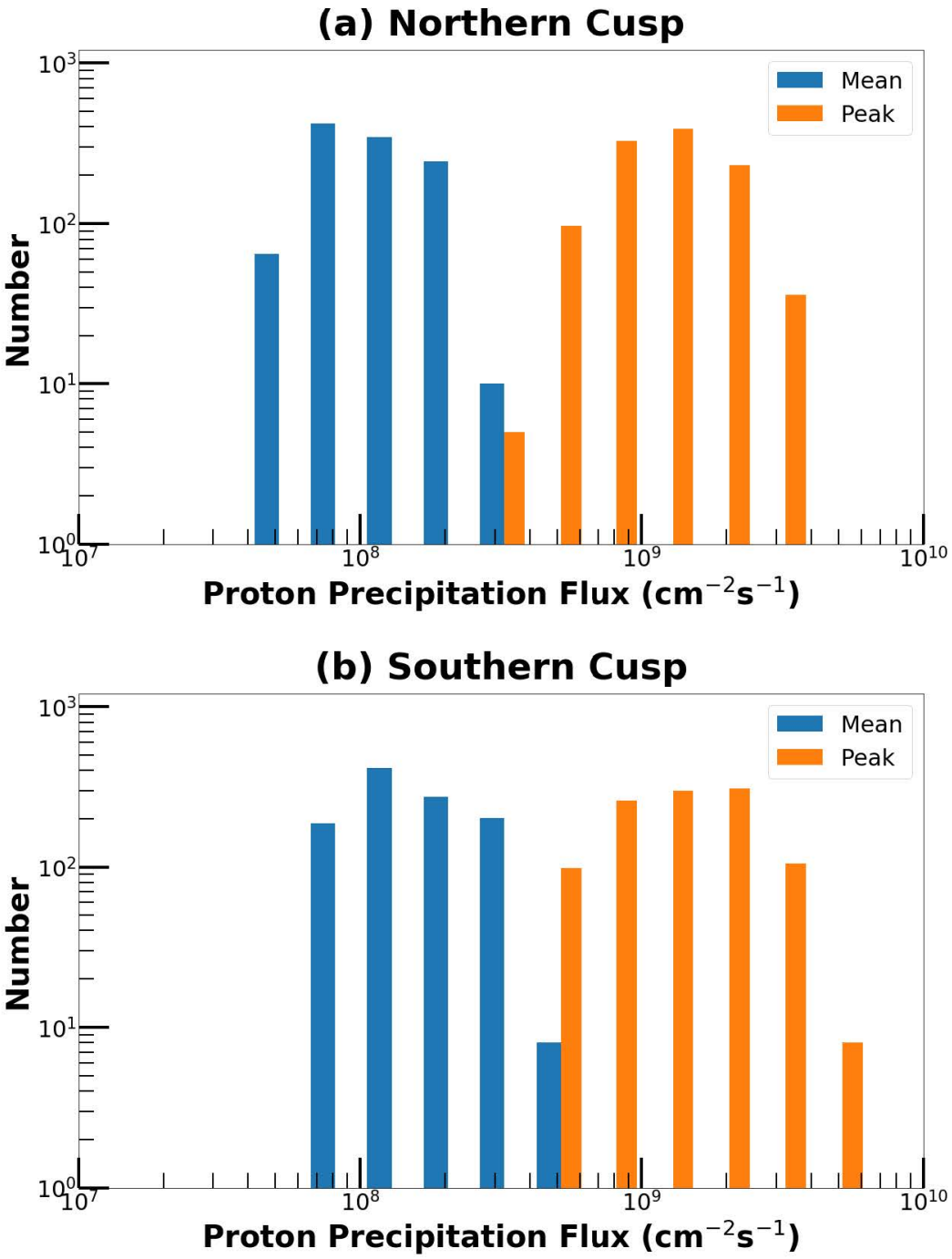

Figure 5-11: Histograms of proton precipitation flux within two cusp regions at each timestamp across all six MHD-AEPIC simulations. The occurrence frequency of mean precipitation flux, defined as the average precipitation flux over the entire cusp region, is shown as blue bars, while the peak precipitation flux is represented by orange bars. Panel (a) and (b) corresponds to the northern and southern cusps, respectively.

Chapter 6 Summary and Future Work

6.1 Summary

In this dissertation, we have used both Hall-MHD and MHD-AEPIC models to simulate Mercury's magnetosphere under a variety of upstream drivings. The main goal of this work is to develop a comprehensive understanding of reconnection-driven dynamics at Mercury's magnetopause, their impact on the global magnetosphere, and how the dynamics vary in response to different solar wind and IMF conditions.

In Chapter 3, we first employed the BATSRUS Hall-MHD model with coupled planetary interior to simulate Mercury's dayside magnetopause dynamics and investigated the impact of external conditions on FTE properties and their contribution to the global coupling and circulation of flux. An automated algorithm has been designed and used to identify the large number of FTEs occurring in the simulations. The simulated FTEs are found to occur every 3 to 9 seconds depending on the upstream conditions applied. Smaller solar wind M_A or larger IMF clock angle result in more frequent formation of FTEs in the simulations, consistent with the MESSENGER observations. The sizes of simulated FTEs fall in the range of 100 km to 2000 km and change in time as the FTEs propagate along the magnetopause. The average FTE size is comparable between cases with 180° and 135° IMF clock angles and is significantly increased in 90° IMF clock angle simulations. We observe that a smaller M_A leads to smaller-size FTEs under 180° and 135° IMF clock angles, but larger ones under 90° IMF clock angle. The simulated FTEs are observed to travel at speeds of 200 - 400 km/s. Larger FTE speeds are generally found in simulations with

lower M_A or larger IMF clock angle. The average core fields of FTEs range from 50 - 170 nT, with their associated flux contents falling between 0.005 MWb and 0.03 MWb. It was also found that FTEs tend to carry more magnetic flux under conditions of smaller IMF clock angle or lower solar wind M_A. Comparing the rate of magnetic flux transported through FTEs to the cross polar cap potential reveals that FTEs can contribute 3% - 13% of the total open flux generated at the dayside magnetopause for the various external conditions considered in the Hall-MHD simulations, confirming that FTEs play an important role in driving Mercury's Dungey cycle.

In Chapter 4, we investigated the kinetic signatures, asymmetries, and FTEs associated with the dayside magnetopause reconnection at Mercury using the newly developed MHD-AEPIC model, in which the BATSRUS Hall-MHD code is two-way coupled with the PIC code, FLEKS. Within the PIC domain, crescent-shaped ion and electron velocity distributions are found near dayside reconnection sites, which is similar to what has been observed in in-situ measurements obtained at Earth's magnetopause and in simulations of other planetary magnetospheres. However, the crescent-shaped distributions seen in the Mercury simulations appear on the magnetosheath side of the reconnection sites, which arise because of enhanced ion and electron temperatures within the magnetosphere as a result of the return flows from the nightside and lack of plasmasphere at Mercury. Other important kinetic signatures associated with the dayside reconnection include anisotropic heating of electrons along the reconnection outflow direction and counter-streaming ion populations in the cusps, implying that dayside magnetopause reconnection could potentially result in plasma instabilities and excitation of plasma waves in the vicinity of the magnetopause. Inside FTEs, the ion and electron distributions are commonly found to be non-Maxwellian and anisotropic. A novel synthesized reconnection score has been established and shown to have great performance when used as the criteria for identifying reconnection X-lines in

the 3D MHD-AEPIC simulations. Our analysis of the spatial distribution of the dayside reconnection sites reveals a notable dawn-dusk asymmetry with 56% to 72% of the reconnection events occurring on the dawnside. Such dawn-dusk asymmetry in reconnection occurrence generally becomes more prominent when the solar wind M_A is smaller or when the IMF clock angle is smaller. Possible mechanisms that can lead to the observed dawn-dusk asymmetry include (1) spreading of X-line due to electron drift in the reconnection current sheet and (2) the Hall effects in 3D. By comparing the MHD-AEPIC simulations with our previous Hall-MHD simulations that used the same upstream drivers, we found that most properties of the FTEs simulated by MHD-AEPIC exhibit similar dependencies on solar wind M_A and IMF clock angle as seen in the Hall-MHD runs, but some of their key properties are strongly influenced by kinetic effects. Specifically, the FTEs and their associated X-lines in the MHD-AEPIC simulations last for a longer period on the magnetopause, which in turn results in slower FTE travelling speeds, reduced FTE occurrence frequency, and increased plasma density within FTEs, in comparison to the Hall-MHD results. The magnetic flux content carried by individual FTEs in MHD-AEPIC is about two times larger. The aggregated FTE contribution to the total open flux generation at the dayside magnetopause ranges from 2.9% to 36.4%, representing a notable increase compared to the corresponding values observed in the Hall-MHD simulations.

In Chapter 5, we further analyzed the simulation outputs of the MHD-AEPIC runs presented in Chapter 4 focusing on the simulated filaments and proton precipitation in Mercury's cusp regions, both of which have important implications for understanding space weathering effects at Mercury. It is found that the characteristics of the simulated cusp filaments are in excellent agreement with those observed by MESSENGER and the cusp filaments indeed map to FTEs formed at the dayside magnetopause. The absence of cusp filaments in our Hall-MHD

simulations implies that kinetic physics might play an important role in forming filaments. By analyzing the particle energy spectrums and pitch angle distributions output from the PIC model, we find that, inside the cusp filaments, the ions and electrons injected into cusps by FTEs are significantly energized due to magnetopause reconnection. This FTE-associated particle energization effect is found to be more prominent within the southern cusp compared to the northern cusp. Our analyses further show that the proton precipitation fluxes are concentrated in two high-latitude bands corresponding to the northern and southern cusps, with the southern band being notably broader than the northern band as a result of Mercury's dipole shift. In both cusps, the peak and mean proton precipitation fluxes differ by approximately an order of magnitude, suggesting that the proton precipitation inside the cusp regions is highly variable both spatially and temporally. The distribution of proton precipitation is not spatially uniform within the cusp nor symmetric around the Sun-Mercury line. Rather, noticeable asymmetries are present in the distribution of precipitation flux between the dawn and dusk sides, which is likely linked to the dawn-dusk asymmetries seen in the magnetopause reconnection occurrence. The average simulated global proton precipitation rate falls within the range of 0.7×10^{25} s^{-1} to 2.5×10^{25} s^{-1} and exhibits an increasing trend with decreasing solar wind Mach number and decreasing IMF clock angle. Furthermore, the precipitation fluxes in the southern cusp are observed to be about two times higher than those in the northern cusp due to the weaker surface field strength in the southern hemisphere.

6.2 Future Work

While the research presented in this dissertation has provided valuable insights into reconnection-driven dynamics at Mercury's dayside, there are still many directions of research

that could be explored in the future. Below we highlight a few important ones that may be pursued in future work.

1. The external parameters we have investigated in this dissertation are the solar wind Alfvénic Mach number and the IMF orientation. Future work that explores the impact of other external parameters, such as the solar wind plasma parameters (for instance, density and velocity) and more realistic IMF conditions (e.g., incorporation of non-zero B_x component), is expected to be useful in order to obtain a complete understanding of the formation of FTEs and their role in driving Mercury's global dynamics.
2. The synthesized reconnection score (denoted as *S*) that we introduced in Chapter 4 has been shown to work reasonably well in finding the reconnection sites in our MHD-AEPIC simulations. However, inclusion of extra reconnection metrics into the definition of *S* may further improve the accuracy of our automated reconnection identification algorithm. Two examples of potential metrics are the current sheet thickness and the topological measure of reconnection, which measures the entanglement of pairs of field lines (*Gekelman et al*., 2020).
3. The PIC code FLEKS used in our MHD-AEPIC simulations has a built-in test particle module. By launching test particles in the simulation and tracking their subsequent energy changes within Mercury's magnetosphere, one could gain a better understanding of the energization and transport of ions and electrons associated with multiple X-line reconnections and resultant FTEs.

As demonstrated by this dissertation and other works published previously, the MHD-AEPIC model provides a very powerful tool for studying the kinetic processes involved in

magnetic reconnection and their impact on the global magnetosphere. Further applications and expansions of the MHD-AEPIC model may help address some of the remaining outstanding questions concerning Mercury's magnetosphere, such as:

1. Adding an additional PIC region on Mercury's nightside to cover the magnetotail reconnection sites. Such simulations in which both dayside and nightside reconnections are modeled by kinetic approach would improve the accuracy of the simulated global reconnection rate and refine our understanding of the role played by FTEs at the magnetopause and plasmoids in the tail in driving Mercury's global dynamics, thereby providing a more realistic description of the substorm cycle at Mercury.
2. Incorporating planetary heavy ions (e.g., sodium ions) into our MHD-AEPIC model by using multispecies MHD. The inclusion of sodium ions would lead to more realistic simulations that may shed new light on the role played by the planetary ions in driving global dynamics and contributing to the dawn-dusk asymmetries observed in various magnetospheric phenomena at Mercury.
3. Adding the adaptive mesh refinement (AMR) capability into FLEKS. In our current MHD-AEPIC simulations, the grid resolution of PIC is approximately twice the electron skin depth, a resolution that might not be fine enough to fully resolve the electron-scale physics. Given that kinetic physics normally becomes important near reconnection sites, with the addition of AMR capability, one can selectively increase the grid resolution in the vicinity of the reconnection diffusion region to avoid under-resolving electron dynamics while still keeping the computational costs affordable. A further enhancement to the MHD-AEPIC model could be implementing a functionality to automatically adjust the AMR region at different timesteps based on the possible locations of reconnection occurrence, as predicted

by the synthesized reconnection score *S* that we have developed for our MHD-AEPIC analysis.

Bibliography

Akhavan-Tafti, M., J. A. Slavin, J. P. Eastwood, P. A. Cassak, and D. J. Gershman (2019a), MMS Multi-Point Analysis of FTE Evolution: Physical Characteristics and Dynamics, *Journal of Geophysical Research: Space Physics*, *124*(7), 5376-5395, https://doi.org/10.1029/2018JA026311.

Akhavan-Tafti, M., J. A. Slavin, W. J. Sun, G. Le, and D. J. Gershman (2019b), MMS Observations of Plasma Heating Associated With FTE Growth, *Geophysical Research Letters*, *46*(22), 12654-12664, https://doi.org/10.1029/2019GL084843.

Anderson, B. J., Johnson, C. L., Korth, H., Purucker, M. E., Winslow, R. M., Slavin, J. A., ... & Zurbuchen, T. H. (2011). The global magnetic field of Mercury from MESSENGER orbital observations. *Science*, *333*(6051), 1859-1862, doi: 10.1126/science.1211001

Baker, D. N., T. I. Pulkkinen, V. Angelopoulos, W. Baumjohann, and R. L. McPherron (1996), Neutral line model of substorms: Past results and present view, *Journal of Geophysical Research: Space Physics*, *101*(A6), 12975-13010, https://doi.org/10.1029/95JA03753.

Birdsall, C.K., & Langdon, A.B. (1991). *Plasma Physics via Computer Simulation (1st ed.).* CRC Press. https://doi.org/10.1201/9781315275048.

Birn, J., J. Drake, M. Shay, B. Rogers, R. Denton, M. Hesse, M. Kuznetsova, Z. Ma, A. Bhattacharjee, and A. Otto (2001), Geospace Environmental Modeling (GEM) magnetic reconnection challenge, *Journal of Geophysical Research: Space Physics*, *106*(A3), 3715-3719, doi:10.1029/1999JA900449.

Birn, J., K. Galsgaard, M. Hesse, M. Hoshino, J. Huba, G. Lapenta, P. Pritchett, K. Schindler, L. Yin, and J. Büchner (2005), Forced magnetic reconnection, *Geophysical research letters*, *32*(6), doi:10.1029/2004GL022058.

Brackbill, J. U., and D. W. Forslund (1982), An implicit method for electromagnetic plasma simulation in two dimensions, *Journal of Computational Physics*, *46*(2), 271-308, https://doi.org/10.1016/0021-9991(82)90016-X.

Burch, J. L., Torbert, R. B., Phan, T. D., Chen, L.-J., Moore, T. E., Ergun, R. E.,…Chandler, M. (2016), Electron-scale measurements of magnetic reconnection in space, *Science*, *352*(6290), aaf2939, doi:10.1126/science.aaf2939.

Burkholder, B. L., K. Nykyri, X. Ma, R. Rice, S. A. Fuselier, K. J. Trattner, K. R. Pritchard, J. L. Burch, and S. M. Petrinec (2020), Magnetospheric Multiscale Observation of an Electron Diffusion Region at High Latitudes, *Geophysical Research Letters*, *47*(15), e2020GL087268, https://doi.org/10.1029/2020GL087268.

Cassak, P. A., and M. A. Shay (2007), Scaling of asymmetric magnetic reconnection: General theory and collisional simulations, *Physics of Plasmas*, *14*(10), doi:10.1063/1.2795630.

Cassak, P., Y. Liu, and M. Shay (2017). A review of the 0.1 reconnection rate problem. *Journal of Plasma Physics, 83*(5), 715830501. doi:10.1017/S0022377817000666.

Chen, Y., G. Tóth, and T. I. Gombosi (2016), A fifth-order finite difference scheme for hyperbolic equations on block-adaptive curvilinear grids, *Journal of Computational Physics*, *305*, 604-621, https://doi.org/10.1016/j.jcp.2015.11.003.

Chen, Y., G. Tóth, P. Cassak, X. Jia, T. I. Gombosi, J. A. Slavin, S. Markidis, I. B. Peng, V. K. Jordanova, and M. G. Henderson (2017), Global Three-Dimensional Simulation of Earth's Dayside Reconnection Using a Two-Way Coupled Magnetohydrodynamics With Embedded Particle-in-Cell Model: Initial Results, *Journal of Geophysical Research: Space Physics*, *122*(10), 10,318-310,335, https://doi.org/10.1002/2017JA024186.

Chen, Y., G. Tóth, X. Jia, J. A. Slavin, W. Sun, S. Markidis, T. I. Gombosi, and J. M. Raines (2019), Studying Dawn-Dusk Asymmetries of Mercury's Magnetotail Using MHD-EPIC Simulations, *Journal of Geophysical Research: Space Physics*, *124*(11), 8954-8973, https://doi.org/10.1029/2019JA026840.

Chen, Y., and G. Tóth (2019), Gauss's Law satisfying Energy-Conserving Semi-Implicit Particle-in-Cell method, *Journal of Computational Physics*, *386*, 632-652, https://doi.org/10.1016/j.jcp.2019.02.032.

Chen, Y., G. Tóth, H. Zhou, and X. Wang (2023), FLEKS: A flexible particle-in-cell code for multi-scale plasma simulations, *Computer Physics Communications*, *287*, 108714, doi:10.1016/j.cpc.2023.108714.

Cheng, A. F., Johnson, R. E., Krimigis, S. M., & Lanzerotti, L. J. (1987). Magnetosphere, exosphere, and surface of mercury. *Icarus*, *71*(3), 430–440. https://doi.org/10.1016/0019-1035(87)90038-8.

Daldorff, L. K., G. Tóth, T. I. Gombosi, G. Lapenta, J. Amaya, S. Markidis, and J. U. Brackbill (2014), Two-way coupling of a global Hall magnetohydrodynamics model with a local implicit particle-in-cell model, *Journal of Computational Physics*, *268*, 236-254, https://doi.org/10.1016/j.jcp.2014.03.009.

De Zeeuw, D. L., Gombosi, T. I., Groth, C. P. T., Powell, K. G., & Stout, Q. F. (2000). An adaptive MHD method for global space weather simulations. *IEEE Transactions on Plasma Science, 28*(6), 1956–1965. https://doi.org/10.1109/27.902224.

DiBraccio, G. A., J. A. Slavin, S. A. Boardsen, B. J. Anderson, H. Korth, T. H. Zurbuchen, J. M. Raines, D. N. Baker, R. L. McNutt Jr, and S. C. Solomon (2013), MESSENGER observations of magnetopause structure and dynamics at Mercury, *Journal of Geophysical Research: Space Physics*, *118*(3), 997-1008, doi:10.1002/jgra.50123.

DiBraccio, G. A., J. A. Slavin, J. M. Raines, D. J. Gershman, P. J. Tracy, S. A. Boardsen, T. H. Zurbuchen, B. J. Anderson, H. Korth, and R. L. McNutt Jr (2015), First observations of Mercury's plasma mantle by MESSENGER, *Geophysical Research Letters*, *42*(22), 9666-9675, doi:10.1002/2015GL065805.

Dungey, J. W. (1961), Interplanetary Magnetic Field and the Auroral Zones, *Physical Review Letters*, *6*(2), 47-48, doi:10.1103/PhysRevLett.6.47.

Eastwood, J.P. et al., (2015), What Controls the Structure and Dynamics of Earth's Magnetosphere, *Space Sci Rev, 188(251)*, doi:10.1007/s11214-014-0050-x

Einfeldt, B., C. D. Munz, P. L. Roe, and B. Sjögreen (1991), On Godunov-type methods near low densities, *Journal of Computational Physics*, *92*(2), 273-295, https://doi.org/10.1016/0021-9991(91)90211-3.

Exner, W., Heyner, D., Liuzzo, L., Motschmann, U., Shiota, D., Kusano, K., & Shibayama, T. (2018). Coronal mass ejection hits Mercury: A.I.K.E.F. hybrid-code results compared to MESSENGER data. *Planetary and Space Science*, 153, 89–99. https://doi.org/10.1016/j.pss.2017.12.016.

Fatemi, S., Poirier, N., Holmstr.m, M., Lindkvist, J., Wieser, M., & Barabash, S. (2018). A modelling approach to infer the solar wind dynamic pressure from magnetic field observations inside Mercury's magnetosphere. *Astronomy and Astrophysics, 614*, A132. https://doi.org/10.1051/0004-6361/201832764.

Fatemi, S., Poppe, A. R., & Barabash, S. (2020). Hybrid simulations of solar wind proton precipitation to the surface of Mercury. *Journal of Geophysical Research: Space Physics, 125*(4), e27706. https://doi.org/10.1029/2019JA027706.

Fear, R. C., J. C. Coxon, and C. M. Jackman (2019), The Contribution of Flux Transfer Events to Mercury's Dungey Cycle, *Geophysical Research Letters*, *46*(24), 14239-14246, https://doi.org/10.1029/2019GL085399.

Gekelman, W., T. DeHaas, C. Prior, and A. Yeates (2020), Using topology to locate the position where fully three-dimensional reconnection occurs, *SN Applied Sciences*, *2*(12), 2187, https://doi.org/10.1007/s42452-020-03896-4.

Gombosi, T. I. (1998), *Physics of the Space Environment*, Cambridge University Press, Cambridge, doi:10.1017/CBO9780511529474.

Gombosi, T. I., G. Toth, D. L. De Zeeuw, K. C. Hansen, K. Kabin, and K. G. Powell (2002), Semi-relativistic magnetohydrodynamics and physics-based convergence acceleration, *J. Comput. Phys*., 177, 176–205, doi:10.1006/jcph.2002.7009.

Gombosi, T. I., Y. Chen, A. Glocer, Z. Huang, X. Jia, M. W. Liemohn, W. B. Manchester, T. Pulkkinen, N. Sachdeva, and Q. Al Shidi (2021), What sustained multi-disciplinary research can achieve: The space weather modeling framework, *Journal of Space Weather and Space Climate*, *11*, 42, doi:10.1051/swsc/2021020.

Heyner, D., Nabert, C., Liebert, E., & Glassmeier, K. H. (2016). Concerning reconnection-induction balance at the magnetopause of Mercury. *Journal of Geophysical Research: Space Physics*, 121, 2935–2961. https://doi.org/10.1002/2015JA021484.

Huang, Z., G. Tóth, B. van der Holst, Y. Chen, and T. Gombosi (2019), A six-moment multi-fluid plasma model, *Journal of Computational Physics*, *387*, 134-153, https://doi.org/10.1016/j.jcp.2019.02.023.

Imber, S. M., Slavin, J. A., Boardsen, S. A., Anderson, B. J., Korth, H., McNutt, R. L., and Solomon, S. C. (2014), MESSENGER observations of large dayside flux transfer events: Do they drive Mercury's substorm cycle?, *J. Geophys. Res. Space Physics*, 119, 5613–5623, doi:10.1002/2014JA019884.

Jia, X., J. A. Slavin, T. I. Gombosi, L. K. S. Daldorff, G. Toth, and B. van der Holst (2015), Global MHD simulations of Mercury's magnetosphere with coupled planetary interior: Induction effect of the planetary conducting core on the global interaction, *Journal of Geophysical Research: Space Physics*, *120*(6), 4763-4775, https://doi.org/10.1002/2015JA021143.

Jia, X., J. A. Slavin, G. Poh, G. A. DiBraccio, G. Toth, Y. Chen, J. M. Raines, and T. I. Gombosi (2019), MESSENGER observations and global simulations of highly compressed

magnetosphere events at Mercury, *Journal of Geophysical Research: Space Physics*, *124*(1), 229-247, https://doi.org/10.1029/2018JA026166.

Kabin, K., T. I. Gombosi, D. L. DeZeeuw, and K. G. Powell (2000), Interaction of Mercury with the Solar Wind, *Icarus*, *143*(2), 397-406, https://doi.org/10.1006/icar.1999.6252.

Kabin, K., M. H. Heimpel, R. Rankin, J. M. Aurnou, N. Gómez-Pérez, J. Paral, T. I. Gombosi, T. H. Zurbuchen, P. L. Koehn, and D. L. DeZeeuw (2008), Global MHD modeling of Mercury's magnetosphere with applications to the MESSENGER mission and dynamo theory, *Icarus*, *195*(1), 1-15, https://doi.org/10.1016/j.icarus.2007.11.028.

Kieokaew, R., B. Lavraud, N. Fargette, A. Marchaudon, V. Génot, C. Jacquey, D. Gershman, B. Giles, R. Torbert, and J. Burch (2021), Statistical Relationship Between Interplanetary Magnetic Field Conditions and the Helicity Sign of Flux Transfer Event Flux Ropes, *Geophysical Research Letters*, *48*(6), e2020GL091257, https://doi.org/10.1029/2020GL091257.

Killen, R., Cremonese, G., Lammer, H., Orsini, S., Potter, A. E., Sprague, A. L., et al. (2007). Processes that promote and deplete the exosphere of Mercury. *Space Science Reviews, 132*(2–4), 433–509. https://doi.org/10.1007/s11214-007-9232-0.

Killen, R. (2020). Seeing Effects on Ground-Based Images of Mercury's Sodium Exosphere. In *European Planetary Science Congress* (pp. EPSC2020-5). AA(Goddard Space Flight Center, Planetary and Geophysics Divisions). https://doi.org/10.5194/epsc2020-5.

Killen, R. M., Morrissey, L. S., Burger, M. H., Vervack, R. J., Tucker, O. J., & Savin, D. W. (2022). The Influence of Surface Binding Energy on Sputtering in Models of the Sodium Exosphere of Mercury. *The Planetary Science Journal*, *3*(6), 139. https://doi.org/10.3847/psj/ac67de.

Kivelson, M. G., and A. J. Ridley (2008), Saturation of the polar cap potential: Inference from Alfvén wing arguments, *Journal of Geophysical Research: Space Physics*, *113*(A5), https://doi.org/10.1029/2007JA012302.

Koren, B. (1993), *A robust upwind discretization method for advection, diffusion and source terms*, Centrum voor Wiskunde en Informatica Amsterdam.

Kuznetsova, M. M., D. G. Sibeck, M. Hesse, Y. Wang, L. Rastaetter, G. Toth, and A. Ridley (2009), Cavities of weak magnetic field strength in the wake of FTEs: Results from global magnetospheric MHD simulations, *Geophysical Research Letters*, *36*(10), https://doi.org/10.1029/2009GL037489.

Lapenta, G. (2012), Particle simulations of space weather, *Journal of Computational Physics*, *231*(3), 795-821, https://doi.org/10.1016/j.jcp.2011.03.035.

Lapenta, G. (2017), Exactly energy conserving semi-implicit particle in cell formulation, *Journal of Computational Physics*, *334*, 349-366, https://doi.org/10.1016/j.jcp.2017.01.002.

Lapenta, G. (2021), Detecting Reconnection Sites Using the Lorentz Transformations for Electromagnetic Fields, *The Astrophysical Journal*, *911*(2), 147, doi:10.3847/1538-4357/abeb74.

Lapenta, G., Schriver, D., Walker, R. J., Berchem, J., Echterling, N. F., El Alaoui, M., & Travnicek, P. (2022). Do we need to consider electrons' kinetic effects to properly model a planetary magnetosphere: The case of Mercury. *Journal of Geophysical Research: Space Physics*, 127, e2021JA030241. https://doi.org/10.1029/2021JA030241.

Lavorenti, F., P. Henri, F. Califano, J. Deca, S. Aizawa, N. André, and J. Benkhoff (2022), Electron dynamics in small magnetospheres-Insights from global, fully kinetic plasma simulations of the planet Mercury, *Astronomy & Astrophysics*, *664*, A133, doi:10.1051/0004-6361/202243911.

Lee, L. C., and Z. F. Fu (1985), A theory of magnetic flux transfer at the Earth's magnetopause, *Geophysical Research Letters*, *12*(2), 105-108, https://doi.org/10.1029/GL012i002p00105.

Li, C., X. Jia, Y. Chen, G. Toth, H. Zhou, J. A. Slavin, W. Sun, and G. Poh (2023), Global Hall MHD Simulations of Mercury's Magnetopause Dynamics and FTEs Under Different Solar Wind and IMF Conditions, *Journal of Geophysical Research: Space Physics*, *128*(5), e2022JA031206, https://doi.org/10.1029/2022JA031206.

Liu, Y.-H., M. Hesse, F. Guo, W. Daughton, H. Li, P. Cassak, and M. Shay (2017), Why does steady-state magnetic reconnection have a maximum local rate of order 0.1?, *Physical Review Letters*, *118*(8), 085101, doi:10.1103/PhysRevLett.118.085101.

Liu, Y.-H., T. C. Li, M. Hesse, W. J. Sun, J. Liu, J. Burch, J. A. Slavin, and K. Huang (2019), Three-Dimensional Magnetic Reconnection With a Spatially Confined X-Line Extent: Implications for Dipolarizing Flux Bundles and the Dawn-Dusk Asymmetry, *Journal of Geophysical Research: Space Physics*, *124*(4), 2819-2830, https://doi.org/10.1029/2019JA026539.

Liu, Y.-H., P. Cassak, X. Li, M. Hesse, S.-C. Lin, and K. Genestreti (2022), First-principles theory of the rate of magnetic reconnection in magnetospheric and solar plasmas, *Communications Physics*, *5*(1), 97, doi:10.1038/s42005-022-00854-x.

Lu, Q., J. Guo, S. Lu, X. Wang, J. A. Slavin, W. Sun, R. Wang, Y. Lin, and J. Zhong (2022), Three-dimensional Global Hybrid Simulations of Flux Transfer Event Showers at Mercury, *The Astrophysical Journal*, *937*(1), 1, doi:10.3847/1538-4357/ac8bcf.

Markidis, S., G. Lapenta, and u. Rizwan (2010), Multi-scale simulations of plasma with iPIC3D, *Mathematics and Computers in Simulation*, *80*(7), 1509-1519, https://doi.org/10.1016/j.matcom.2009.08.038.

Mason, R. J. (1981), Implicit moment particle simulation of plasmas, *Journal of Computational Physics*, *41*(2), 233-244, https://doi.org/10.1016/0021-9991(81)90094-2.

Milillo, A., Wurz, P., Orsini, S., Delcourt, D., Kallio, E., Killen, R. M., et al. (2005). Surface-exosphere-magnetosphere system of Mercury. *Space Science Reviews, 117*(3–4), 397–443. https://doi.org/10.1007/s11214-005-3593-z.

Millilo, A., M. Fujimoto, G. Murakami, et al. (2020), Investigating Mercury's environment with the two-spacecraft BepiColombo mission, *Space Science Reviews*, https://doi.org/10.1007/s11214-020-00712-8.

Müller, J., Simon, S.,Wang, Y. C.,Motschmann,U.,Heyner,D., Schüle, J., & Pringle,G. J. (2012). Origin of Mercury's double magnetopause: 3D hybrid simulation study with A.I.K.E.F. *Icarus*, 218, 666–687. https://doi.org/10.1016/j.icarus.2011.12.028.

Ness, N. F., Behannon, K. W., Lepping, R. P., Whang, Y. C., & Schatten, K. H. (1974). Magnetic Field Observations near Mercury: Preliminary Results from Mariner 10. *Science*, *185*(4146), 151–160. https://doi.org/10.1126/science.185.4146.151.

Ness, N. F., Behannon, K. W., Lepping, R. P., & Whang, Y. C. (1975). The magnetic field of Mercury, 1. *Journal of Geophysical Research (1896-1977)*, *80*(19), 2708–2716. https://doi.org/10.1029/JA080i019p02708.

Norgren, C., Graham, D. B., Khotyaintsev, Y. V., André, M., Vaivads, A., Chen, L.-J., et al. (2016), Finite gyroradius effects in the electron outflow of asymmetric magnetic reconnection, *Geophysical Research Letters*, *43*(13), 6724-6733, https://doi.org/10.1002/2016GL069205.

Parker, E. N. (1958), Dynamics of the Interplanetary Gas and Magnetic Fields, *The Astrophysical Journal*, *128*, 664, doi:10.1086/146579.

Poh, G., Slavin, J. A., Jia, X., DiBraccio, G. A., Raines, J. M., Imber, S. M., et al. (2016). MESSENGER observations of cusp plasma filaments at Mercury. *Journal of Geophysical Research: Space Physics, 121*(9), 8260–8285. https://doi.org/10.1002/2016JA022552.

Poh, G., J. A. Slavin, X. Jia, J. M. Raines, S. M. Imber, W.-J. Sun, D. J. Gershman, G. A. DiBraccio, K. J. Genestreti, and A. W. Smith (2017), Coupling between Mercury and its nightside magnetosphere: Cross-tail current sheet asymmetry and substorm current wedge formation, *Journal of Geophysical Research: Space Physics*, *122*(8), 8419-8433, https://doi.org/10.1002/2017JA024266.

Powell, K. G., P. L. Roe, T. J. Linde, T. I. Gombosi, and D. L. De Zeeuw (1999), A solution-adaptive upwind scheme for ideal magnetohydrodynamics, *Journal of Computational Physics*, *154*(2), 284-309, doi:10.1006/jcph.1999.6299.

Raines, J. M., G. A. DiBraccio, T. A. Cassidy, D. Delcourt, M. Fujimoto, X. Jia, V. Mangano, A. Milillo, M. Sarantos, J. A. Slavin, and P. Wurz (2015), Plasma sources in planetary magnetospheres: Mercury, *Space Science Reviews,* doi:10.1007/s11214-015-0193-4.

Raines, J. M., Dewey, R. M., Staudacher, N. M., Tracy, P. J., Bert, C. M., Sarantos, M., et al. (2022), Proton Precipitation in Mercury's Northern Magnetospheric Cusp, *Journal of Geophysical Research: Space Physics*, *127*(11), e2022JA030397, https://doi.org/10.1029/2022JA030397.

Russell, C. T., and R. Elphic (1978), Initial ISEE magnetometer results: Magnetopause observations, *Space Science Reviews*, *22*, 681-715, doi:10.1007/BF00212619.

Sarantos, M., Reiff, P. H., Hill, T. W., Killen, R. M., & Urquhart, A. L. (2001). A Bx-interconnected magnetosphere model for Mercury. *Planetary and Space Science*, *49*(14–15), 1629–1635. https://doi.org/10.1016/S0032-0633(01)00100-3.

Schindler, K., M. Hesse, and J. Birn (1988), General magnetic reconnection, parallel electric fields, and helicity, *Journal of Geophysical Research: Space Physics*, *93*(A6), 5547-5557, https://doi.org/10.1029/JA093iA06p05547.

Scudder, J., & Daughton, W. (2008). Illuminating electron diffusion regions of collisionless magnetic reconnection using electron agyrotropy. *Journal of Geophysical Research*, *113*, A06222. https://doi.org/10.1029/2008JA013035

Shay, M. A., T. D. Phan, C. C. Haggerty, M. Fujimoto, J. F. Drake, K. Malakit, P. A. Cassak, and M. Swisdak (2016), Kinetic signatures of the region surrounding the X line in asymmetric (magnetopause) reconnection, *Geophysical Research Letters*, *43*(9), 4145-4154, https://doi.org/10.1002/2016GL069034.

Shepherd, L. S., and P. A. Cassak (2012), Guide field dependence of 3-D X-line spreading during collisionless magnetic reconnection, *Journal of Geophysical Research: Space Physics*, *117*(A10), https://doi.org/10.1029/2012JA017867.

Shou, Y., V. Tenishev, Y. Chen, G. Toth, and N. Ganushkina (2021), Magnetohydrodynamic with Adaptively Embedded Particle-in-Cell model: MHD-AEPIC, *Journal of Computational Physics*, *446*, 110656, https://doi.org/10.1016/j.jcp.2021.110656.

Shue, J.-H., J. K. Chao, H. C. Fu, C. T. Russell, P. Song, K. K. Khurana, and H. J. Singer (1997), A new functional form to study the solar wind control of the magnetopause size and shape, *J. Geophys. Res.,* 102, 9497 – 9511, doi:10.1029/97JA00196.

Slavin, J. A., and R. E. Holzer (1979), The effect of erosion on the solar wind stand-off distance at Mercury, *Journal of Geophysical Research: Space Physics*, *84*(A5), 2076-2082, doi:10.1029/JA084iA05p02076.

Slavin, J. A., and R. E. Holzer (1981), Solar wind flow about the terrestrial planets 1. Modeling bow shock position and shape, *J. Geophys. Res.*, *86*(A13), 11401–11418, doi:10.1029/JA086iA13p11401.

Slavin J. A. (2004), Mercury's magnetosphere, *Advances in Space Research, 33(11)*, 1859–1874, doi:10.1016/j.asr.2003.02.019.

Slavin, J. A., Acuña, M. H., Anderson, B. J., Baker, D. N., Benna,M., Boardsen, S. A., & Zurbuchen, T. H. (2009).MESSENGER observations of magnetic reconnection in Mercury's magnetosphere. *Science*, 324, 606. https://doi.org/10.1126/science.1172011.

Slavin, J. A., B. J. Anderson, D. N. Baker, M. Benna, S. A. Boardsen, G. Gloeckler, R. E. Gold, G. C. Ho, H. Korth, and S. M. Krimigis (2010a), MESSENGER observations of extreme loading and unloading of Mercury's magnetic tail, *Science*, *329*(5992), 665-668, doi:10.1126/science.1188067.

Slavin, J. A., Lepping, R. P., Wu, C.-C., Anderson, B. J., Baker, D. N., Benna, M., et al. (2010b). MESSENGER observations of large flux transfer events at Mercury. *Geophysical Research Letters, 37*(2), L02105. https://doi.org/10.1029/2009GL041485.

Slavin, J. A., Anderson, B. J., Baker, D. N., Benna, M., Boardsen, S. A., Gold, R. E., & Zurbuchen, T. H. (2012). MESSENGER and Mariner 10 flyby observations of magnetotail structure and dynamics at Mercury. *Journal of Geophysical Research*, 117, 1215. https://doi.org/10.1029/2011JA016900

Slavin, J. A., DiBraccio, G. A., Gershman, D. J., Imber, S. M., Poh, G. K., Zurbuchen, T. H., et al. (2014). MESSENGER observations of Mercury's magnetosphere under extreme solar wind conditions. *Journal of Geophysical Research: Space Physics, 119*(10), 8087–8116. https://doi.org/10.1002/2014JA020319.

Slavin, J., H. Middleton, J. Raines, X. Jia, J. Zhong, W. J. Sun, S. Livi, S. Imber, G. K. Poh, and M. Akhavan-Tafti (2019), MESSENGER observations of disappearing dayside magnetosphere events at Mercury, *Journal of Geophysical Research: Space Physics*, *124*(8), 6613-6635, doi:10.1029/2019JA026892.

Stout, Q. F., D. L. D. Zeeuw, T. I. Gombosi, C. P. T. Groth, H. G. Marshall, and K. G. Powell (1997), Adaptive Blocks: A High Performance Data Structure, paper presented at SC '97: Proceedings of the 1997 ACM/IEEE Conference on Supercomputing, 15-21 Nov. 1997.

Sun, W. J., S. Y. Fu, J. A. Slavin, J. M. Raines, Q. G. Zong, G. K. Poh, and T. H. Zurbuchen (2016), Spatial distribution of Mercury's flux ropes and reconnection fronts: MESSENGER observations, *Journal of Geophysical Research: Space Physics*, *121*(8), 7590-7607, https://doi.org/10.1002/2016JA022787.

Sun, T. R., B. B. Tang, C. Wang, X. C. Guo, and Y. Wang (2019), Large-Scale Characteristics of Flux Transfer Events on the Dayside Magnetopause, *Journal of Geophysical Research: Space Physics*, *124*(4), 2425-2434, https://doi.org/10.1029/2018JA026395.

Sun, W. J., Slavin, J. A., Smith, A. W., Dewey, R. M., Poh, G. K., Jia, X., et al. (2020), Flux Transfer Event Showers at Mercury: Dependence on Plasma β and Magnetic Shear and Their Contribution to the Dungey Cycle, *Geophysical Research Letters*, *47*(21), e2020GL089784, https://doi.org/10.1029/2020GL089784.

Sun, W., Slavin, J. A., Milillo, A., Dewey, R. M., Orsini, S., Jia, X., et al. (2022a), MESSENGER Observations of Planetary Ion Enhancements at Mercury's Northern Magnetospheric Cusp During Flux Transfer Event Showers, *Journal of Geophysical Research: Space Physics*, *127*(4), e2022JA030280, https://doi.org/10.1029/2022JA030280.

Sun, W., R. M. Dewey, S. Aizawa, J. Huang, J. A. Slavin, S. Fu, Y. Wei, and C. F. Bowers (2022b), Review of Mercury's dynamic magnetosphere: Post-MESSENGER era and comparative magnetospheres, *Science China Earth Sciences*, *65*(1), 25-74, https://doi.org/10.1007/s11430-021-9828-0.

Swisdak, M. (2016). Quantifying gyrotropy in magnetic reconnection. *Geophysical Research Letters, 43*, 43–49. https://doi.org/10.1002/2015GL066980.

Tóth, G. (2000), The ∇· B= 0 constraint in shock-capturing magnetohydrodynamics codes, *Journal of Computational Physics*, *161*(2), 605-652, doi:10.1006/jcph.2000.6519.

Tóth, G., Y. Ma, and T. I. Gombosi (2008), Hall magnetohydrodynamics on block-adaptive grids, *Journal of Computational Physics*, *227*(14), 6967-6984, doi:10.1016/j.jcp.2008.04.010.

Tóth, G., B. Van der Holst, I. V. Sokolov, D. L. De Zeeuw, T. I. Gombosi, F. Fang, W. B. Manchester, X. Meng, D. Najib, and K. G. Powell (2012), Adaptive numerical algorithms in space weather modeling, *Journal of Computational Physics*, *231*(3), 870-903, doi:10.1016/j.jcp.2011.02.006.

Tóth, G., Y. Chen, T. I. Gombosi, P. Cassak, S. Markidis, and I. B. Peng (2017), Scaling the ion inertial length and its implications for modeling reconnection in global simulations, *Journal of Geophysical Research: Space Physics*, *122*(10), 10,336-310,355, doi:10.1002/2017JA024189.

Trávníček, P. M., D. Schriver, P. Hellinger, D. Herčík, B. J. Anderson, M. Sarantos, and J. A. Slavin (2010), Mercury's magnetosphere–solar wind interaction for northward and southward interplanetary magnetic field: Hybrid simulation results, *Icarus*, *209*(1), 11-22, https://doi.org/10.1016/j.icarus.2010.01.008.

Wang, X., Y. Chen, and G. Tóth (2022), Global Magnetohydrodynamic Magnetosphere Simulation With an Adaptively Embedded Particle-In-Cell Model, *Journal of Geophysical Research: Space Physics*, *127*(8), e2021JA030091, https://doi.org/10.1029/2021JA030091.

Winslow, R. M., B. J. Anderson, C. L. Johnson, J. A. Slavin, H. Korth, M. E. Purucker, D. N. Baker, and S. C. Solomon (2013), Mercury's magnetopause and bow shock from

MESSENGER Magnetometer observations, *Journal of Geophysical Research: Space Physics*, *118*(5), 2213-2227, https://doi.org/10.1002/jgra.50237.

Winslow, R. M., Johnson, C. L., Anderson, B. J., Gershman, D. J., Raines, J. M., Lillis, R. J., et al. (2014). Mercury's surface magnetic field determined from proton-reflection magnetometry. *Geophysical Research Letters, 41*(13), 4463–4470. https://doi.org/10.1002/2014GL060258.

Zenitani, S., Hesse, M., Klimas, A., & Kuznetsova, M. (2011). New measure of the dissipation region in collisionless magnetic reconnection. *Physical Review Letters, 106*(19), 195,003.

Zhang, W., A. Myers, K. Gott, A. Almgren, and J. Bell (2021), AMReX: Block-structured adaptive mesh refinement for multiphysics applications, *The International Journal of High Performance Computing Applications*, *35*(6), 508-526, doi:10.1177/10943420211022811.

Zhou, H., G. Tóth, X. Jia, Y. Chen, and S. Markidis (2019), Embedded Kinetic Simulation of Ganymede's Magnetosphere: Improvements and Inferences, *Journal of Geophysical Research: Space Physics*, *124*(7), 5441-5460, https://doi.org/10.1029/2019JA026643.

Zhou, H., G. Toth, X. Jia, and Y. Chen (2020), Reconnection-driven dynamics at Ganymede's upstream magnetosphere: 3-D global Hall MHD and MHD-EPIC simulations, *Journal of Geophysical Research: Space Physics*, *125*(8), e2020JA028162, doi:10.1029/2020JA028162.

Zou, Y., B. M. Walsh, Y. Nishimura, V. Angelopoulos, J. M. Ruohoniemi, K. A. McWilliams, and N. Nishitani (2018), Spreading Speed of Magnetopause Reconnection X-Lines Using Ground-Satellite Coordination, *Geophysical Research Letters*, *45*(1), 80-89, https://doi.org/10.1002/2017GL075765.

Zurbuchen, T. H., Raines, J. M., Slavin, J. A., Gershman, D. J., Gilbert, J. A., Gloeckler, G., et al. (2011). MESSENGER observations of the spatial distribution of planetary ions near mercury. *Science, 333*(6051), 1862–1865. https://doi.org/10.1126/science.1211302.